REVEALING HIDDEN TOPOLOGIES IN PHOTONIC CRYSTALS

SAMUEL JOHN PALMER

Submitted in partial fulfillment for the degree of
Doctor of Philosophy (PhD)

Department of Physics
Faculty of Natural Sciences
Imperial College London
June 2021

DECLARATION

Except where otherwise noted, this thesis and the work within have been completed solely by myself under the supervision of Dr Vincenzo Giannini and Professor Richard Craster.

London, June 2021

Samuel John Palmer

ABSTRACT

This thesis is part of an effort to bring together two very active fields of physics: band topology and photonics. The field of band topology has revealed exotic phenomena such as robust, unidirectional edge states that occur at the interfaces between materials that belong to different topological phases. The Nobel Prize in Physics 2016 was awarded to Thouless, Haldane, and Kosterlitz, for predicting such phases in electronic systems where the topological edge states may revolutionise electronics and quantum computing. There is now great interest in reproducing such topological phases in photonics using *photonic crystals*: periodic nanostructures with tunable photonic bands. Realising such topological edge states in photonic devices could revolutionise optical data transport and optical quantum computing. In this thesis, we focus on two symmetry-protected topological phases that have been difficult to realise in photonics: the quantum spin-Hall effect (QSHE, protected by the fermionic time-reversal symmetry of electrons) and square-root topological semimetals (protected by chiral symmetry, also known as sublattice symmetry).

We introduce a new topological index for $C_2\mathcal{T}$ symmetric crystals that emulate the QSHE using the angular momentum of light to mimic the spin of electrons. For example, in 2015 Wu & Hu [1] proposed a photonic analogue of the QSHE where the crystalline symmetries and bosonic time-reversal symmetries of the photons generated a *pseudo-fermionic* time-reversal symmetry. Subsequent works suggested that this crystal was a trivial phase rather than a non-trivial QSHE phase. However, we believe that our new topological index demonstrates the non-trivial QSHE-like nature of the photonic crystal introduced by Wu & Hu while accounting for all of the valence bands determined from full-wave calculations.

We then study the topology of networks of voids and narrow connecting channels that are formed by the space between closely spaced perfect conductors. In photonics, chiral symmetry is often broken by long-range interactions, but Vanel *et al* [2] showed that such void-channel networks can be mapped to analagous mass-spring systems in an asymptotically rigorous manner and therefore have only short-range interactions. We demonstrate that topological tight-binding models, such as square-root semimetals, can be reproduced in these void-channel networks with appropriate boundary conditions.

Finally, we discuss an interesting application of closely spaced nanoscopic metallic particles in the mid-to-far infrared and larger wavelengths. We show that despite being composed of highly dispersive and lossy metals, the effective dielectrics are virtually dispersion-

free throughout the infrared spectrum and can be even more transparent than natural dielectrics such as germanium in the far-infrared. The effective index can be tuned locally, allowing us to design gradient-index lenses where light is guided by a continuously varied local refractive index. We propose a novel gradient-index lens that exploits the simultaneous transparency and high metallic filling fraction of the effective dielectrics to create intense 'doubly-enhanced' hotspots where light is focused on the microscale and the electric field 'squeezed' between the metallic particles on the nanoscale.

ACKNOWLEDGMENTS

There are many people I would like to thank for their support and encouragement over these years.

To my supervisors. Thank you Vincenzo for sharing your passion and enthusiasm for physics with me; the excitement with which I left some of our meetings kept me going and they will always be remembered as a highlight of the PhD. Thank you Richard for breaking down what seemed like an insurmountable thesis into pieces I could manage, and for always making time for me in what must have been one of the busiest years of your career.

To my academic sister, Marie. I cannot imagine how I would have stuck at this through the COVID-19 lockdowns without our virtual office. Thank you for always checking in, and congratulations for successfully defending your own thesis!

To my past and present housemates during the COVID-19 pandemic: Anthony, Denisse, Jermyn, and Eliot. Your company and friendship has been appreciated more than ever in such isolating times.

To Keenjee. You are more than I could have dreamed of. Thank you for your support and your patience. *Mahal kita*.

Finally, to my family. Thank you for raising me to be curious and encouraging me to persue my interests. I promise I am nearly done with school!

CONTENTS

Figure 4.5 (a) Schematic of an SSH-like void-channel chain that is analagous to the capped mass-spring chain introduced in Figure 4.4. The grey region is a perfect conductor, and the white is air. Only the beginning of the chain is shown. The bulk of the chain consists of equally sized voids of half-width H and length L connected by channels of alternating half-widths h_1 and h_2. The precise shapes of the voids and channels are defined in the main text. Note that the bulk region runs from $x = -L/4$ to $(N + 1/4)L$ such that we have well defined curvature at the narrowest point of each channel. The half-width at the end of the bulk region is h_{end}; the chain is then capped by larger voids that are roughly circular with diameter L. (b) Squared frequency spectrum of the void-channel chain (obtained via finite-element simulations, red crosses, $H = L/10$, $h_1 = H/400$, $h_2 = H/100$) and analagous mass-spring chain (obtained by solving the dynamical matrix equation, black dots, $k_1 = 0.01k_0$, $k_2 = 0.02k_0$, $m = 0.1m_0$, $M = \pi/4m_0$). The frequencies are normalised by $\omega_0 = \sqrt{k_0/m_0}$ for the mass-spring model and $\omega_0 = 2\pi c_0/L$ for the void-channel model. The chains consist of 20 masses/voids (or 22 including the pair of larger masses/voids at the end). (c-d) The magnetic field (red positive, blue negative) of the two edge modes of the void-channel chain. We see that the chain preserves chiral symmetry well: magnetic field is relatively weak in the large capping voids and each edge mode is well localised to just one sublattice. 100

LIST OF TABLES

ACRONYMS

BZ Brillouin Zone

QHE Quantum Hall Effect

QSHE Quantum spin-Hall Effect

SPT Symmetry Protected Topology

TE Transverse Electric

TM Transverse Magnetic

SSH Su-Schrieffer-Heeger

PWEM Plane-Wave Expansion Method

YIG Yttrium-Iron-Garnet

MG Maxwell Garnett

PC Perfect Conductor

GRIN Gradient-Index

DFT Discrete Fourier Transform

FEM Finite Element Method

FDFD Finite-Difference Frequency-Domain

PUBLICATIONS

Some ideas and figures have appeared previously in the following publications:

[1] S. J. Palmer, X. Xiao, N. Pazos-Perez, L. Guerrini, M. A. Correa-Duarte, S. A. Maier, R. V. Craster, R. A. Alvarez-Puebla, and V. Giannini. "Extraordinarily transparent compact metallic metamaterials." In: *Nature Communications* 10.1 (2019), pp. 1–7.

[2] S. J. Palmer and V. Giannini. "Peacock.jl: Photonic crystals in Julia." In: *Journal of Open Source Software* 5.54 (2020), p. 2678.

[3] S. J. Palmer and V. Giannini. "Berry bands and pseudo-spin of topological photonic phases." In: *Physical Review Research* 3.2 (2021), p. L022013.

[4] S. J. Palmer, Y. Ignatov, R. V. Craster, and M. Makwana. "Asymptotically exact photonic approximations of chiral symmetric topological tight-binding models." In: *New Journal of Physics* (2021), accepted for publication.

1 INTRODUCTION TO TOPOLOGICAL MATERIALS

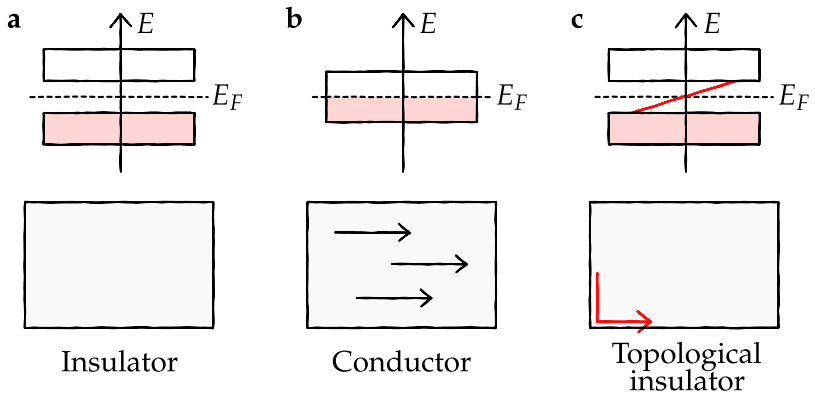

Figure 1.1: A comparison between **(a)** insulators, **(b)** conductors, and **(c)** a topological phase (the quantum Hall state). The upper panels show the energies, E, of the simplified band structures. The Fermi energy, E_F, is marked by the dashed line and the occupied bands are shaded. The lower panels show the conductivity of the materials. The topological state is a new phase of matter with an insulating interior and conducting surfaces.

1.1 OVERVIEW

Manufacturing topologically non-trivial phases of light could revolutionise fields such as optical data transport and optical quantum computing by eliminating losses due to backscattering. Topological photonics brings together two very active fields of physics: band topology, which was historically the topology of electronic bands, and photonics. We therefore begin the thesis with a review of the general background and state of the art of electronic topological phases, before introducing photonic systems in the following chapters. In this chapter, we review the discrete non-spatial symmetries (time-reversal, particle-hole, and chiral symmetry), and the 'ten-fold way' of classifying topological materials. We then introduce three gapped topological phases (the quantum Hall effect, the quantum spin-Hall effect, and the 1D Su-Schrieffer-Heeger model) and one gapless topological phase (topological semimetals). Our discussion will remain relatively qualitative throughout this chapter, focused on the definition and features of topological phases of matter. In the next chapter, we will describe the quantitative analysis of topological materials, including the calculation of topological indices from first principles.

1.2 AN INTRODUCTION TO TOPOLOGICAL PHASES OF MATTER

1.2.1 *Importance and applications*

For many years it was believed that electronic materials could be classed as either band insulators or (semi-)conductors based on the occupancy of the bulk bands, as shown in Figures 1.1a-b. However, the discovery of the QHE in the 1980s [3, 4] revealed that applying a strong magnetic field to a 2D metal could produce a third type of matter, shown in Figure 1.1c. This did not fit into either category as while the bulk bands resembled an insulator, the presence of gapless edge states across the valence-conduction band gap meant that the surface was conducting. Curiously, the surface states were also precisely quantised in number, extremely robust, and unidirectional—no backscattering was observed, even in the presence of disorder. This new type of material was later understood in terms of the topology of its band structure [4, 5].

Topology has proved to be a rich field in condensed matter theory, and as such the Nobel Prize in Physics of 2016 was awarded to Thouless, Haldane, and Kosterlitz "for theoretical discoveries of topological phase transitions and topological phases of matter" [6]. A topological band analysis[1] allows us to consider the bulk Hamiltonians of two materials and answer the following questions:

1. Is it necessary that a particular energy gap closes if we continuously deform between the Hamiltonians of the materials?[2]

2. If so, does this gap-closing condition result in any interesting phenomena at the interface between the two materials such as topologically protected edge states?

The unusual edge states of topological materials have attracted a great deal of attention for their possible applications. For example, in the QHE the current is so precisely quantised irrespective of particular microscopic details and disorder of the system that it is now used as part of the definition of the kilogram within the International System of Units (the SI units) [3, 8].

Topological materials could also provide a platform for electronic devices where electrons are transported without backscattering at

1 Note that topological band analysis is a subsection of topology. More advanced systems, particularly those with interacting components such as the fractional quantum Hall effect [7], require topological field theories. For this thesis where the focus is on the topology of non-interacting photonic bands, a topological band analysis will be sufficient.

2 This analysis can also pertain to gapless Hamiltonians such as topological semimetals where we consider a dimensional reduction of the Hamiltonian, $\hat{H}(k_1, k_2) \to \hat{H}_{k_2}(k_1)$, where the reduced Hamiltonian $\hat{H}_{k_2}(k_1)$ is gapped for certain values of k_2 and changing k_2 acts as a continuous deformation that can induce a topological phase transition (see Section 1.6).

impurities [9, 10], and materials that can be switched in and out of a topological phase by applying an external field could act as efficient transistors [11, 12]. Beyond traditional electronics, the charge transport in some topological materials is spin-polarised, presenting opportunities to develop spintronic devices [11, 13].

There is also hope that topological materials will offer a platform for fault-tolerant quantum computing [13–16]. In particular, the edge states of some topological materials are Majorana particles whose non-Abelian braiding statistics could be exploited for quantum computing. Topological quantum-bits are expected to be immune to some local causes of decoherence suffered by non-topological solid state spin-based quantum computers, such as electron-phonon interactions [15].

Although topological phases were first discovered in electronic systems, the underlying principles can be applied to wave systems in general, including photonic and acoustic systems [17, 18]. Just as discussed for their electronic counterparts, it is hoped that in the short to medium term, topological photonic materials could improve the performance of photonic devices by reducing backscattering, especially when guiding light around sharp corners, and in the longer term could offer a platform for fault-tolerant quantum computers in photonics [18–20]. One application that is unique to topological photonic materials is the design of more efficient lasers in which the topological edge mode acts as a cavity in which light propagates and is amplified unidirectionally and coherently despite imperfections in the crystal [21–23]. This was first proposed [24] and experimentally realised [25–27] in one-dimensional systems before being realised in a two-dimensional device [28]. Another application that is unique to topological photonics is the cloaking of large photon sources from each other using the polarisation of light [29].

1.2.2 *Topological phases and transitions*

Topology is the study of properties that are invariant when a system is smoothly and continuously deformed [30]. In topological materials the topological quantities are rather abstract and hard to visualise, arising from the manner in which the eigenmodes of the bands evolve as they are parallel transported around the BZ. Fortunately, more familiar examples of topology also exist in geometric surfaces.

An intuitive example of a topological property is the genus (number of holes) of a closed surface, as shown in Figure 1.2. The surfaces with the same genus are connected by continuous transformations, and are said to belong to the same topological phase: only a topological phase transition (in this case, adding or removing a hole) can change the genus.

Topological invariants are discrete, global properties of the system that label the topological phase. Although global quantities cannot

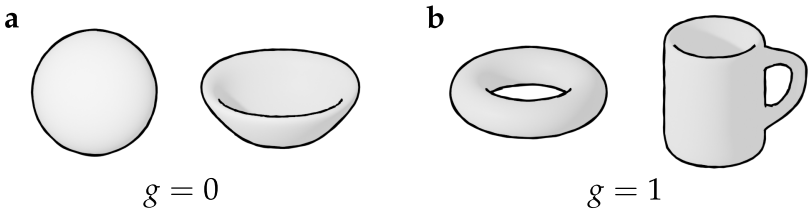

Figure 1.2: (a) A sphere can be continuously deformed to a bowl and (b) a torus can be continuously deformed to a coffee cup shape, but continuously deforming a sphere to a torus is impossible because a continuous deformation cannot add or remove holes in a surface. The topological invariant associated with the number of holes in a closed surface is the genus, g.

be determined by a single local measurement, they may be expressed as the integration of a local quantity over the global parameter space. This can help us understand the meaning of a "continuous" or "discontinuous" transformation. For example, the genus, g, may be expressed as an integral of the Gaussian curvature, $K(\vec{r})$, over the entire surface [16],

$$2(1-g) = \frac{1}{2\pi}\int_{\text{surface}} K(\vec{r})\,\mathrm{d}^2 r. \tag{1.1}$$

As the genus is invariant under continuous transformations and changes discretely with discontinuous transformations, we can deduce that a continuous transformation may redistribute but not increase or decrease the total curvature of the system. On the other hand, a discontinuous transformation must instantaneously change the total curvature by adding or removing a hole. We shall see later that there are similar curvatures and other topological quantities that may be defined upon band structures, based on the evolution of the eigenmodes as they are parallel transported around the BZ.

1.2.3 *Bulk-boundary correspondence and the periodic table of topological phases*

For us, the topological objects of interest are the energy bands embedded in the periodic crystal momentum space, $\vec{k}$. As a Hamiltonian is perturbed, a particular band or set of bands are said to deform continuously when they remain isolated from the other bands by an energy gap for all $\vec{k}$ [30, 31].

> *Definition 1:* Topological phase of a gapped Hamiltonian
> Two gapped Hamiltonians are in different topological phases when it is impossible to continuously deform from one to the other without closing the isolating energy gap [31].

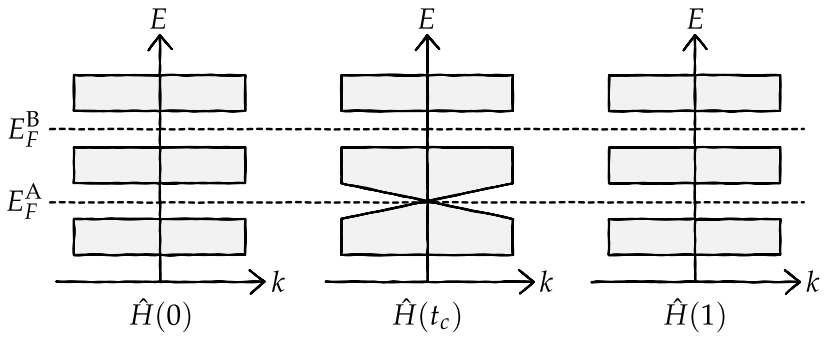

Figure 1.3: Whether we consider gapped Hamiltonians to be in different topological phases depends on the gap(s) that are of interest. In topological electronic systems, such as the quantum Hall effect, it is usually the topology of the valence-conduction band gap that is of interest. Consider the band energies, E, of the Hamiltonians $\hat{H}(0)$ and $\hat{H}(1)$, where the lower of the two energy gaps closes for any smooth and continuous deformation between the Hamiltonians, as depicted by the critical Hamiltonian $\hat{H}(t_c)$. In the quantum Hall effect the parameter t may relate to the strength of a time-reversal symmetry breaking perturbation such as the external magnetic field strength. As a result of this band-closing condition, we would expect chiral edge states to emerge in the lower gap at an interfaces between the two materials. If the Fermi level lay in the lower energy gap, $E_F = E_F^{\mathrm{A}}$, such that the existence of partially filled chiral edge states in the lower gap would contribute to the quantum Hall conductance of the material, then we would say that the two Hamiltonians belonged to *different* quantum Hall phases. On the other hand, if the Fermi level lay in the upper energy gap, $E_F = E_F^{\mathrm{B}}$, the chiral edge states of the lower gap would be completely filled and would not contribute to the quantum Hall conductance. In that case, we would say that two Hamiltonians belonged to the *same* quantum Hall phase.

For materials of particular dimensions, such as the 2D electron gas in the QHE, this "gap-closing" condition can lead to unusual phenomena such as robust unidirectional transport at the interfaces of two materials belonging to different topological phases. This is because far away from the interfaces, each material is well described by the respective bulk Hamiltonian, but the topological phase transition across the interface ensures the existence of states localised to the interface that span the energy gap [10]. The robustness may be understood by modeling the states near the interface as Dirac Hamiltonians with a spatially dependent mass that inverts sign at the interface [32].

> *Definition 2:* Bulk-boundary correspondence
>
> The existence of observable phenomena such as robust topological edge states that arise at the boundary between two different topological phases is known as a bulk-boundary correspondence [33].

If there are multiple isolating gaps, then whether we say that two Hamiltonians belong to the same or different topological phases depends on which isolating gap is of interest to us. In electronic systems, this is usually the valence-conduction band gap. For example, in Figure 1.3 we have a pair of hypothetical Hamiltonians, $\hat{H}(0)$ and $\hat{H}(1)$, where it is impossible to deform between the two without closing and reopening the isolating energy gap between the lowest two sets of bands. If the emergence of topological phenomena in the lower isolating gap was more interesting, for example if the Fermi energy lay at $E_F = E_F^{\mathrm{A}}$ such that the existence of topological edge states spanning this gap would affect the conductivity of the interface, then we would say that $\hat{H}(0)$ and $\hat{H}(1)$ belonged to different topological phases. On the other hand, if the Fermi energy lay at $E_F = E_F^{\mathrm{B}}$, then we may say that $\hat{H}(0)$ and $\hat{H}(1)$ belonged to the same topological phase. In other words, a topological analysis can allow us to predict particular phenomena within a common band gap at the interface between two materials but the analysis, including the classification of topological phase, depends on the band gap(s) we are interested in.

The topological classification of gapped Hamiltonians can be refined further by symmetries [34–36]. These Symmetry Protected Topology (SPT) phases may also have topologically protected gapless edge states, depending on the dimension of the material and the particular symmetries that are present.

> *Definition 3:* Symmetry-protected topological phase
>
> Two gapped Hamiltonians belong to different symmetry-protected phases when it is impossible to continuously deform from one to the other without closing the isolating gap or breaking the protecting symmetry [31].

Symmetry classes and the ten-fold way

Table 1.1 is known as the periodic table of topological insulators (and superconductors). It shows the relationship between dimension, symmetry class, and number of topologically edge states for the different discrete non-spatial symmetry classes of gapped Hermitian systems.[3] Each material is labelled as either 0, $\mathbb{Z}_2$, or $\mathbb{Z}$, meaning that there is one, two, or an arbitrary integer number of topological phases for this symmetry class and dimension, as shown in Figure 1.4. In this section, we explain why the three discrete non-spatial symmetries (time-reversal symmetry ($\mathcal{T}$), particle-hole symmetry ($\mathcal{C}$), and chiral symmetry ($\mathcal{S}$, also known as sublattice symmetry)) lead to ten unique symmetry classes.

In materials with time-reversal symmetry, the anti-unitary operator $\hat{\mathcal{T}}$ acts on the Bloch Hamiltonian as [10]

$$\hat{\mathcal{T}}\hat{H}(\vec{k})\hat{\mathcal{T}}^{-1} = \hat{H}(-\vec{k}). \tag{1.2}$$

The time-reversal operator squares to $+1$ for bosonic systems and to -1 for fermionic systems. Similarly, the particle-hole symmetry acts on the Bloch Hamiltonian as [10]

$$\hat{\mathcal{C}}\hat{H}(\vec{k})\hat{\mathcal{C}}^{-1} = -\hat{H}(-\vec{k}), \tag{1.3}$$

where $\hat{C}$ is an anti-unitary operator that squares to either ± 1.

Finally, chiral symmetry acts on the Bloch Hamiltonian as [10]

$$\hat{\mathcal{S}}\hat{H}(\vec{k})\hat{\mathcal{S}}^{-1} = -\hat{H}(\vec{k}), \tag{1.4}$$

where $\hat{\mathcal{S}}$ is a unitary operator that squares to $+1$.

While chiral symmetry may be constructed by composing time-reversal and particle hole-symmetry, $\hat{\mathcal{S}} = \hat{\mathcal{T}} \cdot \hat{\mathcal{C}}$, a system can also be chiral symmetric even if both $\mathcal{T}$ and $\mathcal{C}$ are broken [36]. Consider, for example, a Hamiltonian where the sites belong to either sublattice A or sublattice B. We define $\hat{P}_\mathrm{A}$ and $\hat{P}_\mathrm{B}$ as the projectors to each sublattice, which obey $\hat{P}_\mathrm{A} + \hat{P}_\mathrm{B} = \hat{I}$ and $\hat{P}_\mathrm{A}\hat{P}_\mathrm{B} = 0$ [33]. If there are no A-A or B-B coupling terms in the Hamiltonian, then $\hat{P}_\mathrm{A}\hat{H}\hat{P}_\mathrm{A} = \hat{P}_\mathrm{B}\hat{H}\hat{P}_\mathrm{B} = 0$ and we may express the Hamiltonian as

$$\hat{H} = \hat{P}_\mathrm{A}\hat{H}\hat{P}_\mathrm{B} + \hat{P}_\mathrm{B}\hat{H}\hat{P}_\mathrm{A}. \tag{1.5}$$

We may then define the chiral symmetry operator as $\hat{S} = \hat{P}_\mathrm{A} - \hat{P}_\mathrm{B}$, such that [33, 37]

$$\hat{S}\hat{H}(\vec{k})\hat{S}^{-1} = \cancelto{0}{\hat{P}_\mathrm{A}\hat{H}\hat{P}_\mathrm{A}} - \hat{P}_\mathrm{A}\hat{H}\hat{P}_\mathrm{B} + \cancelto{0}{\hat{P}_\mathrm{B}\hat{H}\hat{P}_\mathrm{B}} - \hat{P}_B\hat{H}\hat{P}_\mathrm{A} = -\hat{H}(\vec{k}), \tag{1.6}$$

3 Note that Table 1.1 is not a complete table of gapped topological phases; there are also (i) those protected by crystalline symmetries, (ii) those without gapless surface states, and (iii) those with non-Hermitian Hamiltonians [10].

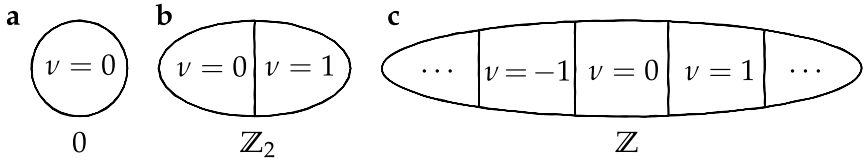

Figure 1.4: Meaning of the 0, $\mathbb{Z}_2$, and $\mathbb{Z}$ that appear in the periodic table of insulators. Each ellipse represents the parameter space of gapped Hamiltonians with a particular dimension and symmetry class. (a) If there are no topological phase transitions when continuously deforming between all gapped Hamiltonians in the parameter space then every phase belongs to the trivial phase, $\nu = 0$. (b) If every Hamiltonian in the parameter space belongs to one of two topological phases, then the topological phases are labelled with a $\mathbb{Z}_2$ topological index, $\nu = 0$ (trivial) or $\nu = 1$ (topological). (c) If the Hamiltonians in the parameter space belong to an arbitrary integer number of different topological phases, then the topological phases are labelled with a $\mathbb{Z}$ topological index, $\nu = 0$ (trivial) or $\nu \neq 0$ (topological).

where we have used $\hat{S}^{-1} = \hat{S}^\dagger = \hat{P}_A^\dagger - \hat{P}_B^\dagger = \hat{P}_A - \hat{P}_B$. In other words, while an ordinary unitary symmetry that commutes with the Hamiltonian allows $\hat{H}$ to be block diagonalised, the chiral symmetry operator *anti-commutes* with the Hamiltonian and $\hat{H}$ may instead be "block off-diagonalised",

$$\hat{H} \begin{bmatrix} \psi_A \\ \psi_B \end{bmatrix} = \begin{bmatrix} 0 & \hat{H}_{AB} \\ \hat{H}_{AB}^\dagger & 0 \end{bmatrix} \begin{bmatrix} \psi_A \\ \psi_B \end{bmatrix}, \tag{1.7}$$

with A-B coupling terms between the different sublattices only. It is for this reason that chiral symmetry is often referred to as sublattice symmetry, particularly in tight-binding models where the electron sites lie on two different sublattices connected by nearest-neighbour couplings such as those we will study in Chapter 4.

The different combinations of time-reversal, particle-hole, and chiral symmetries result in 10 distinct symmetry classes as shown in the first column of Table 1.1. The symmetries of these classses are shown in the following columns, where a 0 indicates that a particular symmetry is not present, whereas a ± 1 indicates that the symmetry is present and squares to ± 1, respectively. This classification is sometimes known as the "ten-fold way" [36, 38, 39] and arises as follows. Time-reversal and particle-hole symmetry may be considered independently, and there are three options for each (0, -1, or $+1$) leading to 9 combinations. Including chiral symmetry in our considerations only increases the number of symmetry classes by one. This is because the presence of chiral symmetry is uniquely determined for 8 of the 9 combinations of time-reveral and particle-hole symmetry. The exception is when

Class	Symmetries			Dimension, d							
	$\mathcal{T}$	$\mathcal{C}$	$\mathcal{S}$	1	2	3	4	5	6	7	8
A	0	0	0	0	$\boxed{\mathbb{Z}}$	0	$\mathbb{Z}$	0	$\mathbb{Z}$	0	$\mathbb{Z}$
AIII	0	0	1	$\boxed{\mathbb{Z}}$	0	$\mathbb{Z}$	0	$\mathbb{Z}$	0	$\mathbb{Z}$	0
AI	+1	0	0	0	0	0	$\mathbb{Z}$	0	$\mathbb{Z}_2$	$\mathbb{Z}_2$	$\mathbb{Z}$
BDI	+1	+1	1	$\mathbb{Z}$	0	0	0	$\mathbb{Z}$	0	$\mathbb{Z}_2$	$\mathbb{Z}_2$
D	0	+1	0	$\mathbb{Z}_2$	$\mathbb{Z}$	0	0	0	$\mathbb{Z}$	0	$\mathbb{Z}_2$
DIII	−1	+1	1	$\mathbb{Z}_2$	$\mathbb{Z}_2$	$\mathbb{Z}$	0	0	0	$\mathbb{Z}$	0
AII	−1	0	0	0	$\boxed{\mathbb{Z}_2}$	$\mathbb{Z}_2$	$\mathbb{Z}$	0	0	0	$\mathbb{Z}$
CII	−1	−1	1	$\mathbb{Z}$	0	$\mathbb{Z}_2$	$\mathbb{Z}_2$	$\mathbb{Z}$	0	0	0
C	0	−1	0	0	$\mathbb{Z}$	0	$\mathbb{Z}_2$	$\mathbb{Z}_2$	$\mathbb{Z}$	0	0
CI	+1	−1	1	0	0	$\mathbb{Z}$	0	$\mathbb{Z}_2$	$\mathbb{Z}_2$	$\mathbb{Z}$	0

Table 1.1: Periodic table of (Hermitian) d-dimensional topological phases with topologically protected $(d-1)$-dimensional surface states arising from the discrete non-spatial symmetries: time-reversal symmetry ($\mathcal{T}$), particle-hole symmetry ($\mathcal{C}$), and chiral symmetry ($\mathcal{S}$, also known as sublattice symmetry) [36]. The numbers in the symmetries column are 0 if the symmetry is not necessarily present, and if the symmetry is enforced then the number indicates whether the symmetry squares to $+1$ or -1. Of particular interest to us are the SSH (class AIII in one dimension), QHE (class A in two dimensions), and QSHE (class AII in two dimensions) topological phases, which have been marked with boxes.

neither time-reversal or particle-hole symmetry are present, resulting in 10 symmetry classes.

In Table 1.1 each dimension and symmetry class is labelled as either 0, $\mathbb{Z}_2$, or $\mathbb{Z}$, meaning that a gapped Hamiltonian of these symmetries and dimension may belong to either a single (trivial) phase, to one of a pair of symmetry-protected phases, or to one of an infinite number of symmetry-protected phases, respectively, as shown in Figure 1.4. This can be determined using methods such as K-theory [35], homotopy groups [34], and dimensional reduction [36].

In the next sections we will review three instances of topological phases in electronics. These have been marked by boxes in Table 1.1. First, we will discuss the QHE (a two-dimensional $\mathbb{Z}$ topological phase, class A). This will introduce the Chern number as a topological index, and act as a stepping stone to our next topological phase, the QSHE (a two-dimensional $\mathbb{Z}_2$ phase protected by fermionic time-reversal symmetry, class AII). The QSHE will allow us to see how the topological indices of symmetry-protected phases can be calculated by decomposing the valence band space into subspaces according to the symmetry, and is particularly relevant to Chapter 3 where we calculate the topological index of a photonic analogue of the QSHE. Finally, we discuss the SSH model of trans-polyacetylene (a one-dimensional $\mathbb{Z}$ phase protected by chiral symmetry, class AIII), in order to form a better understanding of how chiral (sublattice) symmetry results in zero energy edge modes, in preparation for Chapter 4 where we study photonic lattices with chiral symmetric limits.

1.3 THE QUANTUM HALL EFFECT

1.3.1 *Landau levels and chiral edge states*

The integer quantum Hall effect, where the Hall conductance is precisely quantised,[4] was first observed in two-dimensional metallic systems exposed to strong magnetic fields at low temperatures [3]. The current was carried in a number of *chiral edge states* [40], meaning that the electrons of these states propagate unidirectionally around the boundary of the sample. This behaviour may be understood semi-classically as the skipping of cyclotron orbits at the edge of the system as shown in Figure 1.5a. At the surfaces, the motion is unidirectional as there are no backwards traveling states for the electrons to backscatter into [41].

The number of edge states is equal to the number of occupied Landau levels (energy levels resulting from the quantisation of the cy-

4 Note that in interacting systems there also exists a fractional quantum Hall effect where the resistance is quantised in fractions of integers [7]. However, we are interested in non-interacting systems and will generally take "quantum Hall effect" to mean "integer quantum Hall effect".

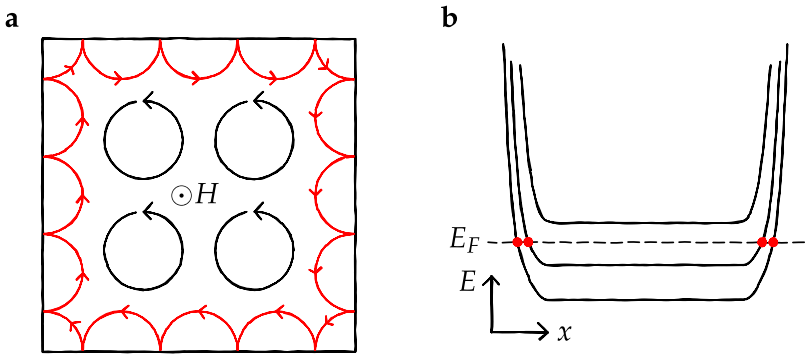

Figure 1.5: (a) Cyclotron orbits of electrons in a strong magnetic field, $\vec{H}$, result in chiral edge states that travel one way around the boundary of the surface. The quantisation of this motion results in Landau levels in the energy spectrum. (b) The energies, E, of the Landau levels increase at the surface of the material. The number of chiral edge states is equal to the number of Landau levels crossing the Fermi level, E_F, at the edge of the material (red circles).

clotron orbits) [41]. Although the QHE resembles an ordinary insulator in the bulk where the occupied and unoccupied states are separated by an energy gap, the confinement of the electrons increases the energy of the Landau levels near the surface resulting in energy states that span the valence-conduction band gap,[5] as shown in Figure 1.5b. The quantum Hall conductance is proportional to the number of these perturbed Landau levels crossing the Fermi level [40].

Although we introduced the QHE in the context of a two-dimensional electron gas in a strong external magnetic field (for historical reasons and for the intuitive imagery of chiral edge states in terms of skipping cyclotron orbits), it was later shown to have topological origins [4] and is a more general phenomenon of gapped Hamiltonians with broken time-reversal symmetry [5]. In particular, the QHE belongs to symmetry class A in two dimensions, which has a $\mathbb{Z}$ topological index as in Table 1.1. In the next sections we will explain how this topological index may be calculated from the *Chern numbers* of the valence bands.

5 The Landau levels resemble the band structure of a regular insulator with a well defined wavevector $\vec{k}$ if we take a unit cell with area hc/eB enclosing a flux quantum [41].

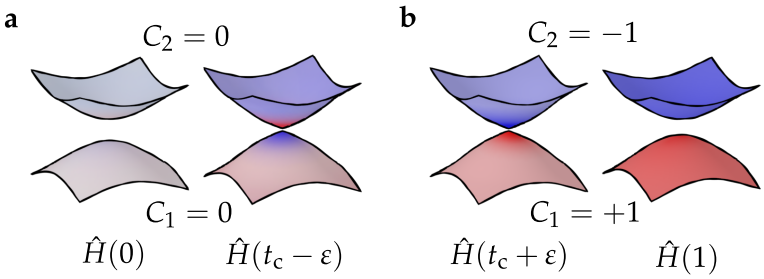

Figure 1.6: The individual Berry curvatures of a pair of bands are not well defined at a degeneracy. Here we sketch the Berry curvature of a two-band Hamiltonian, $\hat{H}(t)$, before and after a topological phase transition at $t = t_c$. Away from the degeneracy the Berry curvatures are finite and well defined. As we approach the degeneracy, $\hat{H}(t_c \pm \epsilon)$ for small ϵ, the Berry curvatures begin to concentrate and diverge near the band crossing. **(a)** Before the topological phase transition, the Chern number of the lower band, C_1, and the upper band, C_2, are both zero. **(b)** After the topological phase transition, the total Chern number is unchanged, but the individual Chern numbers have changed. Berry curvature was exchanged between the bands at the degeneracy.

1.3.2 *Berry curvature and Chern numbers*

The Chern number, C_n, of a single band that is isolated from all other bands by an energy gap for all $\vec{k}$ may be expressed as an integral of a local quantity over the Brillouin zone,[6]

$$C_n = \frac{1}{2\pi} \int_{\mathrm{BZ}} \mathcal{F}_n(\vec{k}) \, \mathrm{d}^2 k, \tag{1.8}$$

where the integrand,

$$\mathcal{F}_n(\vec{k}) = i \left[\left\langle \frac{\partial u_n}{\partial k_x} \middle| \frac{\partial u_n}{\partial k_y} \right\rangle - \left\langle \frac{\partial u_n}{\partial k_y} \middle| \frac{\partial u_n}{\partial k_x} \right\rangle \right], \tag{1.9}$$

is the *Berry curvature* of the nth band and describes how the eigenmodes of the band evolve as they are parallel transported through $\vec{k}$-space (see Section 2.5.1.1). This is closely analagous to Equation (1.1) for the genus of a geometric surface.

In Section 1.2.3 we stated that a set of bands deforms continuously when they remain isolated from the other bands by an energy gap for all $\vec{k}$. It may not be obvious why closing an energy gap between bands should be analagous to poking a hole in a geometric surface. In Chapter 2, when we show how to evaluate the Chern number numerically, we shall see that the Chern number is quantised and may

6 We are able to define a Brillouin zone for the QHE by taking the unit cell as the area enclosing a flux quantum, as noted in the previous footnote.

be interpretated as the number of obstructions to a process known as Wannierisation, where the Bloch bands are Fourier transformed to an exponentially localised basis known as the Wannier states [42, 43]. For now, the role of the Chern number as a topological index can be understood by considering the Berry curvature of the bands before, near, and after a topological phase transition.

Figure 1.6 shows a hypothetical two-band Hermitian Hamiltonian, $\hat{H}(t)$, that is smoothly deformed from $t = 0$ to $t = 1$ with the isolating gap between the bands closing at $t = t_c$. Away from the phase transition, the Berry curvature is finite and well defined, and the Chern number of each band is integer as will be demonstrated in Section 2.5.3. In this example, for $t < t_c$ the positive and negative Berry curvature within each band cancel and Chern number of each band is $C_1 = C_2 = 0$, as shown in Figure 1.6a. However, as the Hamiltonian approaches the degeneracy, $t \to t_c - \varepsilon$ for small ε, the Berry curvature begins to concentrate in the region where the bands are close to touching, approaching the form of a delta function [44]. As the gap closes, the Berry curvature of each band diverges and becomes ill-defined[7]. When the isolating gap reopens for $t > t_c$, we see from Figure 1.6b that the bands have exchanged Berry curvature and the Chern numbers of the lower and upper bands are $C_1 = +1$ and $C_2 = -1$, respectively.

1.3.3 *Chern numbers and the $\mathbb{Z}$ topological index*

Although Equation (1.9) for the Berry curvature of a single band may not be well defined at band crossings, there is a multiband formulation for the Berry curvature of a set of bands. We will introduce the multiband Berry curvature formally in Section 2.6. Until then, it is sufficient to note that in the multiband formulation the *total* Berry curvature of a set of bands remains well defined even if there are crossings between bands within the set, so long as the bands inside the set are isolated from all other bands outside of the set by an energy gap. For example, in Figure 1.6 the total Berry curvature of the two bands remains finite and well defined for all t, even as the individual Berry curvatures diverge as $t \to t_c$.

In the QHE, the $\mathbb{Z}$ topological index is the total Chern number of all the valence bands.[8] It can be shown [45] that the net number of chiral edge states spanning the valence-conduction gap between two QHE states is

$$N_R - N_L = C_{val}^{II} - C_{val}^{I}, \tag{1.10}$$

7 In fact, the Berry curvature of the individual bands at the degeneracy of the critical Hamiltonian is not well defined as either positive or negative. This is because the Berry phase around a Dirac cone is -1 [33].

8 Each Landau level carries a of Chern number of $+1$. The total Chern number of the occupied states, C_{val}, is therefore equivalent to the number of occupied Landau levels [41].

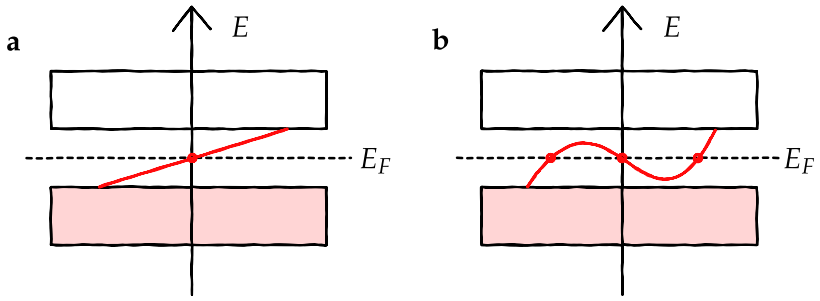

Figure 1.7: Panels (a) and (b) show the band energies, E, of two different realisations of the same quantum Hall phase, with the chiral edge states shown in red. In (a), there is one right travelling chiral edge state crossing the Fermi level, E_F. In (b), there are two right travelling and one left travelling chiral edge states that cross the Fermi level. The net number of right travelling chiral edge states is the same for both realisations of the same quantum Hall phase. Recreation of a figure from [41].

where $C^{\mathrm{I/II}}_{\mathrm{val}} = \sum_{n\in\mathrm{val}} C^{\mathrm{I/II}}_n$ are the total Chern numbers of the valence bands of the first and second material, respectively. It is important to consider the total Chern number of all the valence bands as we must be sure that it is the valence-conduction band gap that closes if we attempt to deform between two Hamiltonians with different topological indices. It is this gap-closing condition that leads to the emergence of the chiral edge states, which only contribute to the conductivity if they span the valence-conduction band gap.

As shown in Figure 1.7, deformations of the system that do not close the valence-conduction gap of the bulks can create or destroy edge states, but only in counter-propagating pairs [41]. The net number of propagating edge states spanning the valence-conduction gap is topologically protected. No symmetry is needed to protect this bulk-boundary correspondence, and the gapless edge states will occur at any interface between the materials, regardless of what symmetries it may break.

While there are no symmetries that must be protected for the QHE, the breaking of time-reversal symmetry is necessary for a non-trivial QHE phase. This is because the Berry curvature of time-reversal symmetric systems is odd, $\mathcal{T}\mathcal{F}_n(\vec{k})\mathcal{T}^{-1} = -\mathcal{F}_n(-\vec{k})$ (see Section 2.5.3.3), and therefore the Chern number will integrate to zero in time-reversal symmetric systems [44]. In the next section, we will see that there are cases where the valence bands can be decomposed by symmetry. This can allow non-zero Chern number in different subspaces of $\mathcal{H}_{\mathrm{val}}$, even if the system is time-reversal symmetric and the total Chern number of the valence band space is zero.

1.4 THE QUANTUM SPIN-HALL EFFECT

1.4.1 *Spin-Chern numbers and helical edge states*

The discovery of the QHE was followed by the closely related quantum spin Hall effect (QSHE), in which there is net *spin-polarised* Hall conductance rather than an overall Hall conductance [46, 47]. Again, this phenomena was shown to have a topological origin, occuring at the interface between two-dimensional materials in different topological phases. Unlike the QHE, the QSHE is a $\mathbb{Z}_2$ symmetry-protected phase, meaning that it is either trivial or non-trivial, whose existence relies on the fermionic time-reversal symmetry of the electrons (class AII in two dimensions).

The topological protection provided by the fermionic time-reversal symmetry is most easily seen by first considering a special case where the out-of-plane spin of the electrons is also conserved, and then deducing which edge states are protected by fermionic time-reversal symmetry even when spin-nonconserving processes are introduced as in Figure 1.8. The spin-conserving Hamiltonians may be considered as two copies of the QHE acting on the different spin spaces [41],

$$\hat{H}|\psi\rangle = \begin{bmatrix} \hat{H}_{\text{QHE}} & 0 \\ 0 & \mathcal{T}\hat{H}_{\text{QHE}} \end{bmatrix} \begin{bmatrix} |\psi_\uparrow\rangle \\ |\psi_\downarrow\rangle \end{bmatrix}. \tag{1.11}$$

By time-reversal symmetry, the total Chern number of all valence bands must be zero, but the Chern numbers of the spin-up valence bands and spin-down valence bands are equal and opposite,

$$C_{\text{val}} = C_\uparrow + C_\downarrow = 0. \tag{1.12}$$

In the special case where perpendicular spin component is conserved (including at the edges of the material) then the edge spectrum consists of $C_\uparrow$ spin-up polarised and $C_\downarrow$ spin-down polarised gapless edge states [41], as shown in Figures 1.8ai and bi. These edge states where spin up and spin down currents propagate in opposite directions are known as *helical edge states*, in analogy with the helicity of particles where spin and momentum are correlated [41].

In the QSHE, the perpendicular spin is not necessarily conserved and the crossings between edge states of opposite spin can be gapped out. If time-reversal symmetry is broken, for example by magnetic impurities, then the edge spectra shown in both Figures 1.8a-b could be gapped out [33]. However, recall from Section 1.2.3 that if fermionic time-reversal symmetry is present, then it will protect the crossings between Kramers' pairs at time-reversal invariant momenta, shown in blue in Figures 1.8a-b. Consequently, only *pairs of crossings* at $\pm\vec{k}$ can be gapped, and lifting spin-conservation can only change the number of edge states by an even number. This ensures that the spin-conserving systems with an odd $C_\uparrow$ or $C_\downarrow$ will always retain at least

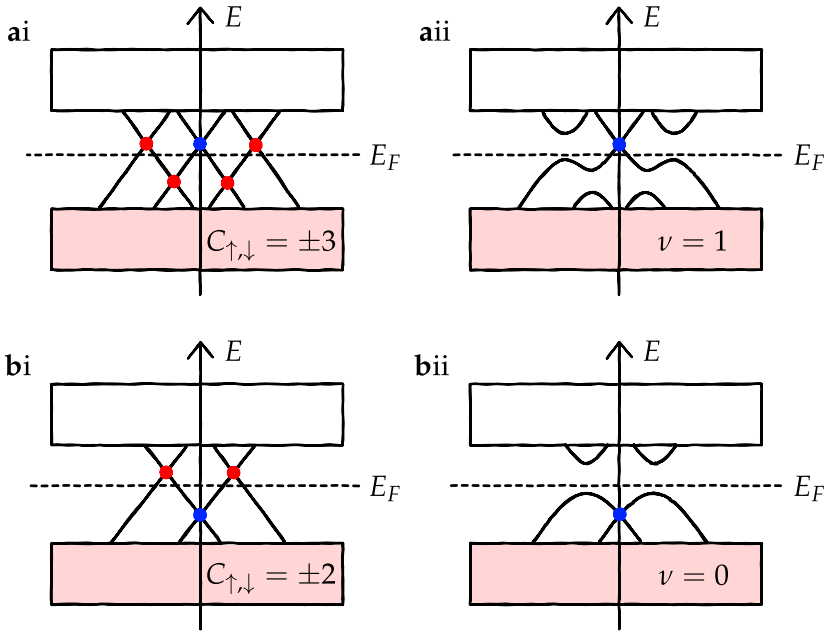

Figure 1.8: Sketches of the edge states in the quantum spin-Hall effect (QSHE) before and after breaking spin-conservation. The crossings between Kramers' partners at time-reversal invariant momenta (blue circles) are protected by fermionic time-reversal symmetry, whereas other crossings between edge states with opposite spin (red circles) may be gapped when spin-conservation is broken. (a) Non-trivial states always have at least one pair of edge states crossing the Fermi level, E_F, which cannot be removed without breaking time-reversal symmetry or closing the valence-conduction band gap. (ai) When spin is conserved we may use the Chern numbers of the spin up and down bands, $C_\uparrow$ and $C_\downarrow$, to predict that there are $C_{\text{spin}} = C_\uparrow - C_\downarrow$ helical edge states in total. (aii) Introducing non-spin-conserving perturbations can gap the crossings between edge states of opposite spin, except for those at the time-reversal invariant momenta. Afterwards, the spin Chern numbers are no longer defined. However, if we begin with odd $C_\uparrow$ and $C_\downarrow$, there will always be at least one pair of edge states crossing the Fermi level. (b) If we begin with an even $C_\uparrow$ and $C_\downarrow$, there is no guarantee that there will be any edge states crossing the Fermi level after spin-nonconserving perturbations are introduced. The QSHE is therefore a $\mathbb{Z}_2$ topological phase with topological index $\nu = C_\uparrow \bmod 2 = C_\downarrow \bmod 2$.

one pair of gapless edge states even after spin-nonconserving terms are introduced, as shown in Figure 1.8aii, whereas the edge spectrum of spin-conserving systems with an even $C_\uparrow$ or $C_\downarrow$ may be gapped completely, as in Figure 1.8bii [41].

1.4.2 *The $\mathbb{Z}_2$ topological index*

The argument above indicates that there is a $\mathbb{Z}_2$ topological phase protected by fermionic time-reversal symmetry, and for the special cases where spin is conserved we may identify the topological invariant as the parity of the spin-Chern numbers,

$$\nu = \mathrm{mod}_2\left(C_\uparrow\right) = \mathrm{mod}_2\left(C_\downarrow\right), \tag{1.13}$$

where $\nu = 0$ indicates the trivial phase and $\nu = 1$ indicates the topological phase [41]. More generally, when spin is not conserved ν may be determined by decomposing the valence band space into two subspaces,

$$\mathcal{H}_{\mathrm{val}} = \mathcal{H}_1 \oplus \mathcal{H}_2, \tag{1.14}$$

ensuring that the projectors to each subspace, $\hat{P}_i(\vec{k})$, are smooth and continuous functions of $\vec{k}$, and that each subspace contains the Kramers' partners of the other subspace [43],

$$\hat{P}_1(+\vec{k}) = \mathcal{T}\hat{P}_2(-\vec{k})\mathcal{T}^{-1}. \tag{1.15}$$

A Chern number may be calculated for each subspace (see Chapter 2), and from this we may then determine ν,

$$\nu = \mathrm{mod}_2\left(C_1\right) = \mathrm{mod}_2\left(C_2\right). \tag{1.16}$$

Note that this is a more general case of Equation (1.13), and retains its meaning even if $C_\uparrow$ and $C_\downarrow$ lose their meaning if spin-nonconserving processes are introduced [41].

In Chapter 3 we will introduce a new method to calculate pseudo-spin Chern numbers of topological photonic crystals, where the spin is emulated by the orbital angular momentum of the light and the topological phase is protected by a combination of bosonic time-reversal symmetry and crystalline symmetries.

1.5 THE SU-SCHRIEFFER-HEEGER MODEL

1.5.1 *Edge states in trans-polyacetylene*

The SSH model is an example of a symmetry-protected phase in 1D. The model was originally proposed as a nearest-neighbour tight-binding approximation of trans-polyacetylene [48], which consists of

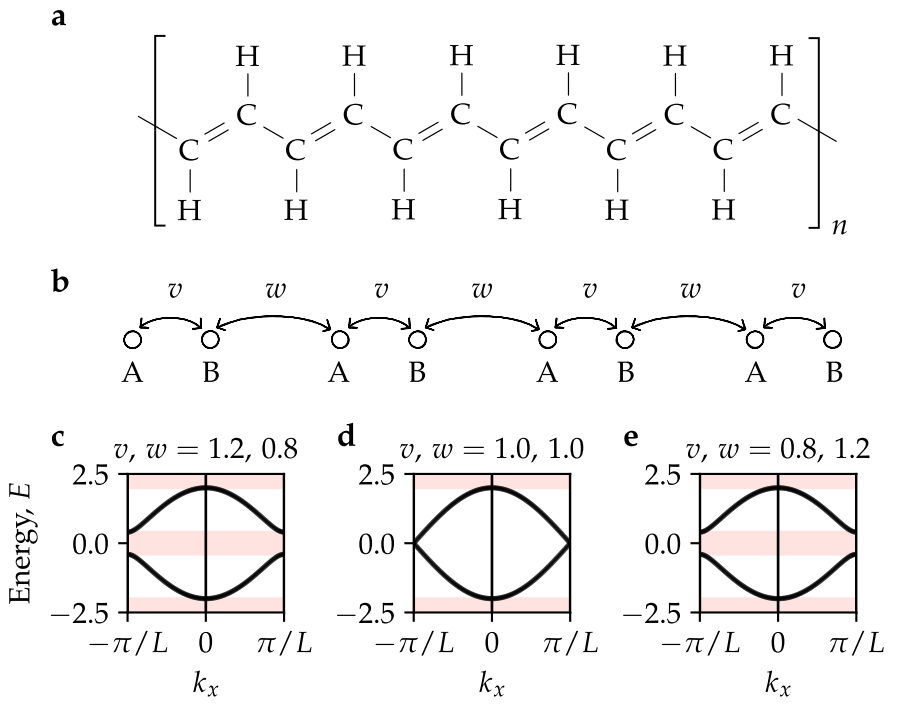

Figure 1.9: (a) Trans-polyacetylene consists of a carbon backbone of alternating single and double bonds. (b) The simplest tight-binding model of trans-polyacetylene, known as the Su-Schrieffer-Heeger model, consists of two carbon atoms per unit cell, one at site A and one at site B. The hydrogen atoms are neglected, and the alternating single and double bonds between the carbon atoms are represented by alternating hopping parameters, v and w. (c-e) Energy eigenvalues of the bulk chain for different pairs of hopping parameters. In the bulk, the energy spectrum is invariant under $v \leftrightarrow w$.

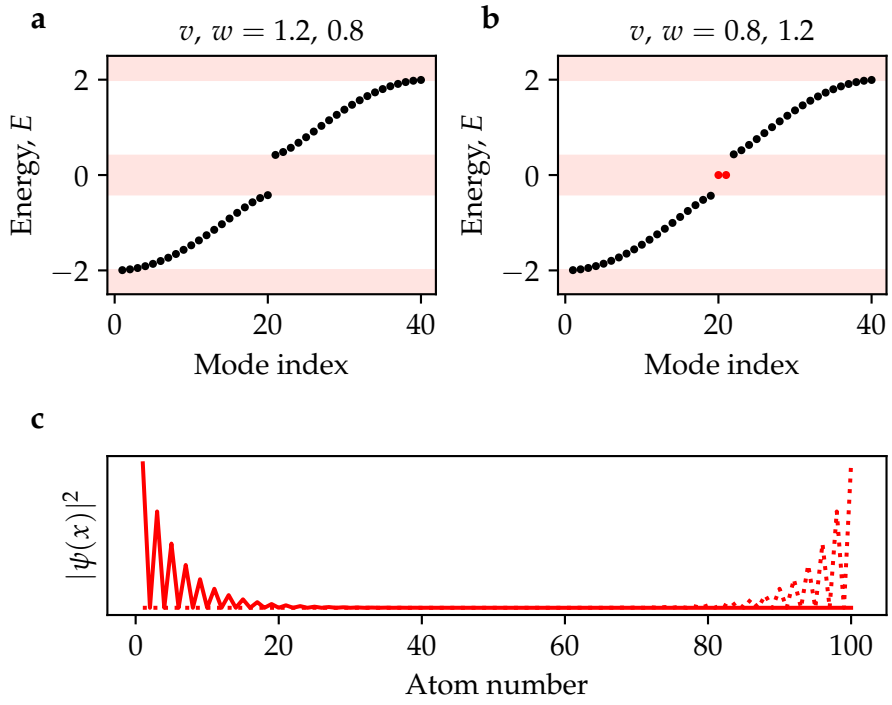

Figure 1.10: (a,b) Energy spectrum of finite Su-Schrieffer-Heeger chains of 40 atoms (20 unit cells). A pair of zero energy edge states are present when $v < w$ (red dots). (c) Visualisation of the left (solid line) and right (dashed line) edge states for a 100 atom chain.

a carbon backbone with alternating single and double bonds between the carbon atoms, as shown in Figure 1.9a.

The tight-binding Hamiltonian of trans-polyacetylene introduced by Su, Schrieffer, and Heeger is [48]

$$\hat{H}^{(\text{bulk})}_{\text{SSH}} \begin{bmatrix} |\psi_{\text{A}}\rangle \\ |\psi_{\text{B}}\rangle \end{bmatrix} = \begin{bmatrix} 0 & v + we^{-ik_x L} \\ v + we^{ik_x L} & 0 \end{bmatrix} \begin{bmatrix} |\psi_{\text{A}}\rangle \\ |\psi_{\text{B}}\rangle \end{bmatrix} = E(k_x) \begin{bmatrix} |\psi_{\text{A}}\rangle \\ |\psi_{\text{B}}\rangle \end{bmatrix}, \tag{1.17}$$

where A and B label the two carbon atoms per unit cell, and the hopping parameters v and w represent the alternating bonds between the carbon atoms as shown in Figure 1.9b. The bulk energy spectrum,

$$E_n(k_x) = \pm\sqrt{v^2 + w^2 + 2vw\cos k_x L}, \tag{1.18}$$

is gapped for $|v| \neq |w|$ and gapless for $v = w$. We shall see that despite the invariance of the bulk energy spectrum when exchanging $v \leftrightarrow w$ (which corresponds to a simple redefinition of the unit cell), the Hamiltonians with $v < w$ and $v > w$ are topologically distinct and a topological phase transition occurs when the band gap closes for $v = w$.

As shown in Figure 1.10, a finite chain with open boundary conditions (given here for a chain of eight atoms, or four unit cells)

$$H_{\text{SSH}}^{(N=8)} = \begin{bmatrix} 0 & v & 0 & 0 & 0 & 0 & 0 & 0 \\ v & 0 & w & 0 & 0 & 0 & 0 & 0 \\ 0 & w & 0 & v & 0 & 0 & 0 & 0 \\ 0 & 0 & v & 0 & w & 0 & 0 & 0 \\ 0 & 0 & 0 & w & 0 & v & 0 & 0 \\ 0 & 0 & 0 & 0 & v & 0 & w & 0 \\ 0 & 0 & 0 & 0 & 0 & w & 0 & v \\ 0 & 0 & 0 & 0 & 0 & 0 & v & 0 \end{bmatrix}, \tag{1.19}$$

has topologically protected zero-energy modes[9] if $v < w$, indicating a topologically non-trivial phase [33, 49].

The topology of the SSH model arises from the chiral (sublattice) symmetry of the Hamiltonian: there are no terms that directly couple A-A or B-B sites. In the periodic table of topological insulators, the SSH model has a $\mathbb{Z}$ topological index as it belongs to the AIII symmetry class in 1D. In the following sections, we will discuss two methods of calculating the topological index.

1.5.2 *Chiral symmetry and winding number as a $\mathbb{Z}$ topological index*

The space of 2×2 Hermitian matrices may be expressed on a basis of Pauli matrices [50],

$$\hat{H}(\vec{d}) = d_x \boldsymbol{\sigma_x} + d_y \boldsymbol{\sigma_y} + d_z \boldsymbol{\sigma_z} + d_0 \boldsymbol{I_2}, \tag{1.20}$$

where σ_x, σ_y, and σ_z are the Pauli matrices,

$$\boldsymbol{\sigma_x} = \begin{bmatrix} 0 & 1 \\ 1 & 0 \end{bmatrix}; \quad \boldsymbol{\sigma_y} = \begin{bmatrix} 0 & -i \\ i & 0 \end{bmatrix}; \quad \boldsymbol{\sigma_z} = \begin{bmatrix} 1 & 0 \\ 0 & -1 \end{bmatrix}, \tag{1.21}$$

and $\boldsymbol{I_2}$ is the 2×2 identity matrix.

For chiral symmetric Hermitian matrices, $\vec{d}$ is restricted to lie in the $(d_x, d_y, 0, 0)$ plane because only $\boldsymbol{\sigma_x}$ and $\boldsymbol{\sigma_y}$ are chiral symmetric. We may define the winding number as

$$\nu = \frac{1}{2\pi i} \int_0^{2\pi/L} \frac{\mathrm{d}}{\mathrm{d}k_x} \log(d_x + i d_y)\, \mathrm{d}k_x,$$

9 Due to the finite length of the change there is a weak hybridisation resulting in an even lower energy mode, $|-\rangle$, and an odd higher energy mode, $|+\rangle$. This decreases exponentially with the length of the chain [33]. In Figure 1.10 we have actually plotted the modes localised to the left and right edges, $|L\rangle = \frac{|+\rangle + |-\rangle}{\sqrt{2}}$ and $|R\rangle = \frac{|+\rangle - |-\rangle}{\sqrt{2}}$ rather than the hybridised modes.

which counts the number of times the $\vec{d}$-vector winds around the origin as $k_x \to k_x + 2\pi/L$ [33]. We cannot continuously deform between the Hamiltonians with different winding numbers unless (i) $\vec{d}(k_x)$ passes through the origin, corresponding to the gap closing and a topological phase transition for some k_x, or (ii) we break chiral symmetry during the deformation, in which case $\vec{d}$ is no longer pinned to the $(d_x, d_y, 0, 0)$ plane and the winding number of $\vec{d}$ is not well defined. Different Hamiltonians with different windings numbers are therefore in different topological phases protected by chiral symmetry, with the winding number as the topological index.

For the bulk SSH Hamiltonian,

$$\hat{H}^{(\text{bulk})}_{\text{SSH}} = (v + w\cos k_x L)\boldsymbol{\sigma_x} + (w \sin k_x L)\boldsymbol{\sigma_y}, \tag{1.22}$$

$$= d_x \boldsymbol{\sigma_x} + d_y \boldsymbol{\sigma_y}, \tag{1.23}$$

we see that the $\vec{d}$-vector, $\vec{d} = (v + w\cos k_x L, w \sin k_x L, 0, 0)$ moves around a circle with origin v and radius w as we bring $k_x \to k_x + 2\pi/L$. The $\vec{d}$-vector therefore winds around the origin once if $v < w$ and zero times if $v > w$, corresponding to the non-trivial and trivial phases, respectively.

Although the winding number is a $\mathbb{Z}$ topological index, the original SSH model has only $\nu = 0$ or $\nu = 1$. This is because we only considered nearest-neighbour couplings between the sites, restricting the $\vec{d}$-vector a simple circle. To access topological states with larger winding numbers, longer range chiral symmetric coupling terms can be introduced [33, 51–53].

1.5.3 *Inversion symmetry and Berry phase as a $\mathbb{Z}_2$ topological index*

As well as being chiral symmetric, the SSH model is inversion symmetric,

$$\hat{\pi}\hat{H}(-k)\hat{\pi} = \hat{H}(k), \tag{1.24}$$

where $\hat{\pi}$ is a unitary operator acting on the internal space of the Hamiltonian [33]. The SSH model can be classified by a quantised *Berry phase*,[10]

$$\gamma_n = \int_{k_x}^{k_x + 2\pi/L} \vec{\mathcal{A}}_n(\vec{k})\, \mathrm{d}k_x, \tag{1.25}$$

where

$$\vec{\mathcal{A}}_n(\vec{k}) = i\langle u_n(\vec{k}) | \vec{\nabla}_{\vec{k}} u_n(\vec{k})\rangle \tag{1.26}$$

10 In one-dimensional systems such as the SSH model, the Berry phase is also known as the *Zak phase*. We shall see in Chapter 2 how the Berry connection, phase, and curvature are closely related.

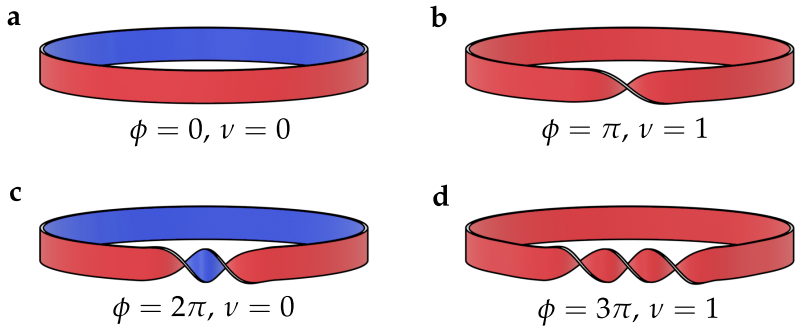

Figure 1.11: Understanding $\mathbb{Z}$ and $\mathbb{Z}_2$ topological phases in 1D with analogies to twisted cylinders. The winding number of the SSH model is a $\mathbb{Z}$ topological index, analagous with the twist of the cylinder, ϕ. The Berry phase of the SSH model is a $\mathbb{Z}_2$ topological index, analagous with the number of sides of the cylinders, ν.

is the *Berry connection* of the nth band [33, 44]. It can be shown (and we will also calculate directly in Chapter 2) that in inversion symmetric systems, the Berry phase of the first band is [33]

$$e^{i\gamma_1} = p_1(0)p_1(\pm\pi/L) = \begin{cases} e^{\pm i\pi} & \text{for } v < w \\ e^0 & \text{for } v > w \end{cases}, \tag{1.27}$$

where $p_1(0)$ and $p_1(\pm\pi/L)$ are the inversion eigenvalues of the first band at the center and edge of the Brillouin zones, respectively.

In the SSH, the winding number is equivalent to the Berry phase modulo 2π [54], as illustrated with an analogy to twisted ribbons in Figure 1.11. Although the Berry phase is a $\mathbb{Z}_2$ topological index, it can also be used to identify the topological phase of the SSH model as the two accessible topological phases have different Berry phases.

Moving beyond the original SSH model, the Berry phase can be useful in systems where chiral symmetry is broken and the winding number is lost, because the quantised Berry phase can survive if the inversion symmetry is preserved [55]. For example, in Chapter 2 we will see a photonic analogue of the SSH model where chiral symmetry is broken by long range interactions, but the emergence of edge states can still be predicted by the quantised Berry phase. However, without chiral symmetry the edge states are not pinned to zero energy and are not guaranteed to lie in the energy gap. In Chapter 4, we will introduce a method to construct photonic lattices with edge states that are protected by chiral symmetry using closely spaced perfect conductors.

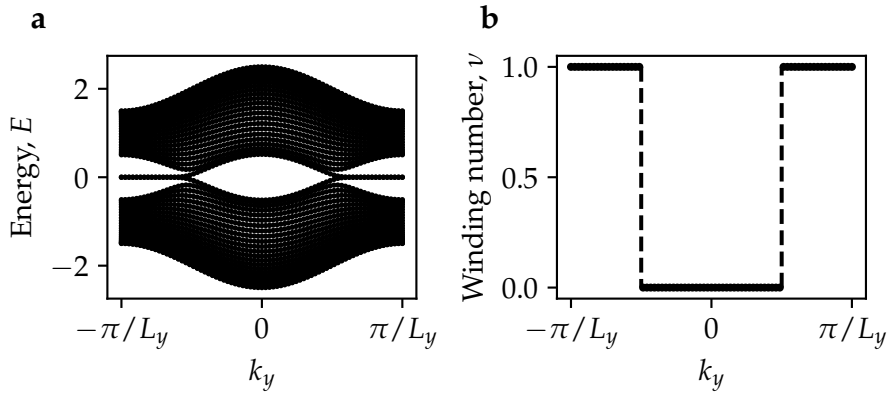

Figure 1.12: A 2D topological semimetal formed by cross-linked SSH chains. The chains are aligned along the x-direction and linked along the y-direction in a chiral symmetric manner. (a) Energy of the chains with an edge introduced along the x-direction for the hopping parameters $v = w = 1$ and $t = 0.25$. Zero energy edge modes are seen at certain values of k_y, originating from topologically protected Dirac cones [56]. (b) The existence of the zero energy edge modes at a given value of k_y corresponds with the winding number of an SSH chain with hopping parameters $v + 2t\cos(k_y L_y)$ and w.

1.6 TOPOLOGICAL SEMIMETALS

So far, we have discussed the band topology of gapped Hamiltonians, but the analysis can also be applied to gapless Hamiltonians. Consider, for example, stacking the SSH chains from Section 1.5 in the y-direction, and introducing a hopping parameter t that couples sites between different chains in a chiral symmetric manner [57],

$$\boldsymbol{H}_{\mathbf{TSM}}^{(\mathbf{bulk})} = \begin{bmatrix} 0 & v + we^{-ik_x L_x} + 2t\cos(k_y L_y) \\ v + we^{ik_x L} + 2t\cos(k_y L_y) & 0 \end{bmatrix}. \tag{1.28}$$

When $v = w$, the bulk energy spectrum of this system is gapless with the two bands meeting at Dirac cones at $(k_x, k_y) = (\pi/L_x, \pm\pi/2L_y)$. In general, for a fixed value of k_y, Equation (1.28) is equivalent to Equation (1.17) for the single SSH chain but with $v \to v + 2t\cos(k_y L_y)$. If we terminate the chains along the x-direction such that k_y remains a good quantum number along the y-direction, then we expect to see zero energy edge states for certain values of k_y as seen in Figure 1.12a. The emergence of the edge states correspond to $v + 2t\cos(k_y L_y) < w$, where the winding number of the reduced SSH Hamiltonian is $\nu = 1$, as shown in Figure 1.12b. The Dirac cones and the edge states are topologically protected by chiral symmetry, and can only be removed if the two Dirac cones annihilate [56].

In Chapter 4 we will study a *square-root* topological semimetal [58–60]. These are systems where the squared Hamiltonian is block-diagonal and where one of the blocks corresponds to the Hamiltonian of a topological semimetal. The spectrum of the square-root system inherits topological features from the topological sector of the squared Hamiltonian [60, 61].

1.7 REMARKS ON CHAPTER 1

In this chapter we have qualitatively introduced the concept of topological phases, and described how the topological indices are related to the valence bands (or, more generally, the bands below the gap of interest). In the next chapter, we will review some of the photonic analogues to the electronic phases we have introduced, but with a focus on solving for photonic bands and evaluating the topological indices numerically. In particular, we will introduce the plane-wave expansion method to solve for the Bloch modes of the photonic crystals, and the discrete forms of the multiband Berry phase and curvature.

2

METHODS TO STUDY PHOTONIC TOPOLOGICAL PHASES

2.1 OVERVIEW

In the last chapter we introduced topological materials in the traditional context of electronic systems. However, the topic of this thesis is photonic topological insulators, which are built using photonic crystals: periodic nanostructures with tunable photonic bands [62, 63]. In order to prepare for Chapters 3 & 4 where we study novel topological photonic systems, we use this chapter to introduce numerical methods to solve Maxwell's equations for photonic crystals and to calculate the topological invariants of the resulting bands. Over the course of the chapter we will introduce photonic analogues of the SSH, QHE, and QSHE in order to demonstrate the methods. First, however, let us discuss some key differences between electronic and photonic topological systems.

2.2 COMPARISON OF PHOTONIC AND ELECTRONIC TOPOLOGY

Although band structures can be engineered in both electronic and photonic crystals, there are some key differences that alter the topological nature of these systems.

In gapped electronic systems we are typically interested in the topology of the valence band subspace (as it is only the partially-filled topological edge states spanning the valence-conduction band gap that contribute to the surface conductance of the electrons, as discussed in Chapter 1), but there is no concept of a Fermi level or band filling in photonic crystals as the photons are bosonic. Instead, there is interest in the existence of edge states in potentially any isolating band gap of a photonic crystal as the photons may be excited over a broad range of frequencies [64]. Although there are no Fermi levels in photonic systems, we will borrow terminology from the electronic systems and refer to the photonic bands above and below whichever gap we are studying as the 'conduction' and 'valence' bands, respectively. The emergence of topological edge states in a gap can be determined by contributions from all the 'valence' bands below that gap [64].

The vectorial nature of the electromagnetic fields and tensorial nature of photonic materials provide a number of avenues to produce

topological bands in photonics.[1] As in the electronic QHE, photonic analogues of the QHE require breaking time-reversal symmetry [65, 66]. This has been achieved using, for example, gyrotropic materials in an external magnetic field [67, 68] (see Sections 2.5.3 and 2.6.4), or using metamaterials with a bianisotropic response [69]. However, the time-reversal symmetry breaking response of common materials is weak in the visible spectrum and therefore there is significant interest in time-reversal symmetric topological photonics [20, 21, 70, 71].

Without fermionic time-reversal symmetry, $\mathcal{T}^2 = -1$, the photonic systems are limited to a different set of symmetry protected classes than the electronic systems (see Table 1.1). Photonic analogues of the QSHE therefore rely on other symmetries to emulate the spin of electrons, such as the duality of the electric and magnetic fields [29] (see Section 2.5.3) or the orbital angular momenta of light in conjunction with crystalline symmetries [1, 72–76] (see Chapter 3). Helical edge states can emerge at the interfaces between the photonic crystals with different $\mathbb{Z}_2$ topological indices, however, if the pseudo-fermionic time-reversal symmetry is broken then the edge states will not be unidirectional. If pseudo-time-reversal symmetry is only weakly broken, then backscattering can remain strongly surpressed [75]. Similarly, chiral symmetry emerges naturally in tight-binding models in electronics, but is generally violated by long range interactions in photonics [51, 54]. In Chapter 4 we explore topological phases in photonic lattices with a chiral symmetric limit.

In the rest of this chapter we will introduce Maxwell's equations and explain how we solved for the bands of photonic crystals using the plane-wave expansion method. We will then introduce particular photonic analogues of the SSH, QHE, and QSHE phases in more detail in order to demonstrate how the topological invariants are calculated. It is not our intention to provide a full review of topological photonic crystals in this chapter, instead we wish to demonstrate the numerical methods for calculating topological indices. For more complete reviews of topological photonics, including three-dimensional phases and valley-Hall phases, we recommend [18, 20, 21, 77].

1 It is also worth noting that loss, gain, and non-linearities are typically absent in electronics but can have important effects on the topology of photonic systems [18] that are beyond the scope of this thesis.

2.3 MAXWELL'S EQUATIONS

2.3.1 *Maxwell's equations in the time-domain*

Classical photonics is governed by Maxwell's equations [78],

$$\vec{\nabla} \times \vec{E}(\vec{r},t) = -\partial_t \vec{B}(\vec{r},t), \tag{2.1a}$$
$$\vec{\nabla} \times \vec{H}(\vec{r},t) = +\partial_t \vec{D}(\vec{r},t) + \vec{j}(\vec{r},t), \tag{2.1b}$$
$$\vec{\nabla} \cdot \vec{\mathcal{D}}(\vec{r},t) = \rho(\vec{r},t), \tag{2.1c}$$
$$\vec{\nabla} \cdot \vec{B}(\vec{r},t) = 0, \tag{2.1d}$$

where

$\vec{E}(\vec{r},t)$	is the electric field,
$\vec{H}(\vec{r},t)$	is the magnetic field,
$\vec{\mathcal{D}}(\vec{r},t)$	is the electric displacement field,
$\vec{B}(\vec{r},t)$	is the magnetic flux density,
$\rho(\vec{r},t)$	is the charge density, and
$\vec{j}(\vec{r},t)$	is the current density.

The material-dependent relations between $\vec{E}$, $\vec{H}$, $\vec{\mathcal{D}}$, and $\vec{B}$ are known as the constitutive relations. For linear materials, the most general relations are convolutions in time and space [79],

$$\vec{\mathcal{D}}(\vec{r},t) = \iint \Big[\varepsilon(\vec{r}',\vec{t}')\vec{E}(\vec{r}-\vec{r}',t-t') + \xi(\vec{r}',t')\vec{H}(\vec{r}-\vec{r}',t-t')\Big]\,\mathrm{d}\vec{r}'\,\mathrm{d}t', \tag{2.2}$$
$$\vec{B}(\vec{r},t) = \iint \Big[\zeta(\vec{r}',\vec{t}')\vec{E}(\vec{r}-\vec{r}',t-t') + \mu(\vec{r}',t')\vec{H}(\vec{r}-\vec{r}',t-t')\Big]\,\mathrm{d}\vec{r}'\,\mathrm{d}t', \tag{2.3}$$

where $\varepsilon(\vec{r})$, $\mu(\vec{r})$, $\xi(\vec{r})$, and $\zeta(\vec{r})$ are known as the permittivity, permeability, and bi-anisotropic material tensors of the material, respectively [79].[2]

Equations (2.2) and (2.3) include convolutions in both space and time as it is assumed that the materials are both temporally and spatially dispersive. While the spatial dispersion of materials can have significant 'non-local' effects in certain regimes, such as when the wavelength is comparable to lattice of the material, these are weak for

2 We have expressed $\vec{\mathcal{D}}$ and $\vec{B}$ as functions of $\vec{E}$ and $\vec{H}$, which is known as the Tellegen representation, however there are other representations, such as the Boys-Post representation where $\vec{\mathcal{D}}$ and $\vec{H}$ are expressed as functions of $\vec{E}$ and $\vec{B}$, which can lead to different permittivities, permeabilities, and bi-anisotropic tensors [79].

the systems we study [78, 79]. We therefore model the response of our materials to the electromagnetic field as

$$\vec{\mathcal{D}}(\vec{r},t) = \int \left[\varepsilon(\vec{r},\vec{t}')\vec{E}(\vec{r},t-t') + \boldsymbol{\xi}(\vec{r},t')\vec{H}(\vec{r},t-t')\right] \mathrm{d}t', \tag{2.4}$$

$$\vec{B}(\vec{r},t) = \int \left[\boldsymbol{\zeta}(\vec{r},\vec{t}')\vec{E}(\vec{r},t-t') + \boldsymbol{\mu}(\vec{r},t')\vec{H}(\vec{r},t-t')\right] \mathrm{d}t', \tag{2.5}$$

where the convolutions over space reduce to the identity.

2.3.2 *Maxwell's equations in the frequency-domain*

It is convenient to Fourier transform from the time domain to the frequency domain,

$$f(\vec{r},\omega) = \frac{1}{\sqrt{2\pi}} \int_{-\infty}^{\infty} f(\vec{r},t) e^{i\omega t}\, \mathrm{d}t, \tag{2.6}$$

such that the time-domain convolutions of Equations (2.4) and (2.5) become simple multiplications,

$$\begin{bmatrix} \vec{\mathcal{D}}(\vec{r},\omega) \\ \vec{B}(\vec{r},\omega) \end{bmatrix} = \begin{bmatrix} \varepsilon(\vec{r},\omega) & \boldsymbol{\xi}(\vec{r},\omega) \\ \boldsymbol{\zeta}(\vec{r},\omega) & \boldsymbol{\mu}(\vec{r},\omega) \end{bmatrix} \begin{bmatrix} \vec{E}(\vec{r},\omega) \\ \vec{H}(\vec{r},\omega) \end{bmatrix}. \tag{2.7}$$

After Fourier transforming each field, $f(\vec{r},t) \to f(\vec{r},\omega)$, Maxwell's equations in the frequency-domain are

$$\vec{\nabla} \times \vec{E}(\vec{r},\omega) = +i\omega\vec{B}(\vec{r},\omega), \tag{2.8a}$$

$$\vec{\nabla} \times \vec{H}(\vec{r},\omega) = -i\omega\vec{\mathcal{D}}(\vec{r},\omega) + \vec{j}(\vec{r},\omega), \tag{2.8b}$$

$$\vec{\nabla} \cdot \vec{\mathcal{D}}(\vec{r},\omega) = \rho(\vec{r},\omega), \tag{2.8c}$$

$$\vec{\nabla} \cdot \vec{B}(\vec{r},\omega) = 0, \tag{2.8d}$$

where $\partial_t \to -i\omega$ follows from the sign convention of our Fourier transform, $f(\vec{r},t) \sim e^{-i\omega t}$ [80].

2.3.3 *Maxwell's source-free equations*

We are interested in the propagation of light through materials without external sources of charge or current. It is therefore useful to separate the current density into two contributions,

$$\vec{j}(\vec{r},\omega) = \vec{j}_{\mathrm{s}}(\vec{r},\omega) + \vec{j}_{\mathrm{c}}(\vec{r},\omega). \tag{2.9}$$

The first contribution, $\vec{j}_{\mathrm{s}}(\vec{r},\omega)$, is from external sources. The other contribution is from *conduction* induced by the electric field,

$$\vec{j}_{c}(\vec{r},\omega) = \boldsymbol{\sigma}(\vec{r},\omega)\vec{E}(\vec{r},\omega), \tag{2.10}$$

where $\sigma(\vec{r},\omega)$ is conductivity [78].

Substituting Equations (2.9) and (2.10) into Equation (2.8b),

$$\vec{\nabla} \times \vec{H}(\vec{r},\omega) = -i\omega\vec{\mathcal{D}}(\vec{r},\omega) + \vec{j}_s(\vec{r},\omega) + \boldsymbol{\sigma}(\vec{r},\omega)\vec{E}(\vec{r},\omega),$$

we see that it is possible to simplify Maxwell's equations by taking an alternate definition of the electric displacement field,

$$\vec{D}(\vec{r},\omega) = \vec{\mathcal{D}}(\vec{r},\omega) + \frac{i\boldsymbol{\sigma}(\vec{r},\omega)}{\omega}\vec{E}(\vec{r},\omega), \tag{2.11}$$

such that

$$\vec{\nabla} \times \vec{H}(\vec{r},\omega) = -i\omega\vec{D}(\vec{r},\omega) + \vec{j}_s(\vec{r},\omega). \tag{2.12}$$

Similarly, by separating the charge density into contributions from external sources and conduction,

$$\rho = \rho_s(\vec{r},\omega) + \rho_c(\vec{r},\omega), \tag{2.13}$$

applying conservation of charge [78],

$$i\omega\rho_c(\vec{r},\omega) = \vec{\nabla} \cdot \vec{j}_c(\vec{r},\omega), \tag{2.14}$$

and substituting Equations (2.13) and (2.14) into Equation (2.8c),

$$\vec{\nabla} \cdot \vec{\mathcal{D}}(\vec{r},\omega) = \rho_s(\vec{r},\omega) + \frac{\vec{\nabla} \cdot \vec{j}_c(\vec{r},\omega)}{i\omega},$$

we find that replacing $\vec{\mathcal{D}}(\vec{r},\omega)$ with $\vec{D}(\vec{r},\omega)$ leads again to a simplified equation,

$$\vec{\nabla} \cdot \vec{D}(\vec{r},\omega) = \rho_s(\vec{r},\omega). \tag{2.15}$$

This alternate definition of the electric displacement field,

$$\vec{D}(\vec{r},\omega) = \boldsymbol{\epsilon}(\vec{r},\omega)\vec{E}(\vec{r},\omega) + \boldsymbol{\xi}(\vec{r},\omega)\vec{H}(\vec{r},\omega), \tag{2.16}$$

which is defined in terms of a *complex permittivity*,

$$\boldsymbol{\epsilon}(\vec{r},\omega) = \boldsymbol{\varepsilon}(\vec{r},\omega) + i\boldsymbol{\sigma}(\vec{r},\omega)/\omega, \tag{2.17}$$

allows for simpler forms of Maxwell's equations because it does not distinguish between polarisation and conduction currents [78]. In the absence of external sources, $\rho_s = 0$ and $\vec{j}_s = \vec{0}$, Maxwell's frequency-domain equations may therefore be expressed sufficiently as

$$\vec{\nabla} \times \vec{E}(\vec{r},\omega) = +i\omega\vec{B}(\vec{r},\omega), \tag{2.18a}$$
$$\vec{\nabla} \times \vec{H}(\vec{r},\omega) = -i\omega\vec{D}(\vec{r},\omega), \tag{2.18b}$$
$$\vec{\nabla} \cdot \vec{D}(\vec{r},\omega) = 0, \tag{2.18c}$$
$$\vec{\nabla} \cdot \vec{B}(\vec{r},\omega) = 0. \tag{2.18d}$$

2.3.4 *Time-reversal symmetry*

As discussed in Section 1.2.2, in order to study the topology of a Hamiltonian it is important to know whether it is time-reversal symmetric. The time-reversal operation acts upon the fields as [79]

$$\hat{T}\left[\vec{E}(\vec{r},\omega)\right] = \vec{E}^*(\vec{r},\omega), \tag{2.19a}$$
$$\hat{T}\left[D(\vec{r},\omega)\right] = \vec{D}^*(\vec{r},\omega), \tag{2.19b}$$
$$\hat{T}\left[\vec{H}(\vec{r},\omega)\right] = -\vec{H}(\vec{r},\omega), \tag{2.19c}$$
$$\hat{T}\left[\hat{B}(\vec{r},\omega)\right] = -\vec{B}(\vec{r},\omega), \tag{2.19d}$$

and therefore the constitutive relations of time-reversal symmetric media must obey [79]

$$\hat{T}\left[\boldsymbol{\epsilon}(\vec{r},\omega)\right] = \boldsymbol{\epsilon}^*(\vec{r},\omega), \tag{2.20a}$$
$$\hat{T}\left[\boldsymbol{\mu}(\vec{r},\omega)\right] = \boldsymbol{\mu}^*(\vec{r},\omega), \tag{2.20b}$$
$$\hat{T}\left[\boldsymbol{\xi}(\vec{r},\omega)\right] = -\boldsymbol{\xi}^*(\vec{r},\omega), \tag{2.20c}$$
$$\hat{T}\left[\boldsymbol{\zeta}(\vec{r},\omega)\right] = -\boldsymbol{\zeta}^*(\vec{r},\omega). \tag{2.20d}$$

We see that the time-reversal symmetry is broken by the imaginary part of the complex permittivity introduced in the previous section.

2.3.5 *The electromagnetic wave equations*

Maxwell's equations support propagating wave solutions: the curl of an electric field generates a magnetic field, the curl of this magnetic field generates an electric field, and so on. The complexity of the wave equation depends on the dimensionality of the system and the complexity of the constitutive relations that describe the material that the wave propagates through. We therefore begin our discussion with some simplifications, and will reintroduce the complexity in later sections as required.

Firstly, we will assume that the materials are not bi-anisotropic,

$$\boldsymbol{\xi}(\vec{r},\omega) = \boldsymbol{\zeta}(\vec{r},\omega) = \mathbf{0}. \tag{2.21}$$

Secondly, we will assume that the permittivity and permeability are anisotropic but diagonal,

$$\boldsymbol{\epsilon}(\vec{r},\omega) = \begin{bmatrix} \epsilon_{xx}(\vec{r},\omega) & 0 & 0 \\ 0 & \epsilon_{yy}(\vec{r},\omega) & 0 \\ 0 & 0 & \epsilon_{zz}(\vec{r},\omega) \end{bmatrix}, \tag{2.22a}$$

$$\boldsymbol{\mu}(\vec{r},\omega) = \begin{bmatrix} \mu_{xx}(\vec{r},\omega) & 0 & 0 \\ 0 & \mu_{yy}(\vec{r},\omega) & 0 \\ 0 & 0 & \mu_{zz}(\vec{r},\omega) \end{bmatrix}. \tag{2.22b}$$

Finally, we will assume that both the materials and the electromagnetic field are homogeneous along the z-direction,

$$\partial_z \vec{E}(\vec{r},\omega) = \partial_z \vec{H}(\vec{r},\omega) = \vec{0}, \tag{2.23}$$
$$\partial_z \boldsymbol{\epsilon}(\vec{r},\omega) = \partial_z \boldsymbol{\mu}(\vec{r},\omega) = \mathbf{0}. \tag{2.24}$$

For a 2D material as described by Equations (2.21)-(2.24), Maxwell's curl equations decouple into Transverse Electric (TE) and Transverse Magnetic (TM) modes as follows. In component form, Equation (2.18a) for the curl of the electric field reads

$$\partial_y E_z(\vec{r},\omega) = i\omega\mu_{xx}(\vec{r},\omega)\vec{H}_x(\vec{r},\omega), \tag{2.25a}$$
$$-\partial_x E_z(\vec{r},\omega) = i\omega\mu_{yy}(\vec{r},\omega)\vec{H}_y(\vec{r},\omega), \tag{2.25b}$$
$$\partial_x E_y(\vec{r},\omega) - \partial_y E_x(\vec{r},\omega) = i\omega\mu_{zz}(\vec{r},\omega)\vec{H}_z(\vec{r},\omega), \tag{2.25c}$$

and Equation (2.18b) for the curl of the magnetic field reads

$$\partial_y H_z(\vec{r},\omega) = -i\omega\epsilon_{xx}(\vec{r},\omega)\vec{E}_x(\vec{r},\omega), \tag{2.26a}$$
$$-\partial_x H_z(\vec{r},\omega) = -i\omega\epsilon_{yy}(\vec{r},\omega)\vec{E}_y(\vec{r},\omega), \tag{2.26b}$$
$$\partial_x H_y(\vec{r},\omega) - \partial_y H_x(\vec{r},\omega) = -i\omega\epsilon_{zz}(\vec{r},\omega)\vec{E}_z(\vec{r},\omega). \tag{2.26c}$$

We may obtain the TM-polarised wave equation by substituting Equations (2.25a) and (2.25b) into Equation (2.26c),

$$-\left(\partial_x \frac{1}{\mu_{yy}(\vec{r},\omega)}\partial_x + \partial_y \frac{1}{\mu_{xx}(\vec{r},\omega)}\partial_y\right) E_z(\vec{r},\omega) = \omega^2\epsilon_{zz}(\vec{r},\omega)E_z(\vec{r},\omega), \tag{2.27}$$

and similarly the TE-polarised wave equation is obtained by substituting Equations (2.26a) and (2.26b) into Equation (2.25c),

$$-\left(\partial_x \frac{1}{\epsilon_{yy}(\vec{r},\omega)}\partial_x + \partial_y \frac{1}{\epsilon_{xx}(\vec{r},\omega)}\partial_y\right) H_z(\vec{r},\omega) = \omega^2\mu_{zz}(\vec{r},\omega)H_z(\vec{r},\omega). \tag{2.28}$$

For isotropic and homogeneous ϵ and μ, it is simple to show that the solutions to the wave Equations (2.27) and (2.28) are of the form $Ae^{i\vec{k}\cdot\vec{r}-i\omega t}$, where $|k| = nk_0$ and $n = \sqrt{\epsilon\mu/\epsilon_0\mu_0}$ is the refractive index of the material and ϵ_0 and μ_0 are the permittivity and permeability of vacuum, respectively. If $\mathrm{Im}[n] = 0$, then the wave propagates without loss in the $\vec{k}$ direction. Otherwise, if $\mathrm{Im}[n] > 0$ or $\mathrm{Im}[n] < 0$, the wave propagates with loss or gain, respectively. Note that these sign conventions were enforced by the sign convention of our Fourier transform in Equation (2.6). For inhomogeneous $\boldsymbol{\epsilon}$ and $\boldsymbol{\mu}$, numerical methods are typically required to find the solutions to the wave equations.

2.4 SOLVING MAXWELL'S EQUATIONS WITH THE PLANE-WAVE EXPANSION METHOD

In order to model our inhomogeneous photonic crystals, we solved Maxwell's wave Equations (2.27) and (2.28) (and their extensions to materials with more complex constitutive relations) using the PWEM [80]. We released our code as `Peacock.jl` [81], an open source package for the `Julia` programming language.[3] As the following sections will detail, in the PWEM the fields are first expanded into sums of plane waves using Fourier series in the spatial dimensions. The expanded fields are substituted in Maxwell's curl equations and the expansion is then truncated, rendering a finite wave matrix equation where $w(\vec{k})$ is the eigenvalue.

One limitation of the PWEM is that the Fourier series can converge poorly if the materials or the fields vary sharply in space, such as when the electric field varies sharply at a metal-dielectric interface [83]. Another limitation of this formulation is that in order to solve the matrix problem for $\omega(\vec{k})$ directly (not iteratively) we must assume that the materials are not dispersive, $\boldsymbol{\epsilon} = \boldsymbol{\epsilon}(\vec{r})$ and $\boldsymbol{\mu} = \boldsymbol{\mu}(\vec{r})$.[4] However, the PWEM is a very efficient method for modelling photonic crystals consisting of dielectrics or other low-contrast materials in air.

2.4.1 *Maxwell's equations in Fourier space*

Bloch's theorem [84] states that in periodic media, the eigenfields may be expressed as Bloch waves,

$$f_{\vec{k}}(\vec{r},\omega) = u_{\vec{k}}(\vec{r},\omega)e^{i\vec{k}\cdot r - i\omega t}, \tag{2.29}$$

where $\vec{k}$ is the Bloch wave vector, and $u_{\vec{k}}(\vec{r},\omega)$ has the same periodicity as the unit cell and can be expanded as a Fourier series,

$$u_{\vec{k}}(x,y) = \sum_{\vec{G}} c_{\vec{k}}(\vec{G})e^{+i\vec{G}\cdot\vec{r}}, \tag{2.30}$$

$$c_{\vec{k}}(\vec{G}) = \frac{1}{A_{\text{cell}}} \iint_{\text{cell}} u_{\vec{k}}(x,y)e^{-i\vec{G}\cdot\vec{r}}\,\mathrm{d}x\mathrm{d}y, \tag{2.31}$$

where the sum over $\vec{G}$ is the sum over all the reciprocal lattice vectors of the cell, $\vec{G}(p,q) = \left(p\vec{b}_1, q\vec{b}_2\right)$ for integer p, q.[5]

3 `Peacock.jl` - or the **P**lane-wave **E**xpansion **A**pproach to **C**haracterising **O**ptical **C**rystals in **k**-space - is named for the irridescent colours of peacock feathers which arise not from pigmentation but from their photonic crystal struture [81, 82].

4 In Chapter 5, we discuss the inverse problem $k_z = k_z(k_x, k_y, \omega; \epsilon(\vec{r},\omega), \mu(\vec{r},\omega))$, which may be solved directly even for dispersive materials.

5 Note that if the geometry and fields are homogeneous along a certain axis then there is no need to retain plane waves along the reciprocal axis. We have done this implicitly here because the electromagnetic field and geometry are homogeneous along the $\vec{a}_3$ axis (the z-axis), and our plane waves were chosen such that $\vec{G}\cdot\vec{b}_3 = 0$.

In the PWEM, this Fourier series is used to expand the electric and magnetic fields as coefficients of plane waves with wave vectors $\vec{k}+\vec{G}$,

$$\vec{E}_{\vec{k}}(\vec{r},\omega) = \sum_{\vec{G}} \vec{S}(\vec{k}+\vec{G},\omega)e^{i(\vec{k}+\vec{G})\cdot\vec{r}}, \tag{2.32}$$

$$\vec{H}_{\vec{k}}(\vec{r},\omega) = \sum_{\vec{G}} \vec{U}(\vec{k}+\vec{G},\omega)e^{i(\vec{k}+\vec{G})\cdot\vec{r}}, \tag{2.33}$$

and the cell-periodic permittivity and permeability are expanded as

$$\boldsymbol{\epsilon}(\vec{r}) = \sum_{\vec{G}} \boldsymbol{a}(\vec{G})e^{i\vec{G}\cdot\vec{r}}, \tag{2.34}$$

$$\boldsymbol{\mu}(\vec{r}) = \sum_{\vec{G}} \boldsymbol{b}(\vec{G})e^{i\vec{G}\cdot\vec{r}}. \tag{2.35}$$

Equations (2.32)-(2.35) may be substituted into Maxwell's curl Equations (2.25a)-(2.26c). For example, substituting the expanded fields into Equation (2.25a),

$$\partial_y E_z(\vec{r},\omega) = i\omega\mu_{xx}(\vec{r})\vec{H}_x(\vec{r},\omega), \tag{2.36}$$

we find

$$\begin{aligned} ik_y &\sum_{\vec{G}} S_z(\vec{k}+\vec{G},\omega)e^{i(\vec{k}+\vec{G})\cdot\vec{r}} \\ &= i\omega \sum_{\vec{G}'} b_{xx}(\vec{G}')e^{i\vec{G}'\cdot\vec{r}} \cdot \sum_{\vec{G}''} U_x(\vec{k}+\vec{G}'',\omega)e^{i(\vec{k}+\vec{G}'')\cdot\vec{r}}, && (2.37)\\ &= i\omega \sum_{\vec{G}'}\sum_{\vec{G}''} b_{xx}(\vec{G}')U_x(\vec{k}+\vec{G}'',\omega)e^{i(\vec{k}+\vec{G}'+\vec{G}'')\cdot\vec{r}}, && (2.38)\\ &= i\omega \sum_{\vec{G}} \left[\sum_{\vec{G}''} b_{xx}(\vec{G}-\vec{G}'')U_x(\vec{k}+\vec{G}'',\omega)\right] e^{i(\vec{k}+\vec{G})\cdot\vec{r}}, && (2.39) \end{aligned}$$

such that (equating each term of the sum over $\vec{G}$)

$$ik_y S_z(\vec{k}+\vec{G},\omega) = +i\omega \sum_{\vec{G}''} b_{xx}(\vec{G}-\vec{G}'')U_x(\vec{k}+\vec{G}'',\omega). \tag{2.40a}$$

Note that the scalar multiplication of $\mu_{xx}(\vec{r},\omega)H_x(\vec{r},\omega)$ in real space becomes a convolution over $\vec{G}''$ in Fourier space. From inspection of the real space Equation (2.36) and the Fourier space Equation (2.40a) we see that we can transform from real space to Fourier space by substituting $E_i \to S_i$, $H_i \to U_i$, $\epsilon_{ij} \to a_{ij}\circledast$, $\mu_{ij} \to b_{ij}\circledast$, and $\partial_i \to ik_i$.

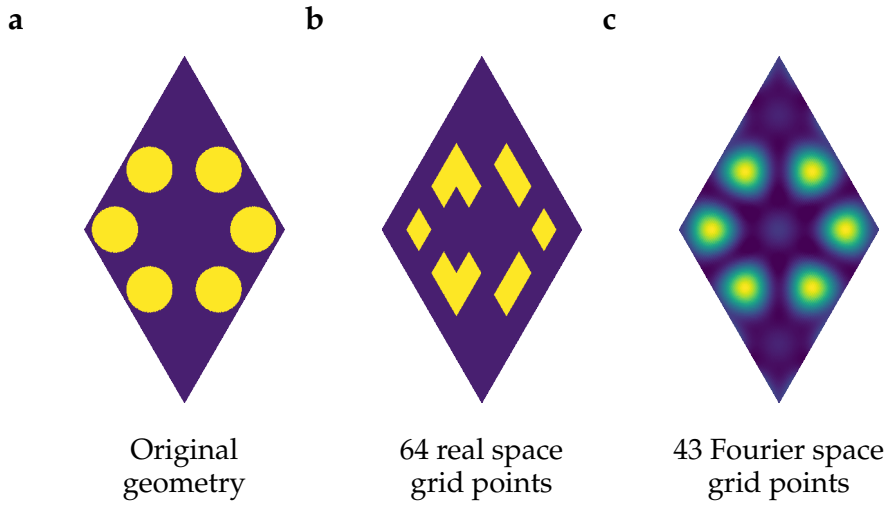

Figure 2.1: (a) A high-resolution view of an example geometry consisting of rings on a triangular lattice. (b) The roundness of the cylinders requires many real space grid points to describe; the size and shape of the cylinders is poorly described by a grid of 64 points in real space. (c) The geometry can be more accurately described in Fourier space; the Fourier series truncated to 43 elements produces a better approximation of the geometry than the real-space grid in panel b.

In this way, the remaining components of Maxwell's curl equations become

$$-ik_x S_z(\vec{k}+\vec{G},\omega) = +i\omega \sum_{\vec{G}''} b_{yy}(\vec{G}-\vec{G}'')U_y(\vec{k}+\vec{G}'',\omega), \tag{2.40b}$$

$$ik_x S_y(\vec{k}+\vec{G},\omega) - ik_y S_x(\vec{k}+\vec{G},\omega) = +i\omega \sum_{\vec{G}''} b_{zz}(\vec{G}-\vec{G}'')U_z(\vec{k}+\vec{G}'',\omega), \tag{2.40c}$$

$$ik_y U_z(\vec{k}+\vec{G},\omega) = -i\omega \sum_{\vec{G}''} a_{xx}(\vec{G}-\vec{G}'')S_x(\vec{k}+\vec{G}'',\omega). \tag{2.40d}$$

$$-ik_x U_z(\vec{k}+\vec{G},\omega) = -i\omega \sum_{\vec{G}''} a_{yy}(\vec{G}-\vec{G}'')S_y(\vec{k}+\vec{G}'',\omega), \tag{2.40e}$$

$$ik_x U_y(\vec{k}+\vec{G},\omega) - ik_y U_x(\vec{k}+\vec{G},\omega) = -i\omega \sum_{\vec{G}''} a_{zz}(\vec{G}-\vec{G}'')S_z(\vec{k}+\vec{G}'',\omega). \tag{2.40f}$$

2.4.2 *The wave matrix equations*

In order to solve the eigenvalue problem numerically, the plane wave expansion of each field is truncated to a finite number of terms. Although this introduces some error, relatively few terms are required to accurately describe low-contrast materials such as dielectrics in air. Figure 2.1a shows an example photonic crystal consisting of rings of cylinders on a triangular lattice. As shown in Figure 2.1b, the geometry is poorly represented by a low resolution real-space grid. However, the Fourier space representation shown in Figure 2.1c is much more accurate while requiring fewer data points to describe the field.

Let us write the coefficients of our truncated Fourier series expansions in arrays denoted by double square brackets,

$$[\![S_i]\!] = \left[S_i(\vec{k}+\vec{G}_1,\omega), S_i(\vec{k}+\vec{G}_2,\omega), \ldots, S_i(\vec{k}+\vec{G}_N,\omega)\right]^T, \tag{2.41}$$

$$[\![U_i]\!] = \left[U_i(\vec{k}+\vec{G}_1,\omega), U_i(\vec{k}+\vec{G}_2,\omega), \ldots, U_i(\vec{k}+\vec{G}_N,\omega)\right]^T, \tag{2.42}$$

where $\vec{G}_n = p_n\vec{b}_1 + q_n\vec{b}_2$ for integers p_n and q_n. Maxwell's curl Equations (2.40a)-(2.40f) may then be written in a matrix form as

$$\boldsymbol{K_y}\,[\![S_z]\!] = \omega \boldsymbol{b}^{\circledast}_{\boldsymbol{xx}}\,[\![U_x]\!]\,, \tag{2.43a}$$

$$-\boldsymbol{K_x}\,[\![S_z]\!] = \omega \boldsymbol{b}^{\circledast}_{\boldsymbol{yy}}\,[\![U_y]\!]\,, \tag{2.43b}$$

$$\boldsymbol{K_x}\,[\![S_y]\!] - \boldsymbol{K_y}\,[\![S_x]\!] = \omega \boldsymbol{b}^{\circledast}_{\boldsymbol{zz}}\,[\![U_z]\!]\,, \tag{2.43c}$$

and

$$\boldsymbol{K_y}\,[\![U_z]\!] = -\omega \boldsymbol{a}^{\circledast}_{\boldsymbol{xx}}\,[\![S_x]\!]\,, \tag{2.44a}$$

$$-\boldsymbol{K_x}\,[\![U_z]\!] = -\omega \boldsymbol{a}^{\circledast}_{\boldsymbol{yy}}\,[\![S_y]\!]\,, \tag{2.44b}$$

$$\boldsymbol{K_x}\,[\![U_y]\!] - \boldsymbol{K_y}\,[\![U_x]\!] = -\omega \boldsymbol{a}^{\circledast}_{\boldsymbol{zz}}\,[\![S_z]\!]\,, \tag{2.44c}$$

where $\boldsymbol{K_i}$ is a diagonal matrix containing the ith component of each wave vector, $(\boldsymbol{K_i})_{nm} = (\vec{k}+\vec{G}_n)_i\delta_{nm}$, and $\boldsymbol{a}^{\circledast}_{\boldsymbol{ij}}$ and $\boldsymbol{b}^{\circledast}_{\boldsymbol{ij}}$ are *convolution matrices*, defined as [80]

$$(\boldsymbol{c}^{\circledast})_{nm} = c(\vec{G}_n - \vec{G}_m) \tag{2.45}$$

such that

$$(\boldsymbol{c}^{\circledast}\cdot[\![U_x]\!])_n = \sum_m c(\vec{G}_n - \vec{G}_{n''})U_x(\vec{k}+\vec{G}_n,\omega). \tag{2.46}$$

We can now express the TM and TE wave Equations (2.27) and (2.28) in matrix form,

$$\boxed{\left(\boldsymbol{K_x}\boldsymbol{b}^{\circledast}_{\boldsymbol{yy}}{}^{-1}\boldsymbol{K_x} + \boldsymbol{K_y}\boldsymbol{b}^{\circledast}_{\boldsymbol{xx}}{}^{-1}\boldsymbol{K_y}\right)[\![S_z]\!] = \omega^2\boldsymbol{a}^{\circledast}_{\boldsymbol{zz}}\,[\![S_z]\!]} \tag{2.47}$$

and

$$\boxed{\left(\boldsymbol{K}_x \boldsymbol{a}_{yy}^{\circledast\,-1} \boldsymbol{K}_x + \boldsymbol{K}_y \boldsymbol{a}_{xx}^{\circledast\,-1} \boldsymbol{K}_y\right) [\![U_z]\!] = \omega^2 \boldsymbol{b}_{zz}^{\circledast} [\![U_z]\!]} \tag{2.48}$$

respectively.

2.4.3 *Creating the material convolution matrices*

In order to use the PWEM, it is important to be able to construct the material convolution matrices [80] as defined by Equation (2.45). The Fourier coefficients of the materials are first obtained by applying a Discrete Fourier Transform (DFT) to arrays that store the permittivity and permeability in a real-space grid, and the appropriate Fourier coefficients are then placed into the convolution matrices. This requires an understanding of how the Fourier coeffients are ordered within the array returned by the DFT routine.

The `AbstractFFTs.jl` package for the Julia programming language defines the discrete Fourier transform along a one-dimensional array A of N elements as

$$\mathrm{DFT}(A)[p] = \frac{1}{N} \sum_{n=1}^{N} \exp\left(-i \frac{2\pi(n-1)(p-1)}{N}\right) A[n]. \tag{2.49}$$

The package also provides the `fftshift` function that shifts the elements of the transformed array such that

$$\begin{aligned} &\mathrm{fftshift}\left(\mathrm{DFT}(A)\right)[p] = \\ &\frac{1}{N} \sum_{n=1}^{N} \exp\Big(-i \frac{2\pi(n-1)(p-1-\mathrm{length}(A) \div 2)}{N}\Big) A[n], \end{aligned} \tag{2.50}$$

where $\div$ represents integer division (rounding down to the nearest integer).

Extending Equation (2.50) to two-dimensions, the array transforms as

$$\begin{aligned} &\mathrm{fftshift}\left(\mathrm{DFT}(A)\right)[p][q] = \\ &\frac{1}{N_{\mathrm{rows}} N_{\mathrm{cols}}} \sum_{n=1}^{N_{\mathrm{rows}}} \sum_{m=1}^{N_{cols}} \exp\Big(-i \frac{2\pi(n-1)(p-p_0)}{N_{\mathrm{rows}}} \\ &\qquad\qquad - i \frac{2\pi(m-1)(q-q_0)}{N_{\mathrm{cols}}}\Big) A[n][m], \end{aligned} \tag{2.51}$$

where $p_0 = 1 - N_{\mathrm{rows}} \div 2$ and $q_0 = 1 - N_{\mathrm{cols}} \div 2$, such that

$$\mathrm{fftshift}\left(\mathrm{DFT}(A)\right)[p_0 + p_n][q_0 + q_n] = a(\vec{G}_n). \tag{2.52}$$

The elements of convolution matrices are therefore given by

$$\begin{aligned}(\boldsymbol{a}_{ij}^{(*)})_{nm} &= a_{ij}(\vec{G}_n - \vec{G}_m) \\ &= \frac{1}{N_{\text{rows}} N_{\text{cols}}} \text{fftshift}\left[\text{DFT}(\epsilon_{ij})\right][p_0 + p_n - p_m][q_0 + q_n - q_m],\end{aligned} \tag{2.53}$$

$$\begin{aligned}(\boldsymbol{b}_{ij}^{(*)})_{nm} &= b_{ij}(\vec{G}_n - \vec{G}_m) \\ &= \frac{1}{N_{\text{rows}} N_{\text{cols}}} \text{fftshift}\left[\text{DFT}(\mu_{ij})\right][p_0 + p_n - p_m][q_0 + q_n - q_m].\end{aligned} \tag{2.54}$$

It is important that the real space arrays of ϵ_{ij} and μ_{ij} that are inputs to Equations (2.53) and (2.53) are created at a relatively high resolution such that the Fourier space coefficients generated by the DFTs are accurate. After the convolution matrices are built, the real space representations of ϵ_{ij} and μ_{ij} may be discarded [80].

2.4.4 *Inner products on a plane-wave basis*

Later in this chapter we will study the topology of the bands calculated with the PWEM. This requires heavy use of overlap integrals between our eigenmodes, defined as

$$\left\langle u_{n\vec{k}_1}(\vec{r}) \middle| u_{m\vec{k}_2}(\vec{r}) \right\rangle = \iint_{\text{cell}} u^*_{n\vec{k}_1}(\vec{r}) \cdot w(\vec{r}) \cdot u_{m\vec{k}_2}(\vec{r})\, \mathrm{d}^2 r, \tag{2.55}$$

where $u_{n\vec{k}_1} = \iint e^{-\vec{k}_1 \cdot \vec{r}} f_n(\vec{r})\, \mathrm{d}^2 r$ and $u_{m\vec{k}_2} = \iint e^{-\vec{k}_2 \cdot \vec{r}} f_m(\vec{r})$ are the cell-periodic parts of the Bloch waves $f_{n\vec{k}_1}(\vec{r})$ and $f_{m\vec{k}_2}(\vec{r})$, respectively, and $w(\vec{r})$ is the weighting function of the inner product [44]. This can be formulated in terms of the plane-wave expanded coefficients.

The weighting $w(\vec{r})$ depends on the equations that are being solved. For a generalised Hermitain eigenvalue problem, $\hat{A}\vec{x} = \lambda \hat{B}\vec{x}$ where $\hat{A}$ is a Hermitian operator and $\hat{B}$ is a positive semi-definite operator, we take $w(\vec{r}) = \hat{B}$ [62]. This means $w(\vec{r}) = \epsilon_{zz}(\vec{r})$ for our TM wave Equation (2.27), and $w(\vec{r}) = \mu_{zz}(\vec{r})$ for our TE wave Equation (2.28).

For the TM modes, the cell-periodic part of our Bloch wave is

$$u^{(E_z)}_{\vec{k}_1}(\vec{r}) = e^{-i\vec{k}_1 \cdot \vec{r}} E_z(\vec{r}), \tag{2.56}$$

and the overlap integral may be expressed on the plane wave basis as

$$\left\langle u^{(E_z)}_{n\vec{k}_1}(\vec{r}) \middle| u^{(E_z)}_{m\vec{k}_2}(\vec{r}) \right\rangle = \iint_{\text{cell}} \left(u^{(E_z)}_{n\vec{k}_1}(\vec{r}) \right)^* \cdot \epsilon_{zz}(\vec{r}) \cdot u^{(E_z)}_{m\vec{k}_2}(\vec{r}) \, \mathrm{d}^2 r, \tag{2.57a}$$

$$= \iint_{\text{cell}} \Big(\sum_{\vec{G}} S_z^*(\vec{k}_1 + \vec{G}) e^{-i\vec{G}\cdot\vec{r}} \sum_{\vec{G}'} a_{zz}(\vec{G}') e^{i\vec{G}'\cdot\vec{r}} \sum_{\vec{G}''} S_z(\vec{k}_2 + \vec{G}'') e^{i\vec{G}''\cdot\vec{r}} \Big) \, \mathrm{d}^2 r, \tag{2.57b}$$

$$= \sum_{\vec{G}} \sum_{\vec{G}'} \sum_{\vec{G}''} S_z^*(\vec{k}_1 + \vec{G}) a_{zz}(\vec{G}') S_z(\vec{k}_2 + \vec{G}'') \cdot A_{\text{cell}} \, \delta(\vec{G}', \vec{G} - \vec{G}''), \tag{2.57c}$$

$$= \sum_{\vec{G}} \sum_{\vec{G}''} S_z^*(\vec{k}_1 + \vec{G}) a_{zz}(\vec{G} - \vec{G}'') S_z(\vec{k}_2 + \vec{G}'') \cdot A_{\text{cell}}, \tag{2.57d}$$

$$= \left[\!\left[S_z(\vec{k}_1) \right]\!\right]^\dagger \boldsymbol{a}^{\circledast}_{zz} \left[\!\left[S_z(\vec{k}_2) \right]\!\right] \cdot A_{\text{cell}}. \tag{2.57e}$$

where we used $\iint_{\text{cell}} e^{i(\vec{G}'+\vec{G}''-\vec{G})\cdot\vec{r}} \, \mathrm{d}^2 r = A_{\text{cell}} \, \delta(\vec{G}', \vec{G} - \vec{G}'')$ between Equations (2.57b) and (2.57c). The overlap integrals between solutions to the TM wave equation are therefore

$$\boxed{\left\langle u^{(E_z)}_{n\vec{k}_1}(\vec{r}) \middle| \epsilon_{zz}(\vec{r}) \middle| u^{(E_z)}_{m\vec{k}_2}(\vec{r}) \right\rangle = \left[\!\left[S_z(\vec{k}_1) \right]\!\right]^\dagger \boldsymbol{a}^{\circledast}_{zz} \left[\!\left[S_z(\vec{k}_2) \right]\!\right],} \tag{2.58}$$

and similarly for the TE modes where the cell-periodic part of the Bloch wave solution is

$$u^{(E_z)}_{\vec{k}_1}(\vec{r}) = e^{-i\vec{k}_1\cdot\vec{r}} E_z(\vec{r}), \tag{2.59}$$

the overlap integrals are

$$\boxed{\left\langle u^{(H_z)}_{n\vec{k}_1}(\vec{r}) \middle| \mu_{zz}(\vec{r}) \middle| u^{(H_z)}_{m\vec{k}_2}(\vec{r}) \right\rangle = \left[\!\left[U_z(\vec{k}_1) \right]\!\right]^\dagger \boldsymbol{b}^{\circledast}_{zz} \left[\!\left[U_z(\vec{k}_2) \right]\!\right],} \tag{2.60}$$

where we have dropped the factor of A_{cell} in Equations (2.58) and (2.60) as we only compute overlaps between solutions of the same for the same A_{cell}.

2.4.5 *Dimensionless units*

When solving Maxwell's equations numerically, it is good practice to first normalise the quantities such as length, frequency, permittivity, and permeability in order to minimise rounding errors when working with floating point numbers [80, 85]. Letting our dimensionless wave vectors be $\tilde{k} = ka$, and our dimensionless (relative) permittivities and permeabilities be $\tilde{\epsilon} = \epsilon/\epsilon_0$ and $\tilde{\mu} = \mu/\mu_0$, it is natural to express frequency in units of a/c_0. For example, the TM wave equation in dimensionless units is

$$\left(\tilde{\boldsymbol{K}}_x \tilde{\boldsymbol{b}}^{\circledast}_{yy}{}^{-1} \tilde{\boldsymbol{K}}_x + \tilde{\boldsymbol{K}}_y \tilde{\boldsymbol{b}}^{\circledast}_{xx}{}^{-1} \tilde{\boldsymbol{K}}_y \right) [\![S_z]\!] = (\omega a/c_0)^2 \, \tilde{\boldsymbol{a}}^{\circledast}_{zz} [\![S_z]\!], \tag{2.61}$$

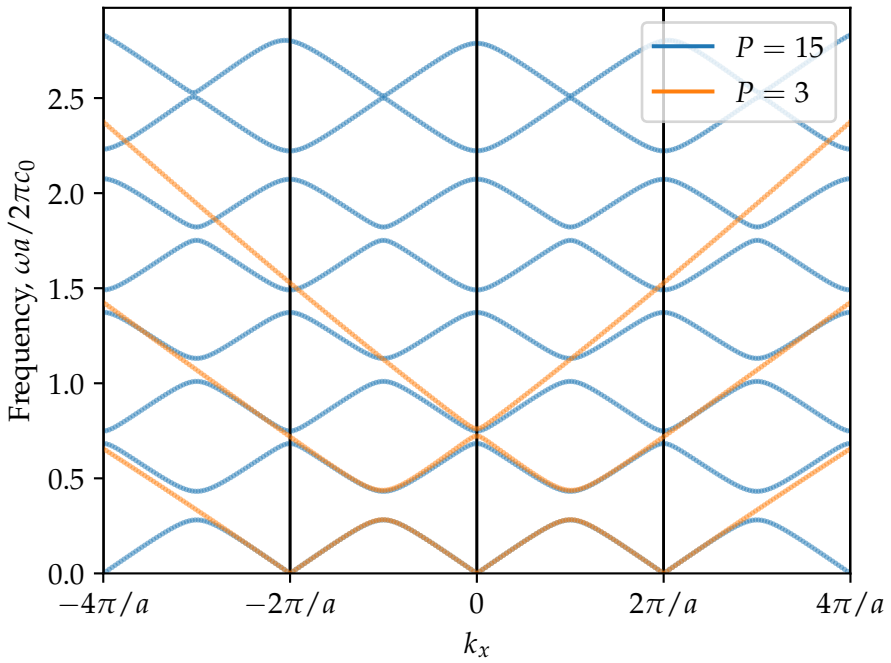

Figure 2.2: Convergence of the PWEM. Here we show the transverse-electric polarised frequency bands for a simple geometry consisting of alternating slabs of permittivity, $\epsilon_1 = 4\epsilon_0$ and $\epsilon_2 = \epsilon_0$, of thicknesses $d_1 = 0.4a$ and $d_2 = 0.6a$, respectively. The solutions calculated using a small plane-wave basis ($P = 3$ plane-waves, orange lines) are only accurate near to $\vec{k} = \vec{0}$ and at lower frequencies. For a larger plane-wave basis ($P = 15$ plane-waves, blue lines) the solutions are more accurate for a wider range of $\vec{k}$ and for higher frequencies.

where $c_0 = 1/\sqrt{\epsilon_0\mu_0}$ is the speed of light in vacuum.

It is common to present on band diagrams the dimensionless frequency as $\omega a/2\pi c_0$ (equivalent to a/λ_0). This is common because Maxwell's equations are scale free for dispersionless materials, meaning that the solutions at one length scale are equal to the solutions at another length scale, but with a rescaled frequency [62].

2.4.6 *Convergence of the plane-wave expansion method*

To demonstrate the nature of the truncation error introduced by the PWEM, Figure 2.2 compares the frequency bands of a simple 1D photonic crystal obtained with the PWEM for a small basis of just 3 plane waves (orange bands) compared to a larger basis of 15 plane waves (blue bands). There is good agreement between the two sets of solutions at low frequencies within the BZ. This is because fewer plane waves are required to accurately describe fields that vary slowly and smoothly in space.

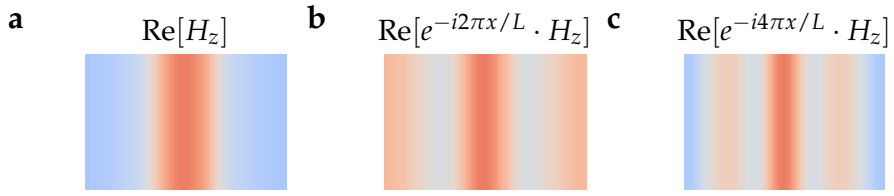

Figure 2.3: Visualisations of the cell-periodic part of the second band of the photonic crystal from Figure 2.2 at (a) $k_x = 0$, (b) $k_x = 2\pi/a$, (c) $k_x = 4\pi/a$. The cell-periodic part of Bloch waves must be different in different Brillouin zones because the full Bloch wave is independent of the choice of Brillouin zone.

As frequency increases, the fields tend to vary more quickly in space and it is not surprising that the accuracy of the PWEM decreases. It may be less clear why the accuracy of the PWEM decreases as $\left|\vec{k}\right|$ increases; this is because although the energy eigenmodes of the photonic crystal are Bloch waves, the plane-wave expansion method solves only for the cell-periodic part of the Bloch wave, $u_{\vec{k}}(\vec{r}) = e^{-i\vec{k}\cdot\vec{r}} f(\vec{r})$. As shown in Figure 2.3, this cell-periodic part of the solution varies more quickly in space for larger $\vec{k}$, requiring a larger plane wave basis to describe accurately.

2.5 TOPOLOGY OF A SINGLE ISOLATED BAND

In Section 1.2.2 we qualitatively introduced some examples of topology in gapped Hamiltonians. In particular, we introduced the SSH model in 1D, and the QHE and QSHE phases in 2D. In the following sections we will study these phases more quantitatively, and explain how the topological indices are calculated from the eigenmodes. We now introduce the Berry phase, curvature, and Chern number of a *single band* that is isolated from all the other bands by an energy gap for all $\vec{k}$, before generalising to the topology of an isolated set of bands in Section 2.6.

2.5.1 *Berry phase of a closed loop*

Consider an isolated band, $\left|u_n(\vec{k})\right\rangle$, and the overlap of its eigenmodes[6] at two different $\vec{k}$-points, $\vec{k}_1$ and $\vec{k}_2$,

$$\left\langle u_n(\vec{k}_2)\middle|u_n(\vec{k}_1)\right\rangle = \left|\left\langle u_n(\vec{k}_2)\middle|u_n(\vec{k}_1)\right\rangle\right| e^{i\gamma_{2,1}}. \tag{2.62}$$

There is a relative phase between the eigenmodes, $e^{i\gamma_{2,1}}$. By itself, this phase is not a meaningful physical quantity as it is gauge-dependent,

6 Note that we consider the overlap between the cell-periodic part of Bloch modes rather than between the full Bloch modes. The overlap between two full Bloch modes with slightly different values of $\vec{k}$ will vanish [44].

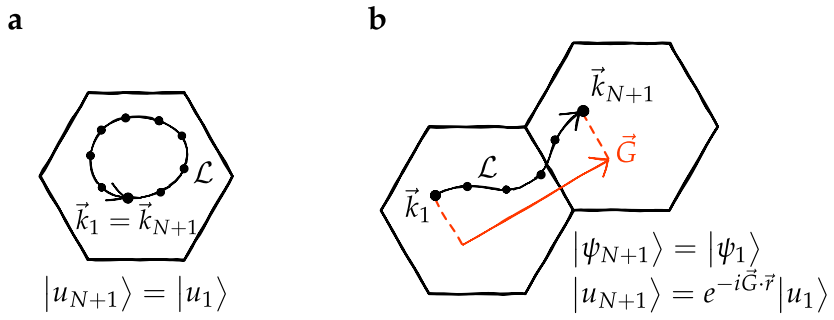

Figure 2.4: Examples of two types of closed loops in a periodic Brillouin zone. (a) A closed loop beginning and ending in the same Brillouin zone, $\vec{G} = \vec{k}_{N+1} - \vec{k}_1 = 0$. (b) A closed loop beginning and ending at the same $\vec{k}$-point, but in different Brillouin zones. For a periodic gauge, $|\psi_{N+1}\rangle = |\psi_1\rangle$, we enforce $|u_{N+1}\rangle = e^{i\vec{G}\cdot\vec{r}}|u_1\rangle$ where $\vec{G} = \vec{k}_{N+1} - \vec{k}_1$.

meaning that it is dependent on our choice of phase for each eigenmode [33],

$$|u_n(\vec{k}_j)\rangle \to e^{i\alpha_j}|u_n(\vec{k}_j)\rangle \quad \Rightarrow \quad e^{i\gamma_{2,1}} \to e^{i\gamma_{2,1}+i(\alpha_2-\alpha_1)}. \tag{2.63}$$

However, the product of these phases along a *closed loop*,

$$\boxed{e^{i\gamma_{\mathcal{L}}} = e^{i\gamma_{1,N}+i\gamma_{N,N-1}+\cdots+i\gamma_{2,1}},} \tag{2.64}$$

is actually a gauge-invariant quantity,

$$e^{i\gamma_{\mathcal{L}}} =\!\!\to e^{i\gamma_{\mathcal{L}}+i(\alpha_1-\alpha_N)+i(\alpha_N-\alpha_{N-1})+\cdots+i(\alpha_2-\alpha_1)} = e^{i\gamma_{\mathcal{L}}}. \tag{2.65}$$

This gauge-invariant phase, $\gamma_{\mathcal{L}}$, is known as the *Berry phase* of the loop [33].

In the continuum limit of increasing the number of points $N \to \infty$ along $\mathcal{L}$, the Berry phase may be written as an integral, $\gamma_{\mathcal{L}} = \oint_{\mathcal{L}} \mathcal{A}(\vec{k})\,\mathrm{d}k$, where $\mathcal{A}(\vec{k}) = \langle u_n(\vec{k})|i\vec{\nabla}_{\vec{k}}u_n(\vec{k})\rangle$ is known as the Berry connection [33, 44]. However, in this work we will only be solving the discrete equation.[7]

While the loop $\mathcal{L}$ must be closed for $\gamma_{\mathcal{L}}$ to be gauge-invariant, the periodicity of the reciprocal space means that the curve may begin and end in different BZs separated by a reciprocal lattice vector $\vec{G}$, as shown in Figure 2.4. In these cases it is important to ensure that the first and last states have the same phase, $|\psi(\vec{k}_1 + \vec{G})\rangle = |\psi(\vec{k}_1)\rangle$ and therefore $|u(\vec{k}_1 + \vec{G})\rangle = e^{-i\vec{G}\cdot\vec{r}}|u(\vec{k}_1)\rangle$, such that the gauge is periodic. The relative phase between the first and the last modes becomes

$$\begin{aligned}\gamma_{1,N} &= \mathrm{Im}\ln\langle u_n(\vec{k}_1 + \vec{G})|u_n(\vec{k}_N)\rangle, \\ &= \mathrm{Im}\ln\langle u_n(\vec{k}_1)|e^{i\vec{G}\cdot\vec{r}}|u_n(\vec{k}_N)\rangle,\end{aligned} \tag{2.66}$$

7 As we are interested in calculating topological invariants which are integer, the exact solution can often be obtained at a relatively low $\vec{k}$-space discretisation [86].

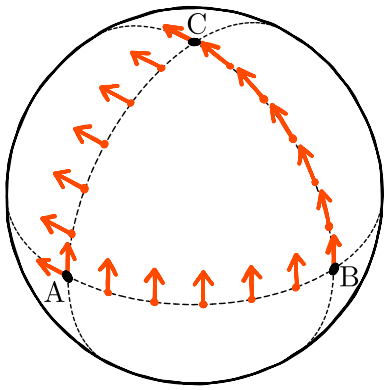

Figure 2.5: A real-space vector can be rotated when parallel transported along a curved surface. For example, the orange vector is rotated by 90 degrees after parallel transport along the closed loop ABCA covering a quarter of the sphere's surface.

such that

$$\boxed{\gamma_{\mathcal{L}} = \operatorname{Im} \ln \left\langle u_n(\vec{k}_1) \middle| e^{i\vec{G}\cdot\vec{r}} \middle| u_n(\vec{k}_N) \right\rangle \left\langle u_n(\vec{k}_N) \middle| u_n(\vec{k}_{N-1}) \right\rangle \ldots \left\langle u_n(\vec{k}_2) \middle| u_n(\vec{k}_1) \right\rangle} \tag{2.67}$$

remains gauge-invariant under all $\left|u_n(\vec{k}_j)\right\rangle \to e^{i\alpha_j}\left|u_n(\vec{k}_j)\right\rangle$.

In the following sections we will explore different interpretations of the Berry phase and how it allows us to distinguish between different topological phases.

2.5.1.1 *Parallel transport*

One interpretation of the Berry phase, $\gamma_{\mathcal{L}}$, is as the gauge-invariant phase accumulated during the *parallel transport* of the eigenvectors around a loop. Figure 2.5 shows the parallel transport of a real vector around a loop. Each vector is maximally aligned with the previous vector in the path, and the curvature of the surface results in a rotation of the vector. Another kind of parallel transport exists for complex vectors, where we ensure that the *phase* of the vectors is maximally aligned [44].

The Berry phase is closely related to the parallel transport of the phase of complex eigenvectors. Consider constructing a *parallel transport gauge* where the phase of the first eigenmode is fixed, $\left|\tilde{u}_n(\vec{k}_1)\right\rangle = \left|u_n(\vec{k}_1)\right\rangle$, and the phase of every subsequent eigenmode is adjusted, $\left|\tilde{u}_n(\vec{k}_i)\right\rangle = e^{i\alpha_i}\left|u_n(\vec{k}_i)\right\rangle$, such that the relative phases between adjacent eigenmodes is zero in this gauge,

$$\tilde{\gamma}_{i+1,i} = \operatorname{Im} \ln \left\langle \tilde{u}_n(\vec{k}_{i+1}) \middle| \tilde{u}_n(\vec{k}_i) \right\rangle = 0. \tag{2.68}$$

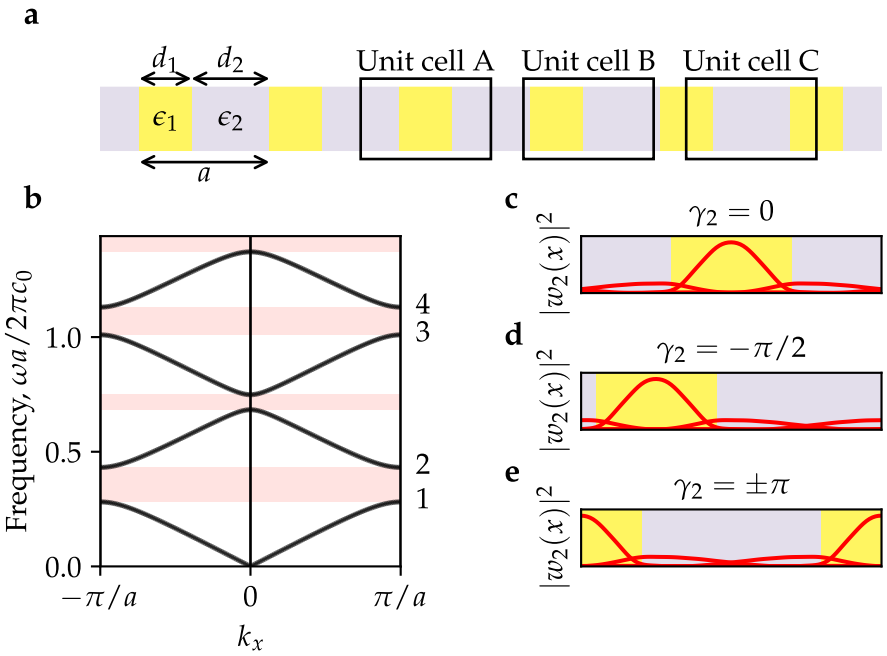

Figure 2.6: **(a)** A photonic SSH-like model made of alternating slabs of permittivity, $\epsilon_1 = 4\epsilon_0$ and $\epsilon_2 = \epsilon_0$, of thicknesses $d_1 = 0.4a$ and $d_2 = 0.6a$, respectively. Three possible choices of unit cell are shown. Unit cells A and C are inversion symmetric. **(b)** The frequency bands of the slabs. The eigenvalues are independent of the choice of unit cell. Each band is isolated from the others by an energy gap for all k_x. **(c-e)** The amplitude of the maximally localised Wannier functions of the second band, $|w_{2R_x}\rangle$, for the unit cells A, B, and C, respectively. The Berry phase of the band, γ_2, is related to the centers of the Wannier functions and is therefore dependent on our choice of unit cell.

Although the Berry phase is gauge-invariant, the expression simplifies in the parallel transport gauge,

$$\gamma_{\mathcal{L}} = \tilde{\gamma}_{1,N} + \cancelto{0}{\tilde{\gamma}_{N,N-1}} + \cdots + \cancelto{0}{\tilde{\gamma}_{2,1}}, \tag{2.69}$$

such that

$$\boxed{\gamma_{\mathcal{L}} = \operatorname{Im} \ln \langle \tilde{u}_n(\vec{k}_1) | e^{i\vec{G}\cdot\vec{r}} | \tilde{u}_n(\vec{k}_N) \rangle.} \tag{2.70}$$

In other words, just as the rotations of a real vector may not match before and after parallel transport, the Berry phase is the phase mismatch after a complex vector is parallel-transported around a closed loop [44].

2.5.1.2 *Example: A photonic Su-Schrieffer–Heeger-like model with broken chiral symmetry*

We can use an SSH-like model to help understand the meaning of the Berry phase, in particular its relation to a process known as *Wannieri-*

Band	Unit cell A	Unit cell B	Unit cell C
γ_1	$\pm\pi$	$+\pi/2$	0
γ_2	0	$-\pi/2$	$\pm\pi$
γ_3	$\pm\pi$	$+\pi/2$	0

Table 2.1: The Berry phases of the first three bands of the photonic SSH model from Figure 2.6. The results depend on the choice of unit cell.

sation. Let us consider a 1D photonic crystal consisting of alternative dielectric slabs of $\epsilon_1 = 4$ and $\epsilon_2 = 1$ with thicknesses $d_1 = 0.4a$ and $d_2 = 0.6a$, as shown in Figure 2.6a. Three possible choices of unit cell are shown: of these cells A and C are inversion symmetric, whereas cell B is not. This geometry was first introduced by Xiao *et al* [87] who described it as a photonic analogue of the SSH model.[8] However, the system is not chiral symmetric. We shall see that the Berry phase is quantised by inversion symmetry and can be used to predict topological edge states (although they are not pinned to a particular frequency) [**stjean2017lasing**, 64, 87], and we will discuss how the Berry phase is related to a process known as *Wannierisation*.

Figure 2.6b shows the frequencies of the 1D TE-polarised solutions, which were solved on a plane-wave basis according to

$$\boldsymbol{K}_x \boldsymbol{a}_{yy}^{\circledast\,-1} \boldsymbol{K}_x [\![U_z]\!] = \omega^2 \boldsymbol{b}_{zz}^{\circledast} [\![U_z]\!]. \tag{2.71}$$

Each band is isolated and orthonormal under the inner product,

$$\langle u_n(\vec{k}) | u_m(\vec{k}) \rangle = \int_{-a/2}^{+a/2} u_n^*(x,\vec{k}) \cancel{\mu_{zz}(x)} \cancel{1} u_m(x,\vec{k})\, \mathrm{d}x = \delta_{nm}, \tag{2.72}$$

where $|u_n(\vec{k})\rangle = e^{-i\vec{k}\cdot\vec{r}} |H_z^{(n)}(\vec{k})\rangle$, and H_z is the out-of-plane component of the magnetic field. Using Equation (2.67), we calculate the Berry phases of each band around a closed loop with $\vec{G} = \frac{2\pi}{a}\hat{x}$,[9]

$$\gamma_n = -\mathrm{Im}\ln \langle u_n(\vec{k}_1) | e^{i\frac{2\pi}{a}x} | u_n(\vec{k}_N) \rangle \langle u_n(\vec{k}_N) | u_n(\vec{k}_{N-1}) \rangle \ldots \langle u_n(\vec{k}_2) | u_n(\vec{k}_1) \rangle. \tag{2.73}$$

However, as shown in Table 2.1, we actually find different Berry phases for the different unit cells. This dependence on our choice of unit cell may be surprising, but is our first hint that these Berry phases are related to some observable position.

The positions that the Berry phases are describing turn out to be the centers of the *maximally localised Wannier functions* of each band.

8 See also [24] for a study of a similar model but with gain and loss.

9 In a 1D Brillouin zone the only possible closed loop is one that begins at $\vec{k}$ and ends at $\vec{k} + \vec{G}$ where $\vec{G} = \pm\vec{b}$. The Berry phase of such a closed loop through a 1D Brillouin zone is often called a Zak phase.

Wannier functions are defined as the inverse Fourier transforms of the Bloch states,

$$\left|w_{nR_x}(x)\right\rangle = \frac{a}{2\pi}\int_{-\pi/a}^{+\pi/a} e^{-ik_xR_x}\left|H_z^{(n)}(k_x)\right\rangle \mathrm{d}k_x, \tag{2.74}$$

where R_x is a lattice vector [44]. This transformation is unitary, and therefore the set of Wannier functions (one for each lattice vector, R_x) form an orthonormal basis that span the same Hilbert space as the Bloch functions.

The construction of the Wannier functions is gauge-dependent—the smoother the gauge, the more localised the Wannier functions. In the previous section we showed that the phase of the parallel transport gauge is smooth, $\tilde{\gamma}_{i+1,i} = 0$, except for a possible phase discontinuity at the end of the loop, $\tilde{\gamma}_{1,N} = \gamma_{\mathcal{L}}$. However, we have just seen that the Berry phase depends on our choice of unit cell, suggesting that this phase discontinuity can be removed with an appropriate choice of unit cell.

In particular, the dependence of the Berry phase on the choice of unit cell is originating from the $e^{i\frac{2\pi}{a}x}$ term of Equation (2.73).[10] If we shift the geometry by x_0, such that $\epsilon(x) \to \epsilon(x - x_0)$ and $u_n(x, \vec{k}) \to u_n(x - x_0, \vec{k})$, we see that the Berry phase changes as

$$\begin{aligned}\gamma'_{\mathcal{L}} &= \operatorname{Im}\ln\int u_n^*(x - x_0, \vec{k}_1)\, e^{i\frac{2\pi}{a}x}\, u_n(x - x_0, \vec{k}_N)\,\mathrm{d}x, \\ &= \operatorname{Im}\ln e^{i\frac{2\pi}{a}x_0}\int u_n^*(x - x_0, \vec{k}_1)\, e^{i\frac{2\pi}{a}(x-x_0)}\, u_n(x - x_0, \vec{k}_N)\,\mathrm{d}x, \\ &= \gamma_{\mathcal{L}} + \frac{2\pi}{a}x_0.\end{aligned} \tag{2.75}$$

By shifting the geometry by $x_0 = -\frac{\gamma_{\mathcal{L}}}{2\pi}a$ we can bring the Berry phase of any band to zero. For the choice of unit cell where the Berry phase vanishes, the parallel transport gauge becomes perfectly smooth and Wannier functions constructed from the parallel transport gauge become exponentially localised around the new origin,

$$\bar{x} = \left\langle w\middle|x - x_0\middle|w\right\rangle = 0. \tag{2.76}$$

In general, the maximally localised Wannier function of each energy band is localised at

$$\boxed{\bar{x} = \frac{\gamma_{\mathcal{L}}^{(n)}}{2\pi}a,} \tag{2.77}$$

as shown in Figure 2.6c-e.[11]

10 The dependence on origin would vanish if the loop began and ended in the same Brillouin zone, $\vec{G} = \vec{0}$. However, this is not possible in 1D.

11 This result is particularly significant in electronics because the the average position of the electronic charge is related to the Berry phase in what is known as the modern theory of polarization [33].

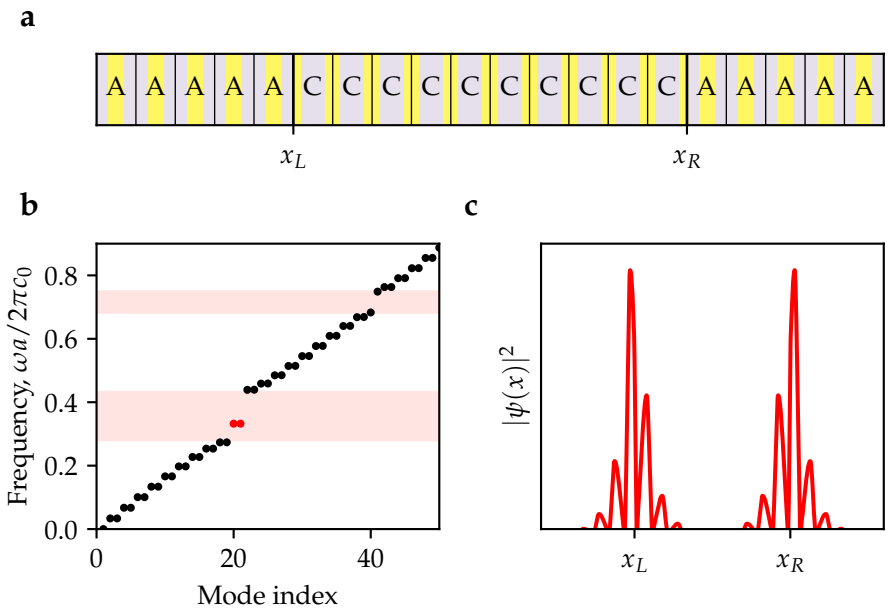

Figure 2.7: Topological states in the photonic SSH-like model. (a) We model the interfaces in a periodic supercell consisting of 10 unit cells of cell A and 10 unit cells of cell B. (b) Normalised frequencies of the supercell sorted in ascending order. The Berry phases of the first band in the different unit cells are $\gamma_1^{\mathrm{A}} = \pm\pi$ and $\gamma_1^{\mathrm{C}} = 0$. As $\gamma_1^{\mathrm{A}} \neq \gamma_1^{\mathrm{C}}$, a topological edge state emerges on each interface, shown as red markers. (c) The edge states are exponentially localised on the left and right interfaces at x_L and x_R.

One subtlety that we have glossed over so far is which branch of the logarithm to take when calculating $\mathrm{Im}(\ln e^{i\gamma_\mathcal{L}})$. However, from Equation (2.77) we see that the different branches, which differ by a value of $2\pi n$, will shift the center of the Wannier function by a lattice vector, na. The set of Wannier functions is invariant under this translation and each choice of branch is therefore equally valid.

Topology of the first gap.—We now examine how the Berry phases relate to the topological phase of a gapped Hamiltonian as introduced in Section 1.2.2. Recall that a topological analysis allows us to look at the bulk Hamiltonians of two materials and answer the question "is it necessary that a particular energy gap closes if we adiabatically deform between the Hamiltonians while preserving a given symmetry?", and consequently "does this lead to the emergence of topological states in this energy gap at the interface between the two materials?".

The answers to these questions depend on which energy gap we are interested in and which symmetries are present. To begin, let us consider the lowest energy gap of Figure 2.6. This gap isolates the first band from the higher energy bands. In the inversion symmetric unit cells, A and C, the Berry phase of each band is quantised as the inversion symmetry dictates that the Wannier functions must be

localised at either the center or the edge of the unit cell. In fact, the inversion symmetry allows us to express the Berry phase of the first band as [33]

$$e^{i\gamma_1} = p_1(0)p_1(\pm\pi/L) = \begin{cases} \pm 1 & \text{in cell A} \\ 0 & \text{in cell C} \end{cases}, \tag{2.78}$$

where $p_1(0)$ and $p_1(\pm\pi/L)$ are the inversion eigenvalues of the first band at the center and edge of the Brillouin zones, respectively. This quantised Berry phase is an example of a symmetry-protected topological index. It is impossible for the Berry phase to change without either breaking inversion symmetry or closing and reopening the gap between bands 1 and 2.

As discussed in Section 1.2.2, the interface between different topological phases can host topological edge states, provided that there is a bulk-boundary correspondance. Figure 2.7a shows a "supercell" simulation of two interfaces between the inversion-symmetric cells. As the first band has a different Berry phase in the different unit cells, there are two eigensolutions in the energy gap between bands 1 and 2 in Figure 2.7b, exponentially localised to each interface as shown in Figure 2.7c.

Having seen that the quantised Berry phase can predict the emergence of edge states, we now turn to the final question - are these edge states topologically protected? While the topological invariant is well defined and protected by inversion symmetry, the bulk-edge correspondence of the original SSH model relies on the chiral symmetry (also known as sublattice symmetry) of the Hamiltonian to "pin" the edge states to zero energy, as discussed in Section 1.5. In the photonic analogue, the long-range interactions between the unit cells break the chiral symmetry of the system and the edge states are not pinned to a particular frequency within the gap, as in Figure 2.7b. In fact, a large perturbation could break the bulk-boundary correspondence of the photonic SSH model by shifting the edge states out of the band gap and into the bulk bands [51, 54]. In Chapter 4 we will study closely spaced perfectly conducting particles where the networks of voids and channels between the particles provide a platform for realising topological phases with chiral symmetry in photonics.

Topology of the second gap.—We now consider whether it is possible to continuously deform from cell A to cell C without breaking inversion symmetry about the origin or closing the *second* band gap. This is determined by the sum[12] of the Berry phases of the bands below the below the gap (modulo 2π) [87]. Although bands 1 and 2 have

12 In this case there are no degeneracies between the energy bands and we can apply the single-band formulation to calculate the Berry phases of each band individually and then sum these together to find the total Berry phase. In Section 2.6 we will introduce the multiband formulation for the Berry phase where we will see that inversion-symmetric perturbations will preserve the total Berry phase of a set of

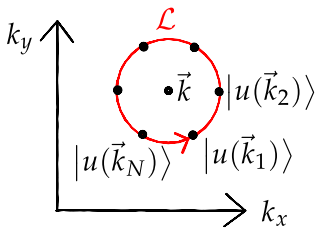

Figure 2.8: The Berry curvature of a band at $\vec{k}$, $\mathcal{F}(\vec{k})$, can be expressed as the Berry phase, $\gamma_{\mathcal{L}}$, per unit area, $A_{\mathcal{L}}$, of a vanishingly small loop $\mathcal{L}$ enclosing $\vec{k}$.

different Berry phases in each of the two inversion-symmetric unit cells, the sum of the Berry phases is the same in either unit cell,

$$\gamma_1^{\mathrm{A}} + \gamma_2^{\mathrm{A}} = \gamma_1^{\mathrm{C}} + \gamma_2^{\mathrm{C}} = \pm\pi. \tag{2.79}$$

This is consistent with the lack of edge states in the second band gap of Figure 2.7b.

2.5.2 *Berry phase, curvature and the Stokes'-like theorem*

In a 1D system, it is always possible to produce a set of exponentially localised Wannier functions using the parallel transport gauge introduced in the previous section [43], and the centers of these Wannier functions (related to the Berry phase) can lead to symmetry-protected phases. In higher dimensions it is not always possible to construct Wannier functions that are exponentially localised in all dimensions [33, 43, 44], but we will see that these "obstructions to Wannierisation" are themselves responsible for many of the topological phases in 2D.

In a 2D BZ, we can define the Berry curvature of a band as

$$\mathcal{F}_n(\vec{k}) = \lim_{A_{\mathcal{L}}\to 0} \frac{\gamma_{\mathcal{L}}^{(n)}}{A_{\mathcal{L}}}, \tag{2.80}$$

where $\gamma_{\mathcal{L}}^{(n)}$ is the Berry phase of a vanishingly small loop with area $A_{\mathcal{L}}$ enclosing $\vec{k}$, as shown in Figure 2.8. Unlike the Berry phases of the 1D SSH model, the Berry curvature is independent of our choice of unit cell because the vanishingly small loop starts and begins in the same Brillouin zone, $\vec{G} = 0$. The Berry curvature is also unbounded, $-\infty < \mathcal{F}_n(\vec{k}) < \infty$, unlike the Berry phase which is only defined modulo 2π.

inversion-symmetric bands, provided that they remain isolated from the other bands outside of the set.

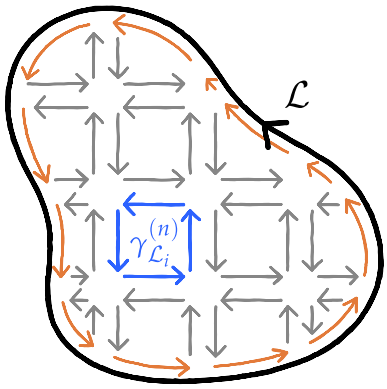

Figure 2.9: The single band Berry phase of the nth band, $\gamma^{(n)}_{\mathcal{L}}$, around a loop, $\mathcal{L}$, is equal (modulo 2π) to the total phase around many infinitesimal loops covering the enclosed surface, $\sum_i \gamma^{(n)}_{\mathcal{L}_i} = \gamma_{\mathcal{L}} + 2\pi n$, according to a Stokes-like theorem where internal contributions to the phase cancel, as shown above [33].

When the Berry curvature is integrated over an area $\mathcal{S}$ of the BZ we obtain a Berry flux,

$$F^{(n)}_{\mathcal{S}} = \lim_{N\to\infty} \sum_i^N \gamma^{(n)}_{\mathcal{L}_i} = \iint_{\mathcal{S}} \mathcal{F}_n(\vec{k})\, \mathrm{d}^2k. \tag{2.81}$$

As shown in Figure 2.9 there is a Stokes'-like theorem between the Berry phase around an area and the Berry flux through the area,

$$\exp\left[iF^{(n)}_{\mathcal{S}}\right] = \exp\left[i\gamma^{(n)}_{\partial\mathcal{S}}\right]. \tag{2.82}$$

However, it does not follow that $F^{(n)}_{\mathcal{S}} = \gamma^{(n)}_{\partial\mathcal{S}}$. Unlike a traditional application of Stokes' theorem, the integrals here are both inside exponentials, and the Berry phase and Berry flux are only equal modulo 2π,

$$\boxed{F^{(n)}_{\mathcal{S}} = \gamma^{(n)}_{\mathcal{L}} + 2\pi m.} \tag{2.83}$$

We shall see in the next section that the disagreement between Berry flux and Berry phase of Equation (2.83) is responsible for the topological invariant known as the Chern number.

2.5.3 *Chern numbers*

2.5.3.1 *Chern numbers as the Berry flux through the Brillouin zone*

Consider the Berry flux through the BZ and the Berry phase around the perimeter of the BZ,

$$F^{(n)}_{\mathrm{BZ}} = \iint_{\mathrm{BZ}} \mathcal{F}_n(\vec{k})\, \mathrm{d}^2k = \gamma^{(n)}_{\partial\mathrm{BZ}} + 2\pi m. \tag{2.84}$$

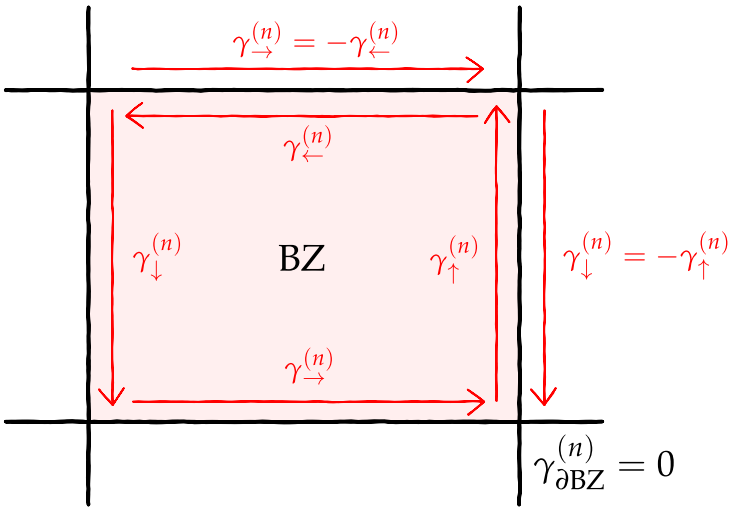

Figure 2.10: The Berry phase around perimeter of Brillouin zone is zero due to periodicity of the eigenmodes, $\gamma_{\partial \mathrm{BZ}}^{(n)} = 0$. Therefore the Berry flux, $F_{\mathrm{BZ}}^{(n)} = \gamma_{\partial \mathrm{BZ}}^{(n)} + 2\pi C_n$ is quantised with integer C_n being the Chern number of the nth band.

As shown in Figure 2.10, the Berry phase around the perimeter of the BZ must cancel to zero,

$$\begin{aligned} \gamma_{\partial \mathrm{BZ}}^{(n)} &= \gamma_{\rightarrow}^{(n)} + \gamma_{\uparrow}^{(n)} + \gamma_{\leftarrow}^{(n)} + \gamma_{\downarrow}^{(n)} \\ &= \gamma_{\rightarrow}^{(n)} + \gamma_{\uparrow}^{(n)} - \gamma_{\rightarrow}^{(n)} - \gamma_{\uparrow}^{(n)} = 0. \end{aligned} \tag{2.85}$$

This is because of the periodicity of the modes in $\vec{k}$-space. It follows that the Berry flux through the BZ is quantised,

$$F_{\mathrm{BZ}}^{(n)} = 2\pi C_n, \tag{2.86}$$

where C_n is an integer known as the Chern number of the nth band [33, 44],

$$\boxed{C_n = \frac{1}{2\pi} F_{\mathrm{BZ}}^{(n)} = \frac{1}{2\pi} \iint_{\mathrm{BZ}} \mathcal{F}_n(\vec{k})\, \mathrm{d}^2 k.} \tag{2.87}$$

The Chern number is a discrete, gauge-invariant topological index for 2D crystals, obtained by a global measurement over the whole 2D BZ. A non-zero Chern number indicates the breakdown of the Stokes' theorem, which occurs when the phase of the eigenmode cannot be globally defined across the BZ in a smooth manner [45].

2.5.3.2 *Chern numbers as obstructions to Wannierisation*

Although Chern numbers can be obtained by calculating and then integrating the Berry curvature as in Equation (2.87), it is insightful

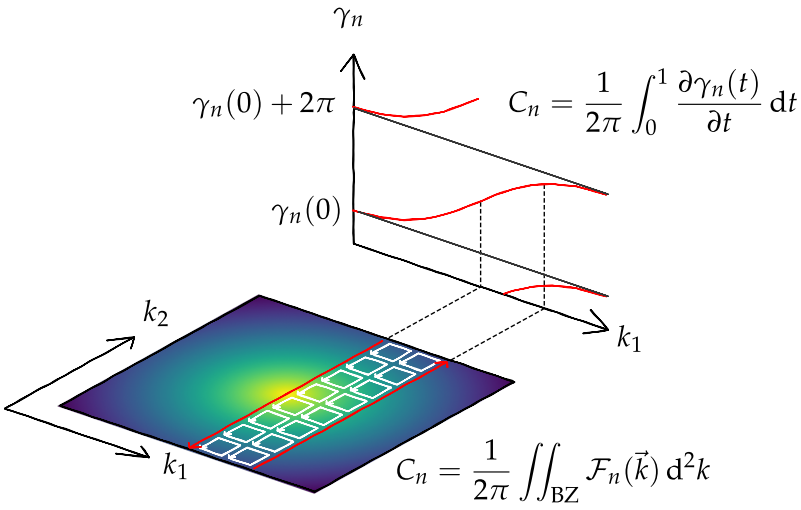

Figure 2.11: Due to the Stokes-like relation between Berry phase and Berry curvature, the integration of the Berry curvature over a strip of the BZ (lower left) is equivalent to the change in Berry phase along each end of the strips (upper right). A non-zero Chern number can be observed as a winding in the Berry phase spectrum [33, 43, 44].

to consider an equivalent expression for the Chern number. First, let us define $\gamma_n(t)$ as the Berry phase of the nth band along a closed loop $\mathcal{L}(t)$ that begins at $t\vec{b}_1$ and ends at $t\vec{b}_1 + \vec{b}_2$ for a given value of t. Because of the Stokes-like relation between Berry phase and curvature shown in Figure 2.9, the difference in $\gamma_n(t)$ for two different values of t is equal to the Berry curvature in the region enclosed between $\mathcal{L}(t_1)$ and $\mathcal{L}(t_2)$, as shown in Figure 2.11. The change in the Berry phase as $t \to t+1$ is therefore equal to the total Berry curvature of the Brillouin zone, which is also the definition of the Chern number,

$$C_n = \int_0^1 \frac{\partial\gamma_n(t)}{\partial t}\,\mathrm{d}t. \tag{2.88}$$

If the Chern number is non-zero, then as $t \to t+1$ the $\gamma_n(t)$ 'winds' from $\gamma_n(0) \to \gamma_n(0) + 2\pi C_n$, as shown in Figure 2.11. Each value of $\gamma_n(t)$ can be interpreted as the Wannier center of a *hybrid* Wannier function maximally localised in the $\vec{a}_2$ direction and periodic (Bloch-like) in the other directions [43],

$$\left|w_{nR_2}(k_1, x_2)\right\rangle = \frac{a_2}{2\pi}\int_{-\pi/a_2}^{+\pi/a_2} e^{-ik_2R_2}\left|H_z^{(n)}(k_1, k_2)\right\rangle \mathrm{d}k_2. \tag{2.89}$$

While the hybrid Wannier function may be localised along $\vec{a}_2$ for a given value of k_1, if the Berry phase winds as in Figure 2.11 then the average center of the hybrid Wannier function drifts between different unit cells as k_1 changes. It is therefore impossible to localise

the Wannier function in two dimensions if the Berry phase winds. As the winding of the Berry phase is equivalent to a non-zero Chern number, we say that the Chern number represents *obstructions to Wannierisation* in two dimensions [43].

2.5.3.3 *Chern numbers and inversion/time-reversal symmetries*

Let us now consider the Berry curvature in inversion and time symmetric systems. Recalling Equation (2.80) for the Berry curvature as the limit of a Berry phase around a vanishingly small loop $\mathcal{L}$ enclosing $\vec{k}$,

$$\mathcal{F}_n(\vec{k}) = \lim_{A\to 0} \frac{\gamma_{\mathcal{L}}^{(n)}}{A}, \tag{2.90}$$

we can infer the symmetry of $\mathcal{F}_n(\vec{k})$ from the behaviour of $\gamma_{\mathcal{L}}^{(n)}$ and the eigenmodes under inversion and time reversal symmetry.

The inversion operator acts on the Berry phase as

$$\begin{aligned}
\hat{\mathcal{I}}\gamma_{\mathcal{L}}^{(n)} &= \hat{\mathcal{I}}\,\mathrm{Im}\ln\left\langle u_n(\vec{k}_1)\middle|u_n(\vec{k}_N)\right\rangle \ldots \left\langle u_n(\vec{k}_2)\middle|u_n(\vec{k}_1)\right\rangle, && (2.91)\\
&= \mathrm{Im}\ln\left\langle u_n(-\vec{k}_1)\middle|u_n(-\vec{k}_N)\right\rangle \ldots \left\langle u_n(-\vec{k}_2)\middle|u_n(-\vec{k}_1)\right\rangle, && (2.92)\\
&= \gamma_{\mathcal{L}_{\mathcal{I}}}^{(n)}, && (2.93)
\end{aligned}$$

where $\mathcal{L}_{\mathcal{I}}$ is the inversion of $\mathcal{L}$ about the origin ($\vec{k} \to -\vec{k}$). In inversion symmetric systems, the Berry phase must be invariant under inversion symmetry, $\hat{\mathcal{I}}\gamma_{\mathcal{L}}^{(n)} = \gamma_{\mathcal{L}}^{(n)}$, and the single band Berry curvature must therefore be an even function of $\vec{k}$ [44],

$$\hat{\mathcal{I}}\hat{H}_{\vec{k}}\hat{\mathcal{I}}^{\dagger} = \hat{H}_{\vec{k}} \quad \Rightarrow \quad \mathcal{F}_n(k) = +\mathcal{F}_n(-k). \tag{2.94}$$

Similarly, the time-reversal operator acts on the Berry phase as

$$\begin{aligned}
\hat{\mathcal{T}}\gamma_{\mathcal{L}}^{(n)} &= \hat{\mathcal{T}}\,\mathrm{Im}\ln\left\langle u_n(\vec{k}_1)\middle|u_n(\vec{k}_N)\right\rangle \ldots \left\langle u_n(\vec{k}_2)\middle|u_n(\vec{k}_1)\right\rangle, && (2.95)\\
&= \mathrm{Im}\ln\left\langle u_n(-\vec{k}_N)\middle|u_n(-\vec{k}_1)\right\rangle \ldots \left\langle u_n(-\vec{k}_1)\middle|u_n(-\vec{k}_2)\right\rangle, && (2.96)\\
&= -\mathrm{Im}\ln\left\langle u_n(-\vec{k}_1)\middle|u_n(-\vec{k}_N)\right\rangle \ldots \left\langle u_n(-\vec{k}_2)\middle|u_n(-\vec{k}_1)\right\rangle, && (2.97)\\
&= -\gamma_{\mathcal{L}_{\mathcal{I}}}^{(n)}, && (2.98)
\end{aligned}$$

and in time-reversal symmetric systems, $\hat{\mathcal{T}}\gamma_{\mathcal{L}}^{(n)} = \gamma_{\mathcal{L}}^{(n)}$, the single band Berry curvature is therefore an odd function of $\vec{k}$ [44],

$$\hat{\mathcal{T}}\hat{H}_{\vec{k}}\hat{\mathcal{T}}^{\dagger} = \hat{H}_{\vec{k}} \quad \Rightarrow \quad \mathcal{F}_n(\vec{k}) = -\mathcal{F}_n(-\vec{k}), \tag{2.99}$$

and the Chern number of an isolated energy band in a time-reversal symmetric system is therefore $C_n = 0$. For a single isolated band to

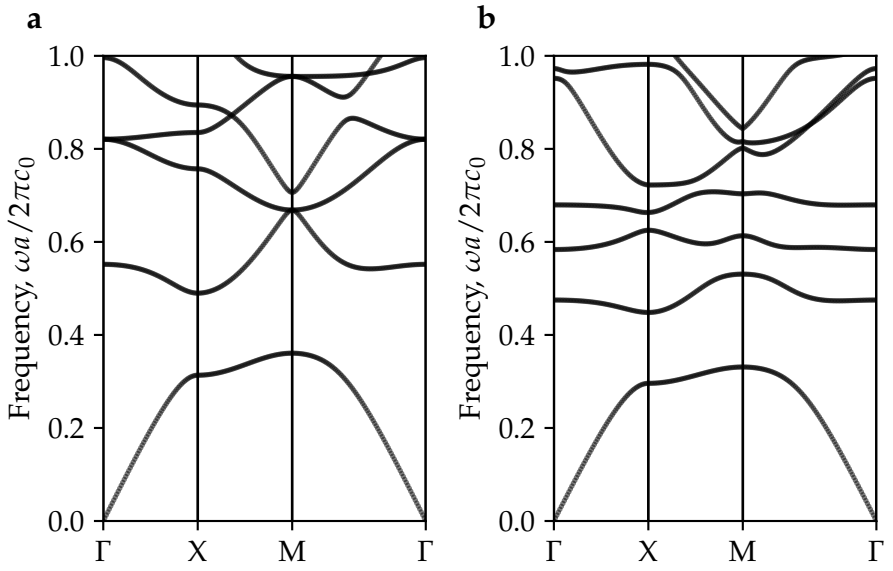

Figure 2.12: Normalised frequency bands of a photonic analogue of the QHE introduced by Wang *et al* [88] (a) in the absence of an external magnetic field ($\mu = \mu_0$, $\kappa = 0$) and (b) with an applied magnetic field ($\mu = 14\mu_0$, $\kappa = 12.4\mu_0$). The external magnetic field lifts the degeneracies between the first four bands, and we are therefore able to apply the single-band formalism of the Berry curvature to calculate the Chern number, C_n, of the first four bands, as in Figure 2.13.

have a non-zero Chern number, the time-reversal symmetry must be broken as in the QHE.

Note that it also follows that in systems with both inversion and time-reversal symmetry, the single band Berry curvature is identically equal to zero everywhere [44],

$$\left(\hat{\mathcal{I}}\hat{\mathcal{T}}\right)\hat{H}_{\vec{k}}\left(\hat{\mathcal{I}}\hat{\mathcal{T}}\right)^{\dagger} = \hat{H}_{\vec{k}} \quad \Rightarrow \mathcal{F}_n(\vec{k}) = -\mathcal{F}_n(\vec{k}) = 0. \tag{2.100}$$

2.5.3.4 *Example: A photonic analogue of the QHE*

Haldane and Raghu were the first to suggest that a photonic QHE phases could exist in photonic crystals [65, 66]. This was soon confirmed by Wang *et al* [67, 88] who proposed a photonic analogue of the QHE for the microwave regime. Their photonic crystal consisted of a square lattice of Yttrium-Iron-Garnet (YIG) rods of radius $r = 0.11a$, where a is the lattice parameter. YIG is a magneto-optic material; in the absence of an external magnetic field the rods have a trivial magnetic response ($\boldsymbol{\mu} = \mu_0 \boldsymbol{I}$), but under an under external magnetic field

applied in the out-of-plane direction, the rods develop a time-reversal breaking gyromagnetic anisotropy of the form [88]

$$\boldsymbol{\mu}(\vec{r}) = \begin{bmatrix} \mu & i\kappa & 0 \\ -i\kappa & \mu & 0 \\ 0 & 0 & \mu_0 \end{bmatrix}. \tag{2.101}$$

For incident light of frequency 4.28 GHz, realistic material parameters for YIG are a permittivity of $\epsilon = 15\epsilon_0$, and $\mu = 14\mu_0$ and $\kappa = 12.4\mu_0$ for an external magnetic field of 1600 Gauss [88].

The wave equation is [88]

$$\left(\vec{\nabla} \times \left[\boldsymbol{\mu}^{-1}(\vec{r})\vec{\nabla} \times \vec{E}\right] = \vec{\epsilon}(\vec{r})\omega^2\vec{E}\right)_z, \tag{2.102}$$

which we transformed to a finite wave matrix equation using the PWEM,

$$\left(\boldsymbol{K}_x\boldsymbol{f}^{\circledast}\boldsymbol{K}_x + \boldsymbol{K}_y\boldsymbol{f}^{\circledast}\boldsymbol{K}_y + i\boldsymbol{K}_x\boldsymbol{g}^{\circledast}\boldsymbol{K}_y - i\boldsymbol{K}_y\boldsymbol{g}^{\circledast}\boldsymbol{K}_x\right)[\![S_z]\!] = \omega^2\boldsymbol{a}_{zz}^{\circledast}[\![S_z]\!], \tag{2.103}$$

where $\boldsymbol{f}^{\circledast}$ and $\boldsymbol{g}^{\circledast}$ are the convolution matrix for the material fields $\mu/(\mu^2-\kappa^2)$ and $\kappa/(\kappa^2-\mu^2)$, respectively, and the other terms are as defined in Section 2.4 where the PWEM was introduced.

Figures 2.12a shows the bands of the time-reversal symmetric system in the absence of an external magnetic field, and Figure 2.12b shows the bands with broken time-reversal symmetry after the external magnetic field has been applied. Of the time-reversal broken bands, the first four are isolated and we can apply the single-band formalism to determine the Chern numbers of each band.

Figure 2.13 shows the calculation of the Chern numbers for the first four bands of the time-reversal broken crystal using the two methods that we have introduced: counting the winding number of the Berry phase, and integrating the Berry curvature.[13] Let us consider, for example, the existence of chiral edge states in the second band gap. Considering the bands below the second gap as the 'valence bands', the total Chern numbers of the valence band space is $C_{\text{val}}^{\text{topo}} = C_1^{\text{topo}} + C_2^{\text{topo}} = 1$. Using the same arguments as for the electronic QHE [65, 66], the change in Chern number at interface between this crystal and a trivial crystal (where the trivial crystal has a band gap that overlaps with the second band gap of the topological crystal) is $\Delta C = C_{\text{val}}^{\text{topo}} - C_{\text{val}}^{\text{triv}} = 1$. There is therefore a chiral edge state in

13 Of the two methods it may appear that integrating the Berry curvature is the simpler approach. For a general topological phase such as the QHE this may be true, but for symmetry-protected phases the winding of the Berry phase can often be determined from the symmetry eigenvalues of the bands at high symmetry points [73, 89], just as the Berry phase of the SSH model was determined by the inversion symmetry eigenvalues in Section 2.5.1.2. In later chapters we will therefore rely more on the winding of the Berry phase to diagnose the topological phase.

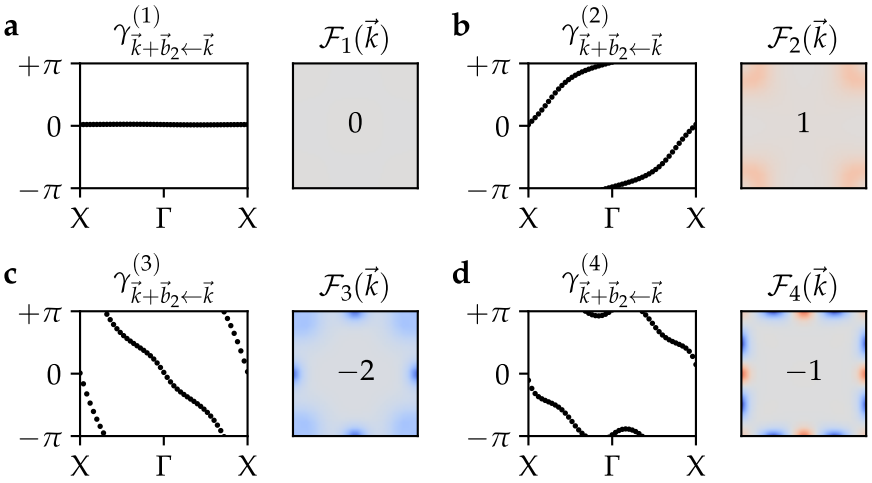

Figure 2.13: Calculating the Chern numbers of the first four bands of the photonic QHE phase in Figure 2.12b. For each band, we calculate the Chern number by both the winding of the Berry phase spectrum (left subpanels) and by integrating the Berry curvature (right subpanels). The numbers within the Berry curvature panels show the Chern number of that band. (a) The first band is trivial with zero Chern number and the Berry phase spectrum does not wind. (b-d) The second to fourth bands are each nontrivial, as indicated by the winding of the Berry phase spectrum and the non-zero Chern numbers.

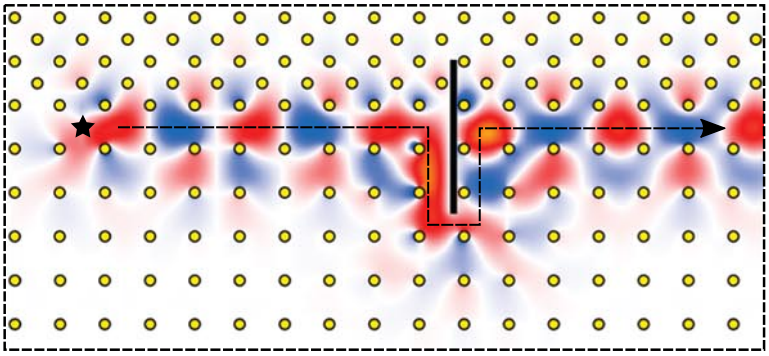

Figure 2.14: Reprint of the chiral edge state observed in finite element calculations by Wang *et al* [88] at an interface between the photonic QHE phase of Figure 2.12 and a trivial crystal with a common band gap. The location of the source is marked by the star. The interface is disrupted by a slab of perfect conductor (black rectangle), but the edge modes were observed to propagate without backscattering. Adapted from Wang *et al*, 2008 [88].

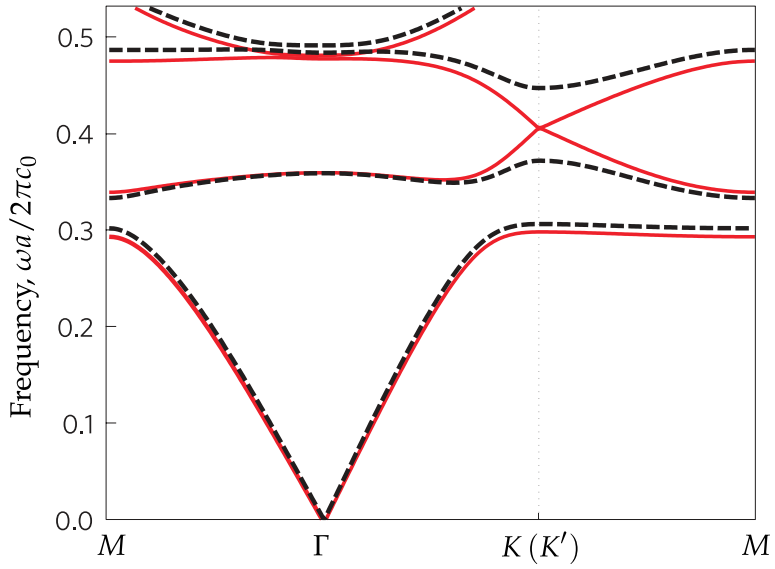

Figure 2.15: The frequency bands of the polarisation degenerate crystal introduced by Khanikaev *et al* [29] for $\chi = 0$ (red lines, trivial) and $\chi = 0.5$ (black dashes, non-trivial). Reprinted with permission from Springer Nature Customer Service Centre GmbH: Springer Nature, Nature Materials [29], Copyright 2013 Macmillan Publishers Limited.

the second band gap, enabling the unidirectional guiding of light with complete transmission around defects and obstacles as shown in Figure 2.14.

Although such chiral edge states have been observed numerically and experimentally in several other time-reversal broken systems, such as reviewed in Ozawa *et al* [18], bringing the photonic QHE to the visible frequency range has faced challenges as the losses are high or the time-reversal breaking response of the materials become too weak, requiring the application of an overly strong magnetic field to open a significant band gap [77]. There is therefore much interest in time-reversal invariants photonic analogues of the QSHE.

2.5.3.5 *Example: A photonic analogue of the QSHE*

While calculating Chern numbers for the photonic QHE is relatively straight forward, determining the spin-Chern numbers of the photonic QSHE is more involved as the bands must be decomposed into pseudo-spin up and down channels. This relies on internal or crystalline symmetries to mimic the fermionic time-reversal symmetry of electrons. While there are a variety of photonic QSHE designs, such as reviewed in [18, 77, 90], here we demonstrate the general principles by reviewing one particular example proposed by Khanikaev *et al* [29] where the photonic bands are decomposed into pseudo-spin channels

according to an internal symmetry. Recalling Maxwell's TE and TM wave equations from Section 2.3.5,

$$-\left(\partial_x \frac{1}{\mu_{yy}(\vec{r},\omega)}\partial_x + \partial_y \frac{1}{\mu_{xx}(\vec{r},\omega)}\partial_y\right) E_z(\vec{r},\omega) = \omega^2 \epsilon_{zz}(\vec{r},\omega) E_z(\vec{r},\omega), \tag{2.104}$$

$$-\left(\partial_x \frac{1}{\epsilon_{yy}(\vec{r},\omega)}\partial_x + \partial_y \frac{1}{\epsilon_{xx}(\vec{r},\omega)}\partial_y\right) H_z(\vec{r},\omega) = \omega^2 \mu_{zz}(\vec{r},\omega) H_z(\vec{r},\omega), \tag{2.105}$$

we see that when $\boldsymbol{\epsilon}/\epsilon_0 = \boldsymbol{\mu}/\mu_0$ then waves of both polarisations propagate identically. Khanikaev *et al* [29] noted that in such *polarisation degenerate* systems a pair of pseudo-spin states can be constructed via a linear combination of the two polarisations, $\psi_\pm(\vec{k}) = E_z(\vec{k}) \pm H_z(\vec{k})$. In the polarisation degenerate systems there exists a symmetry $\hat{\mathcal{D}} E_z(\vec{k}) = H_z(-\vec{k})$ and $\hat{\mathcal{D}} H_z(\vec{k}) = -\hat{\mathcal{D}} E_z(-\vec{k})$ such that $\hat{\mathcal{D}}$ acts on $\psi_\pm(\vec{k})$ as a pseudo-fermionic time-reversal symmetry, $\hat{\mathcal{D}}^2 \psi_\pm(\vec{k}) = -\psi_\pm(\vec{k})$, resulting in symmetry-protected Kramers' degeneracies at time-reversal invariant momenta [18, 29].

The authors showed that for a polarisation degenerate uniaxial metamaterial,

$$\boldsymbol{\epsilon} = \boldsymbol{\mu} = \begin{bmatrix} \alpha & 0 & 0 \\ 0 & \alpha & 0 \\ 0 & 0 & \beta \end{bmatrix}, \tag{2.106}$$

with a bi-anisotropy that preserved the polarisation degeneracy,

$$\boldsymbol{\xi} = \boldsymbol{\zeta}^\dagger = \begin{bmatrix} 0 & i\chi_{xy} & 0 \\ -i\chi_{xy} & 0 & 0 \\ 0 & 0 & 0 \end{bmatrix}, \tag{2.107}$$

the degenerate pseudo-spin states obey the wave equation [29]

$$(\mathcal{L}_0 \pm \mathcal{L}_1)\psi_\pm(\vec{r},t) = \left(\frac{\omega}{c}\right)^2 \beta(\vec{r})\psi_\pm(\vec{r},t), \tag{2.108}$$

where $\psi_\pm = E_z \pm H_z$, for the operators $\mathcal{L}_0 = -\partial_x \tilde{\alpha}^{-1}\partial_x - \partial_y \tilde{\alpha}^{-1}\partial_y$ and $\mathcal{L}_1 = -i\partial_x \theta \partial_y + i\partial_y \theta \partial_x$ with $\tilde{\alpha} = \alpha/(\alpha^2 - \chi^2)$ and $\theta = \beta/(\beta^2 - \chi^2)$, and $\chi = \chi_{xy}/\alpha^2$.

Figure 2.15 shows the bands of the photonic crystal taken from the paper by Khanikaev *et al* [29] consisting of a triangular lattice of cylinders ($r = 0.34a$) of the polarisation degenerate uniaxial metamaterial ($\alpha = 14$, $\beta = 1$) without bi-anisotropy ($\chi = 0$, red lines) and with bi-anisotropy ($\chi = 0.5$, dashed lines). The cylinders are assumed to be

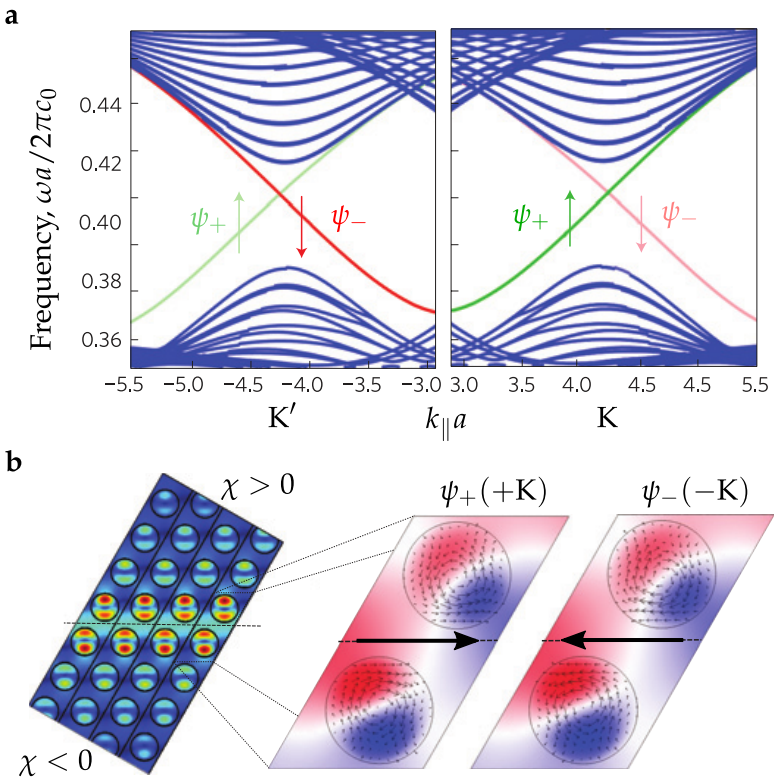

Figure 2.16: Helical edge states observed by Khanikaev *et al* [29]. (a) Pseudo-spin up (green) and pseudo-spin down (red) edge states emerge at K and K′. The opaque bands correspond to a $\chi < 0$ to $\chi > 0$ interface, and the semi-transparent bands correspond to a $\chi < 0$ to $\chi > 0$ interface. (b) Absolute value of an edge state, $|\psi_\pm|$, at an interface between crystals with opposite bi-anisotropy, χ. The mode is exponentially localised to the interface. The zoomed regions show the real part of the field for the pseudo-spin up and pseudo-spin down edge modes at this interface. The power flux (black arrows) of the modes rotate in opposite directions. Reprinted with permission from Springer Nature Customer Service Centre GmbH: Springer Nature, Nature Materials [29], Copyright 2013 Macmillan Publishers Limited.

surrounded by air or vacuum. When the bi-anisotropy is switched on, the Dirac cone at K is broken open.

Each band shown is doubly degenerate with its pseudo-spin partner, so there are two spin-up and two spin-down bands below the broken Dirac cone. Despite this, the spin up/down equations are decoupled and ψ_+ and ψ_- are distinct and well defined across the entire BZ. It is therefore possible to calculate the Chern numbers of spin-up and spin-down bands using the single-band Berry curvature formula,

$$C^{\pm}_{\text{val}} = C^{\pm}_1 + C^{\pm}_2 = \pm 1.$$

These spin-Chern numbers are supported by the edge states observed by the authors [29]; their results are shown in Figure 2.16.

This example demonstrates that internal symmetries can allow pseudo-spin up and down subspaces to be defined in photonic crystals. However, the construction of this particular example is relatively complex as the required bi-anisotropic material response does not occur with the necessary strength in natural materials. Instead, the photonic crystal consists of an array of cylinders, and each cylinder is composed of a bi-anisotropic metamaterial [29, 77]. Two years after this proposal, Wu and Hu [1] proposed an elegant all-dielectric analogue of the QSHE that exploits crystalline symmetries to produce the pseudo-fermionic time-reversal symmetry. However, the rigorous decomposition of the valence band space into pseudo-spin up/down channels has remained an open problem for Wu and Hu's proposal [73]. In Chapter 3 we introduce a method of decomposing the valence band space and determining the spin-Chern numbers for the crystal of Wu and Hu [1], but first we must introduce the multiband formulation of the Berry phase and curvature.

2.6 TOPOLOGY OF AN ISOLATED SET OF BANDS

2.6.1 *Failure of the single-band Berry phase*

So far, we have considered the topology of a single, isolated band. We now introduce the generalisation of the Berry phase/curvature to an isolated *set of bands*, where bands within the set may or may not cross or touch each other, but are isolated from (do not cross or touch) any bands outside of the set for all $\vec{k}$. This multiband Berry phase/curvature is necessary because the single band formulation breaks down at band crossings. For example, Figure 2.17a shows the photonic SSH model introduced in Figure 2.6, but with the size of the unit cell doubled to $2a = 2(d_1 + d_2)$. This results in the 'folding' of the primitive band structure into a smaller BZ spanning $|k_x| < \pi/2a$, creating degeneracies at the edge of the reduced BZ as shown in

Figure 2.17b. As shown in Figures 2.17c-d, the eigenmodes of the first band are not continuous across the BZ boundary,

$$\lim_{\epsilon\to 0}\left\langle u_1(\pi/2a-\epsilon)\middle|u_1(\pi/2a+\epsilon)\right\rangle = 0. \tag{2.109}$$

The single-band Berry phase formulation would therefore fail to characterise this doubled unit cell even though it represents the same bulk material as the original unit cell.

2.6.2 *Multiband parallel transport*

Recall from Equation (2.70) that the single-band Berry phase of a closed loop can be interpreted as the phase mismatch of the nth eigenmode before and after parallel transport around the loop,

$$e^{i\gamma_{\mathcal{L}}^{(n)}} = e^{i\tilde{\gamma}_{1,N}^{(n)}} = \left\langle \tilde{u}_n(\vec{k}_1)\middle|e^{i\vec{G}\cdot\vec{r}}\middle|\tilde{u}_n(\vec{k}_N)\right\rangle, \tag{2.110}$$

where $\vec{G} = \vec{k}_N - \vec{k}_1$ and $\tilde{u}_n(\vec{k}_i)$ are the parallel transported modes. The multiband Berry phase and Berry curvature can be defined from a similar multiband parallel transport process for an isolated set of J bands, such as the valence bands of an insulator [44].

Consider constructing a *multiband parallel transport gauge* where the first eigenmodes are unchanged, $\left|\tilde{u}_n(\vec{k}_1)\right\rangle = \left|u_n(\vec{k}_1)\right\rangle$, and the subsequent eigenmodes at each $\vec{k}_i$ along the parallel transport path are mixed by some matrix,

$$\left|\tilde{u}_m(\vec{k}_{i+1})\right\rangle = \sum_{n=1}^{J} X_{mn}(\vec{k}_{i+1},\vec{k}_i)\left|u_n(\vec{k}_{i+1})\right\rangle. \tag{2.111}$$

One possibility would be to take X_{mn} as the overlap matrix between the original gauge at $\vec{k}_{i+1}$ and the parallel transport gauge at $\vec{k}_i$,

$$\tilde{M}_{mn}(\vec{k}_{i+1},\vec{k}_i) = \left\langle u_m(\vec{k}_{i+1})\middle|\tilde{u}_n(\vec{k}_i)\right\rangle. \tag{2.112}$$

This would ensure that each $\left|\tilde{u}_n(\vec{k}_{i+1})\right\rangle$ and $\left|\tilde{u}_n(\vec{k}_i)\right\rangle$ are as aligned as possible in both phase and composition [44]. However, taking $X_{mn} = \tilde{M}_{mn}$ would be problematic because the overlap matrix $\tilde{\boldsymbol{M}}$ is generally non-unitary. If we wish for orthogonal modes to remain orthogonal after multiband parallel transport then we must ensure the transformation is unitary. The multiband parallel transport gauge is therefore defined as

$$\boxed{\left|\tilde{u}_m(\vec{k}_{i+1})\right\rangle = \sum_{n=1}^{J} \tilde{\mathcal{M}}_{mn}(\vec{k}_{i+1},\vec{k}_i)\left|u_n(\vec{k}_{i+1})\right\rangle,} \tag{2.113}$$

where

$$\tilde{\boldsymbol{\mathcal{M}}} = \boldsymbol{\mathcal{V}}\boldsymbol{\mathcal{W}}^{\dagger} \tag{2.114}$$

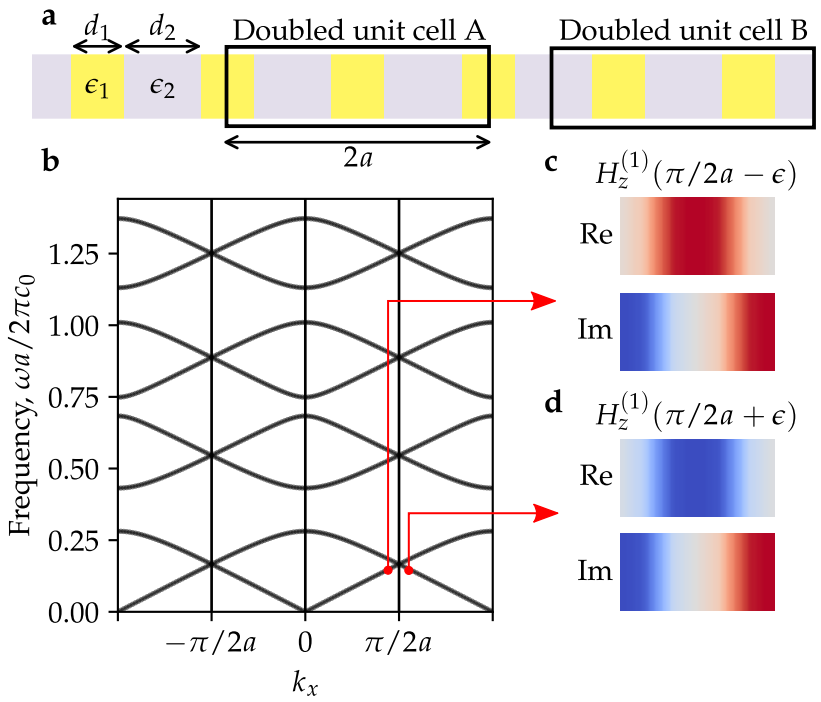

Figure 2.17: (a) The same SSH-like geometry as in Figure 2.6, consisting of alternating slabs of permittivity, $\epsilon_1 = 4\epsilon_0$ and $\epsilon_2 = \epsilon_0$, of thicknesses $d_1 = 0.4a$ and $d_2 = 0.6a$, respectively, but considering a doubled unit cell of length $2a = 2(d_1 + d_2)$. (b) The normalised frequency bands of the doubled unit cell are the same as in Figure 2.6, but are folded into a smaller Brillouin zone. This band folding produces a degeneracy between bands 1 and 2 at the edge of the Brillouin zone of the doubled unit cell. (c-d) Visualisation of the eigenmodes of the first band of the doubled unit cell (c) just before and (d) just after the degeneracy at $k_x = \pi/2a$. The projection operators onto the first band, $|u_1(k_x)\rangle\langle u_1(k_x)|$ are not smooth and continuous functions of $\vec{k}$ across the whole Brillouin zone, and the single-band formulation of the Berry phase fails because $\langle H_z^{(1)}(\pi/2a - \epsilon)|H_z^{(1)}(\pi/2a + \epsilon)\rangle \to 0$ as $\epsilon \to 0$. It is necessary to consider a multiband Berry phase at crossings between bands.

is the *best unitary approximation* of $\tilde{\boldsymbol{M}}$ obtained by the *singular value decomposition* of the overlap matrix [44],

$$\tilde{\boldsymbol{M}} = \boldsymbol{\mathcal{V}}\boldsymbol{\Sigma}\boldsymbol{\mathcal{W}}^{\dagger}, \tag{2.115}$$

where $\boldsymbol{\mathcal{V}}$ and $\boldsymbol{\mathcal{W}}$ are $J \times J$ unitary matrices and $\boldsymbol{\Sigma}$ is a matrix containing the *singular values* of $\tilde{\boldsymbol{M}}$ along the diagonal. While the mixed eigenmodes of Equation (2.113) may no longer be pure energy eigenstates, the mixed and the unmixed eigenmodes span the same subspace because the mixing is unitary [44],

$$\sum_{n=1}^{J} \left|\tilde{u}_n(\vec{k}_i)\right\rangle\left\langle\tilde{u}_n(\vec{k}_i)\right| = \sum_{n=1}^{J} \left|u_n(\vec{k}_i)\right\rangle\left\langle u_n(\vec{k}_i)\right|. \tag{2.116}$$

Note that Equations (2.111) and (2.113) would be equivalent in the continuum limit $N \to \infty$.

The parallel transport of an isolated set of J bands around a closed loop in $\vec{k}$-space, $\vec{k}_N - \vec{k}_1 = \vec{G}$ where $\vec{G}$ is a reciprocal lattice vector, therefore results in an overall unitary mixing [44],

$$(\boldsymbol{W}_{\mathcal{L}})_{mn} = \left\langle\tilde{u}_m(\vec{k}_1)\right|e^{i\vec{G}\cdot\vec{r}}\left|\tilde{u}_n(\vec{k}_N)\right\rangle, \tag{2.117}$$

where $\boldsymbol{W}_{\mathcal{L}}$ is a $J \times J$ matrix known as a *Wilson loop matrix*. As $\boldsymbol{W}_{\mathcal{L}}$ is unitary, the Wilson loop eigenvalues are of the form $\lambda_n = e^{i\gamma_{\mathcal{L}}^{(n)}}$ where the $\gamma_{\mathcal{L}}^{(n)}$ are the multiband Berry phases of the set of bands [44]. The total Berry phase of the J bands around the loop is therefore [44]

$$\gamma_{\mathcal{L}}^{\text{total}} = \sum_{n=1}^{J} \gamma_{\mathcal{L}}^{(n)} = \operatorname{Im} \ln \det \boldsymbol{W}_{\mathcal{L}}. \tag{2.118}$$

In the continuum limit the Wilson loop operator (related to the Wilson loop matrix as $(\boldsymbol{W}_{\mathcal{L}})_{nm} = \left\langle u_n(\vec{k}_1)\right|\hat{W}_{\mathcal{L}}\left|u_n(\vec{k}_N)\right\rangle$) may be expressed as [43, 44]

$$\hat{W}_{\mathcal{L}}^{\{n\}} = e^{i\vec{G}\cdot\vec{r}} \lim_{N\to\infty} \hat{P}(\vec{k}_N)\hat{P}(\vec{k}_{N-1})\ldots\hat{P}(\vec{k}_2)\hat{P}(\vec{k}_1), \tag{2.119}$$

where the $\hat{P}(\vec{k}_i) = \sum_{n=1}^{J} \left|u_n(\vec{k}_i)\right\rangle\left\langle u_n(\vec{k}_i)\right|$ are projectors onto the subspace of interest. Although Equation (2.119) only strictly agrees with Equation (2.113) in the continuum limit, I include it here because it offers the interpretation that the Wilson loop operators are really a function of the Hilbert space that the bands occupy, rather than the particular bands themselves.

Finally, note that at times we will also refer to Wilson *line* operators, which is the same as a Wilson loop operator except that the path is not a closed loop, and the operator is therefore not gauge invariant.

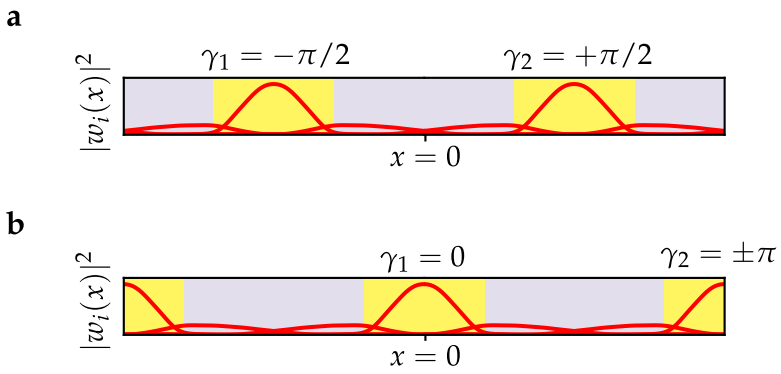

Figure 2.18: Wannier functions and Berry phases of the first two bands of the doubled unit cell introduced in Figure 2.17. (a) If we take the origin $x = 0$ as the center of the lower refractive index region (purple region), then the doubled cell is trivial, $\gamma_{\mathcal{L}}^{\text{total}} = \pi/2 - \pi/2 = 0$. (b) If we take the origin as the center of the higher refractive index region (yellow region), then the doubled cell is non-trivial, $\gamma_{\mathcal{L}}^{\text{total}} = 0 \pm \pi = \pm\pi$.

2.6.3 *Multiband Berry phase example*

We can now apply the multiband formulation to the doubled unit cells of the SSH-like photonic crystal in Figure 2.17 where the single-band formulation had failed because of the band folding at the edge of the BZ. Applying Equation (2.118) to the first two bands of the doubled unit cell, we find $\gamma_{\mathcal{L}}^{\text{total}} = 0$ and $\gamma_{\mathcal{L}}^{\text{total}} = \pm\pi$ for the choices of origin shown in Figures 2.18a and b, respectively. This could also have been determined from the position of the Wannier functions shown by the red curves in Figure 2.18: the total Berry phase (modulo 2π) is equal to the sum of the Wannier function centers (modulo a lattice vector). As the two cells in Figure 2.18 have different values of $\gamma_{\mathcal{L}}^{\text{total}}$, the multiband Berry phase is compatible with the observation of the edge states in Figure 2.7, which can be considered as a supercell of 5 doubled unit cells of the type shown in Figure 2.18a and 5 of the type shown in Figure 2.18b.

2.6.4 *Multiband Berry curvature example*

We can also determine the Chern numbers of the photonic QHE using the multiband Berry phase/curvature. Figure 2.19 shows the multiband Berry phase and curvature of the (a) first band, (b) first two bands, (c) first three bands, and (d) first four bands of the photonic QHE phase of Wang *et al* [88] that we first discussed in Section 2.5.3.4.

Compared to the single band formulation in Figure 2.19, the multiband Berry curvature is simpler. This is because the fluctuations

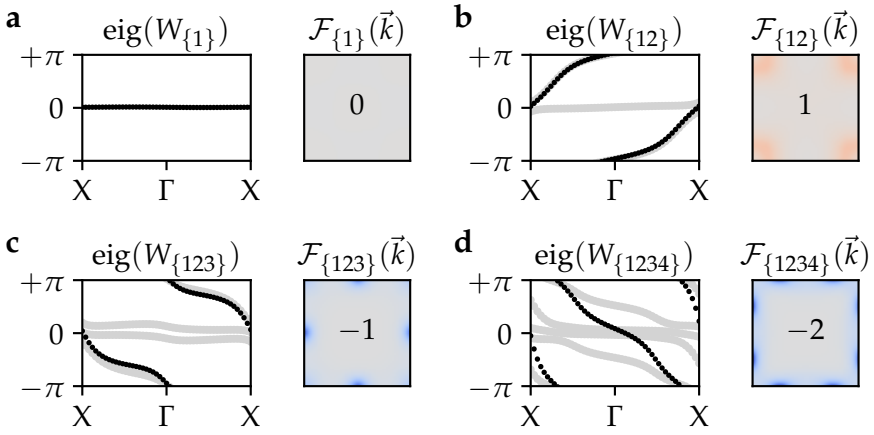

Figure 2.19: Calculating the total Chern numbers of the non-trivial QHE phase of Wang *et al* [88] (we showed the energy bands of this crystal in Figure 2.12b) using the multiband Berry phase and Berry curvature of (a) the first band, (b) the first two bands, (c) the first three bands, (d) the first four bands. In the left subpanels we show the individual eigenvalues of the Wilson loops in grey, and the sum of the Wilson loop eigenvalues (i.e. the total multiband Berry phase) in black. In the right subpanels we show the total multiband Berry curvature (red and blue are positive and negative curvatures, respectively). The numbers within each Berry curvature panel show the total Chern number of the considered bands.

caused by the exchange of Berry curvature between bands *within* each set are not seen; only the Berry curvature that has been exchanged to or received from bands outside of the set is visible.

The total Chern number of the isolated set of bands is always integer because the total projection operator onto the bands,

$$\hat{P}_{\{n\}}(\vec{k}) = \sum_{n\in\{n\}} \left|u_n(\vec{k})\right\rangle\left\langle u_n(\vec{k})\right|,$$

is a smooth and periodic function of $\vec{k}$ [43]. However, it is important to note that the individual Wilson loop eigenvalues of Figure 2.19 do not all wind by an integer multiple of 2π. As we discuss in the next section, this is because the projection operators to the individual eigenvectors of the Wilson loop, $\left|\tilde{u}_i(\vec{k})\right\rangle\left\langle\tilde{u}_i(\vec{k})\right|$, are not necessarily smooth and periodic functions of $\vec{k}$, leading to non-integer (and meaningless) Chern numbers [43].

2.6.5 *Meaning of individual Chern numbers*

As Gresch *et al* demonstrate [43, Appendix E], a set of bands will have an integer total Chern number if the projection operators to the set of

bands, $\hat{P}_{\text{set}}(\vec{k})$, is a smooth and continuous function of $\vec{k}$. Furthermore, any decomposition of the band space into N different subspaces $\mathcal{H}_i$,

$$\mathcal{H}_{\text{set}} = \bigoplus_{i=1}^{N} \mathcal{H}_i, \tag{2.120}$$

$$\hat{P}_{\text{set}}(\vec{k}) = \sum_{i=1}^{N} \hat{P}_i(\vec{k}), \tag{2.121}$$

will have well-defined integer Chern numbers C_i associated with each subspace $\mathcal{H}_i$ if the projection operators onto each subspace, $\hat{P}_i(\vec{k})$, are continuous and periodic functions of $\vec{k}$ [43, Appendix E]. The individual Chern numbers will add up to the total Chern number of the set,

$$\boxed{C_{\text{set}} = \sum_{i=1}^{N} C_i.} \tag{2.122}$$

There are many ways in which $\mathcal{H}_{\text{set}}$ may be decomposed, but not all have meaningful Chern numbers. For example, the spin-Chern numbers in the QSHE are only meaningful if the set of valence bands is decomposed into two subspaces [43],

$$\mathcal{H}_{\text{val}} = \mathcal{H}_+ \oplus \mathcal{H}_-, \tag{2.123}$$

$$\hat{P}_{\text{val}}(\vec{k}) = \hat{P}_+(\vec{k}) + \hat{P}_-(\vec{k}) \tag{2.124}$$

where the two subspaces are connected by time-reversal symmetry,

$$\mathcal{T}\,\hat{P}_\pm(+\vec{k})\,\mathcal{T}^{-1} = \hat{P}_\mp(-\vec{k}). \tag{2.125}$$

In the non-trivial QSHE phase, the subspaces $\mathcal{H}_+$ and $\mathcal{H}_-$ have *odd* Chern numbers. However, it is also possible to decompose $\mathcal{H}_{\text{val}}$ of the non-trivial QSHE phase into two subspaces with trivial Chern numbers (or the trivial QSHE phase into two subspaces with non-trivial Chern numbers) if we disregard the time-reversal symmetry constraint of Equation (2.125) [91]. When considering the individual Chern numbers of subspaces of $\mathcal{H}_{\text{val}}$ it is important that the decomposition of $\mathcal{H}_{\text{val}}$ has been constrained in a meaningful manner, i.e. by the relevant symmetries.

2.7 REMARKS ON CHAPTER 2

In this chapter, we introduced the methods that we will use to study topological photonics in the following chapters, including numerical methods to solve Maxwell's equations [80, 81], and the single band and multiband formulations of Berry phase, Berry curvature, and Chern numbers [33, 43, 44]. We demonstrated the methods on example photonic analogues of the SSH, QHE, and QSHE from previous works.

For the photonic QSHE phase, we chose to review a particular crystal [29] for which the decomposition of the valence bands into pseudo-spin up and pseudo-spin down channels, $\psi_+(\vec{k})$ and $\psi_-(\vec{k})$, was relatively straightforward because of an internal symmetry of the materials (polarisation degeneracy) which decoupled Maxwell's equations into two independent pseudo-spin channels [29]. In the next chapter we study the elegant all-dielectric photonic analogue of the QSHE introduced by Wu & Hu [1]. This phase is protected by a combination of bosonic time reversal and crystalline symmetries. Other works have suggested that this crystal is a trivial phase, but we introduce a new method of decomposing the valence band space that allows the topological nature of this crystal to be determined from rigorous full-wave calculations for the first time.

3

PSEUDO-SPIN IN TOPOLOGICAL PHOTONIC CRYSTALS

3.1 OVERVIEW

In this chapter, we introduce a new method to classify photonic analogues of the QSHE in which the spin degree of freedom is mimicked by the orbital angular momentum of light [1, 72–76]. This research was originally published in Physical Review Research [92]. As we reviewed in Chapters 1 and 2, the QSHE is a symmetry-protected phase where the total Chern number of the valence bands is zero, $C_{\text{val}} = 0$. If the valence band space is decomposed in a time-reversal symmetric manner [43],

$$\mathcal{H}_{\text{val}} = \mathcal{H}_+ \oplus \mathcal{H}_-, \tag{3.1}$$

where the projection operators to the subspaces, $\hat{P}_1(\vec{k})$ and $\hat{P}_2(\vec{k})$, are smooth and continuous functions of $\vec{k}$ and are exchanged under time-reversal symmetry,

$$\mathcal{T}\hat{P}_\pm(+\vec{k})\mathcal{T}^{-1} = \hat{P}_\mp(-\vec{k}), \tag{3.2a}$$

then the subspaces $\mathcal{H}_1$ and $\mathcal{H}_2$ carry equal and opposite Chern numbers that are *odd* in the non-trivial QSHE phase. At the interfaces between trivial and non-trivial QSHE phases, helical edge states emerge that are protected by fermionic time-reversal symmetry, $\mathcal{T}^2 = -1$.

In photonic analogues of the QSHE, we can consider a certain group of bands below a certain energy band gap as our 'valence' bands. A pseudo-fermionic time-reversal symmetry can arise from crystalline symmetries [1] or other symmetries of the constitutive relationships [29]. The challenge is then to decompose $\mathcal{H}_{\text{val}}$ into "pseudo-spin" subspaces in a meaningful way. In some cases, this is straightforward. For example, in the polarisation degenerate ($\epsilon = \mu$) crystal of Khanikaev *et al* [29] that we discussed in Section 2.5.3.5, there were an even number of valence bands and the particular choice of constitutive relations produced an obvious decoupling of the solutions to Maxwell's equations into two equally sized subspaces, $\psi_+(\vec{k}) = E_z(\vec{k}) + H_z(\vec{k})$ and $\psi_-(\vec{k}) = E_z(\vec{k}) - H_z(\vec{k})$, which are continuous and well defined over the full BZ. It was then straightforward to calculate the Chern number of each subspace and determine the topological phase. In other cases, our understanding of photonic QSHE analogues has been hindered by not having a well-defined pseudo-spin basis for the valence bands over the whole BZ.

If we have an *odd* number of valence bands, it is not possible to decompose the valence band space into two equally sized subspaces. Here, we propose decomposing the valence band subspace of $C_2\mathcal{T}$-symmetric photonic crystals with an odd number of valence bands into pseudo-spinful subspaces *and a pseudo-spinless* subspace,

$$\mathcal{H}_{\text{val}} = \mathcal{H}_\varnothing \oplus \mathcal{H}_+ \oplus \mathcal{H}_-, \tag{3.3}$$

where the projection operators to the pseudo-spinless subspace obey

$$C_2\, \hat{P}_\varnothing(+\vec{k})\, C_2^{-1} = \hat{P}_\varnothing(-\vec{k}), \tag{3.4a}$$
$$\mathcal{T}\, \hat{P}_\varnothing(+\vec{k})\, \mathcal{T}^{-1} = \hat{P}_\varnothing(-\vec{k}), \tag{3.4b}$$

and the projection operators to the pseudo-spinful subspaces obey

$$C_2\, \hat{P}_\pm(+\vec{k})\, C_2^{-1} = \hat{P}_\pm(-\vec{k}), \tag{3.5a}$$
$$\mathcal{T}\, \hat{P}_\pm(+\vec{k})\, \mathcal{T}^{-1} = \hat{P}_\mp(-\vec{k}). \tag{3.5b}$$

In this chapter, we will explain why $\nu = \text{mod}_2(C_\pm)$ is a $C_2\mathcal{T}$-protected $\mathbb{Z}_2$ topological index where C_+ and C_- are the Chern numbers of the pseudo-spinful subspaces $\mathcal{H}_+$ and $\mathcal{H}_-$. We will demonstrate our method on the photonic crystals where the spin degree of freedom is mimicked by the angular momentum of the light, such as the well-known example of Wu & Hu [1]. Previous works have suggested that this crystal is a special kind of trivial phase known as an *obstructed atomic limit* [42] and is not topological [73, 93, 94]. However, the $C_2\mathcal{T}$-protected $\mathbb{Z}_2$ topological index we identify confirms that the crystal of Wu & Hu [1] is indeed a photonic analogue of the QSHE with weakly broken pseudo-fermionic time-reversal symmetry at the interfaces. We explain how the obstructed atomic limit is distinct from, but compatible with, interpreting the crystal as a photonic analogue of the QSHE. In particular, we discuss how our $C_2\mathcal{T}$-protected $\mathbb{Z}_2$ topological index allows the prediction of symmetry-protected helical edge states at slowly graded interface regions between the trivial and non-trivial phases.

3.2 LIMITATIONS OF THE STANDARD WILSON LOOP APPROACH

3.2.1 *Wu & Hu's scheme for silicon topological photonics*

In 2015, Wu & Hu [1] introduced an all-dielectric photonic crystal intended to emulate the QSHE. In their work, they considered a honeycomb lattice of dielectric cylinders, as shown in Figure 3.1a-b. When the unit cell is taken as the primitive rhombus containing two cylinders, then the BZ contains Dirac cones at the $\tilde{K}$ and $\tilde{K}'$ positions, as shown in Figure 3.1c. When considering a larger hexagonal unit cell containing a ring of six cylinders, the folding of the bands produces a double Dirac

cone at the Γ-point of the new Brillouin zone. Wu & Hu [1] perturbed the honeycomb lattice by shrinking or expanding these hexagonal rings of cylinders and observed that the reduction of symmetry broke the double Dirac cone, as shown in Figures 3.1d-f. They demonstrated that the effective Hamiltonian of this broken double Dirac cone [1] is equivalent (in the vicinity of Γ) to the Bernevig-Hughes-Zhang model [95] of the QSHE.

The eigenmodes of the effective Hamiltonians mimic the spin of electrons using the angular momentum of the light, and obey a pseudo-fermionic time-reversal symmetry resulting from a combination of the (bosonic) time-reversal symmetry of the photons and the C_6 symmetry of the crystal [1]. By calculating the spin-Chern numbers from the effective Hamiltonians, Wu & Hu argued that the shrunken-ring cell corresponds to the trivial phase, and that the expanded-ring cell corresponds to the non-trivial phase. At interfaces between the shrunken-ring and expanded-ring unit cells, as in Figure 3.2a, there are edge states that closely resemble the helical edge states of the QSHE, as shown in Figure 3.2b. There is a small gap in the edge modes as the presence of the interface is a C_6 breaking perturbation that lifts the pseudo-fermionic time-reversal symmetry and allows a small amount of backscattering [1, 75]. However, if the interface and any disorder can be considered as relatively weak C_6-breaking perturbations, then the backscattering of the edge states is largely surpressed [75].

3.2.2 *Obstructed atomic limits and fragile topology*

Although Wu & Hu [1] argued that the shrunken-ring and expanded-ring cells corresponded to trivial and non-trivial photonic QSHE phases, respectively, the effective Hamiltonians behind this argument only account for the four bands of the double Dirac point (bands 2-5 of the full Hamiltonian), and are based on $k \cdot p$ expansions that are only accurate in the vicinity of the Γ-point. As the spin-Chern numbers are obtained by integrating the Berry curvature of the pseudo-spin channels over the entire BZ, it is important to verify the spin-Chern numbers using the full Hamiltonian.

Blanco de Paz *et al* [73, 93] analysed the topology of all three bands below the broken Dirac point (which we shall refer to as the 'valence' bands) using Wilson loops. In the full Hamiltonian, there are degeneracies between the first and second bands at K and between the second and third bands at Γ. All three bands must therefore be considered simultaneously, as discussed in Section 2.6. However, Blanco de Paz *et al* found that the three-band Wilson loop spectra of the shrunken-ring or the expanded-ring cells of Wu & Hu do not wind, as shown in Figures 3.3a-b. This indicates that it is possible to construct localised Wannier functions that span the subspace of the three valence bands. However, the localised Wannier functions of the expanded-ring and

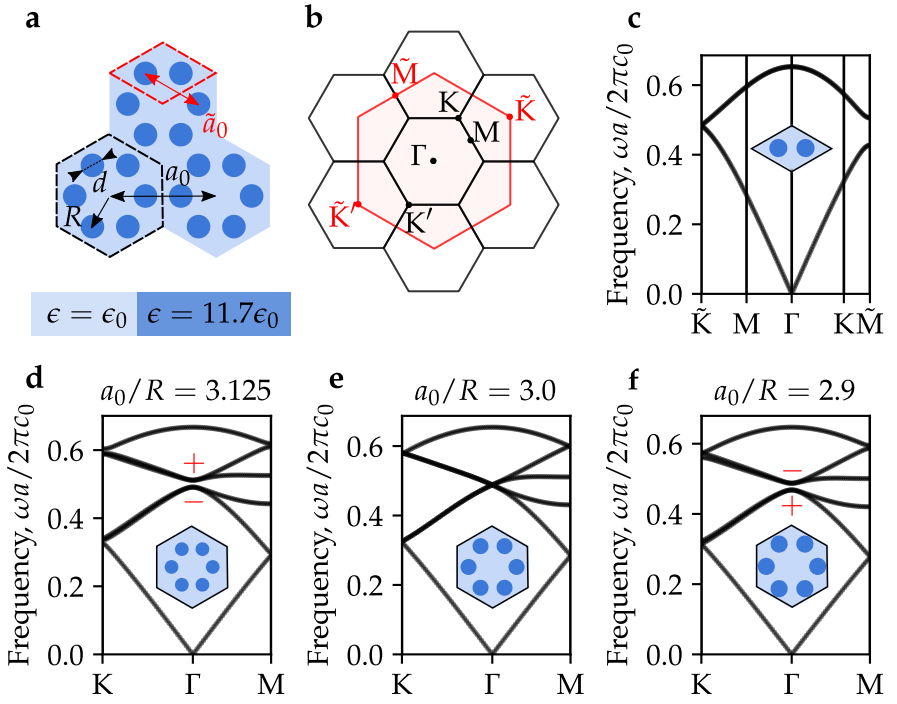

Figure 3.1: (a) The photonic crystal introduced by Wu & Hu [1] consists of dielectric cylinders of permittivity $\epsilon = 11.7\epsilon_0$ on a honeycomb lattice of lattice parameter $\tilde{a}_0$ (unit cell shown in red). This can also be considered as *rings of cylinders* on a triangular lattice of a larger lattice parameter a_0 (unit cell shown in black). The distance of each cylinder from the center of the ring is R, and the diameters of the cylinders are $d = 2R/3$. (b) The large BZ corresponding to the primitive unit cell (red) and the smaller BZ corresponding to the larger hexagonal unit cell (black). Note that the $\tilde{\mathrm{K}}$ and $\tilde{\mathrm{K}}'$ points of the larger BZ lie at $\tilde{\Gamma}$ of the smaller BZ. (c) The energy bands of the primitive unit cell feature Dirac cones at $\tilde{\mathrm{K}}$ and $\tilde{\mathrm{K}}'$. (d-f) Energy bands of the hexagonal unit cell for (d) a shrunken ring of cylinders, $a_0/R > 3$, (e) an unperturbed honeycomb arrangement, $a_0/R = 3$, and (f) an expanded ring of cylinders, $a_0/R < 3$. Note that shrunken and expanded geometries depicted in the insets are exaggerated. In the unperturbed system, (e) the Dirac cones at $\tilde{\mathrm{K}}$ and $\tilde{\mathrm{K}}'$ of the primitive BZ are folded to a double Dirac point at $\tilde{\Gamma}$ in the new BZ. In the shrunken and expanded systems, (d,f) the Dirac cone is broken open by the reduction in symmetry. The C_2 eigenvalues of the modes of the broken Dirac cone are shown in red; note that the order of the bands is inverted in the expanded-ring unit cell, $a_0/R < 3$.

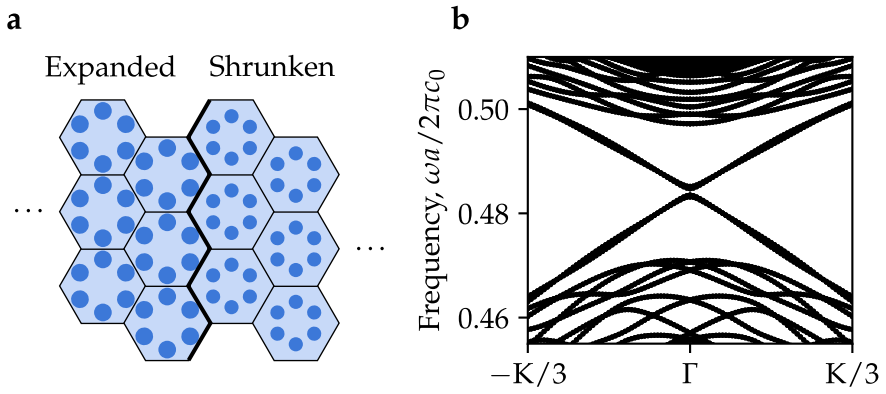

Figure 3.2: (a) Schematic of a zig-zag interface between the expanded-ring and shrunken-ring unit cells of Wu & Hu [1]. Note that the geometries have been exaggerated. (b) Edge states and minigap for a "supercell" calculation of a zig-zag interface between 10 shrunken-ring unit cells and 10 expanded-ring unit cells. This calculation was performed using the `MPB` software [96].

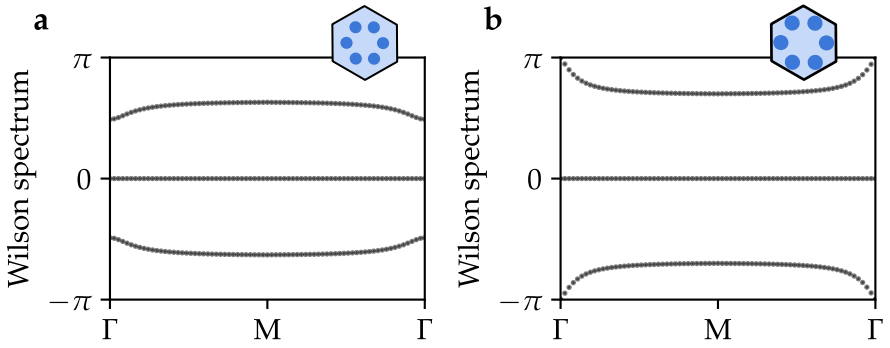

Figure 3.3: The Wilson loop spectra of the 'valence' bands (first three bands) of the (a) shrunken-ring unit cell and (b) expanded-ring unit cell of Wu & Hu [1]. In both cases, there is no winding of the Wilson loop spectrum. In the expanded-ring unit cell, however, the two sets of the Wilson loop eigenvalues are localised around $\pm\pi$, indicating that the corresponding Wannier functions are localised at the edges of the unit cell. This is known as an obstructed atomic limit [73].

shrunken-ring cells are centered at edges[1] and the origin of the unit cells, respectively, and it is not possible to continuously deform between the two cells without breaking the rotational symmetry about the origin of the unit cell. Systems such as the expanded-ring unit cell where the Wannier functions are localised at the edges of the unit cells are known as *obstructed atomic limits*[2] [42, 73].

Obstructed atomic limits can be identified using the method of Benalcazar *et al* [97] to classify $C_n\mathcal{T}$ symmetric phases according to the rotation symmetry eigenvalues at the high symmetry points of the BZ. Each topological phase is labelled with a topological index vector $\vec{X}$, where $\vec{X} = \vec{0}$ indicates a trivial atomic limit and $\vec{X} \neq 0$ indicates an obstructed atomic limit. For crystals with $C_2\mathcal{T}$ symmetry on a triangular lattice, the topological index of Benalcazar *et al* [97] is

$$\vec{X} = \left(\left[M_1^{(2)} \right], \left[M_1'^{(2)} \right], \left[M_1''^{(2)} \right] \right), \tag{3.6}$$

where M, M′, and M″ are the C_2-invariant momenta of the Brillouin zone related by $M'' = C_6 M' = C_6^2 M$ (see Appendix C), and where $\left[\Pi_p^{(n)}\right] = \#\Pi_p^{(n)} - \#\Gamma_p^{(n)}$ and $\#\Pi_p^{(n)}$ is the number of bands below the topological band gap with eigenvalue $\exp(2\pi i(p-1)/n)$, where Γ is $\vec{k} = 0$ and where Π denotes any high symmetry point such as M or K. For the shrunken-ring cell of Wu & Hu $\vec{X} = 0$, indicating a trivial atomic phase, and for the expanded-ring cell $\vec{X} = (-2, -2, -2)$, indicating an obstructed atomic limit.[3]

However, Blanco de Paz *et al* [73] found that by perturbing the crystal as in Figure 3.4a, it was possible to introduce an isolating energy gap between the first and second bands, allowing the Wilson loop spectrum of the trivial first band, shown in Figure 3.4c, and of the second and third bands, shown in Figure 3.4d, to be calculated separately. The second and third bands had a *non-trivial* winding. On the other hand, the Wilson loop spectra of all three bands, shown in Figure 3.4e, still indicated that all three bands together formed a *trivial* obstructed atomic limit phase. The second and third bands were said to be *fragilely* topological bands [98] because the Wilson loop winding was not robust against the addition of the trivial first band.

Blanco de Paz *et al* [73] showed that the fragilely topological bands were a result of the C_2 symmetry of the crystal "pinning" the Wilson

1 Blanco de Paz *et al* showed that the Wannier functions are s-like orbitals centered on a kagome lattice [73]. The positions of these Wannier functions can be verified using nested Wilson loops.

2 In a regular atomic limit, the valence bands are Wannierisable and the Wannier functions are all localised around the center of the unit cell. It is also possible to increase the distance between unit cells without closing the valence-conduction band gap. In an obstructed atomic limit, the valence bands are Wannierisable but one or more of the Wannier functions are localised at the edges of the unit cell, making it impossible to increase the distance between the unit cells without undergoing a topological phase transition [42].

3 See Appendix C for the determination of $\vec{X}$ from the C_2 eigenvalues of the crystal.

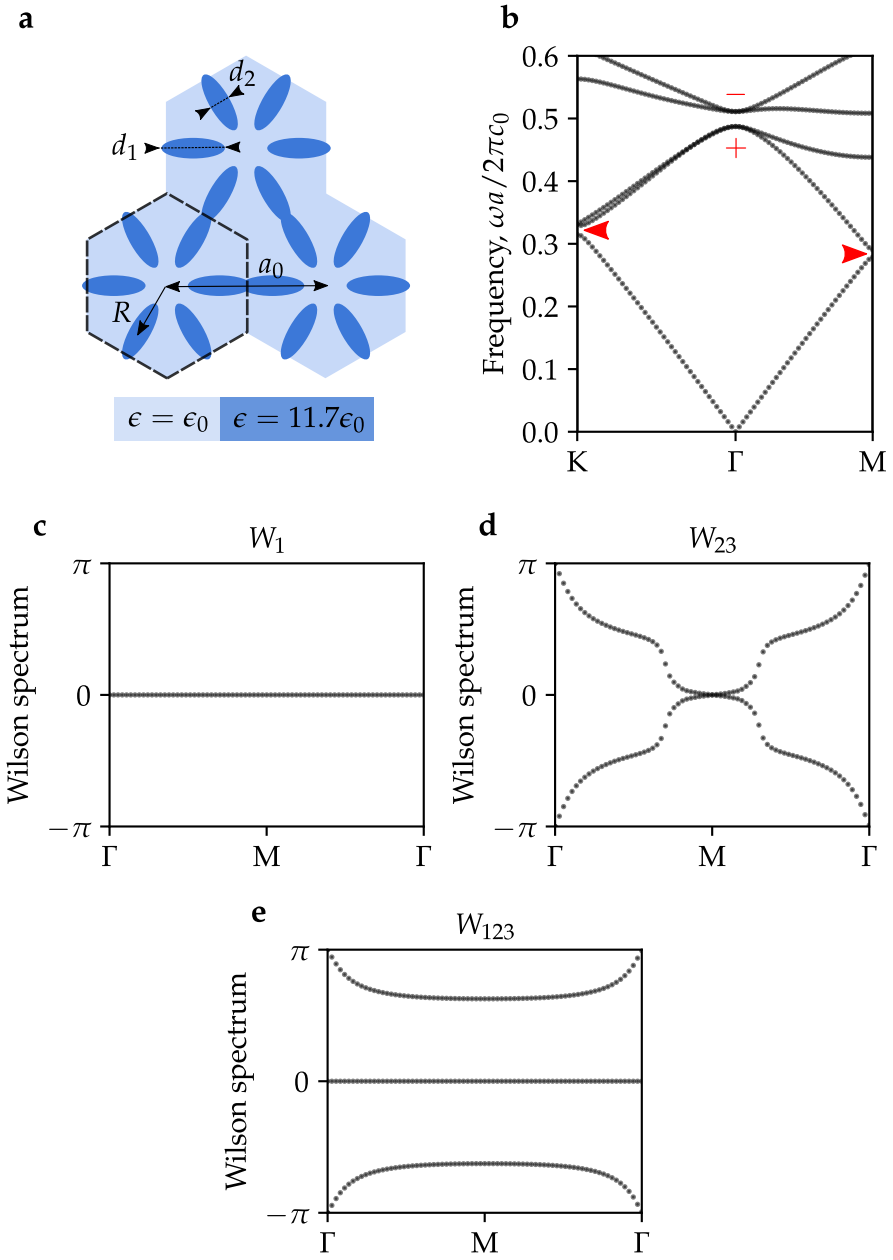

Figure 3.4: (a) The photonic crystals studied by Blanco de Paz *et al* [73] consist of rings of dielectric elliptical cylinders on a triangular lattice. The lattice has lattice parameter a_0, and the cylinders are a distance $R = a_0/3$ from the center of the rings. The elliptical cylinders have axes of lengths d_1 and d_2. (b) The normalised frequency of the photonic crystal with $d_1 = 0.4$ and $d_2 = 0.13$. There is a band-inversion at the broken double Dirac cone (the parities of the eigenmodes are labelled in red), similar to the expanded-ring unit cell of Wu & Hu [1], but in this case there is also an isolating band gap between bands 1 and 2 (red arrows). (c) The Wilson loop spectrum of the first band, W_1, indicates that it is topologically trivial, as is expected for an isolated time-reversal symmetric band. (d) The spectrum of a Wilson loop through the second and third bands simultaneously, W_{23}, features a non-trivial topological winding. (e) The Wilson loop spectrum of all three bands simultaneously, W_{123}, indicates an obstructed atomic limit with no topological winding. The second and third bands are therefore known as *fragilely topological* bands [73].

loop spectra to either 0 or $\pm\pi$ at Γ and M. To understand this pinning, recall that the straight Wilson loops as introduced in Figure 2.11 are defined as $\hat{W}(\vec{k}) = \hat{W}_{\vec{k}+\vec{b}_2\leftarrow\vec{k}}$, such that $\hat{W}(\Gamma) = \hat{W}_{\vec{b}_2\leftarrow\vec{0}}$ and $\hat{W}(\mathrm{M}) = \hat{W}_{\frac{1}{2}\vec{b}_1+\vec{b}_2\leftarrow\frac{1}{2}\vec{b}_1}$. These Wilson loops can be considered as the product of two smaller Wilson lines,

$$\begin{aligned} W_{nm}(\Gamma) &= \big\langle u_n(\vec{b}_2)\big|\hat{W}_{\vec{b}_2\leftarrow\vec{0}}\big|u_m(\vec{0})\big\rangle, \\ &= \sum_p \big\langle u_n(\vec{b}_2)\big|\hat{W}_{\vec{b}_2\leftarrow\frac{1}{2}\vec{b}_2}\big|u_p(\tfrac{1}{2}\vec{b}_2)\big\rangle\big\langle u_p(\tfrac{1}{2}\vec{b}_2)\big|\hat{W}_{\frac{1}{2}\vec{b}_2\leftarrow\vec{0}}\big|u_m(\vec{0})\big\rangle. \end{aligned} \tag{3.7}$$

Noting that

$$\begin{aligned} &\big\langle u_n(\vec{b}_2)\big|\hat{W}_{\vec{b}_2\leftarrow\frac{1}{2}\vec{b}_2}\big|u_p(\tfrac{1}{2}\vec{b}_2)\big\rangle \\ &= \big\langle e^{\pm i\vec{b}_2\cdot\vec{r}}u_n(\vec{0})\big|\hat{W}_{\vec{0}\leftarrow-\frac{1}{2}\vec{b}_2}\big|e^{\pm i\vec{b}_2\cdot\vec{r}}u_p(-\tfrac{1}{2}\vec{b}_2)\big\rangle &(3.8)\\ &= \big\langle u_n(\vec{0})\big|\hat{W}_{\vec{0}\leftarrow-\frac{1}{2}\vec{b}_2}\big|u_p(-\tfrac{1}{2}\vec{b}_2)\big\rangle, &(3.9) \end{aligned}$$

Blanco de Paz *et al* [73] realised that if the modes being fed to the Wilson loop have equal C_2 eigenvalues at the C_2-invariant momenta, $C_2\big|u_n(\Pi)\big\rangle = \lambda_{C_2}(\Pi)\big|u_n(\Pi)\big\rangle$ for all n and for $\Pi \in \{\Gamma, \mathrm{M}\}$, then the first Wilson line may be expressed as the inverse of the second Wilson line,

$$\begin{aligned} &\big\langle u_n(\vec{0})\big|\hat{W}_{\vec{0}\leftarrow-\frac{1}{2}\vec{b}_2}\big|u_p(-\tfrac{1}{2}\vec{b}_2)\big\rangle \\ &\quad= \lambda^\dagger_{C_2}(\Gamma)\lambda_{C_2}(\mathrm{M})\cdot\big\langle u_n(\vec{0})\big|\hat{W}_{\vec{0}\leftarrow\frac{1}{2}\vec{b}_2}\big|u_p(\tfrac{1}{2}\vec{b}_2)\big\rangle &(3.10)\\ &\quad= \lambda^\dagger_{C_2}(\Gamma)\lambda_{C_2}(\mathrm{M})\cdot\big\langle u_n(\vec{0})\big|\hat{W}^{-1}_{\frac{1}{2}\vec{b}_2\leftarrow\vec{0}}\big|u_p(\tfrac{1}{2}\vec{b}_2)\big\rangle, &(3.11) \end{aligned}$$

such that the Wilson loop simplifies to

$$W_{nm}(\Gamma) = \lambda^\dagger_{C_2}(\Gamma)\cdot\lambda_{C_2}(\mathrm{M})\cdot\delta_{nm}. \tag{3.12}$$

Similarly, if $C_2\big|u_n(\Pi)\big\rangle = \lambda_{C_2}(\Pi)\big|u_n(\Pi)\big\rangle$ for all n and for $\Pi \in \{\mathrm{M}', \mathrm{M}''\}$, Blanco de Paz *et al* [73] also showed that

$$\begin{aligned} W_{nm}(\mathrm{M}) &= \big\langle u_n(\tfrac{1}{2}\vec{b}_1+\vec{b}_2)\big|\hat{W}_{\frac{1}{2}\vec{b}_1+\vec{b}_2\leftarrow\frac{1}{2}\vec{b}_1}\big|u_m(\tfrac{1}{2}\vec{b}_1)\big\rangle &(3.13)\\ &= \lambda^\dagger_{C_2}(\mathrm{M}')\cdot\lambda_{C_2}(\mathrm{M}'')\cdot\delta_{nm}, &(3.14) \end{aligned}$$

where $\mathrm{M}' = \frac{1}{2}\vec{b}_1$ and $\mathrm{M}'' = \frac{1}{2}\vec{b}_1 + \frac{1}{2}\vec{b}_2$. For the second and third bands of the fragilely topological crystal of Figure 3.4, the C_2 eigenvalues were $\lambda_{C_2}(\Gamma) = +1$, and $\lambda_{C_2}(\mathrm{M}) = -1$, such that the eigenvalues of $W_{nm}(\Gamma)$ were pinned to $e^{i\gamma} = -1$ and the eigenvalues of $W_{nm}(\mathrm{M})$ were pinned to $e^{i\gamma} = +1$, producing the fragile topological winding.

However, the pinning is broken when considering Wilson loops of all three valence bands simultaneously because the first band has different C_2 eigenvalues to the second and third bands. In such cases

Equations (3.12) and (3.14) do not hold and there is no Wilson loop winding as in Figures 3.3b and 3.4e. This has led to the interpretation that the photonic crystals presented by Wu & Hu and Blanco de Paz *et al* are not photonic analogues of the QSHE [94]. In this chapter, we challenge this interpretation on the basis that all symmetry-protected phases are Wannierisable. For example, the valence bands of the non-trivial electronic QSHE state are also Wannierisable if one does not enforce that the Wannier functions must come in time-reversal symmetric pairs [91]. Detection of (obstructed) atomic limits does not necessarily mean that the system is trivial; symmetry-protected phases can often be detected only with particular forms of Wilson loops such as bent and/or nested Wilson loops [89]. In the following sections, we identify a QSHE-like phase in the bulk topology of these crystals by considering a particular form of nested Wilson loop that is equivalent to treating the multiband Berry curvature as a band structure in its own right.

3.3 BERRY BANDS AS PSEUDO-SPIN IN $C_2\mathcal{T}$-SYMMETRIC CRYSTALS

Wilson loops are unitary operators (see Section 2.6.2), and we can therefore form a Hermitian eigenvalue problem for the multiband Berry curvature, $\mathcal{F}_i(\vec{k})$,

$$\boxed{\hat{H}_{\mathcal{F}}(\vec{k})\big|\tilde{u}_i(\vec{k})\big\rangle = \mathcal{F}_i(\vec{k})\big|\tilde{u}_i(\vec{k})\big\rangle,} \tag{3.15}$$

where

$$\hat{H}_{\mathcal{F}}(\vec{k}) = \lim_{A\to 0}[-i\log \hat{W}^{\text{val}}_{\mathcal{L}}/A], \tag{3.16}$$

$$\mathcal{F}_i(\vec{k}) = \lim_{A\to 0}[\gamma_i(\vec{k})/A], \tag{3.17}$$

and

$$\hat{W}^{\text{val}}_{\mathcal{L}}\big|\tilde{u}_i(\vec{k})\big\rangle = \gamma_i(\vec{k})\big|\tilde{u}_i(\vec{k})\big\rangle \tag{3.18}$$

is a Wilson loop of the valence bands around the vanishingly small path $\mathcal{L}$ of area A enclosing $\vec{k}$.[4] This transforms the original energy eigenvalue problem, $E(\vec{k})$, to a "Berry band" eigenvalue problem, $\mathcal{F}(\vec{k})$, where the Berry bands span the valence band space. By taking the Wilson loop operator in Equation (3.16) through the *full* valence

4 Note that if taking this approach to calculate Berry curvatures numerically, the $\vec{k}_i$ of the small Wilson loop should be chosen carefully such that the overlap between eigenmodes at adjacent $\vec{k}_i$ is non-zero. This can occur frequently at rotationally symmetric $\vec{k}$-points. For example, it is common that $\langle u_n(\Delta k, 0)\big|u_m(0,\Delta k)\rangle \to 0$ as $\Delta k \to 0$. This can be resolved by discretising the Wilson loop more finely such that the new overlaps, for example $\langle u_n(\Delta k,0)\,|u_m\left(\Delta k/\sqrt{2}, \Delta k\sqrt{2}\right)\rangle \cdot \langle u_n\left(\Delta k/\sqrt{2}, \Delta k\sqrt{2}\right)|u_m(0,\Delta k)\rangle$, are non-zero.

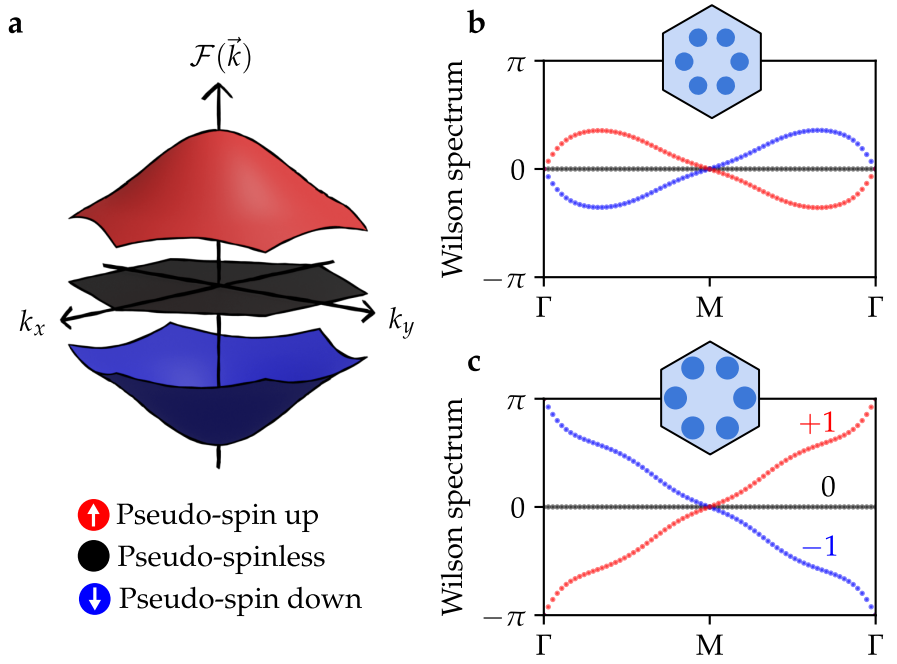

Figure 3.5: In $C_2\mathcal{T}$-symmetric crystals, the Berry bands are pinned to zero (pseudo-spinless) or come in positive/negative pairs (pseudo-spinful). (a) Schematic of the Berry bands for the shrunken-ring and expanded-ring unit cells introduced by Wu & Hu [1]. In both cases all three of the Berry bands are isolated by gaps of Berry curvature for all $\vec{k}$. (b-c) Wilson loops through the pseudo-spin up (red), pseudo-spinless (black), and pseudo-spin up (blue) Berry bands for the (b) shrunken-ring and (c) expanded-ring unit cells introduced by Wu & Hu [1]. All three Berry bands of the shrunken-ring unit cell are trivial, whereas the pseudo-spinful Berry bands of the expanded-ring unit cell are non-trivial with pseudo-spin Chern numbers $C_\pm = \pm 1$.

band space, $\hat{W}_{\mathcal{L}}^{\text{val}}$, we ensure that different realisations of the same symmetry-protected phase are treated equally, irrespective of the particular energy gaps or crossings among the valence bands.

In crystals with simultaneous C_2 and $\mathcal{T}$ symmetries the Berry bands transform as [89, 99]

$$C_2\mathcal{T}\,\hat{H}_{\mathcal{F}}(\vec{k})\,(C_2\mathcal{T})^{-1} = -\hat{H}_{\mathcal{F}}(\vec{k}), \tag{3.19}$$

such that each Berry band is either pinned to zero Berry curvature, or belongs to a pair of Berry bands with equal and opposite Berry curvature as shown in the schematic of Figure 3.5a. It follows from Equation (3.19) that a pair of Berry bands with equal and opposite non-zero Berry curvature must have opposite angular momentum,[5]

$$\left|\tilde{u}_{\pm}(\vec{k})\right\rangle = \frac{1}{\sqrt{2}}\left|u_1(\vec{k})\right\rangle \pm \frac{i}{\sqrt{2}}\left|u_2(\vec{k})\right\rangle, \tag{3.20}$$

where $C_2\mathcal{T}\left|\tilde{u}_{\pm}\right\rangle = \left|\tilde{u}_{\mp}(\vec{k})\right\rangle$, and $\left|u_1(\vec{k})\right\rangle$ and $\left|u_2(\vec{k})\right\rangle$ are invariant under $C_2\mathcal{T}$. This suggests that the Berry bands are a natural basis of pseudo-spin for photonic crystals that emulate spin using orbital angular momentum. We therefore refer to the pairs of Berry bands with opposite angular momentum, $\left|\tilde{u}_{\pm}(\vec{k})\right\rangle$, as the *pseudo-spinful* Berry bands. If there are an odd number of valence bands, we refer to the remaining Berry band which has no angular momentum and is pinned to zero Berry curvature for all $\vec{k}$ as the pseudo-spinless Berry band, $\left|\tilde{u}_{\varnothing}(\vec{k})\right\rangle$.

For the crystals of Wu & Hu and Blanco de Paz we found that each Berry band was isolated from the others by a Berry curvature gap for all $\vec{k}$. We were therefore able to calculate the Wilson loop winding of each Berry band individually, as shown for the shrunken-ring and expanded-ring cells of Wu & Hu in Figures 3.5b-c, respectively, and summarised for all the crystals of Wu & Hu and Blanco de Paz *et al* in Appendix A. The winding of the Wilson loop spectra in Figure 3.5b indicates that all three Berry bands of the shrunken-ring cell are trivial. On the other hand, the winding in Figure 3.5c indicates that the pseudo-spinful Berry bands of the expanded-ring cell carry equal and opposite non-zero Chern numbers.[6]

To understand the non-trivial topology of the Berry bands, we now consider their symmetries. Following the approach of Bradlyn *et al* [89], we show in Appendix B that the Berry band Hamiltonian

5 The spatial rotation C_2 will rotate the modes without altering the angular momentum, whereas time-reversal symmetry $\mathcal{T}$ will reverse the angular momentum. The combined symmetry $C_2\mathcal{T}$ will therefore reverse the angular momentum.

6 Note that the Chern numbers of these Berry bands is defined by integrating the Berry curvature of the Berry bands, which can be considered as a form of nested Wilson loop [100–102], rather than the original Berry curvature.

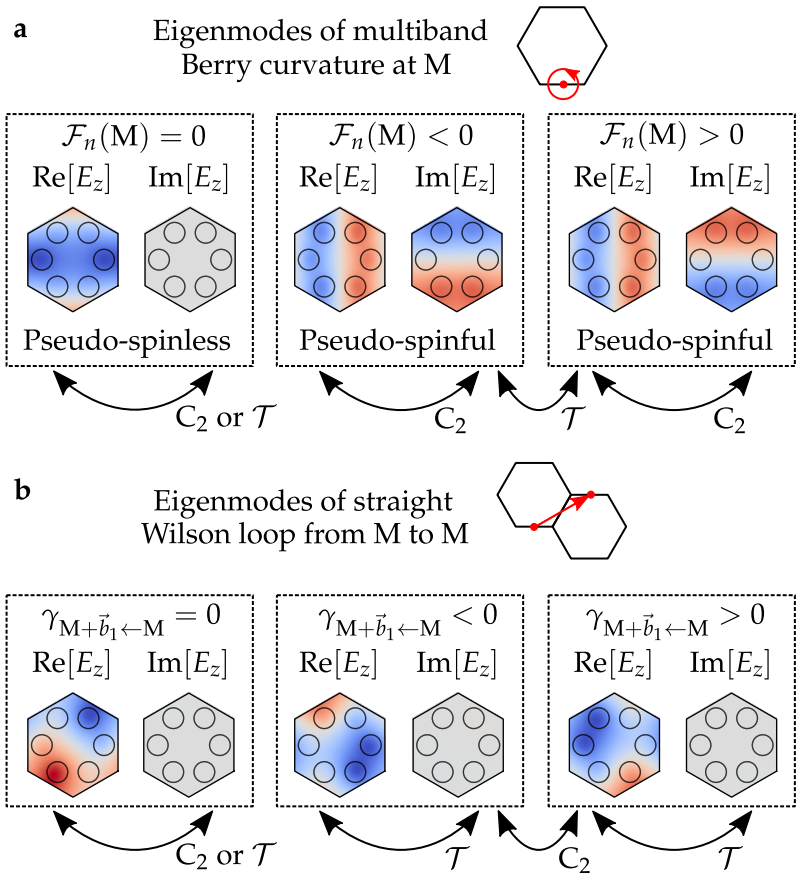

Figure 3.6: Contrasting the symmetries of circular and straight Wilson loops beginning and ending at M. (a) The eigenmodes of a circular Wilson loop enclosing M commute with C_2 symmetry and anti-commute with time-reversal symmetry. The multiband Berry curvature eigenmodes with opposite Berry curvature are therefore exchanged by time-reversal symmetry and can be considered pseudo-spinful in combination with the pseudo-fermionic time-reversal symmetry proposed by Wu & Hu [1]. (b) On the other hand, the straight Wilson loops anti-commute with C_2 symmetry and commute with time-reversal symmetry. The eigenmodes are not generally symmetric and are not exchanged by time-reversal symmetry, and are therefore not a good basis for pseudo-spin.

may be simultaneously diagonalised with the C_2, C_3, and C_6 rotation operators at M, K, and Γ, respectively,

$$C_2\,\hat{H}_{\mathcal{F}}(\mathrm{M})\,C_2^{-1} = \hat{H}_{\mathcal{F}}(\mathrm{M}), \tag{3.21}$$

$$C_3\,\hat{H}_{\mathcal{F}}(\mathrm{K})\,C_3^{-1} = \hat{H}_{\mathcal{F}}(\mathrm{K}), \tag{3.22}$$

$$C_6\,\hat{H}_{\mathcal{F}}(\Gamma)\,C_6^{-1} = \hat{H}_{\mathcal{F}}(\Gamma). \tag{3.23}$$

For example, we see in Figure 3.6a that the Berry bands of the expanded-ring cell of Wu & Hu are all C_2 symmetric at M, and that the pseudo-spinful bands are exchanged by time-reversal symmetry (complex conjugation). The Chern number of a particular Berry band that is isolated from the others by a Berry curvature gap for all $\vec{k}$ can therefore be determined from the pinning of the Wilson loop spectrum to 0 or $\pm\pi$ by the C_2 eigenvalues at the C_2 invariant momenta, similar to the fragilely topological bands introduced by Blanco de Paz *et al* [73] but applicable even when there are energy degeneracies between the valence bands as in the case of Wu & Hu [1]. On the other hand, we see in Figure 3.6b that the eigenmodes of the straight Wilson loop $\hat{W}_{\{123\}}(\mathrm{M})$ (which correspond to the eigenvalues at M in Figure 3.3b) will generally be a poor basis of pseudo-spin because the eigenmodes are not C_2 symmetric and are instead invariant under time-reversal symmetry.

The Wilson loop winding of the Berry bands can be considered as a special form of nested Wilson loop [100–102]. Although the Wilson loop winding of an individual Berry band is well defined only if the Berry band is isolated from the others by a Berry curvature gap for all $\vec{k}$, we will show that there is a $C_2\mathcal{T}$-protected $\mathbb{Z}_2$ topological index that survives even if crossings are induced between the Berry bands.

3.3.1 *Defining the $C_2\mathcal{T}$-protected $\mathbb{Z}_2$ topological index*

3.3.1.1 *Decomposing the valence band space*

Consider an odd number of Berry bands with unknown or arbitrary crossings, as shown in Figure 3.7a.[7] While the individual Chern numbers of each Berry band may not be well defined because of the possible crossings between the Berry bands, we can identify a $C_2\mathcal{T}$-protected $\mathbb{Z}_2$ topological index by considering hypothetical $C_2\mathcal{T}$-symmetric deformations of the system where the valence-conduction band gap is kept open, such that the system remains in the same $C_2\mathcal{T}$-protected topological phase.

Figures 3.7b-c show the Berry bands from Figure 3.7a after two of these hypothetical deformations for which each of the final Berry bands is isolated from the others by a Berry curvature gap for all $\vec{k}$.

7 The following discussion may also apply to $C_2\mathcal{T}$-symmetric photonic crystals with even bands, but we will address a possible complication in the concluding remarks of this chapter.

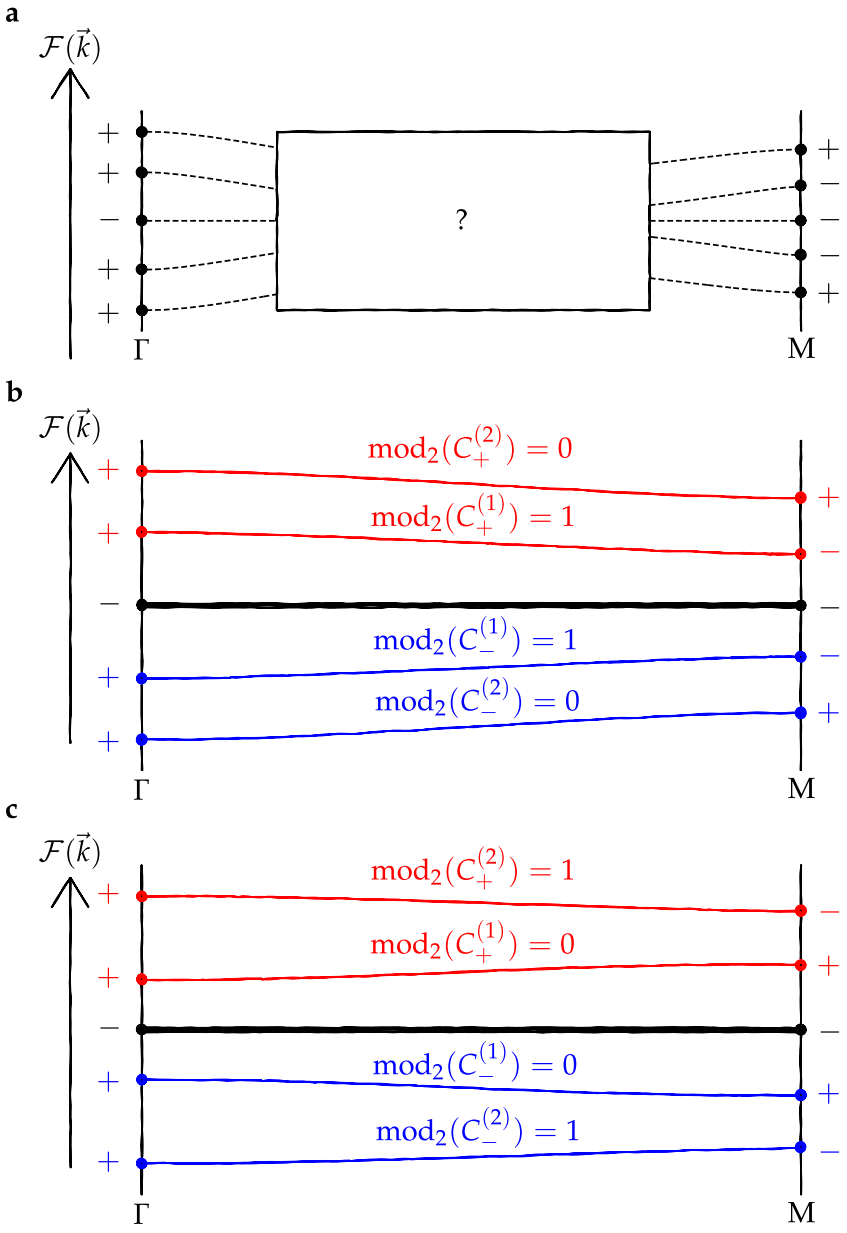

Figure 3.7: (a) In general, there may be arbitrary crossings between the Berry bands. The individual Chern numbers of the Berry bands are not stable because perturbing the crystal may close or reopen the gaps between Berry bands, even if we perturb in a $C_2\mathcal{T}$-symmetric manner without closing the valence-conduction band gap. (b-c) Hypothetical deformations where we perturb the crystal in a $C_2\mathcal{T}$-symmetric way without closing the valence-conduction band gap until each Berry band is isolated from the others by a gap of Berry curvature. Despite the Berry bands of (b) and (c) having different orderings of the C_2 eigenvalues (denoted by the $+$ and $-$ signs) at Γ (left-hand side) and M (right-hand side), the parity of the total Chern numbers of the pseudo-spin up (red) and pseudo-spin down (blue) subspaces, $C_+ = \sum C_+^{(n)}$ and $C_- = \sum C_-^{(n)}$, is unchanged between (b) and (c). We show in the main text that $\nu = \mathrm{mod}_2(C_+) = \mathrm{mod}_2(C_-)$ is a $C_2\mathcal{T}$-protected topological index.

In each system, we can identify the Berry band pinned to zero Berry curvature (black line) as the pseudo-spinless Berry band, $\mathcal{T}\left|\tilde{u}_\varnothing(\vec{k})\right\rangle = \left|\tilde{u}_\varnothing(-\vec{k})\right\rangle$, and the Berry bands above and below this as belonging to the pseudo-spin up (red lines) and down (blue lines) subspaces, respectively, $\mathcal{T}\left|\tilde{u}^{(n)}_\pm(\vec{k})\right\rangle = \left|\tilde{u}^{(n)}_\mp(-\vec{k})\right\rangle$. The Chern numbers of the isolated Berry bands in the deformed systems are well defined, and the parity of these Chern numbers can be determined from Equations (3.12) and (3.14): a pseudo-spinful band with the same C_2 eigenvalue at Γ and M must have an even Chern number, whereas a pseudo-spinful band with different C_2 eigenvalues at Γ and M must have an odd Chern number.[8] Crucially, we see that the parity of the total spin-Chern numbers, C_+ and C_-, is the same in Figure 3.7b as it is in Figure 3.7c. We shall show that the parity of these spin-Chern numbers is a $C_2\mathcal{T}$-protected topological invariant.

Inspired by the symmetries of the Berry bands, we decompose the valence band subspace into pseudo-spinful and pseudo-spinless subspaces,

$$\mathcal{H}_{\text{val}} = \mathcal{H}_\varnothing \oplus \mathcal{H}_+ \oplus \mathcal{H}_-, \tag{3.24}$$

where the projection operators to these subspaces,

$$\hat{P}_\varnothing(\vec{k}) = \left|\tilde{u}_\varnothing(\vec{k})\right\rangle\left\langle\tilde{u}_\varnothing(\vec{k})\right|, \tag{3.25a}$$

$$\hat{P}_\pm(\vec{k}) = \sum_n \left|\tilde{u}^{(n)}_\pm(\vec{k})\right\rangle\left\langle\tilde{u}^{(n)}_\pm(\vec{k})\right|, \tag{3.25b}$$

are smooth and continuous functions of $\vec{k}$ where

$$C_2\,\hat{P}_\varnothing(+\vec{k})\,C_2^{-1} = \hat{P}_\varnothing(-\vec{k}), \tag{3.26a}$$

$$\mathcal{T}\,\hat{P}_\varnothing(+\vec{k})\,\mathcal{T}^{-1} = \hat{P}_\varnothing(-\vec{k}), \tag{3.26b}$$

and

$$C_2\,\hat{P}_\pm(+\vec{k})\,C_2^{-1} = \hat{P}_\pm(-\vec{k}), \tag{3.27a}$$

$$\mathcal{T}\,\hat{P}_\pm(+\vec{k})\,\mathcal{T}^{-1} = \hat{P}_\mp(-\vec{k}), \tag{3.27b}$$

for all $\vec{k}$.

For the time-reversal invariant pseudo-spinless band, $\mathcal{T}\left|\tilde{u}_\varnothing(\vec{k})\right\rangle = \left|\tilde{u}_\varnothing(-\vec{k})\right\rangle$, the Chern number is zero [33], $C_\varnothing = 0$, as discussed in Section 2.5.3.3. On the other hand, the pseudo-spin up/down subspaces have equal and opposite Chern numbers, $C_+ + C_- = 0$, where C_+ and C_- are the total Chern numbers of the pseudo-spin up and pseudo-spin down subspaces, respectively. In analogy with the QSHE, we propose a new $C_2\mathcal{T}$-protected $\mathbb{Z}_2$ topological index for crystals with an odd number of valence bands [43],

$$\boxed{\nu = \text{mod}_2\, C_+ = \text{mod}_2\, C_-.} \tag{3.28}$$

8 Here we are assuming C_6 symmetry about the origin of the unit cell; later when we discuss crystals with only C_2 symmetry about the origin we must also consider the C_2 eigenvalues at M′ and M″.

We shall demonstrate that this index can be expressed solely in terms of the C_2 eigenvalues of the valence bands at the C_2-invariant momenta, and is therefore robust against continuous $C_2\mathcal{T}$-symmetric deformations that do not close the gap between the valence and conduction energy bands.

3.3.1.2 *Defining ν from the C_2 eigenvalues of the valence bands*

Let $n_{\text{val}}^{\text{even}}(\Pi)$ and $n_{\text{val}}^{\text{odd}}(\Pi)$ be the number of valence bands that are C_2-even and C_2-odd, respectively, at the C_2-invariant momenta, i.e. $\Pi \in \{\Gamma, M, M', M''\}$ for a C_2 symmetric unit cell on a triangular lattice. If we continue to assume there are an odd number of valence bands, $n_{\text{val}} = n_{\text{val}}^{\text{even}}(\Pi) + n_{\text{val}}^{\text{odd}}(\Pi)$, then either $n_{\text{val}}^{\text{even}}(\Pi)$ or $n_{\text{val}}^{\text{odd}}(\Pi)$ must be an odd integer. We have the same number of Berry bands as we do valence bands, and we know that the pseudo-spinful Berry bands come in time-reversed pairs with equal C_2 eigenvalues. An odd $n_{\text{val}}^{\text{even}}(\Pi)$ or $n_{\text{val}}^{\text{odd}}(\Pi)$ therefore indicates the symmetry of the unpaired pseudo-spinless band,

$$n_{\emptyset}^{\text{e/o}}(\Pi) = \text{mod}_2\left(n_{\text{val}}^{\text{e/o}}(\Pi)\right), \tag{3.29}$$

where "e/o" stands for either "even" or "odd". The number of pseudo-spinful bands that are even or odd under C_2 symmetry is therefore

$$\begin{aligned} n_{+}^{\text{e/o}}(\Pi) + n_{-}^{\text{e/o}}(\Pi) &= n_{\text{val}}^{\text{e/o}} - n_{\emptyset}^{\text{e/o}}(\Pi), \\ &= n_{\text{val}}^{\text{e/o}} - \text{mod}_2\left(n_{\text{val}}^{\text{e/o}}(\Pi)\right). \end{aligned} \tag{3.30}$$

For example, in Figure 3.7 the pseudo-spinless band is odd at Γ,

$$n_{\emptyset}^{\text{even}}(\Gamma) = \text{mod}_2\left(n_{\text{val}}^{\text{even}}(\Gamma)\right) = \text{mod}_2\left(4\right) = 0, \tag{3.31}$$

$$n_{\emptyset}^{\text{odd}}(\Gamma) = \text{mod}_2\left(n_{\text{val}}^{\text{odd}}(\Gamma)\right) = \text{mod}_2\left(1\right) = 1, \tag{3.32}$$

and also at M,

$$n_{\emptyset}^{\text{even}}(M) = \text{mod}_2\left(n_{\text{val}}^{\text{even}}(M)\right) = \text{mod}_2\left(2\right) = 0, \tag{3.33}$$

$$n_{\emptyset}^{\text{odd}}(M) = \text{mod}_2\left(n_{\text{val}}^{\text{odd}}(M)\right) = \text{mod}_2\left(3\right) = 1. \tag{3.34}$$

Each pseudo-spinful Berry band has the same C_2 eigenvalues as its time-reversed partner. We can therefore deduce the number of C_2-even or C_2-odd pseudo-spin up/down Berry bands as

$$\boxed{n_{+}^{\text{e/o}}(\Pi) = n_{-}^{\text{e/o}}(\Pi) = \frac{1}{2}\left(n_{\text{val}}^{\text{e/o}}(\Pi) - \text{mod}_2(n_{\text{val}}^{\text{e/o}}(\Pi))\right).} \tag{3.35}$$

If we were to hypothetically deform our system until each Berry band was isolated from the others by a Berry curvature gap for all $\vec{k}$ without breaking $C_2\mathcal{T}$ symmetry or closing the valence-conduction energy band gap then the net number of pseudo-spin up/down Berry

bands with different C_2 eigenvalues at Γ and M would be $n_\pm^{e/o}(\Gamma) - n_\pm^{e/o}(M)$. From Equations (3.12) and (3.14), we know that each band with different C_2 eigenvalues at Γ and M must carry an *odd* Chern number, and the parity of the total Chern number of the pseudo-spin up/down subspaces is therefore

$$\boxed{\nu = \mathrm{mod}_2\left(n_\pm^{e/o}(\Gamma) - n_\pm^{e/o}(M)\right).} \tag{3.36}$$

We need only consider either the C_2-even or the C_2-odd modes, for example, in Figure 3.7 we have $n_\pm^{even}(\Gamma) - n_\pm^{even}(M) = 2 - 1 = 1$ and therefore $\nu = \mathrm{mod}_2(1) = 1$, which is consistent with $n_\pm^{odd}(\Gamma) - n_\pm^{odd}(M) = 0 - 1 = -1$ and therefore $\nu = \mathrm{mod}_2(-1) = 1$.[9]

For crystals that are C_2 symmetric but not necessarily C_6 symmetric about the origin, the Chern number is odd if the Wilson loop from $\Gamma \to \Gamma + \vec{b}_2$ is pinned to 0 and the Wilson loop from $M \to M + \vec{b}_2$ is pinned to $\pm\pi$, or vice versa, and Equation (3.36) generalises to

$$\boxed{\nu = \mathrm{mod}_2\left(n_\pm^{e/o}(\Gamma) - n_\pm^{e/o}(M) + n_\pm^{e/o}(M') - n_\pm^{e/o}(M'')\right).} \tag{3.37}$$

3.4 MEANING OF THE $\mathbb{Z}_2$ TOPOLOGICAL INDEX

We have introduced a $C_2\mathcal{T}$-protected $\mathbb{Z}_2$ topological index associated with the winding of the Berry bands that is stable against $C_2\mathcal{T}$-preserving deformations that do not close the valence-conduction gap of the energy bands. We now return to the concrete examples of Wu & Hu [1] and Blanco de Paz *et al* [73] to demonstrate that our $\mathbb{Z}_2$ topological index is compatible with, but distinct from, other classifications that are determined from the centers of localised Wannier functions, such as obstructed atomic limits [42, 97]. We demonstrate that helical edge states can be predicted with our topological index, and conclude that these crystals are indeed photonic analogues to the QSHE in the bulk with a weak pseudo-time-reversal breaking at the interfaces, as originally suggested by Wu & Hu [1].

3.4.1 *Origin independence*

Let us now consider how our choice of origin can affect the topological classification. Figure 3.8 shows four unit cells: the shrunken-ring and expanded-ring unit cells of Wu & Hu [1], as well as a shifted copy of each. The shift of origin can change the C_2 eigenvalues at the C_2 invariant momenta other than Γ [33]. Table 3.1 shows the number of C_2-even pseudo-spin up modes at Γ, M, M′, and M″ from which we determine the topological index ν using Equation (3.37). We see that each shifted cell has the same index ν as its unshifted counterpart. On

9 Note that we take the convention that $\mathrm{mod}_2(-n) = \mathrm{mod}_2(+n)$.

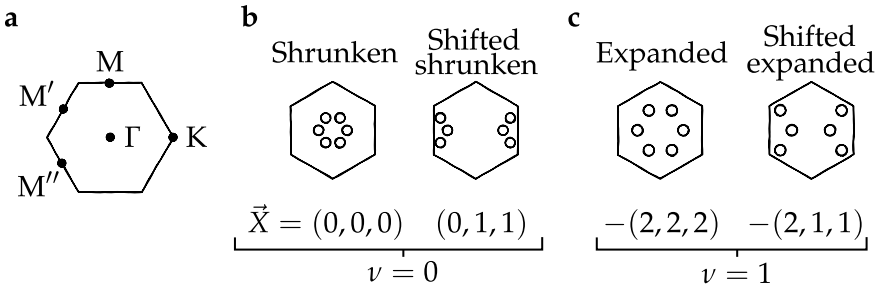

Figure 3.8: (a) Positions of M, M′, and M″ for the BZ of a triangular lattice with C_2 symmetry. (b-c) Schematics of shrunken-ring and expanded-ring unit cells of Wu & Hu [1] and their shifted counterparts. Although it is impossible to continuously deform between any of these unit cells without either closing the topological band gap or breaking $C_2\mathcal{T}$ symmetry *about the origin of the unit cell*, as indicated by the $\vec{X}$ topological index introduced by Benalcazar *et al* [97], some of the cells have equal pseudo-spin topological index, ν. (b) The shrunken-ring cell of Wu & Hu [1] and its shifted counterpart are both trivial, $\nu = 0$. (c) The expanded-ring cell of Wu & Hu [1] and its shifted counterpart are both topological, $\nu = 1$.

Geometry	n_+^{even} at...				ν
	Γ	M	M′	M″	
Shrunken	0	0	0	0	$0-0+0-0=0$
Shifted shrunken	0	0	1	1	$0-0+1-1=0$
Expanded	1	0	0	0	$1-0+0-0=1$
Shifted expanded	1	0	1	1	$1-0+1-1=1$

Table 3.1: Applying Equation 3.37 to determine our topological index ν from the number of C_2-even eigenmodes at Γ, M, M′, and M″, for the shrunken-ring and expanded-ring unit cells of Wu & Hu [1] and their shifted counterparts shown in Figure 3.8.

the other hand, the method of Benalcazar *et al* [97] (where $\vec{X} \neq (0,0,0)$ indicates a fragilely topological or obstructed atomic limit phase as discussed in Section 3.2.2) classifies all four unit cells of Figure 3.8 as different topological phases (see Appendix C for the determination of $\vec{X}$ from the C_2 eigenvalues).

The apparent contradiction of the two methods arises because the classification as an obstructed atomic limit is based on the absolute positions of localised Wannier centers within the cell, whereas our $\mathbb{Z}_2$ topological index is constructed from the relative flow of the Wannier centers in the gauge of the Berry bands and is independent of our choice of origin. It is impossible to deform between two bulks with different values of our index ν without breaking $C_2\mathcal{T}$ symmetry or closing the valence-conduction band gap, even if the origin of the $C_2\mathcal{T}$ symmetry is not fixed. On the other hand, it is impossible to deform between two bulks with different values of $\vec{X}$ without breaking $C_2\mathcal{T}$ symmetry *about the origin of the unit cell* or closing the valence-conduction band gap. We shall demonstrate that our origin-independent $\mathbb{Z}_2$ topological index is more relevant to predicting the existence of helical edge states.

3.4.2 *Helical edge states at adiabatically graded interfaces*

Our $\mathbb{Z}_2$ topological index allows us to predict the existence of edge states at *adiabatically graded* (locally C_2 symmetric) interfaces between photonic crystals. Let us consider graded interfaces between unshifted and shifted cells with the same values of ν, as in Figure 3.8b. Despite the bulks having different values of $\vec{X}$, there exists a choice of slowly graded interface between the two bulks for which the band gap does not close. At this interface region, which consists of $N \pm 1/2$ unit cells (but could be adiabatically squashed or stretched to fill the space of, for example, N or $N+1$ unit cells), there are no helical edge states.

On the other hand, if we consider an interface between the photonic crystals with different values of ν, as in Figure 3.8c, we cannot find a slowly graded interface that is locally C_2 symmetric for which helical edge states do not emerge, regardless of whether the unit cells are shifted or not. These edge states will survive as the interface region is made increasingly sharp, provided that the interface remains a relatively weak C_6-breaking perturbation.

3.4.3 *Relation to fragilely topological bands*

Let us now compare the fragilely topological unit cell of Blanco de Paz *et al* [73] with the expanded-ring unit cell of Wu & Hu [1], pictured in

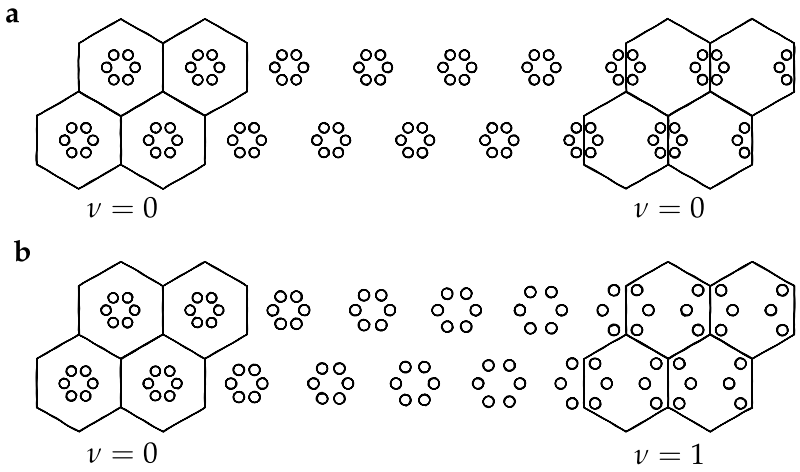

Figure 3.9: Schematics of adiabatically graded (locally $C_2\mathcal{T}$-symmetric) interface regions between shifted and unshifted unit cells. (a) It is possible to find an adiabatically graded interface between trivial ($\nu = 0$) shifted and unshifted cells for which the topological band gap does not close. There are no helical edge states at this interface. (b) On the other hand, the topological band gap closes at all adiabatically graded interfaces between cells with different values of ν, such as the one depicted here, resulting in helical edge states. The edge states of the adiabatically graded interface will survive as the interface is made increasingly sharp so long as the interface remains a relatively weak C_6 breaking perturbation.

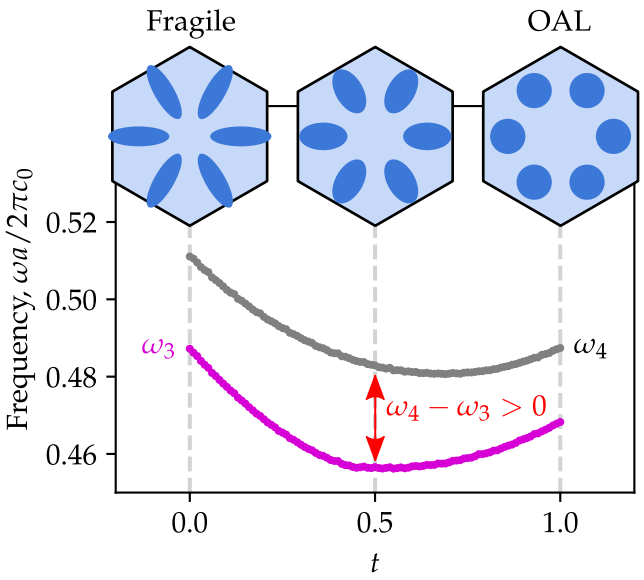

Figure 3.10: It is possible to continuously deform between the fragilely topological crystal introduced by Blanco de Paz *et al* [73] ($a_0/R = 3$, $d_1 = 0.4a_0$, $d_2 = 0.13a_0$) and the expanded-ring unit cell of Wu & Hu [1] ($a_0/R = 2.9$, $d_1 = d_2 = 2R/3$) without breaking $C_2\mathcal{T}$ symmetry or closing the topological band gap, $\omega_4 - \omega_3 > 0$. We therefore say that the two crystals belong to the same $C_2\mathcal{T}$-protected topological phase.

the left and right insets of Figure 3.10, respectively. For both crystals, we have $n_{\text{val}}^{\text{even}}(\Gamma) = 3$ and $n_{\text{val}}^{\text{even}}(\text{M}) = 1$, such that

$$n_{+}^{\text{even}}(\Gamma) = \frac{1}{2}\left(3 - \text{mod}_2(3)\right) = 1, \tag{3.38}$$

$$n_{+}^{\text{even}}(\text{M}) = \frac{1}{2}\left(1 - \text{mod}_2(1)\right) = 0, \tag{3.39}$$

and therefore

$$\nu_{\text{expanded}} = \nu_{\text{fragile}} = \text{mod}_2\left(n_{+}^{\text{even}}(\Gamma) - n_{+}^{\text{even}}(\text{M})\right) = 1, \tag{3.40}$$

indicating that both crystals belong to the same non-trivial $C_2\mathcal{T}$-protected topological phase and in agreement with the non-trivial Berry band winding observed for both crystals in Appendix A. This is also supported by the main panel of Figure 3.10 where we show that it is possible to deform between the fragilely topological crystal introduced by Blanco de Paz *et al* [73] and the expanded-ring unit cell of Wu & Hu [1] in a $C_2\mathcal{T}$-symmetric manner without closing the band gap between the third and fourth energy bands. See the supplementary material of [92] for the full band diagrams of the crystal at different stages of the deformation.

The relation between pseudo-spin and the fragile topology observed by Blanco de Paz *et al* [73] can be understood by colouring the valence

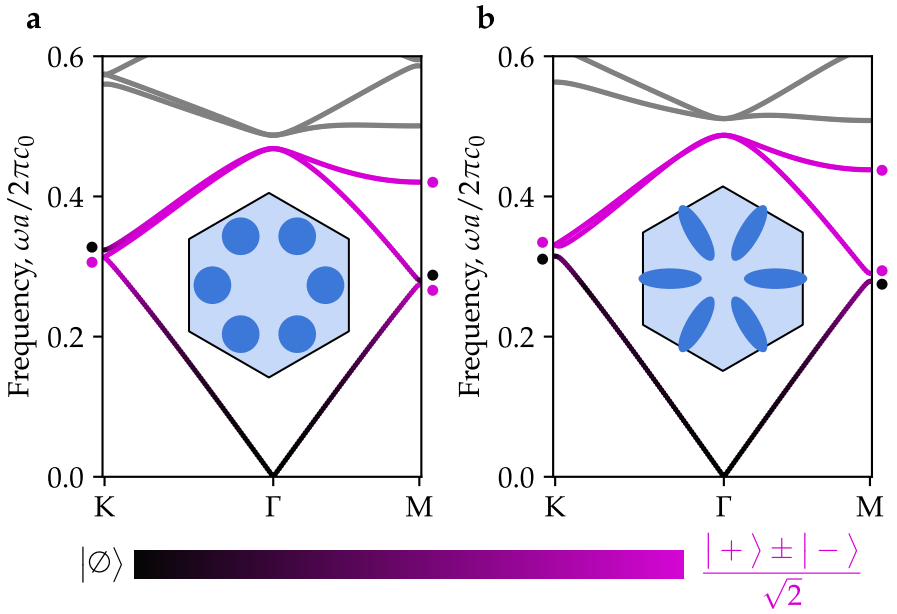

Figure 3.11: TM polarised bands of the (a) expanded-ring cell of Wu & Hu [1] ($a_0/R = 2.9$, $d_1 = d_2 = 2R/3$) and (b) the fragilely topological crystal of Blanco de Paz *et al* [73] ($a_0/R = 3$, $d_1 = 0.4a_0$, $d_2 = 0.13a_0$). By colouring the bands according to their pseudo-spin composition, we see that the fragilely topology bands are purely pseudo-spinful at the high symmetry points. Considering the topology of the pseudo-spinful subspaces allows us to determine the non-trivial topology, $\nu = 1$, of both crystals.

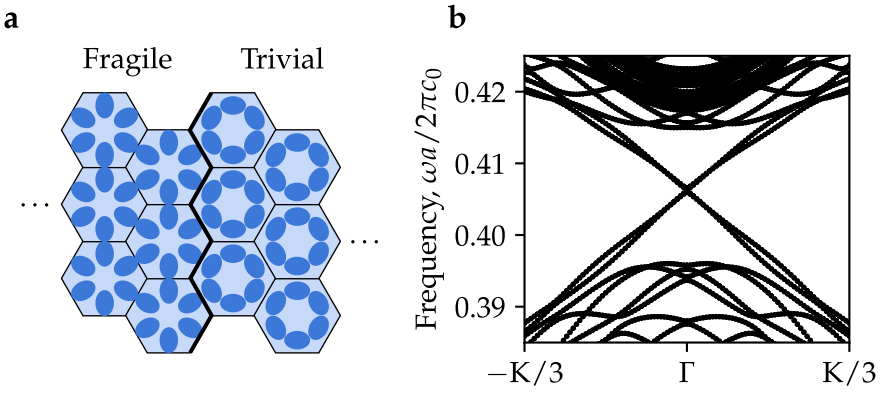

Figure 3.12: Observation of helical edge states at an interface between a fragilely topological ($a_0/R = 3$, $d_1 = 0.35a_0$,$d_2 = 0.25a_0$, $\nu = 1$) and a trivial ($a_0/R = 3$, $d_1 = 0.25a_0$, $d_2 = 0.35a_0$, $\nu = 0$) crystal. The parameters were chosen so the two crystals had an overlapping band gap at $\omega a_0/2\pi c \approx 0.4$. The emergence of these edge states agrees with the change of the topological index ν at the interface.

bands of the crystals by their pseudo-spin composition. We see that the pseudo-spinful and pseudo-spinless states are mixed between the three valence bands of the expanded-ring cell of Wu & Hu, as shown in Figure 3.11a. On the other hand, the fragilely topological bands of Blanco de Paz *et al* consist of pure pseudo-spinful states at the high symmetry points, as shown in Figure 3.11b.[10] In other words, the fragilely topological bands are observed when an energy gap happens to isolate the pseudo-spinless mode from the pseudo-spinful modes.

We also found that that helical edge states occur at the interface between the trivial and fragilely topological crystals, as shown in Figure 3.12. Here, as in other works [1, 75, 103], there is a small energy gap in the edge modes (around 3% of the bulk valence-conduction gap) as the presence of the interface is a C_6-breaking perturbation that lifts the pseudo-Kramers degeneracy. This could be reduced by considering a graded interface [75]. However, the quality of the edge states supports the idea that the fragilely topological and obstructed atomic limit crystals belong to the same $C_2\mathcal{T}$ topological phase (when considering the band gap between bands 3 and 4 as the topological gap of interest).

3.5 REMARKS ON CHAPTER 3

In this chapter we introduced a $C_2\mathcal{T}$-protected $\mathbb{Z}_2$ topological index to identify photonic analogues of the QSHE where the spin degree

10 Away from the high symmetry points there is some mixing of the pseudo-spinful/spinless subspaces, but this does not change the pinning of the Wilson loop spectrum by the C_2 eigenvalues of the Berry bands at Γ and M.

of freedom is mimicked by the angular momentum of the light. We believe the index we introduced is the first that demonstrates the non-trivial QSHE-like nature of the photonic crystal introduced by Wu & Hu [1] and its many relatives [72–75] while also accounting for all of the valence bands determined from full-wave calculations.

We presented two methods to calculate the topological index. First, we considered the multiband Berry curvature of the valence bands, which we called the Berry bands. We noted that $C_2\mathcal{T}$ symmetric crystals with an odd number of valence bands have exactly one 'pseudo-spinless' Berry band that is pinned to zero Berry curvature for all $\vec{k}$ and is invariant under time-reversal symmetry, $\mathcal{T}\left|\tilde{u}_\varnothing(\vec{k})\right\rangle = \left|\tilde{u}_\varnothing(-\vec{k})\right\rangle$. The remaining Berry bands are 'pseudo-spinful', where the pseudo-spin up and pseudo-spin down Berry bands have opposite Berry curvature and are exchanged under time-reversal symmetry, $\mathcal{T}\left|\tilde{u}_\pm^{(n)}(\vec{k})\right\rangle = \left|\tilde{u}_\mp^{(n)}(-\vec{k})\right\rangle$. For the shrunken-ring and expanded-ring cells of Wu & Hu [1] we found that the Berry bands were isolated from each other by a Berry curvature gap for all $\vec{k}$, and we were able to calculate Chern numbers of the individual Berry bands. The pseudo-spin Chern numbers agreed with the expected topologies of the crystals. We then expressed this topological index as a simple function of the C_2 eigenvalues of the valence bands at the C_2-invariant momenta. This is more efficient than calculating the Chern numbers of the Berry bands as it is only necessary to solve for the eigenmodes at the high symmetry points, rather than across the whole BZ, and it is also more general as it can be used regardless of any possible crossings between the Berry bands.

We also discussed how our topological index is distinct from, but compatible with, the classification of the non-trivial crystals as obstructed atomic limits. Our topological index is based on the *relative* flow of Wannier centers and is therefore independent of the origin, whereas classifications such as obstructed atomic limits are based on the *absolute* position of the Wannier centers and are dependent on the position of the origin. We demonstrated by observation that the origin independence of our topological index allows us to predict the emergence of helical edge states at adiabatically graded interface regions. These edge states will survive as the interface region is made increasingly sharp, provided that the interface remains a relatively weak C_6-breaking perturbation such that the pseudo-fermionic time-reversal symmetry is only weakly broken at the interface [1, 75].

Finally, we would like to remark on a possible complication when applying our method to $C_2\mathcal{T}$ symmetric crystals with an *even* number of valence bands. We showed that for an odd number of valence bands there will be exactly one pseudo-spinless Berry band for all $\vec{k}$. This is not always true for an even number of valence bands. For example, Figure 3.13 shows a hypothetical pair of Berry bands where the C_2 eigenvalues are different at Γ and the same at M. Attempting to

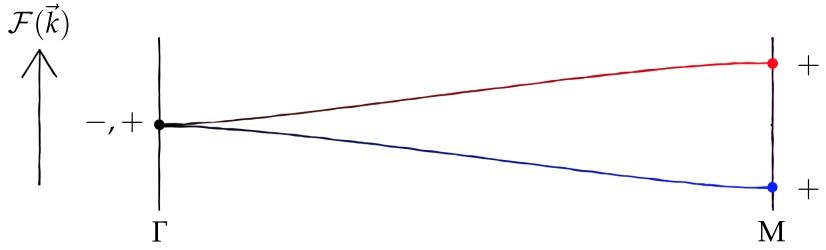

Figure 3.13: Possible breakdown of the pseudo-spinful/pseudo-spinless decomposition for an even number of valence bands. The hypothetical pair of Berry bands have different C_2 eigenvalues at Γ, and the same C_2 eigenvalues at M. The Berry bands appear pseudo-spinless at Γ. This is because the bands cannot be exchanged under $\mathcal{T}$ symmetry at Γ due to their differing C_2 eigenvalues. The bands are therefore invariant under $\mathcal{T}$ symmetry; recalling that $\mathcal{T}$ symmetry flips the sign of the Berry curvature we see that these Berry bands must be pinned to zero Berry curvature at Γ. On the other hand, the Berry bands appear pseudo-spinful at M because they have the same C_2 eigenvalues and are exchanged by $\mathcal{T}$ symmetry. The even number of bands cannot be consistently decomposed into pseudo-spinless or pseudo-spinful for all $\vec{k}$.

classify these bands as pseudo-spinful/pseudo-spinless as defined in Section 3.3.1 leads to a contradiction: at Γ they appear pseudo-spinless but at M they appear pseudo-spinful. Whether the $C_2\mathcal{T}$-protected topological index can be generalised to even-dimensional valence band spaces remains an open question. One way of proceeding may be to consider the Berry bands as a particle-hole symmetric system, because the bosonic time-reversal symmetry acts as $\mathcal{T}\hat{H}_{\mathcal{F}}(\vec{k})\mathcal{T}^{-1} = -\hat{H}_{\mathcal{F}}(-\vec{k})$ where $\mathcal{T}$ is anti-unitary. The topology of particle-hole symmetric systems is well studied [36, 38, 39], and it may be possible to relate the topological index introduced in this chapter to an established topological index of particle-hole symmetric systems such as the trace, determinant, or Pfaffian of the projection of $C_2\mathcal{T}$ onto the valence bands.

4

CHIRAL SYMMETRY IN PHOTONIC VOID-CHANNEL NETWORKS

4.1 OVERVIEW

In this chapter, we study the band topology of TE-polarised light that propagates in the voids and narrow connecting channels located between perfect conductors, as shown in Figure 4.1a. For low frequencies and narrow channels, the photonic system behaves like a *discrete* classical network of inductors and capacitors (or equivalently as a classical network of masses and springs, as shown in Figure 4.1b) in an asymptotically exact manner [2, 104]. In photonics, chiral symmetry is often broken by long range interactions [51, 54], as we discussed in Section 2.5.1.2. However, the void-channel networks have vanishing long range interactions as the channels are made increasingly narrow, thus certain configurations of the void-channel networks have a chiral (sublattice) symmetric limit (up to a shift of constant frequency).

In tight-binding models, terminating the lattice freely does not change the onsite potential and therefore preserves chiral symmetry. In mass-spring and void-channel models, the free boundary condition generally breaks chiral symmetry [105, 106]. We propose that the chiral symmetry can be restored at the interfaces by "capping" the mass-spring/void-channel networks with heavy masses/large voids, respectively. We use the familiar SSH model [33] to demonstrate the principle, and demonstrate that void-channel SSH geometry features chiral symmetry protected edge states.

The void-channel geometries are also a promising platform to realise *square-root topological systems* where the squared Hamiltonian is block-diagonal and at least one of the blocks corresponds to a known non-trivial topological system [58]. For example, Maimaiti *et al* [105] showed that the nearest-neighbour tight-binding model of the honeycomb-kagome lattice is a *square-root semimetal* that inherits the topology from the honeycomb sector of the squared Hamiltonian. The authors also proposed an analagous mass-spring model using a gravitational potential energy term to adjust the onsite terms of the equations of motion [105]. However, it is not apparent to us if an analogue of this gravitational term exists for the void-channel geometries. Instead, we produced a photonic analogue of the square-root semimetal by capping our void-channel network with large voids, thereby ensuring that the chiral symmetry of the squared Hamiltonian was preserved at the interfaces. We study the interfaces in a ribbon

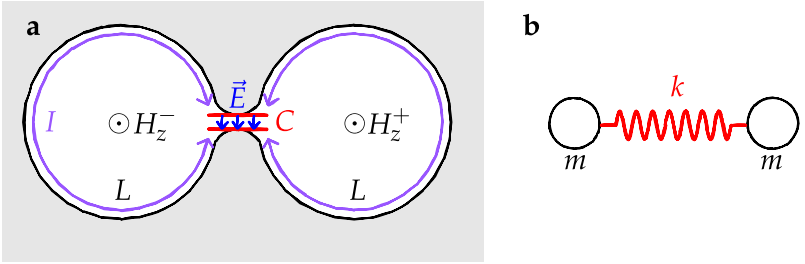

Figure 4.1: (a) Two voids of vacuum (white) and a narrow connecting channel embedded in perfect conductor (grey) will behave like a pair of inductors and a capacitor for transverse-electric polarised light at low frequencies and for narrow channels [2, 104]. The voids act as inductors with inductance L because the currents, I, circulate around the surface of the voids and induce an out-of-plane magnetic fields within the voids. We label the magnetic field within the left and right voids as H_z^- and H_z^+, respectively. The channel acts as a capacitor because the difference of magnetic field across the channel generates an electric field, $\vec{E}$, across the gap. This analogy can be extended to larger networks of voids and channels. (b) The void-channel or inductor-capacitor network is also analagous to a mass-spring network, where masses m are connected by spring constants k, and the masses oscillate in and out of the page.

and a triangular metaparticle, and observe that topologically protected edge and corner states can be excited.

4.2 METHODOLOGY

4.2.1 *Mapping between void-channel and mass-spring networks*

We apply the method of Vanel *et al* [2] to map the TE-polarised Maxwell's equations within networks of voids and narrow channels formed between closely spaced perfect conductors[1] (as in Figure 4.1a) to equivalent networks of resonators in an asymptotically exact manner. The voids behave as inductors and the channels behave as capacitors where a difference in the out-of-plane magnetic field across a channel, $H_z^+ - H_z^-$, results in an electric field, $\vec{E}$, perpendicular to the channel [2, 104]. Equivalently, we may consider a mass-spring network where the voids are mapped to masses and the channels are mapped to springs, as shown in Figure 4.1b.

1 The method applies to any wave field p obeying the wave equation $\partial^2 p/\partial^2 t - c^2\nabla^2 p = 0$ and satisfying the Neumann boundary condition at the inclusions, $\vec{n} \cdot \vec{\nabla} p = 0$ where $\vec{n}$ is the normal of the inclusion [104]. In our case we take p to be the out-of-plane magnetic field component, H_z, but the discussions here also apply to the propagation of acoustic pressure waves through voids and channels between rigid inclusions.

By performing matched asymptotic expansions, Vanel *et al* [2] demonstrated that the precise values of the masses and spring constants corresponding to a particular network of voids and channels can be determined in a remarkably simple manner at low frequencies and in the limit of narrow channels. They demonstrate, for example, that in periodic systems with period a and channels of half-width h, $h/a \to 0$, where h is the half-width of the channel and a is the periodicity of the lattice. The masses are proportional to the area of the voids,

$$\boxed{m_i = A_i \cdot m_0/a^2,} \tag{4.1}$$

and the spring constants are a function of the half-width of the channel, h, and the radius of curvature of the two sides of the channel, R_1 and R_2,

$$\boxed{k = \frac{1}{\pi}\sqrt{\frac{h}{R_1} + \frac{h}{R_2}}.} \tag{4.2}$$

Equations (4.1) and (4.2) allow us to accurately model the void-channel network governed by the continuous wave equation using the much simpler equations of motion of discrete masses and springs without any fine tuning or fitting of the parameters. The reverse mapping allows us to propose new photonic void-channel models where the coupling of the field between different voids is highly controllable. This offers great control over the symmetries of the Hamiltonian and suggests the void-channel networks could be a powerful platform for realising symmetry-protected photonic topological phases.

4.2.2 *Preserving chiral symmetry in mass-spring networks*

As a first step to constructing photonic void-channel networks with a chiral symmetric limit, let us consider the equations of motion of an SSH-like mass-spring network consisting of equal masses, m, and alternating spring constants, k_1 and k_2, as shown in the inset of Figure 4.2,

$$\begin{bmatrix} \frac{k_1}{m} + \frac{k_2}{m} & -\frac{k_1}{m} - \frac{k_2}{m}e^{-ika} \\ -\frac{k_1}{m} - \frac{k_2}{m}e^{+ika} & \frac{k_1}{m} + \frac{k_2}{m} \end{bmatrix} \begin{bmatrix} u_1(k) \\ u_2(k) \end{bmatrix} = \omega^2(k) \begin{bmatrix} u_1(k) \\ u_2(k) \end{bmatrix}. \tag{4.3}$$

We see in Figure 4.2 that the squared frequency spectrum of this chain resembles the energy spectrum of the electronic SSH tight-binding Equation (1.17). Unlike the tight-binding model, however, the diagonal of Equation (4.3) is non-zero, but in this case the two diagonal terms are equal and correspond to a simple shift of the frequency by $\sqrt{k_1/m + k_2/m}$,

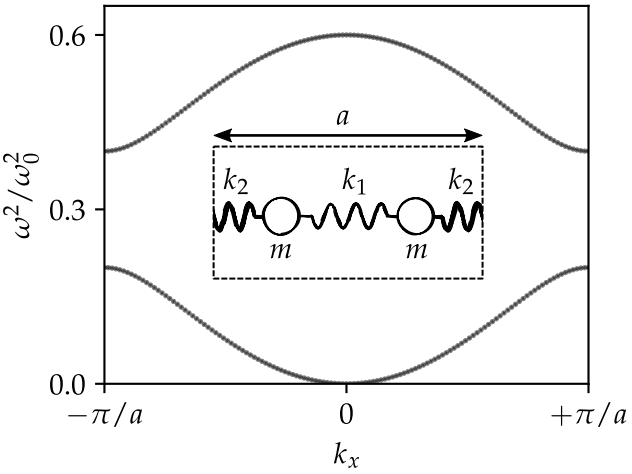

Figure 4.2: Squared frequency spectrum (normalised by $\omega_0 = \sqrt{k_0/m_0}$) of a mass-spring chain with equal masses, $m = 0.1m_0$, and alternating spring constants $k_1 = 0.01k_0$ and $k_2 = 0.02k_0$, as shown in the inset. The width of the unit cell is a. The spectrum closely resembles the energy spectrum of the electronic SSH tight-binding model, except that the squared frequency has been shifted by $(k_1 + k_2)/m = 0.3\omega_0^2$.

$$\begin{bmatrix} 0 & -\frac{k_1}{m} - \frac{k_2}{m}e^{-ika} \\ -\frac{k_1}{m} - \frac{k_2}{m}e^{+ika} & 0 \end{bmatrix} \begin{bmatrix} u_1(k) \\ u_2(k) \end{bmatrix} = \left(\omega^2(k) - \frac{k_1+k_2}{m}\right) \begin{bmatrix} u_1(k) \\ u_2(k) \end{bmatrix}, \quad (4.4)$$

such that the chiral symmetry of the bulk equations of motion is preserved. The mass-spring model differs from the original SSH tight-binding model because the forces on the masses are proportional to the *differences* of the mass displacements, whereas in tight-binding models the hopping is proportional to the wavefunction amplitudes themselves [107].

Based on the similarities between Equation (4.4) and the original tight-binding Equation (1.17), it may appear that the finite mass-spring chain with free boundary conditions shown in Figure 4.3a could exhibit SSH-like topological edge states. However, the equations of motion for this chain are

$$\begin{bmatrix} -\frac{k_1}{m} & -\frac{k_2}{m} & & & \\ -\frac{k_2}{m} & 0 & -\frac{k_1}{m} & & \\ & -\frac{k_1}{m} & 0 & -\frac{k_2}{m} & \\ & & -\frac{k_2}{m} & 0 & \ddots \\ & & & \ddots & \ddots \end{bmatrix} \begin{bmatrix} u_1 \\ u_2 \\ u_3 \\ u_4 \\ \vdots \end{bmatrix} = \left(\omega^2 - \frac{k_1+k_2}{m}\right) \begin{bmatrix} u_1 \\ u_2 \\ u_3 \\ u_4 \\ \vdots \end{bmatrix},$$

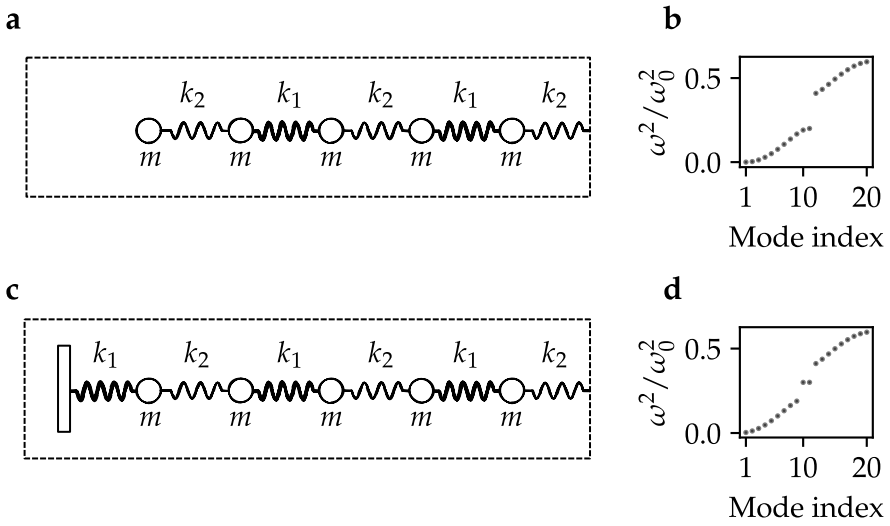

Figure 4.3: An SSH-like mass-spring chain with free and "wall" boundary conditions. The mass-spring chain consists of equal masses, m, connected by springs of alternating spring constants k_1 and k_2. (a-b) Schematic and squared frequency spectrum of an SSH-like mass-spring chain with free boundary conditions. The chain is 20 masses long and we take $k_1 = 0.01$, $k_2 = 0.02$, and $m = 0.1m_0$. Although the winding number of the bulk Hamiltonian is non-trivial, no edge states are observed because the free boundary condition breaks the chiral symmetry. (c-d) Schematic and squared frequency spectrum of the same chain but with the "wall" boundary condition, where the edges of the SSH-like mass-spring chain are attached to immovable walls with springs of spring constant k_2. The wall boundary condition restores the chiral symmetry of the chain and symmetry-protected edge states are observed in the bulk band gap.

(4.5)

where the chiral symmetry is broken by the non-zero term on the diagonal of the matrix, and therefore there are no topological edge states in the energy spectrum of Figure 4.3b. This chiral symmetry breaking term occurs because the end masses are only connected to one spring; we can restore the chiral symmetry by anchoring the chain to an immovable wall with a spring of spring constant k_2 as shown in Figure 4.3c. The equations of motion of this chain with the "wall" boundary condition are then

$$\begin{bmatrix} 0 & -\frac{k_2}{m} & & & \\ -\frac{k_2}{m} & 0 & -\frac{k_1}{m} & & \\ & -\frac{k_1}{m} & 0 & -\frac{k_2}{m} & \\ & & -\frac{k_2}{m} & 0 & \ddots \\ & & & \ddots & \ddots \end{bmatrix} \begin{bmatrix} u_1 \\ u_2 \\ u_3 \\ u_4 \\ \vdots \end{bmatrix} = \left(\omega^2 - \frac{k_1+k_2}{m}\right) \begin{bmatrix} u_1 \\ u_2 \\ u_3 \\ u_4 \\ \vdots \end{bmatrix}, \tag{4.6}$$

and we see in Figure 4.3d that the chiral symmetry is restored and SSH-like edge states emerge at the mid-gap frequency $\sqrt{k_1/m + k_2/m}$.

Although the chiral symmetry can be restored by the wall boundary condition for the mass-spring systems, we are interested in mapping topological mass-spring systems to void-channel systems where (to our knowledge) there is no mechanism to implement an exact analogue of this boundary condition. In the next sections, we discuss how we can approximate the wall boundary condition by capping the mass-spring models with heavy masses, and how we can therefore largely restore the chiral symmetry in our photonic void-channel models by capping the systems with large voids.

Consider the equations of motion of the mass-spring chain capped by large masses M as shown in Figure 4.4a,

$$\begin{bmatrix} \frac{k_2}{M} - \frac{k_1+k_2}{m} & \frac{-k_2}{M} & & & & \\ \frac{-k_2}{m} & 0 & \frac{-k_1}{m} & & & \\ & \frac{-k_1}{m} & 0 & \frac{-k_2}{m} & & \\ & & \frac{-k_2}{m} & 0 & \frac{-k_1}{m} & \\ & & & \frac{-k_1}{m} & 0 & \ddots \\ & & & & \ddots & \ddots \end{bmatrix} \begin{bmatrix} u_0 \\ u_1 \\ u_2 \\ u_3 \\ u_4 \\ \vdots \end{bmatrix} = \left(\omega^2 - \frac{k_1+k_2}{m}\right) \begin{bmatrix} u_0 \\ u_1 \\ u_2 \\ u_3 \\ u_4 \\ \vdots \end{bmatrix}, \tag{4.7}$$

where u_0 and u_{N+1} are the displacements of the heavy capping masses. If M is large but finite, then the chiral symmetry is broken at the edges of the chain. However, the effect will be weak for large M because the chiral symmetry breaking terms are inversely proportional to M.

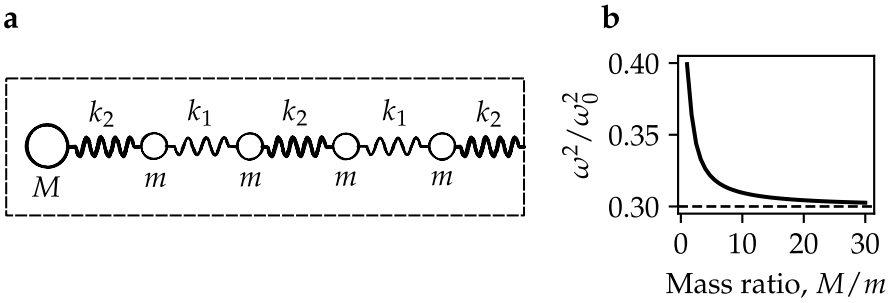

Figure 4.4: (a) The "wall" boundary condition of the SSH-like mass-spring chain introduced in Figure 4.3b can be approximated by replacing the walls with heavy masses, M. (b) The average frequency of the pair of edge states for the mass-spring chain capped with heavy masses (dots) compared with that for the mass-spring chain with the wall boundary condition (solid line), for the same values of m, k_1, and k_2 as before. Each chain contain 20 masses of mass m, and the capped chain has two capping masses of mass M on each end for a total of 22 masses. For capping masses that are an order of magnitude heavier than the masses in the rest of the chain, $M \gtrsim 10m$, the squared frequencies of the edge states of the two chains agree within about 3% error.

We can eliminate u_0 and u_{N+1} from Equation (4.7) by rearranging the first and last rows of the matrix equation for

$$u_0 = \frac{1}{1 - \frac{\omega^2 M}{k_2}} u_1, \tag{4.8}$$

$$u_{N+1} = \frac{1}{1 - \frac{\omega^2 M}{k_2}} u_N, \tag{4.9}$$

and substituting these into the second and second-to-last rows of the matrix equation, respectively. For frequencies $\omega > 0$, then $u_0, u_{N+1} \to 0$ in the limit of $M \to \infty$, and Equation (4.7) reduces to the chiral symmetric Equation (4.6) with topological edge states pinned to $\omega_{\text{edge}} = \sqrt{k_1/m + k_2/m}$, as shown in Figure 4.4b.

4.2.3 *Mapping to void-channel networks with a chiral symmetric limit*

We now propose a photonic analogue of the SSH model that consists of a one-dimensional network of voids and channels as shown in Figure 4.5a. The ends of the chain are capped by larger voids that act to restore the chiral symmetry, analagous the heavier masses in Figure 4.4. To emulate equal masses connected by alternating spring constants we require equally sized voids connected by relatively thin channels of alternating widths. A simple choice for the shape of the upper and lower walls of the geometry is

$$y(x) = \pm \left[H \sin^2(\pi x/L) + h_1 \sin^2(\pi x/2L) + h_2 \cos^2(\pi x/2L) \right], \tag{4.10}$$

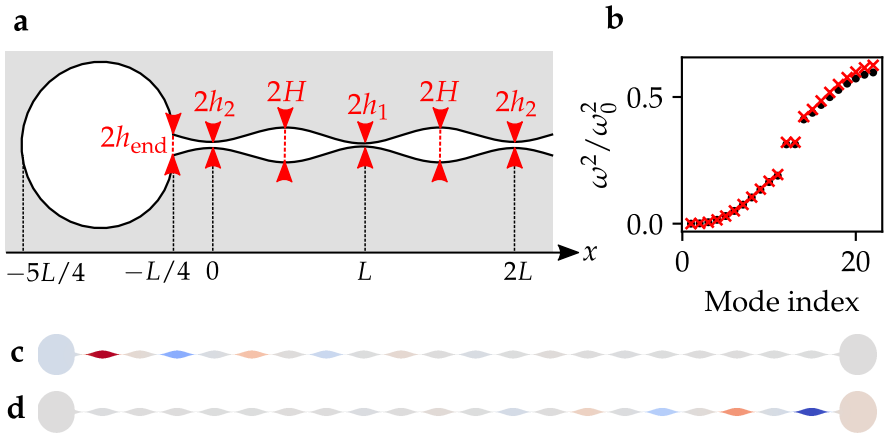

Figure 4.5: (a) Schematic of an SSH-like void-channel chain that is analagous to the capped mass-spring chain introduced in Figure 4.4. The grey region is a perfect conductor, and the white is air. Only the beginning of the chain is shown. The bulk of the chain consists of equally sized voids of half-width H and length L connected by channels of alternating half-widths h_1 and h_2. The precise shapes of the voids and channels are defined in the main text. Note that the bulk region runs from $x = -L/4$ to $(N + 1/4)L$ such that we have well defined curvature at the narrowest point of each channel. The half-width at the end of the bulk region is h_{end}; the chain is then capped by larger voids that are roughly circular with diameter L. (b) Squared frequency spectrum of the void-channel chain (obtained via finite-element simulations, red crosses, $H = L/10$, $h_1 = H/400$, $h_2 = H/100$) and analagous mass-spring chain (obtained by solving the dynamical matrix equation, black dots, $k_1 = 0.01k_0$, $k_2 = 0.02k_0$, $m = 0.1m_0$, $M = \pi/4m_0$). The frequencies are normalised by $\omega_0 = \sqrt{k_0/m_0}$ for the mass-spring model and $\omega_0 = 2\pi c_0/L$ for the void-channel model. The chains consist of 20 masses/voids (or 22 including the pair of larger masses/voids at the end). (c-d) The magnetic field (red positive, blue negative) of the two edge modes of the void-channel chain. We see that the chain preserves chiral symmetry well: magnetic field is relatively weak in the large capping voids and each edge mode is well localised to just one sublattice.

where we took the half-width of the bulk voids as $H = L/10$, and the alternating half-widths of the channels as $h_1 = H/400$ and $h_2 = H/100$. Note that the upper and lower walls run from $x = -\frac{1}{4}L$ to $x = (N + \frac{1}{4})L$ to ensure that the radius of curvature of each channel from $x = 0$ to $x = NL$ are well defined. The local radius of curvature of the walls of each channel is $R = L^2/(2\pi^2 H)$. As $h_1, h_2 \ll H$, the area of each void in the bulk region is approximately $A_{\text{bulk}} \approx 2\int_0^L H \sin^2(\pi x/L)\,\mathrm{d}x = HL$.

The walls are capped by roughly circular voids of diameter L. On the left hand side,

$$x_{\text{L}}(\theta) = \frac{L}{2}\cos(\theta) - \frac{3}{4}L, \tag{4.11}$$

$$y_{\text{L}}(\theta) = \frac{L}{2}\sin(\theta) + h_{\text{end}}\cos(\theta/2), \tag{4.12}$$

for $\theta = [0, 2\pi]$ and on the right hand side,

$$x_{\text{R}}(\theta) = \frac{L}{2}\cos(\theta) + (N + \frac{3}{4})L, \tag{4.13}$$

$$y_{\text{R}}(\theta) = \frac{L}{2}\sin(\theta) - h_{\text{end}}\sin(\theta/2), \tag{4.14}$$

for $\theta = [-\pi, \pi]$, where the $h_{\text{end}} = y(-L/4) = y(NL + L/4)$ term is included to ensure that the walls of the geometry are continuous. As $h_{\text{end}} \lesssim L$, we can take the area of the large capping voids as approximately $A_{\text{cap}} = \pi L^2/4$. Note that this is a slight underestimate of the true area of the caps because we don't account for the region $-L/4 \leq x \leq 0$ or for the extra height of the void described by Equations (4.11)-(4.14) compared to a circle of diameter L.

The alternating spring constants of the corresponding mass-spring network are

$$k_1 = \frac{1}{\pi}\sqrt{2h_1/R}\cdot k_0 = 0.01k_0,$$
$$k_2 = \frac{1}{\pi}\sqrt{2h_2/R}\cdot k_0 = 0.02k_0,$$

the masses in the bulk of the chain are

$$m = A_{\text{bulk}}\cdot m_0/L^2 = 0.1m_0,$$

and the larger capping masses are

$$M = A_{\text{cap}}\cdot m_0/L^2 = \frac{\pi}{4}m_0,$$

such that $M/m \approx 8$, where k_1, k_2, m, and M are as defined earlier in Figure 4.4. As the capping mass is roughly an order of magnitude larger than the bulk masses, we expect that the chiral symmetry is largely restored to the model. Indeed, Figure 4.5b shows that the

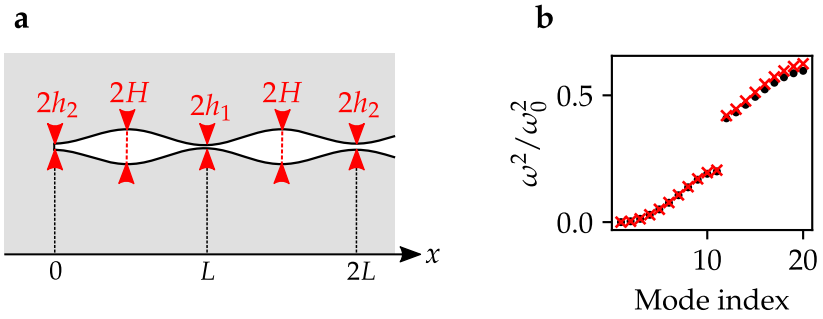

Figure 4.6: (a) Schematic of the same void-channel chain as in Figure 4.5 but without the large capping voids. (b) There is good agreement between the squared frequency spectrum of the void-channel chain (obtained via finite-element simulations, red crosses) and the corresponding mass-spring chain with free boundary conditions (obtained by solving the dynamical matrix equation, black points). The frequencies are normalised by $\omega_0 = \sqrt{k_0/m_0}$ for the mass-spring model and $\omega_0 = 2\pi c_0/L$ for the void-channel model. Without the large capping voids/heavy capping masses chiral symmetry is broken at the edges of these chains and there are no topological edge states in the band gap.

energy spectra of both the void-channel network[2] (red) and the mass-spring network (black) behave as non-trivial SSH chains with a pair of topological edge states in the energy gap.

Overall there is good agreement between the void-channel and mass-spring models; in particular we see similar band gaps and a pair of topological edge states in each model. The models agree well at lower frequencies because the mapping between the models is valid for frequencies below a cutoff frequency that scales as $\omega^2_{\text{cutoff}} \sim 1/h$ [104]. We shall explore this error in more detail later when we study the honeycomb-kagome lattice.

The edge states are largely localised on separate sublattices and decay quickly into the bulk, as shown for the void-channel model in Figures 4.5c-d. It is intuitive that in the mass-spring model the heavy capping masses will oscillate with a smaller amplitude than the other masses, and we see that correspondingly the fields in the capping voids of the void-channel model are weak. The non-zero field within capping voids indicates that the chiral symmetry is not perfectly restored. This could be improved by increasing the size of the capping voids, however this does not seem necessary as the chiral symmetry violation is weak enough that the energies of the edge states remain reasonably centered within the band gap.

2 The void-channel solutions were obtained using `FreeFem++` [108] to solve Poisson's equation for the interior region with Neumann boundary conditions along the surface of the perfect conductor [2, 104]. To do so, we modified `FreeFem++` scripts that were originally published by Vincent Laude to model phononic crystals [109].

For completeness, we show in Figure 4.6a the same SSH-like chain as in Figure 4.5 but without the capping voids. Figure 4.6b shows the squared frequency spectrum of the void-channel model (red crosses) and the corresponding mass-spring model with free boundary conditions (black points). As expected, there are no edge states because the chiral symmetry is strongly broken at the ends of the chains.

4.3 TOPOLOGICAL EDGE STATES IN THE HONEYCOMB-KAGOME LATTICE

Having established that the chiral symmetry of the mass-spring/void-channel networks can be restored by capping the interfaces with sufficiently heavy masses/large voids, we now turn to a more complex case of a square-root semimetal where the topology is protected by the chiral symmetry of the honeycomb sector of the *squared* Hamiltonian [58, 60]. We shall see that despite the differences between the mass-spring/void-channel models and the original tight-binding model, capping the interfaces again allows the protecting symmetry to be restored and for the topological edge states to be observed.

4.3.1 *Tight-binding model*

Before we introduce our mass-spring and void-channel models, let us review the tight-binding model introduced by Mizoguchi *et al* [60] and explain its topological origins. Figure 4.7a shows the nearest-neighbour tight-binding model of the honeycomb-kagome lattice, also known as the decorated honeycomb lattice. The Hamiltonian has a block off-diagonal form [60],

$$\boldsymbol{H}^{\mathrm{hk}}_{\vec{k}} \begin{bmatrix} u_1 \\ \vdots \\ u_5 \end{bmatrix} = \begin{bmatrix} \mathbf{0}_{2\times 2} & t\boldsymbol{\Psi}^{\dagger}_{\vec{k}} \\ t\boldsymbol{\Psi}_{\vec{k}} & \mathbf{0}_{3\times 3} \end{bmatrix} \begin{bmatrix} u_1 \\ \vdots \\ u_5 \end{bmatrix}, \tag{4.15}$$

where u_1 & u_2 are amplitudes at the honeycomb sites, u_3, u_4, & u_5 are amplitudes at the kagome sites, t is the hopping strength, $\mathbf{0}_{n\times m}$ is an $n \times m$ matrix of zeros, and

$$\boldsymbol{\Psi}_{\vec{k}} = \begin{bmatrix} 1 & 1 \\ e^{i\vec{k}\cdot\vec{a}_1} & 1 \\ e^{i\vec{k}\cdot\vec{a}_2} & 1 \end{bmatrix}. \tag{4.16}$$

As there are only hoppings between sites belonging to *different* sublattices, this tight-binding model is chiral symmetric as discussed in Section 1.2.3. The unitary chiral symmetry operator is

$$\boldsymbol{\Gamma} = \begin{bmatrix} \boldsymbol{I}_2 & \mathbf{0}_{2\times 3} \\ \mathbf{0}_{3\times 2} & -\boldsymbol{I}_3 \end{bmatrix}, \tag{4.17}$$

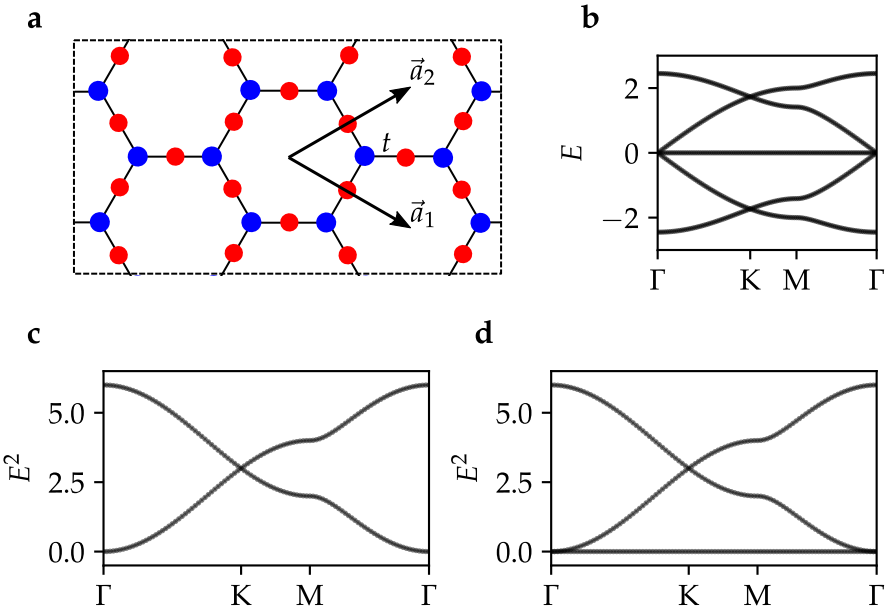

Figure 4.7: (a) Schematic of the tight-binding Hamiltonian of the honeycomb-kagome lattice, $\hat{H}^{\mathrm{hk}}$, with nearest-neighbour hopping parameter t, as introduced by [60]. The honeycomb and kagome sites are shown in blue and red, respectively, and $\vec{a}_1$ and $\vec{a}_2$ are the lattice parameters. (b) The energy spectrum of $\hat{H}^{\mathrm{hk}}$ is symmetric about $E = 0$ because of the chiral symmetry. The flat band and Dirac crossings at K are reminiscent of the nearest-neighbour tight-binding models on the honeycomb and kagome lattices, $\hat{H}^{\mathrm{h}}$ and $\hat{H}^{\mathrm{k}}$, respectively. This is because $\left(\hat{H}^{\mathrm{hk}}\right)^2$ is block-diagonal, with the blocks proportional to the energy spectra of $\hat{H}^{\mathrm{h}}$ and $\hat{H}^{\mathrm{k}}$ up to a constant shift of energy as shown in (c-d) for the honeycomb and kagome sectors of $\left(\hat{H}^{\mathrm{hk}}\right)^2$, respectively. The energy spectrum of $\hat{H}^{\mathrm{hk}}$ therefore inherits features, including topology, from $\hat{H}^{\mathrm{h}}$ and $\hat{H}^{\mathrm{k}}$. In particular, $\hat{H}^{\mathrm{h}}$ is a topological semimetal as discussed in Section 1.6, and $\hat{H}^{\mathrm{hk}}$ is therefore known as a *square-root topological semimetal* [58, 60].

where $\boldsymbol{I}_n$ is an $n \times n$ identity matrix.

The energy bands of the tight-binding model Equation (4.15) are shown in Figure 4.7b. The spectrum is symmetric about $E = 0$ due to the chiral symmetry. Curiously, the spectrum contains features of both the underlying honeycomb and kagome lattices, such as the symmetry-protected Dirac cones at K [56] and the flat band [110]. This is because Equation (4.15) belongs to a class of Hamiltonians known as *square-root Hamiltonians*, meaning that the square of Equation (4.15) is block diagonal,

$$\left(\boldsymbol{H}^{\mathrm{hk}}_{\vec{k}}\right)^2 = \begin{bmatrix} t^2\boldsymbol{\Psi}^{\dagger}_{\vec{k}}\boldsymbol{\Psi}_{\vec{k}} & \boldsymbol{0}_{2\times 3} \\ \boldsymbol{0}_{3\times 2} & t^2\boldsymbol{\Psi}_{\vec{k}}\boldsymbol{\Psi}^{\dagger}_{\vec{k}} \end{bmatrix} = \begin{bmatrix} \boldsymbol{H}^{\mathrm{h}}_{\vec{k}} & \boldsymbol{0}_{2\times 3} \\ \boldsymbol{0}_{3\times 2} & \boldsymbol{H}^{\mathrm{k}}_{\vec{k}} \end{bmatrix}, \tag{4.18}$$

where

$$\boldsymbol{H}^{\mathrm{h}}_{\vec{k}} = \begin{bmatrix} 3t^2 & (1 + e^{+i\vec{k}\cdot\vec{a}_1} + e^{+i\vec{k}\cdot\vec{a}_2})t^2 \\ (1 + e^{-i\vec{k}\cdot\vec{a}_1} + e^{-i\vec{k}\cdot\vec{a}_2})t^2 & 3t^2 \end{bmatrix} \tag{4.19}$$

is the tight-binding Hamiltonian of a honeycomb lattice with nearest-neighbour hopping strength t^2 and on-site potential $3t^2$, and

$$\boldsymbol{H}^{\mathrm{k}}_{\vec{k}} = \begin{bmatrix} 2t^2 & (1 + e^{-i\vec{k}\cdot\vec{a}_1})t^2 & (1 + e^{-i\vec{k}\cdot\vec{a}_2})t^2 \\ (1 + e^{+i\vec{k}\cdot\vec{a}_1})t^2 & 2t^2 & (1 + e^{-i\vec{k}(\vec{a}_2 - \vec{a}_1)})t^2 \\ (1 + e^{+i\vec{k}\cdot\vec{a}_2})t^2 & (1 + e^{+i\vec{k}(\vec{a}_2 - \vec{a}_1)})t^2 & 2t^2 \end{bmatrix} \tag{4.20}$$

is the tight-binding Hamiltonian of a kagome lattice with nearest-neighbour hopping strength t^2 and on-site potential $2t^2$ [60]. The squared energy spectrum of the honeycomb and kagome sectors of Equation (4.18) as shown in Figures 4.7c-d, respectively.

Arkinstall *et al* [58] introduced a class of topological materials whose non-trivial topology is inherited from the squared Hamiltonian. They named these materials *square-root topological insulators*. As we reviewed in Section 1.6, the nearest-neighbour tight-binding model of the honeycomb lattice is a topological semi-metal. The honeycomb-kagome lattice is therefore a *square-root* topological semi-metal, with the non-trivial topology inherited from the honeycomb sector of the squared Hamiltonian [60, 61]. In the following sections, we introduce mass-spring and void-channel analogues of the square-root topological semimetal on the honeycomb lattice and study the symmetry protected edge states.

4.3.2 *Mass-spring and void-channel models*

Figure 4.8a shows a mass-spring model of a honeycomb-kagome lattice where the honeycomb masses, m_h, and kagome masses, m_k, are

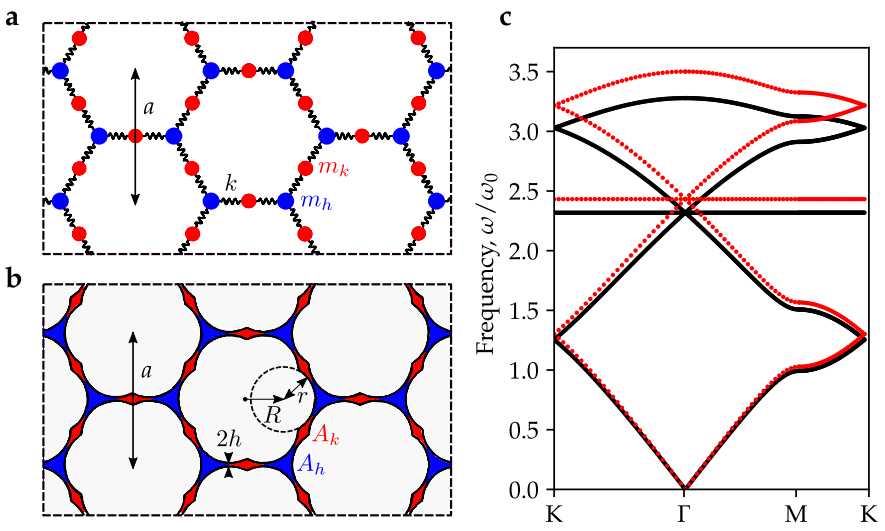

Figure 4.8: Mass-spring and void-channel models of a honeycomb-kagome lattice with nearest-neighbour coupling. (a) In the mass-spring model, the masses at honeycomb sites (m_h, blue) and kagome sites (m_k, red) are connected by springs of equal spring constants k. (b) In the void-channel model, voids and channels are formed between flower-shaped perfectly conducting particles arranged on a triangular lattice of lattice parameter a. The flower shapes consist of six cylinders of radius r arranged in a ring of radius R. The voids at honeycomb the honeycomb sites have area A_h (blue voids) and the voids at kagome sites have area A_h (red voids). The channels have equal half-widths h. (c) Bulk frequency bands of the mass-spring model (black points, $m_h = 0.01104m_0$, $m_k = 0.00736m_0$, $k = 0.01978k_0$) and the void-channel model (red points, $A_h = 0.01104a^2$, $A_k = 0.00736a^2$, $2h = 0.001a$). The frequencies are normalised by $\omega_0 = \sqrt{k_0/m_0}$ for the mass-spring model and $\omega_0 = 2\pi c_0/a$ for the void-channel model. There is good agreement between the two models, particularly at the lower frequencies. We chose the masses and areas such that $m_h/m_k = A_h/A_h = 3/2$ in order that the models resemble the tight-binding model of Figure 4.7c but with a shift of frequency, as discussed in the main text. The mass-spring calculations were performed by Yordan Ignatov using parameters that I provided.

connected by springs of spring constant k. Let us compare the tight-binding Equation (4.15) to the equations of motion of this mass-spring network,

$$\begin{bmatrix} \frac{3k}{m_h}\boldsymbol{I}_{2\times 2} & -\frac{k}{m_h}\boldsymbol{\Psi}_{\vec{k}}^{\dagger} \\ -\frac{k}{m_k}\boldsymbol{\Psi}_{\vec{k}} & \frac{2k}{m_k}\boldsymbol{I}_{3\times 3} \end{bmatrix} \begin{bmatrix} u_1 \\ u_2 \\ u_3 \\ u_4 \\ u_5 \end{bmatrix} = \omega^2(\vec{k}) \begin{bmatrix} u_1 \\ u_2 \\ u_3 \\ u_4 \\ u_5 \end{bmatrix}. \tag{4.21}$$

First, note that the *unsquared* equations have eigenvalue ω^2, and the squared equations would have eigenvalue ω^4. Next, we note that in the mass-spring model the block-diagonal terms are non-zero and the two off-diagonal block matrices are scaled by different factors m_h and m_k. In a recent study of tight-binding and mass-spring honeycomb-kagome lattices, Mizoguchi *et al* [60] reproduced the tight-binding model by letting $m_h = m_k$ and setting the block-diagonal of the matrix to zero by adding a gravitional potential term in which the masses roll around in dents on a floor. Our interest is in mapping the mass-spring models to void-channel networks but no analogue of these dents for the void-channel network was apparent to us. However, we shall demonstrate the *squared* tight-binding and mass-spring models are analagous regardless. First, we decompose the unsquared mass-spring matrix equation as

$$\begin{bmatrix} \frac{3k}{m_h}\boldsymbol{I}_{2\times 2} & -\frac{k}{m_h}\boldsymbol{\Psi}_{\vec{k}}^{\dagger} \\ -\frac{k}{m_k}\boldsymbol{\Psi}_{\vec{k}} & \frac{2k}{m_k}\boldsymbol{I}_{3\times 3} \end{bmatrix} = \frac{\alpha k}{m_0}\boldsymbol{I}_{5\times 5} + \begin{bmatrix} +\frac{\beta k}{m_0}\boldsymbol{I}_{2\times 2} & -\frac{k}{m_h}\boldsymbol{\Psi}_{\vec{k}}^{\dagger} \\ -\frac{k}{m_k}\boldsymbol{\Psi}_{\vec{k}} & -\frac{\beta k}{m_0}\boldsymbol{I}_{3\times 3} \end{bmatrix}, \tag{4.22}$$

where

$$\alpha = \frac{3/m_h + 2/m_k}{2} m_0, \tag{4.23}$$

$$\beta = \frac{3/m_h - 2/m_k}{2} m_0. \tag{4.24}$$

Taking the $\alpha k/m_0$ term to the right hand side of the equations of motion we obtain

$$\begin{bmatrix} +\frac{\beta k}{m_0}\boldsymbol{I}_{2\times 2} & -\frac{k}{m_h}\boldsymbol{\Psi}_{\vec{k}}^{\dagger} \\ -\frac{k}{m_k}\boldsymbol{\Psi}_{\vec{k}} & -\frac{\beta k}{m_0}\boldsymbol{I}_{3\times 3} \end{bmatrix} \begin{bmatrix} u_1 \\ \vdots \\ u_5 \end{bmatrix} = (\omega^2(\vec{k}) - \frac{\alpha k}{m_0}) \begin{bmatrix} u_1 \\ \vdots \\ u_5 \end{bmatrix}. \tag{4.25}$$

Note that the equations of motion are only chiral symmetric about $\omega^2 = \alpha k/m_0$ if we choose $2m_h = 3m_k$ such that $\beta = 0$.

The matrix of Equation (4.25) squares to

$$\begin{bmatrix} +\frac{\beta k}{m_0}\boldsymbol{I}_{2\times 2} & -\frac{k}{m_h}\boldsymbol{\Psi}_{\vec{k}}^{\dagger} \\ -\frac{k}{m_k}\boldsymbol{\Psi}_{\vec{k}} & -\frac{\beta k}{m_0}\boldsymbol{I}_{3\times 3} \end{bmatrix}^2 = \left(\frac{\beta k}{m_0}\right)^2 \boldsymbol{I} + \begin{bmatrix} \frac{k^2}{m_k m_h}\boldsymbol{\Psi}_{\vec{k}}^{\dagger}\boldsymbol{\Psi}_{\vec{k}} & \boldsymbol{0}_{2\times 3} \\ \boldsymbol{0}_{3\times 2} & \frac{k^2}{m_k m_h}\boldsymbol{\Psi}_{\vec{k}}\boldsymbol{\Psi}_{\vec{k}}^{\dagger} \end{bmatrix}, \tag{4.26}$$

such that the squared equations of motion are

$$\begin{bmatrix} \frac{k^2}{m_k m_h}\boldsymbol{\Psi}_{\vec{k}}^\dagger \boldsymbol{\Psi}_{\vec{k}} & \mathbf{0}_{2\times 3} \\ \mathbf{0}_{3\times 2} & \frac{k^2}{m_k m_h}\boldsymbol{\Psi}_{\vec{k}} \boldsymbol{\Psi}_{\vec{k}}^\dagger \end{bmatrix} \begin{bmatrix} u_1 \\ \vdots \\ u_5 \end{bmatrix} = \left[\left(\omega^2(\vec{k}) - \frac{\alpha k}{m_0}\right)^2 - \left(\frac{\beta k}{m_0}\right)^2 \right] \begin{bmatrix} u_1 \\ \vdots \\ u_5 \end{bmatrix}, \tag{4.27}$$

which is analagous to the squared tight-binding Equation (4.18) with $t^2 \leftrightarrow k^2/m_k m_h$ and $E^2 \leftrightarrow \left(\omega^2(\vec{k}) - \frac{\alpha k}{m_0}\right)^2 - \left(\frac{\beta k}{m_0}\right)^2$. Note that for the squared equations of motion, $\beta \neq 0$ simply corresponds to another shift in frequency and does not break any symmetries of the squared equations.

Next, we propose a photonic analogue of this mass-spring network. Our network of voids and channels is formed between "flower" shaped particles of perfect conductor arranged on a triangular lattice with lattice parameter a, where each flower consists of six cylinders of radius r that are distributed along a ring of radius R as shown in Figure 4.8b. The voids at the honeycomb and kagome sites (shown in blue and red, respectively) are connected by narrow channels of half-width h, where

$$R\cos\frac{\pi}{6} = \frac{a}{2} - r - h. \tag{4.28}$$

We fixed the surface-to-surface gap as $2h = a/1000$, similar to the ratio as we used for the SSH in the previous section.[3] For a given value of r, we can then determine $R = (a/2 - h - r)/\cos(\pi/6)$ and numerically calculate the areas of the honeycomb and kagome voids, A_h and A_k. We settled on $r = 0.259a$, for which $R = 0.27771a$, $A_h = 0.01104a^2$, and $A_k = 0.00736a^2$, such that $A_h/A_k = 3/2$. As shown in Figure 4.8c, there is good agreement between the system of voids and channels (red) and the discrete system of masses and springs (black) where

$$m_h = A_h \cdot m_0/a^2 = 0.01104 m_0, \tag{4.29}$$

$$m_k = A_k \cdot m_0/a^2 = 0.00736 m_0, \tag{4.30}$$

$$k = \frac{1}{\pi}\sqrt{\frac{2h}{r}} = 0.01978 k_0. \tag{4.31}$$

We verify in Appendix D that the agreement between the mass-spring and void-channel networks improves as the channels are made more narrow. We have chosen these particular parameters such that $A_h/A_k = m_h/m_k = 3/2$ and therefore $\beta = 0$ in order that the mass-spring and void-channel models more closely resemble the tight-binding model of Figure 4.7. When we study the edge states in a later section, we shall see that the topological edge states survive even if $m_h/m_k \neq 3$ and $\beta \neq 0$.

3 While this is quite a small ratio of h/a, we shall see in the concluding remarks that less extreme ratios of h/a would also be viable.

Now that we have introduced our photonic geometry, let us compare and contrast our work with some recent studies of the honeycomb-kagome lattice in photonics and acoustics. Maimaiti *et al* [105] studied the response of triangular array of metallic cylinders to microwave radiation. They noted that the voids between the cylinders lie on a honeycomb-kagome lattice and used Monte Carlo methods to fit to a honeycomb-kagome tight-binding model. However, the cylinders were not closely spaced and the authors did not consider any topological aspects of the array; it is likely that the quality of the edge states in this system would be reduced by longer-ranged coupling between voids and their next-nearest-neighbours. On the other hand, Yan *et al* [111] studied a honeycomb-kagome array of acoustic resonators connected by narrow channels and considered the symmetry protected topology. However, in their work the width of the channels were alternated to produce a square-root topological insulator where the topology was inherited from the *breathing kagome* sector of the squared Hamiltonian, whereas we study the lattice with equal channel widths which is akin to the mass-spring/tight-binding models of Mizoguchi *et al* where the non-trivial topology is inherited from the honeycomb sector of the squared Hamiltonian [60].

4.3.3 *Edge states in a ribbon*

In order to produce topological edge states, we must introduce interfaces in a manner that preserves (i) the block-diagonal nature of the squared equations and (ii) the chiral symmetry of the honeycomb sector of the squared equations [60]. This can be achieved by capping the interface with heavy masses/large voids placed at the honeycomb sites.[4]

Figure 4.9a shows a ribbon of our flower-shaped particles that is terminated with slabs of perfect conductor along the top and bottom edge. This results in large voids that cap the ribbon at the topmost and bottommost honeycomb sites, shown in magenta, forming a "zig-zag" edge from the perspective of the honeycomb lattice. Using the same values of h, r and R as for the bulk calculations of Figure 4.8, the magenta capping voids have an area of $A = 0.12247a^2$, roughly an order of magnitude larger than the regular honeycomb and kagome voids.

Figure 4.9b shows a comparison between the void-channel model (red) and the mass-spring model (black, with the same values of k,

4 When we take the square of the tight-binding model with free boundary conditions, the sites at the edges of the model will gain a different onsite potential to the sites of the same sublattice in the bulk. As we want to retain the chiral symmetry of the honeycomb lattice, we ensure that the tight-binding model has the kagome sites at the edges of the model. The edges of the mass-spring model therefore consist of kagome sites capped by heavy masses to emulate the free boundary condition on the kagome sites.

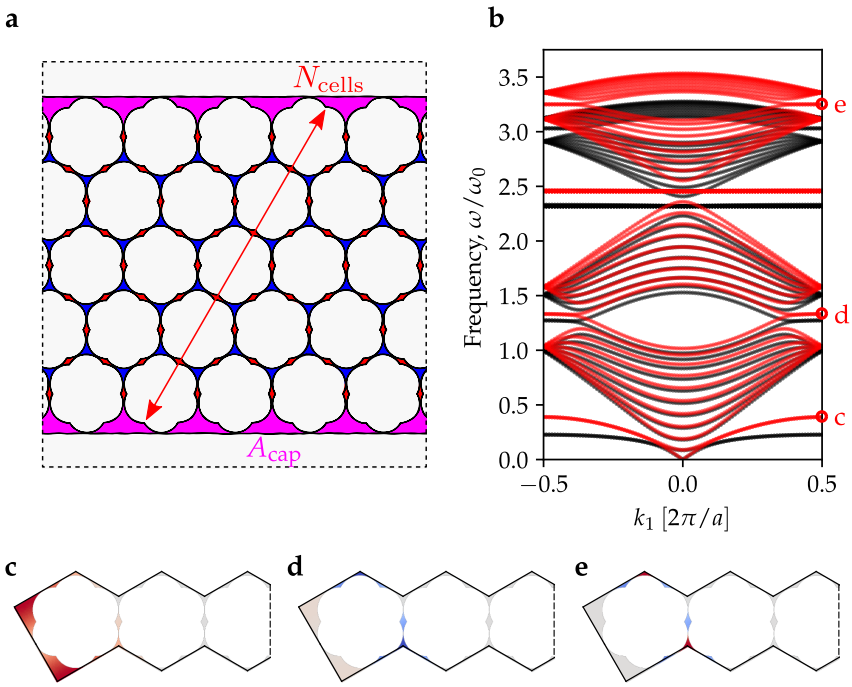

Figure 4.9: (a) Schematic of a ribbon of the honeycomb-kagome void-channel network introduced in Figure 4.8, but terminated by slabs of perfect conductor at the top and bottom. The large magenta voids at the boundary have area A_{cap} and reduce the chiral symmetry breaking at the interfaces. (b) Frequency bands of a ribbon that is $N_{\text{cells}} = 10$ unit cells long. The frequencies are normalised by $\omega_0 = \sqrt{k_0/m_0}$ for the mass-spring model (black points, obtained by solving the dynamical matrix equation) and $\omega_0 = 2\pi c_0/a$ for the void-channel model (red points, obtained via finite-element simulations). (c-e). Visualisations of the labelled eigenmodes in panel b. For each shown here, this is also an energy degenerate inversion symmetric partner at the other edge. (c) The lowest pair of bands are excitations in the large voids, whereas (d-e) are topological edge states protected by the chiral symmetry of the honeycomb sector of the squared equations of motion.

m_h, and m_k as before, and capped with masses of $M = A \cdot m_0/a^2 = 0.12247 m_0$ at the honeycomb sites along the interface). As before, there is good agreement between the mass-spring and void-channel models but decreasing accuracy with increasing frequency. We observe several new states that were not present in the bulk eigenmodes, as marked by the red circles labelled c, d, and e, and visualised in Figures 4.9c-e, respectively.

We see from Figure 4.9c that the lowest pair of bands correspond to excitations within the large voids. As we increase the size of the capping voids, these bands would flatten to zero frequency. On the other hand, Figures 4.9d-e show the pair of topological edge states arising from the non-trivial topology of the honeycomb sector of the squared equations [60].

If the squared system was exactly chiral symmetric then the topological edge states should be flat [60]; instead there is a slight tilt indicating a weak symmetry breaking. Interestingly, the field within the large voids is weaker for the higher energy eigenmode in Figure 4.9e, suggesting that the chiral symmetry of the squared system is better preserved at the higher frequencies. This is because the frequency and character of the unwanted excitation in the capping voids (Figure 4.9c) is more similar to the edge state with lower frequency (Figure 4.9d, honeycomb and kagome sites are in phase) than the edge state with higher frequency (4.9e, honeycomb and kagome sites are out of phase). The unwanted mode therefore couples more strongly to the lower frequency edge state.

In Figure 4.10 we relax the constraint $2m_h = 3m_k$ such that $\beta \neq 0$. This breaks the chiral symmetry of the unsquared equations yet the edge states remain flat and robust against this perturbation because the honeycomb sector of the *squared* equations remains chiral symmetric. On the other hand, we verify in Figure 4.11 that the topological edge states are not present in the ribbon without the heavy capping masses/large capping voids.

4.3.4 *Edge and corner states in a triangular metaparticle*

We now study corner and edge states in a large but finite "triangular metaparticle" of the honeycomb-kagome lattice, as shown in the upper-left inset of Figure 4.12a. Having established the validity of the mass-spring model for the bulk and at the edges, we model the system using only the discrete mass-spring equations as these are much faster to solve but retain the features we are interested in. As with the ribbon, we cap the ends with heavy masses at honeycomb sites to reduce the breaking of the chiral symmetry in the honeycomb sector of the squared equations.

The main panel of Figure 4.12a shows the energy spectrum of a triangular metaparticle with $N_{\text{cells}} = 19$ unit cells along each edge for

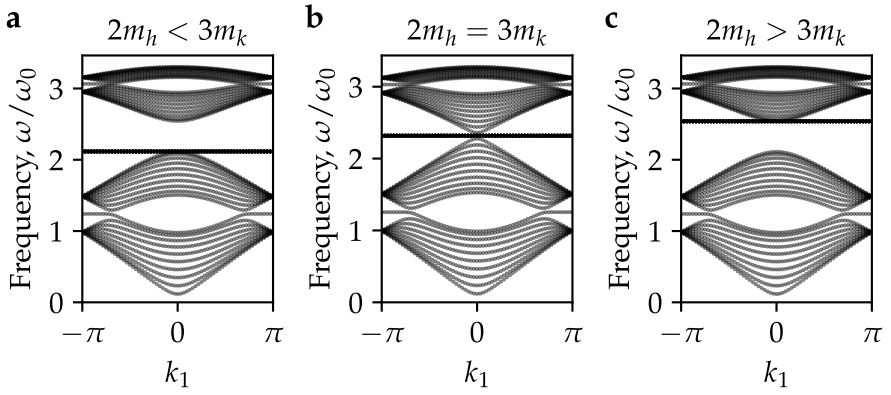

Figure 4.10: The edge states of the square-root semimetal are protected by the chiral symmetry of the *squared* equations, and may survive even as the chiral symmetry of the unsquared equations is broken. We plot the frequencies (normalised by $\omega = \sqrt{k_0/m_0}$) of the mass-sping model of the mass-spring ribbon from Figure 4.9 for (a) $2m_h < 3m_k$, (b) $2m_h = 3m_k$, and (c) $2m_h > 3m_k$, where m_h and m_k are the masses at the honeycomb and kagome sites, respectively. The edge states are robust in all three systems even though the unsquared equations are not chiral symmetric for $2m_h \neq 3m_h$. This is because the topological edge states are protected by the chiral symmetry of the honeycomb sector of the *squared* equations [60], which can be preserved even as the chiral symmetry of the unsquared equations is lost.

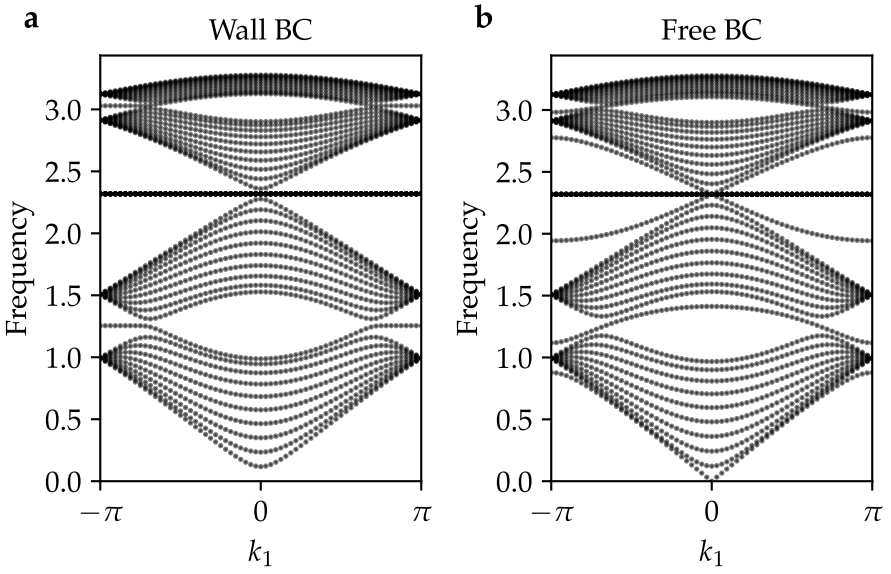

Figure 4.11: Edge states of the ribbon of honeycomb-kagome mass-spring model introduced in Figure 4.9 with $2m_h = 3m_k$ for (a) the ideal 'wall' boundary condition on the kagome sites (infinitely heavy capping masses at the honeycomb sites) and (b) the free boundary condition on the kagome sites (no capping masses). The edge states in (b) are not pinned to a particular energy because the honeycomb sector of the squared equations of motion is not chiral symmetric.

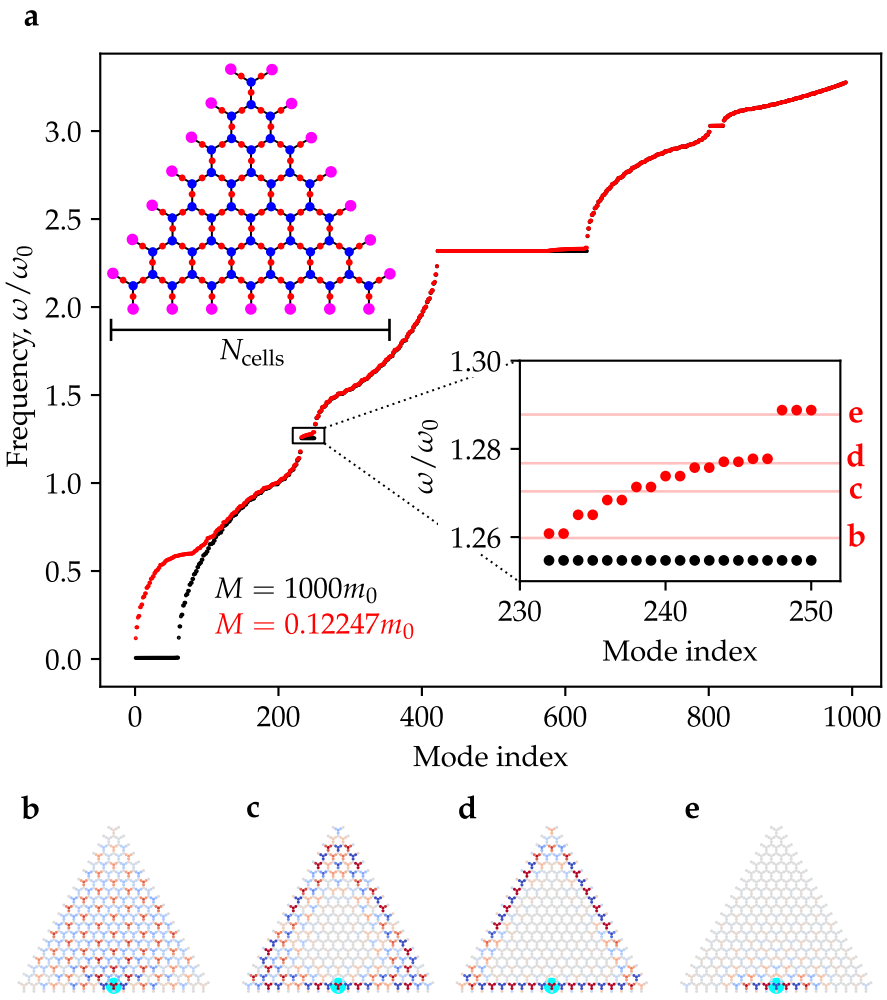

Figure 4.12: (a) Frequency eigenspectrum of a triangular metaparticle built from the mass-spring honeycomb-kagome network of the honeycomb-kagome void-channel network introduced in Figure 4.8. The edges are capped with extremely heavy masses ($M = 1000m_0$, black points) or realistic masses ($M = 0.12247m_0$, as in Figure 4.9). The frequencies are normalised by $\omega_0 = \sqrt{k_0/m_0}$. The upper left inset shows a schematic of the triangular metaparticle with the heavy masses shown in magenta. The schematic shows a particle with $N_{\text{cells}} = 7$ unit cells along each edge, but $N_{\text{cells}} = 19$ was used in the calculations. The lower right inset shows a zoom of the lower frequency set of edge and corner states. (b)-(e) Steady state fields after driving the system with a harmonic force at the honeycomb site at the center of the blue highlighted region for the frequencies labelled in the lower right inset of panel a.

a realistic capping mass ($M = 0.12247m_0$, red) and for a very large capping mass where the chiral symmetry of the honeycomb sector of the squared equations is near-perfectly restored ($M = 1000m_0$, black). We identify the large flat region of eigenmodes at $\omega \approx 2.4\omega_0$ as the bulk flat band inherited from the kagome lattice, and the smaller flat regions of eigenmodes at $\omega \approx 1.25\omega_0$ and $\omega \approx 3.1\omega_0$ as the topological edge states inherited from the honeycomb lattice. The lower-right inset of Figure 4.12a shows the energy eigenmodes of the lower frequency edge state in more detail. Although the edge state is extremely flat for the unrealistically large value of M, there is actually an advantage to using the more realistic value of M for which the protecting symmetry is weakly broken.

Figures 4.12b-e show the steady-state solutions of the triangular mass-spring metaparticles capped by realistic masses and driven by time-harmonic forces centered at the honeycomb sites highlighted in light blue for the four frequencies labelled in the lower-right inset of Figure 4.12a.[5] In Figure 4.12b the energy propagates freely through the particle. This is because the lowest two eigenmodes that are close to the driving frequency are actually bulk eigenmodes corresponding to the Dirac cones at K and $-$K of Figure 4.8c. In Figure 4.12c-d we see that the energy propagates around the edge of the particle but not into the bulk. As the energy increases the modes become more localised to the edges. Figure 4.12e shows that the field is localised in all directions when driving at the edge of the triangle at the frequency just below the group of triply degenerate eigenstates. This is because these eigenstates are corner eigenstates, as shown in Figure 4.13.[6] Crucially, the weak breaking of chiral symmetry has lifted the degeneracies between the bulk and the edge/corner states, allowing these to be excited at different frequencies.

4.3.5 *Operating frequencies and length scales*

Finally, let us consider the feasibility of manufacturing the honeycomb-kagome network of voids and channels and the frequencies and length scales at which it could operate. We must find a balance the size of the gaps, the size of the particles, the frequencies at which the edge states occur, and the frequencies at which the metals may be treated as perfect conductors.

For example, let us consider the parameters required for to obtain edge states at $\omega = 1\,\text{THz}$. The lower frequency edge states have a normalised frequency of $\omega/\omega_0 \approx 1.3$, where $\omega_0 = 2\pi c_0/a$ and c_0 is

5 Note that we forced the system at frequencies just below the resonances because the energy of the closed mass-spring system solution diverges if we drive at the exact frequency of the resonance.

6 We found that driving the triangle at the corner lead to excitation of both the corner and edge states. We therefore plotted the eigenmodes rather than the forcing in Figure 4.13 to demonstrate that these are corner states.

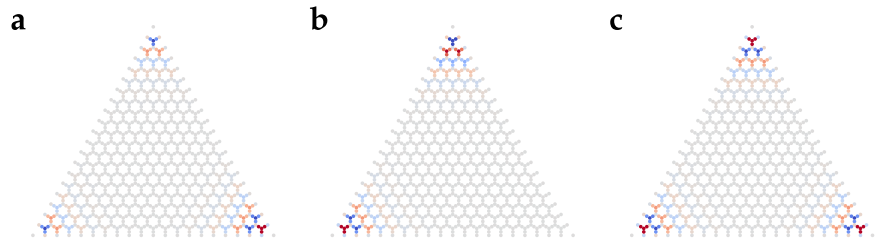

Figure 4.13: Visualisation of the triply degenerate eigenmodes of the triangular metaparticle for the mode indices (a) 248, (b) 249, (c) 250 of Figure 4.12a. The fields reveal that these eigenmodes are corner states. The modes are degenerate because of the C_3 symmetry of the triangle; the eigensolver has therefore returned arbitrary linear superpositions of the three corner eigenmodes.

the speed of light in vacuum, corresponding to a lattice parameter of $a \approx 1.3 \cdot 2\pi c_0/\omega = 2.4\,\text{mm}$. This would correspond to channel half-widths of $h = a/2000 \approx 1.2\,\mu\text{m}$ using the ratio from earlier, although we show in Appendix D that this could likely be relaxed to $h \sim a/100$ while still achieving reasonable accuracy when mapping between the mass-spring and void-channel models. Both a and h are orders of magnitude greater than the skin depth of gold which is on the order of 50 nm for $\omega = 1\,\text{THz}$, and it would therefore be reasonable to treat the gold particles as perfectly conductors.[7]

4.4 REMARKS ON CHAPTER 4

In this chapter we have shown that networks of voids and narrow connecting channels are a promising platform for mimicking chiral or square-root topological tight-binding models with photonics. This was done by mapping the tight-binding models to mass-spring models, and then mapping these mass-spring models to the void-channel networks using an asymptotically exact method [2, 104]. We found that although introducing interfaces to the mass-spring/void-channel networks could break the symmetries that protected the topological edge states, these symmetries could be restored by capping the interfaces with heavy masses/large voids.

One question we have not addressed is how resilient the topological edge states are to disorder. In fact, the chiral symmetry of the mass-spring/void-channel networks is not robust against disorder. This is because the systems are only chiral symmetric if the diagonal elements of the governing equations are proportional to the identity matrix and can be separated out as a constant shift in frequency such as in Equation 4.4. Disorder may introduce variance in the elements of the diagonal which would break the chiral symmetry. However, if the

7 See for example Figure 5.12 of the next chapter, where we show that the metallic particles behave as perfect conductors when much larger than the skin depth.

disorder remains low enough that the variance is small compared to the non-diagonal elements then the bulk-boundary correspondence remains a good approximation [53].

In this chapter, the materials were assumed to be perfectly conducting, meaning that the skin depth is much smaller than the particles and the electromagnetic field does not penetrate far into the particles. In the next chapter, we study closely packed metallic nanoparticles in the opposite limit where the electromagnetic field penetrates into the particles. We find that these nanoparticle arrays act as effective dielectrics that are surprisingly transparent to mid-to-far infrared radiation.

5

EFFECTIVE DIELECTRICS IN THE TERAHERTZ REGIME

5.1 OVERVIEW

In this chapter, we explain how densely packed arrays of metallic nanoparticles form effective dielectrics for wavelengths in the mid-to-far-infrared and beyond. These are low-loss and virtually dispersion-free, allowing the design of ultra-broadband and highly transparent devices constructed from highly lossy and dispersive metals. These effective dielectrics can even be more transparent than traditional dielectrics. For example, Figure 5.1 demonstrates that mid-to-far-infrared radiation penetrates further into an array of cylinders that is 75% titanium by volume than it does into germanium, which is renowned for its transparency in the infrared. Additionally, the local effective index of the arrays can be controlled by tuning the size, shape, spacing, and local environment of the nanoparticles, allowing for the design of more complex devices such as gradient-index lenses.

This research, which was published in Nature Communications [113] with our experimental collaborators, will be presented as follows. First, we will describe the principle behind the effective dielectrics: that nanocylinders of the appropriate size act as "meta-atoms" or "meta-molecules" that polarise under an electric field, in analogy with atoms or molecules in real dielectrics. This will be accompanied by theoretical and experimental proof-of-concepts. Next, we will explain a novel method of linearising a quadratic eigenvalue problem in order to efficiently solve for the refractive index of the effective dielectrics. We then use our method to study how the effective index is determined by the wavelength of light, the choice of the metal, the size and spacing of the nanoparticles, and we comment on the accuracy of analytical mixing formulae. Finally, we exploit the simultaneous transparency, tunability, and high metallic filling fraction of the effective dielectrics to design a novel device intended to enhance the sensitivity of nonlinear infrared spectroscopy. The device simultaneously focuses light on the microscale and 'squeezes' the electric field between the metallic particles on the nanoscale, producing 'doubly-enhanced' electric field hotspots, $|E/E_0|^2 > 10^3$, over a broad range of frequencies and with minimal heat production.

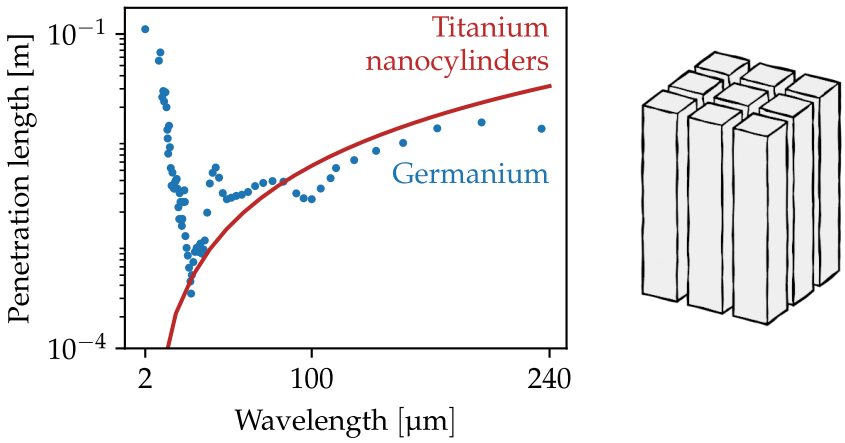

Figure 5.1: The metallic nanoparticle arrays we introduce in this chapter can be more transparent than dielectrics such as germanium for the mid-to-far-infrared wavelengths. Here we see that the effective penetration length of transverse-electric polarised light through an effective dielectric (an array of square titanium cylinders with a high filling fraction, $f = 75\%$, and a surface-to-surface separation of $G = 2\,\text{nm}$) is comparable to germanium. The penetration length of germanium was derived from the refractive index tables of Palik's handbook of optical constants of solids [112] and the effective penetration of the titanium nanocylinders was calculated using the numerical method that will be introduced in Section 5.3.

5.2 PRINCIPLE AND PROOF-OF-CONCEPTS

5.2.1 *Metals, dielectrics, and effective dielectrics*

Although no material is truly homogeneous on the atomic scale, many materials can be characterised by homogeneous macroscopic properties such as refractive index by averaging out the atomistic inhomogeneities that are smaller than the wavelengths of light [114]. This principle also holds for materials with larger scale inhomogeneities including man-made structures known as *metamaterials*, provided that the artificial structuring remains sufficiently subwavelength [115–118].

Very early research on metamaterials included arrays of centimeter-scale metallic particles capable of guiding and focusing radio waves like a dielectric [119]. In contrast to the nanoscale building blocks of modern metamaterials, the metallic particles were much larger than the skin depth of the metal and could be treated as perfect conductors, resulting in very low losses.

Figure 5.2 shows how metals, dielectrics, and effective dielectrics composed of metallic nanoparticles respond to a slowly varying electric field. In metals, the electric field drives the free electrons to the surfaces until the field induced by the build up of surface charge cancels with the applied field, as in Figure 5.2a. On the other hand, the build up of surface charge is restricted in dielectrics because the

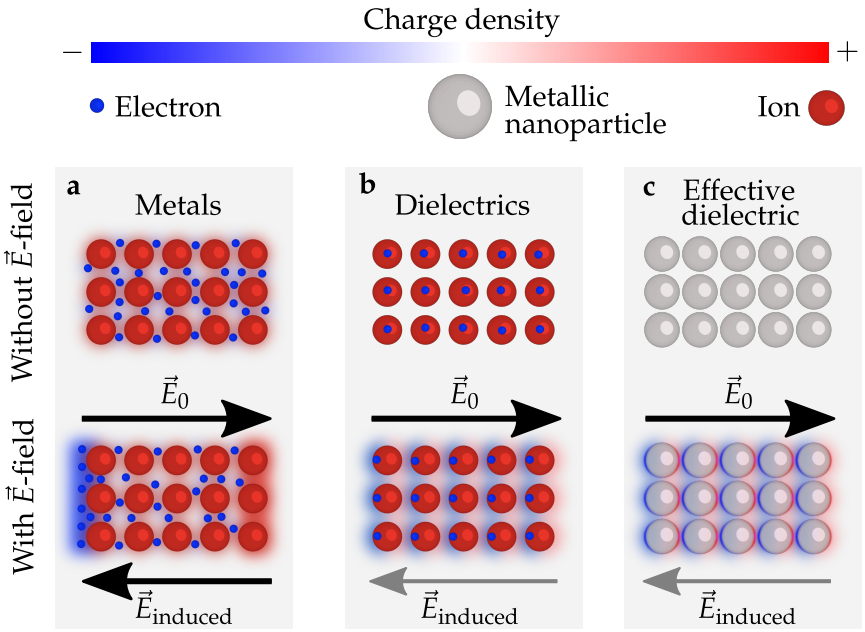

Figure 5.2: The response of metals, dielectrics, and effective dielectrics to a slowly varying electric field. (a) In metals, the electrons build up at the surfaces until the applied electric field, $\vec{E}_0$, and the induced electric field, $\vec{E}_{\text{induced}}$ cancel within the bulk. In (b) dielectrics and (c) effective dielectrics, the induced field is weaker than the applied field because the surface charge is generated by the polarisation of the (meta-)atoms or (meta-)molecules.

electrons are bound to the parent atoms/molecules [120], and the induced field resulting from the polarisation of the dielectric molecules is weaker than the applied field, as in Figure 5.2b. While the effective dielectrics are composed mostly of metal, the bounded motion of the electrons within the metallic nanoparticles resembles the polarisation of atoms and molecules in real dielectrics, as in Figure 5.2c.

The effective dielectric behaviour of these lattices is restricted to the infrared wavelengths and longer, as exciting the localised surface plasmon resonances of the metallic particles at optical frequencies results in a highly dispersive and lossy metallic response, even for filling fractions as low as 1% [121, 122]. At high filling fractions, plasmonic coupling produces electric field hotspots between closely spaced particles [123], but these suffer from the high losses (heat generation) and narrow bandwidths associated with localised surface plasmon resonances [124].

There have been recent studies on building effective dielectrics using nanoscale metallic particle arrays for the visible and infrared. Chung *et al* [125] showed that the effective permittivity and permeability of such arrays can be tuned independently, but assumed long wavelengths without considering losses. Other studies have demonstrated that such arrays can have unnaturally high refractive indices [126], but in experimental realisations the samples were only a few layers of nanoparticles thick such that losses could be largely ignored [127, 128].

In the following sections we discuss in detail the losses of the effective dielectrics in the mid-to-far-infrared. We show that effective dielectrics remain highly transparent to infrared radiation even when the size of the particles is on the order of the skin depth, and when the particles are tightly packed such that there are strong inter-particle interactions.

5.2.2 *Numerical proof-of-concept*

5.2.2.1 *Effect of polarisation*

In Figure 5.3 we display the calculated effective permittivity of arrays of metallic nanocylinders for different polarisations.[1] We see that for TE-polarised light, where the electric field drives the electrons towards the surfaces of the nanocylinders, the array behaves as an effective dielectric ($\epsilon_{\text{eff}} > 0$). This is because the transverse motion of the electrons is restricted by the surfaces of the nanocylinders. In contrast, the nanocylinders respond to TM-polarised light (blue line) similarly to the bulk metal (grey dashes) as the nanocylinders do not restrict the longitudinal motion of electrons.

Figure 5.4 shows that arrays of nanospheres behave as effective dielectrics regardless of the incident polarisation, as the motion of

1 The method of calculation will be discussed shortly in Section 5.3.

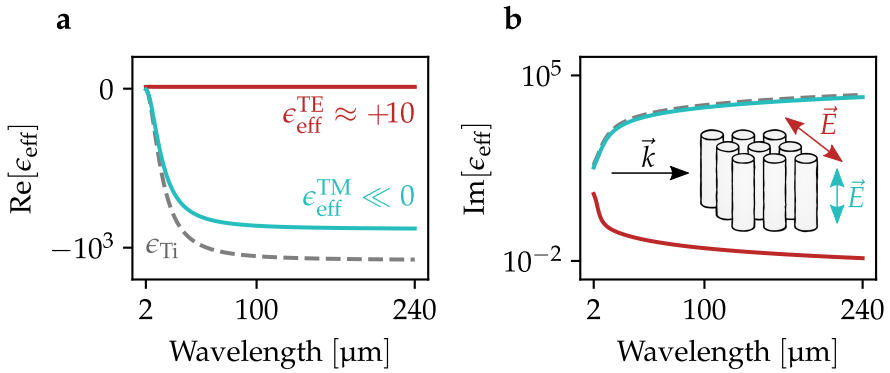

Figure 5.3: The real and imaginary parts of the effective permittivity, ϵ_{eff}, of arrays of titanium nanocylinders for transverse electric (TE, red curve) and transverse magnetic (TM, blue curve) polarised light compared to the permittivity of solid titanium, ϵ_{Ti} (dashed curve). The nanocylinders have diameters $d = 38\,\mathrm{nm}$ and surface-to-surface gap $G = 2\,\mathrm{nm}$.

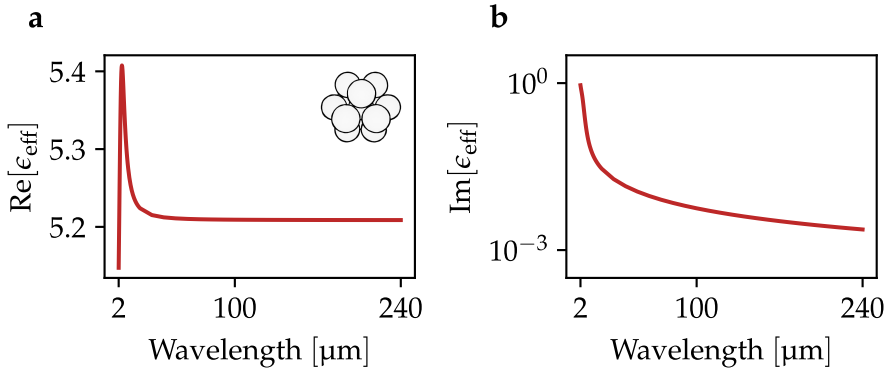

Figure 5.4: The real and imaginary parts of the effective permittivity, ϵ_{eff}, of titanium nanospheres of diameter $d = 20\,\mathrm{nm}$ and surface-to-surface gap $G = 2\,\mathrm{nm}$ for unpolarised light. Unlike the nanocylinders, the nanospheres behave as an effective dielectric for both polarisations because the motion of the electrons is confined in all directions.

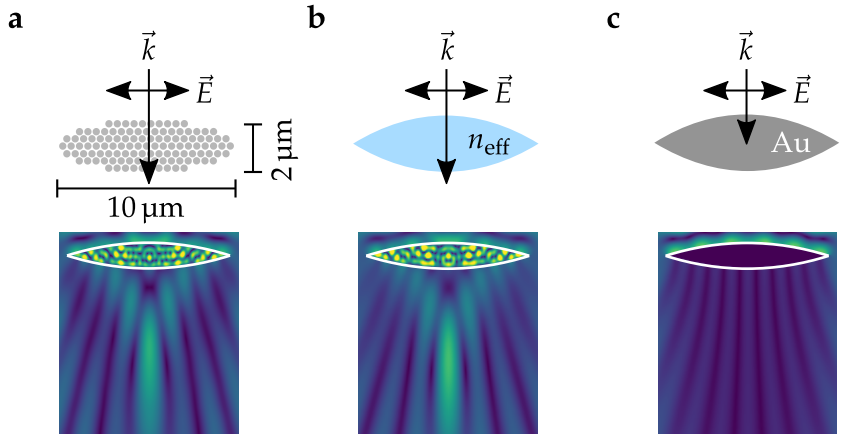

Figure 5.5: The effective dielectrics are transparent enough to act as micrometer-scale lenses. The transverse-electric polarised electric field, $\vec{E}$, propagates with in-plane wave vector $\vec{k}$. (a) A simple lens shape constructed from two intersecting circles is filled with a triangular lattice of gold cylinders of diameter $d = 38\,\text{nm}$ and surface-to-surface gap $G = 2\,\text{nm}$. In the simulation a plane wave is incident from the top and the lens focuses this wave in the lower region, as shown by the magnetic near-field for infrared radiation of wavelength $\lambda = 2\,\mu\text{m}$. (b) There is good agreement between the full geometry and the homogenised geometry, $n_{\text{eff}} = 3.2 + 0.5i$. (c) On the other hand, there is no transmission through solid gold of the same shape. The fringes of intensity are caused by diffraction around the lens. These finite-difference time-domain simulations were performed by Dr Xiaofei Xiao [113] using the full and effective geometries that I provided.

the electrons is restricted in all directions by the surfaces of the nanospheres. In this chapter we study in detail the response of nanocylinders to TE-polarised light, but the conclusions should also apply to arrays of nanospheres of similar sizes.

5.2.2.2 *Micrometer scale lenses built from effective dielectrics*

Figures 5.5a-c show finite-difference time-domain simulations of a plane wave with wavelength $\lambda = 2\,\mu\text{m}$ incident upon the primitive lens shapes composed of three different materials. At this wavelength, the skin depth of gold is around 13 nm. The lens thickness of 2 µm was chosen to be many orders of magnitude larger than this skin depth.

Figure 5.5a shows that the arrays of nanocylinders are indeed capable of focusing infrared radiation. Figure 5.5b shows that the nanocylinder array is well approximated by a homogeneous lens of effective index $n_{\text{eff}} = 3.2 + 0.5i$. Figure 5.5c shows that, as expected, there is no transmission through the solid gold lens. Instead, the fringes of intensity observed in Figure 5.5c are the result of diffraction around the lens. The transparency of the effective dielectric is remarkable considering that the lens is 82% gold by volume and that the diameter

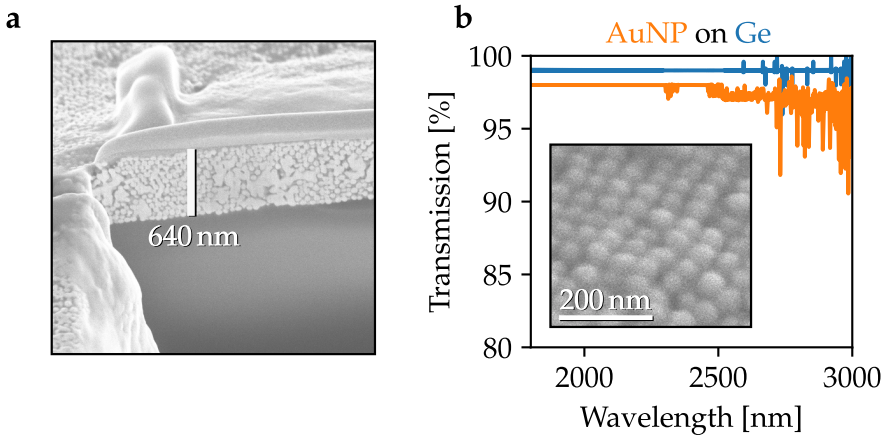

Figure 5.6: Experimental demonstration of the transparency of a metallic nanoparticle array to infrared radiation. (a) Microscopy image of a gold colloidal supercrystal composed of spheres with an approximate diameter of $d = 60\,\text{nm}$. (b) The transmission through the effective dielectric on a germanium substrate (orange line) was only a few percent lower than the baseline measurement of transmission through the germanium substrate (blue line), demonstrating the feasability of constructing the effective dielectrics in the laboratory. The effective dielectrics were synthesised, imaged, and the transmission was measured by our collaborators, Nicolas Pazos-Perez, Luca Guerrini, Miguel A Correa-Duarte, and Ramon A Alvarez-Puebla as described in the supplementary material of [113].

of each nanocylinder, $d = 38\,\text{nm}$, is not much larger than the skin depth.

5.2.3 *Experimental proof-of-concept*

To demonstrate the feasibility of manufacturing the effective dielectrics, our collaborators produced a highly ordered colloidal supercrystal [129] consisting of gold nanoparticles approximately 60 nm in diameter deposited on a germanium substrate (see supplementary note 7 of the original paper [113]).

The supercrystal was characterised with a UV-visible-NIR spectrophotometer and the transmission through the sample was measured to be over 90% through the 640 nm thick sample [113], as shown in Figure 5.6b. For comparison, the transmission through the same thickness of solid gold would be virtually zero as gold has an expected penetration length in the tens of nanometers at these wavelengths.

5.3 CALCULATING THE EFFECTIVE INDEX

Before studying the effective dielectrics in more detail, let us explain the method used to calculate the effective refractive indices, how it

differs from the band structure calculations of the previous chapters, and justify the decisions behind it.

In the previous chapters we solved for frequency as a function of wavevector. This was relatively straight forward since the permittivity and permeability of the materials studied in Chapters 2-4 could be treated as constant over the range of frequencies we studied, allowing us to solve directly for the frequency of the eigenmodes,

$$\omega = \omega(\epsilon, \mu, \vec{k}). \tag{5.1}$$

For this chapter, we wished to study metallic particles over a broad range of frequencies for which the metals were very dispersive,[2] resulting in a recursive relationship,

$$\omega = \omega(\epsilon(\omega), \mu(\omega), \vec{k}). \tag{5.2}$$

While Equation (5.2) could be solved iteratively, it is challenging as the permittivities of the metals change by orders of magnitude over the frequencies we studied. Instead, we opted to solve the inverse problem,

$$k_z = k_z(\omega, \epsilon(\omega), \mu(\omega), k_x, k_y), \tag{5.3}$$

where the wavevector is a direct function of frequency. For $k_x = k_y = 0$, as shown in Figure 5.7, it is simple to retrieve the effective index along the z-axis as $n_{\text{eff}} = k_z/k_0$.[3] In the following sections we will demonstrate how we formulated a solution to Equation (5.3).

5.3.1 *Forming the quadratic eigenvalue problem*

In order to solve for $k_z(\omega)$, we first discretised Maxwell's equations using a real-space scheme such as finite-differences or finite-elements. We decided to discretise using real-space methods because the metallic particles are high contrast in comparison to the background and are closely packed together, and Fourier space methods such as the PWEM converge poorly in these situations [83]. After discretisation the resulting wave matrix equation has a block tri-diagonal symmetry,

$$\begin{bmatrix} \ddots & & & & \\ \boldsymbol{a} & \boldsymbol{b} & \boldsymbol{c} & & \\ & \boldsymbol{a} & \boldsymbol{b} & \boldsymbol{c} & \\ & & \boldsymbol{a} & \boldsymbol{b} & \boldsymbol{c} \\ & & & & \ddots \end{bmatrix} \begin{bmatrix} \vdots \\ [\![U_{n-1}]\!] \\ [\![U_n]\!] \\ [\![U_{n+1}]\!] \\ \vdots \end{bmatrix} = \vec{0}, \tag{5.4}$$

2 The permittivities of the metals that we considered (gold, silver, aluminium, and titanium) were obtained from the Lorentz-Drude models fitted by Rakić *et al* [130].

3 Note that we are now assuming that the wave-vector is parallel to the z-axis, whereas in the previous chapters we assumed the propagation was within the x-y plane. In this chapter, the material may be inhomogeneous along all three dimensions. When calculating the effective indices of the two-dimensional cylinders, we take the y-axis as the inhomogeneous axis.

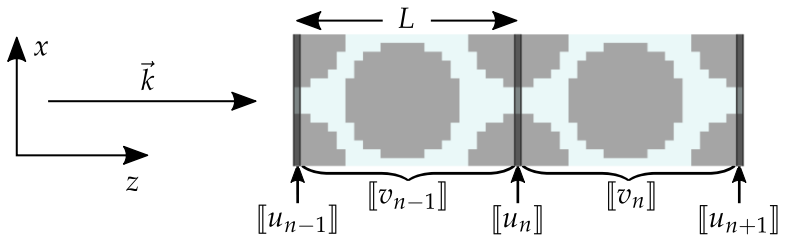

Figure 5.7: The grid points of the nth cell are separated into those that lie on a z-inversion symmetric plane, $[\![u_n]\!]$, and the remaining points that do not, $[\![v_n]\!]$. We are able to linearise the quadratic eigenvalue problem more efficiently by algebraically eliminating the degrees of freedom associated with $[\![v_n]\!]$.

where $[\![U_n]\!]$ is a vector containing the electric or magnetic field components at every grid point of the nth unit cell, and the $\boldsymbol{a}$, $\boldsymbol{b}$, $\boldsymbol{c}$ matrices describe how the fields in adjacent unit cells are coupled. Note that each cell is described by the same $\boldsymbol{a}$, $\boldsymbol{b}$, $\boldsymbol{c}$ matrices because of the periodicity of the array.

Next, we inserted a Bloch wave ansatz, $[\![U_{n+1}]\!] = e^{ik_z L_z} [\![U_n]\!]$. This forms a quadratic eigenvalue problem,

$$(\boldsymbol{a}e^{-ik_z L_z} + \boldsymbol{b} + \boldsymbol{c}e^{+ik_z L_z}) [\![U_n]\!] = \vec{0}, \tag{5.5}$$

where $e^{ik_z L_z}$ is our eigenvalue. The general equation $(\lambda^2 \boldsymbol{M} + \lambda \boldsymbol{C} + \boldsymbol{K})\vec{x} = \vec{0}$ can be linearised by inserting, for example, $\vec{y} = \lambda \vec{x}$ to find [131]

$$\begin{bmatrix} \boldsymbol{0} & \boldsymbol{I} \\ -\boldsymbol{K} & -\boldsymbol{C} \end{bmatrix} \begin{bmatrix} \vec{x} \\ \vec{y} \end{bmatrix} - \lambda \begin{bmatrix} \boldsymbol{I} & \boldsymbol{0} \\ \boldsymbol{0} & \boldsymbol{M} \end{bmatrix} \begin{bmatrix} \vec{x} \\ \vec{y} \end{bmatrix} = \begin{bmatrix} \vec{0} \\ \vec{0} \end{bmatrix}. \tag{5.6}$$

However, this comes at the cost of doubling the number of degrees of freedom: if there are N grid points per unit cell, then we must solve a $2N \times 2N$ matrix equation. In the next section we explain how we exploited the inversion symmetry of the arrays to reduce the degrees of freedom to just $M \times M$, where M is the number of grid points in a longitudinal cross-section of the unit cell.

5.3.2 *Efficient linearisation for inversion-symmetric lattices*

Let us take Equation 5.4 and separate each $[\![U_n]\!]$ array into two subarrays,

$$\begin{bmatrix} \ddots & & & & & & & \\ \boldsymbol{a}_u & \boldsymbol{b}_u & \boldsymbol{c}_u & & & & & \\ & \boldsymbol{a}_v & \boldsymbol{b}_v & \boldsymbol{c}_v & & & & \\ & & \boldsymbol{a}_u & \boldsymbol{b}_u & \boldsymbol{c}_u & & & \\ & & & \boldsymbol{a}_v & \boldsymbol{b}_v & \boldsymbol{c}_v & & \\ & & & & \boldsymbol{a}_u & \boldsymbol{b}_u & \boldsymbol{c}_u & \\ & & & & & \boldsymbol{a}_v & \boldsymbol{b}_v & \boldsymbol{c}_v \\ & & & & & & & \ddots \end{bmatrix} \begin{bmatrix} \vdots \\ [\![u_{n-1}]\!] \\ [\![v_{n-1}]\!] \\ [\![u_n]\!] \\ [\![v_n]\!] \\ [\![u_{n+1}]\!] \\ [\![v_{n+1}]\!] \\ \vdots \end{bmatrix} = \vec{0}. \tag{5.7}$$

where $[\![u_n]\!]$ is the field along a z-inversion symmetric cross-section of the nth unit cell, and $[\![v_n]\!]$ are the remaining grid points as shown in Figure 5.7. We may eliminate the degrees of freedom associated with the grid points outside of the inversion-symmetric plane, $[\![v_n]\!]$, using a process termed 'slice absorption' by Rumpf *et al* [80] (sometimes known as decimation in condensed matter theory). In doing so, we reduce the matrix equation to

$$\begin{bmatrix} \ddots & & & & \\ \boldsymbol{a}' & \boldsymbol{b}' & \boldsymbol{c}' & & \\ & \boldsymbol{a}' & \boldsymbol{b}' & \boldsymbol{c}' & \\ & & \boldsymbol{a}' & \boldsymbol{b}' & \boldsymbol{c}' \\ & & & & \ddots \end{bmatrix} \begin{bmatrix} \vdots \\ [\![u_{n-1}]\!] \\ [\![u_n]\!] \\ [\![u_{n+1}]\!] \\ \vdots \end{bmatrix} = \vec{0},$$

where

$$\boldsymbol{a}' = -\boldsymbol{a}_u \boldsymbol{b}_v{}^{-1} \boldsymbol{a}_v, \tag{5.8a}$$

$$\boldsymbol{b}' = \boldsymbol{b}_u - \boldsymbol{a}_u \boldsymbol{b}_v{}^{-1} \boldsymbol{c}_v - \boldsymbol{c}_u \boldsymbol{b}_v{}^{-1} \boldsymbol{a}_v, \tag{5.8b}$$

$$\boldsymbol{c}' = -\boldsymbol{c}_u \boldsymbol{b}_v{}^{-1} \boldsymbol{c}_v. \tag{5.8c}$$

Substituting in the Bloch wave ansatz, we find the reduced quadratic eigenvalue problem,

$$(\boldsymbol{a}' e^{-ik_z L_z} + \boldsymbol{b}' + \boldsymbol{c}' e^{+ik_z L_z}) [\![u_n]\!] = \vec{0}. \tag{5.9}$$

This reduced the dimensions of the matrices from $N \times N$ to $M \times M$, where N is the total number of grid points and M is the number of grid points in a longitudinal cross-section.

While the original $N \times N$ wave matrices $\boldsymbol{a}$, $\boldsymbol{b}$, and $\boldsymbol{c}$ of Equation 5.4 are sparse matrices, the reduced $M \times M$ wave matrices $\boldsymbol{a}'$, $\boldsymbol{b}'$, and $\boldsymbol{c}'$

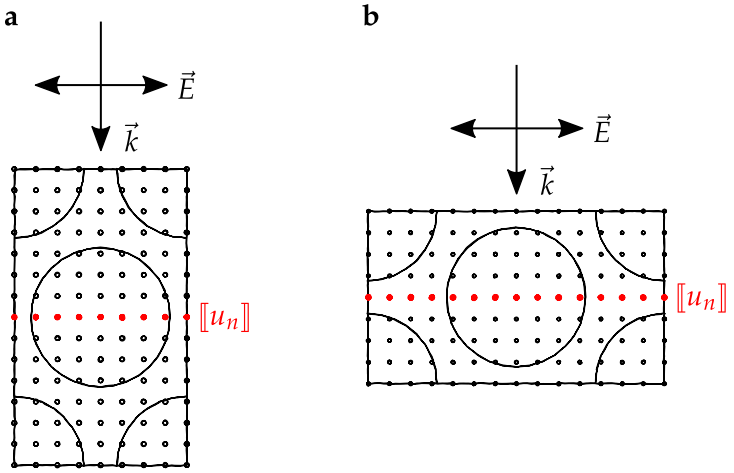

Figure 5.8: In general, the effective index varies with the orientation of the unit cell. However, if it is known by symmetry that the lattice is isotropic it is only necessary to measure the effective index for a single orientation. For the triangular lattice of circular cylinders shown above, it is more efficient to measure the effective index of (a) the vertically aligned cell than (b) the horizontally aligned cell, because the z-inversion cross-section (shown in red), is smaller in the vertically aligned cell than in the horizontally aligned cell. This results in fewer degrees of freedom, $[\![u_n]\!]$, in the reduced linearised Equation (5.12).

of Equation (5.12) are dense matrices. It is therefore important that we minimise the number of cross-sectional points, M. For isotropic materials, this can be achieved with a properly oriented unit cell as shown in Figure 5.8. More generally, discretising the equations onto a non-uniform mesh using the Finite Element Method (FEM) results in fewer cross-sectional points than discretising onto a uniform grid using the Finite-Difference Frequency-Domain (FDFD).[4]

In addition to the reducing the size of matrices, we were able to linearise Equation (5.9) without increasing the degrees of freedom by exploiting the mirror symmetry of our lattices. For each solution $U(x, y, z, \omega)$ there is a mirror symmetric solution, $\tilde{U}(x, y, z, \omega) = U(x, y, -z, \omega)$. The mirror equation may be written as

$$\begin{aligned} &\left(\boldsymbol{a}' e^{+ik_z L_z} + \boldsymbol{b}' + \boldsymbol{c}' e^{-ik_z L_z}\right) [\![\tilde{u}_n]\!] \\ &= \left(\boldsymbol{a}' e^{+ik_z L_z} + \boldsymbol{b}' + \boldsymbol{c}' e^{-ik_z L_z}\right) [\![u_n]\!] = 0, \end{aligned} \tag{5.10}$$

where we have used that $[\![\tilde{u}_n]\!] = [\![u_n]\!]$ because the elements of $[\![\tilde{u}_n]\!]$ and $[\![u_n]\!]$ lie in the same mirror symmetric plane. Summing Equations (5.9) and (5.10), we found

$$\left[\left(\boldsymbol{a}' + \boldsymbol{c}'\right) \cos(k_z L_z) + \boldsymbol{b}'\right] [\![u_n]\!] = \vec{0}, \tag{5.11}$$

which may be rearranged to the generalised linear eigenvalue problem,[5]

$$\boxed{-\left(\boldsymbol{a}' + \boldsymbol{c}'\right) [\![u_n]\!] = \Lambda \cdot \boldsymbol{b}' [\![u_n]\!],} \tag{5.12}$$

where $\Lambda = 1/\cos(k_z L_z)$. The effective refractive index may be determined from this linear eigenvalue problem as

$$\boxed{n_{\text{eff}} = \frac{k_z}{k_0} = \frac{\cos^{-1}(1/\Lambda)}{k_0 L_z}.} \tag{5.13}$$

When taking the inverse cosine there is a choice of branch for the real part and a choice of sign overall. As the system is lossy, the overall sign of n_{eff} was chosen such that the imaginary part is negative. We assume that the effective wavelength is larger than the unit cell, $\text{Re}\,[k_z]\, L_z \ll \pi$, and that the mode therefore lies in the first Brillouin zone, $|\text{Re}\,[k_z]| < \pi/L_z$.

It is worth emphasising that it was only possible to formulate Equation (5.12) after the $[\![v_n]\!]$ grid points outside of the mirror symmetric plane had been eliminated, such that $[\![\tilde{u}_n]\!] = [\![u_n]\!]$ for all of the remaining grid points. For example, Veres *et al* [133] used a similar

4 In this work, we implemented the solver for both finite-elements and finite-differences in 2D. In 3D, we only implemented the solver for finite-differences. The efficiency of our 3D simulations could be greatly improved with a 3D finite-element scheme.

5 It is important to take $\boldsymbol{b}'$ to the right-hand side as it is known that the $\boldsymbol{b}'$ matrices are invertible [132], but we found that the $\boldsymbol{a}'$ and $\boldsymbol{c}'$ matrices are generally not invertible.

process of algebraic elimination to arrive at an equation similar to Equation (5.9), but retained the unit cells around the entire perimeter of the unit cell and would therefore have been unable to proceed to an equivalent of Equation (5.12). For an approximately square cell, our approach retains approximately a quarter[6] of the number of degrees of freedom compared to the method of Veres *et al* [133], and therefore one-sixteenth of the memory to store the matrix equations.

5.3.3 *Assuming a weak magnetic response*

Although we solve only for the effective refractive index, n_{eff}, we can assume a negligible non-magnetic response, μ_{eff}. For example, the work of Chung *et al* [125] suggests that we may expect an effective permittivity of around $\mu_{\text{eff}} = 0.996$ for the simple lens design presented in Figure 5.5, which is our 'worst case' scenario of our largest particles and smallest wavelengths. We verified that the effective magnetic response of this lens is weak by repeating the homogenised calculations for using the same effective refractive index, n_{eff}, but different effective magnetic responses, μ_{guess} (which determines our choice of $\epsilon_{\text{guess}} = n_{\text{eff}}^2/\mu_{\text{guess}}$), as shown in the supplementary material of [113]. We found best agreement between the full geometry and the homogenised simulation for a negligible magnetic response.

It would be necessary to consider the magnetic response for larger particles or shorter wavelengths than considered here, such as those described by Chung *et al* [125]. However, note that we may still comment on the transparency of such systems, even if the effective permeability/permeability are unknown, as the transparency is determined from the imaginary part of the effective index, $\text{Im}[n_{\text{eff}}]$.

5.4 ACCURACY OF THE MIXING FORMULAE

In this section we compare the effective index of the nanocylinder arrays to two mixing formulae: the Maxwell Garnett (MG) formula and the Rayleigh formula. In general we find that the real part of the effective index is predicted well by these simple analytic formulae, but the imaginary part is typically underestimated by a few orders of magnitude. It is therefore important to consider the full calculations when estimating the losses of the effective dielectrics.

5.4.1 *Effect of lattice*

Figure 5.9 shows the effective index of square and triangular arrays of metallic nanocylinders compared to two mixing formula: the MG for-

6 Compared to Veres *et al* [133], we half the degrees of freedom twice: once by retaining only the cross-sectional grid points rather than all points on the perimeter, and again by exploiting inversion symmetry in the linearisation process.

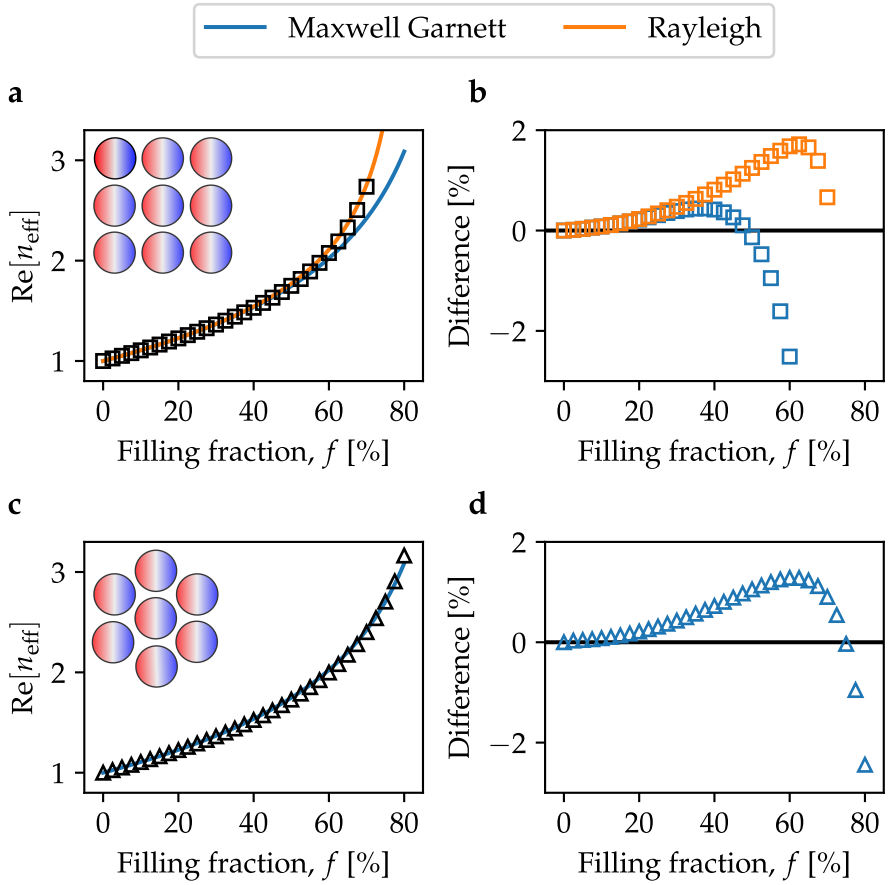

Figure 5.9: The Maxwell Garnett (blue) and Rayleigh (orange) mixing formulae are compared to the calculated effective indices, n_{eff}, for cylinders on square lattices and triangular lattices. This helps to reveal how the interparticle interactions depend on the arrangement of the nanocylinders. The lattice parameter is fixed at $L = 40\,\text{nm}$ and the filling fraction is varied up to a minimum surface-to-surface gap of $G = 2\,\text{nm}$. The cylinders are gold and the wavelength is $2\,\mu\text{m}$. (a-b) For the cylinders on the square lattice, the Maxwell Garnett formula significantly underestimates the effective index at high filling fractions where interparticle interactions are stronger. The Rayleigh formula, which takes into account the interparticle interactions, performs much better. (c-d) For the cylinders on the triangular lattice the interparticle interactions are less significant as dipoles are staggered, and the Maxwell Garnett is more accurate than it was for the square lattice.

mula and the Rayleigh formula. The MG formula [134–136] is derived by approximating each particle as a non-interacting dipole with the polarisability of the dipole given by the electrostatic polarisability of the original particle. For cylindrical particles in air or vacuum, the MG formula reads [137]

$$\epsilon_{\mathrm{MG}}^{\mathrm{cyl}} = \frac{\epsilon + \epsilon_0 + f(\epsilon - \epsilon_0)}{\epsilon + \epsilon_0 - f(\epsilon - \epsilon_0)}, \tag{5.14}$$

where ϵ and f are the permittivity and filling fraction of the nanocylinders, respectively. Although the MG formula is dependent on the filling fraction, it is independent of our choice of lattice as the interactions between dipoles are neglected. Figures 5.9a-b show that the MG formula underestimates the effective index for $f \gtrsim 50\%$. This is because the dipole-dipole interactions that MG formula neglects are attractive and act to increase the effective polarisability of the array.

The Rayleigh formula is an extension of the Maxwell-Garnett formula that takes into account interactions between dipoles, and is therefore dependent on the arrangement of the particles. For a square lattice of cylinders in air/vacuum, the effective index predicted by the Rayleigh formula is [137]

$$\epsilon_{\mathrm{Rayleigh}} = 1 + \frac{2f}{\frac{\epsilon+\epsilon_0}{\epsilon-\epsilon_0} - f - \frac{\epsilon-\epsilon_0}{\epsilon+\epsilon_0}(0.3058f^4 + 0.0134f^8)}, \tag{5.15}$$

where the coefficients of f^4 and f^8 are determined by the integration of Greens functions [138]. By accounting for these interactions, the Rayleigh formula provides a significantly more accurate estimation of the effective index for the square lattice of metallic nanocylinders.

Figures 5.9c-d show the effective index of triangular arrays of metallic nanocylinders compared to the MG formula. In principle, a similar formula to Equation (5.15) could be derived for cylinders on a triangular lattice, but this does not appear necessary for $f \lesssim 75\%$ as the MG formula is more accurate for the triangular lattice than it was for the square lattice. This is because the alignment of the dipoles is staggered for the triangular lattice, and the importance of the dipole-dipole interactions is reduced. However, it is clear from Figure 5.9d that the MG formula continues to underestimate the effective index at the highest filling fractions where the dipole-dipole interactions are strongest.

5.4.2 *Choice of metal*

Figures 5.10a-b show the real and imaginary parts of the effective index for arrays of nanocylinders built from different metals. We see that all four effective dielectrics appear to be converging to the same effective index as the wavelength increases, despite the differences in the underlying metal. There are two important factors that play into this. Firstly, at long wavelengths the permittivity of the Drude metals

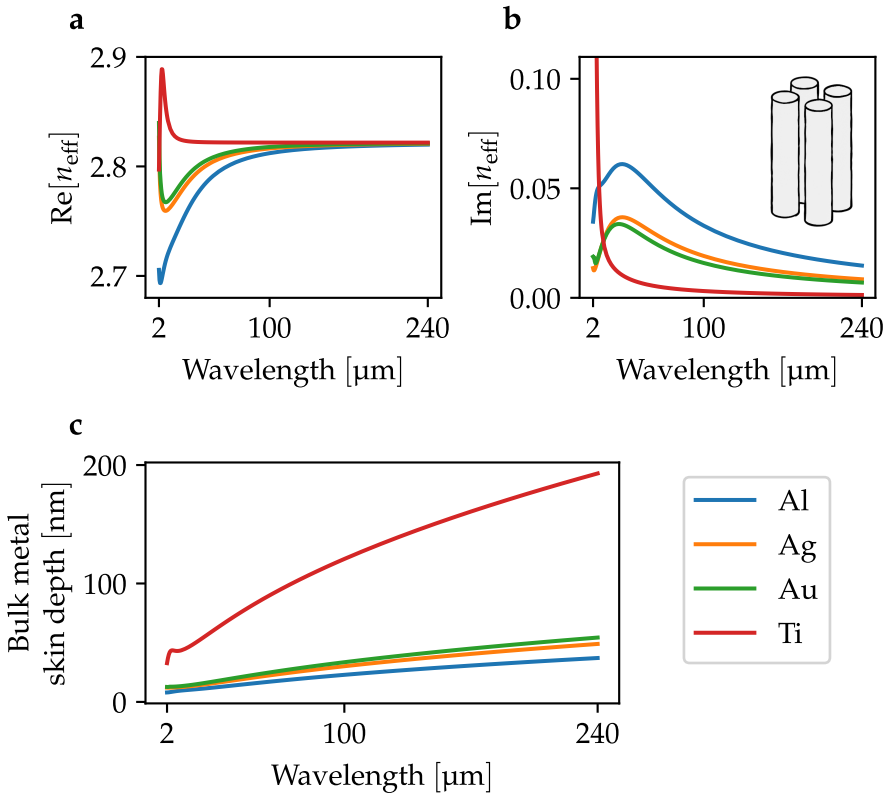

Figure 5.10: (a-b) The real and imaginary parts of the effective index, n_{eff}, of square arrays of circular nanocylinders (diameter $d = 38\,\text{nm}$ and surface-to-surface separation $G = 2\,\text{nm}$, resulting in a metallic filling fraction of $f \approx 71\%$) composed of aluminium, gold, silver, and titanium. (c) The increase in skin depth of each bulk metal with wavelength is correlated to the decrease in losses seen in panel b.

is very large [139], $|\epsilon| \gg 1$, for which the MG mixing formula is (to first order in ϵ) both real and independent of ϵ,

$$\epsilon_{\mathrm{MG}}^{\mathrm{cyl}} \approx \frac{1+f}{1-f} - \frac{4f}{(1-f)^2}\frac{1}{\epsilon} + \mathcal{O}\left(\frac{1}{\epsilon^2}\right). \tag{5.16}$$

Secondly, as the wavelength increases, the skin depth of the metal [78], $\delta_s = \lambda/4\pi\mathrm{Im}[n]$, also increases. For Drude metals, the skin depth tends to increase with wavelength as $\delta \sim \sqrt{\lambda}$ throughout the infrared. We observe that the metals with the larger skin depths, shown in Figure 5.10c, produce arrays that are more transparent and less dispersive, and their refractive indices converge faster to metal-independent limit.

An exception to this trend is titanium around the $\lambda = 2\,\mu\mathrm{m}$ to $10\,\mu\mathrm{m}$ range where the titanium arrays are very lossy despite titanium having the largest skin depth of the metals we considered. This is because ϵ_{Ti} is not very large or negative for these wavelengths [130], and therefore the complex $1/\epsilon$ term of Equation (5.16) contributes a significant loss to the array. In other words, titanium is a poor metal at these wavelengths.

5.4.3 *Effect of particle size and skin depth*

The effect of skin depth can also be seen when changing the size of the particles. Figures 5.11a-b show the effective index of two arrays, but the particle and gap sizes in Figure 5.11a are twice as large as those in Figure 5.11b. The MG mixing formula (shown as dashed lines) is equal for both arrays as the filling fractions are equal.

As before, the calculated effective index is larger than the MG mixing formula because the calculation accounts for the interparticle interactions. However, it is clear that the array of smaller particles is better described by the MG mixing formula. This is because for any given skin depth the electric field is more uniform inside the smaller particles; this is closer to the assumption of the MG mixing formula that the particles are well described by their *electrostatic* polarisability.

This behaviour is explored further in Figure 5.12, which displays the effective index of arrays of nanocylinders over a wide range of particle sizes. The filling fraction of each curve is constant, and the wavelength ($\lambda = 200\,\mathrm{nm}$), metal (aluminium), and therefore skin depth (8 nm) are fixed.

As expected, the MG mixing formula is a good estimate of the effective index when the filling fraction is low and the particles are small compared to the skin depth, $d \ll \delta_s$. As the size of the particles is increased compared to the skin depth, the electric field becomes less uniform within the particles and the quasi-electrostatic approximation breaks down. At first, the losses rise as the electric field is retarded. However, when the particles become much larger than the skin depth,

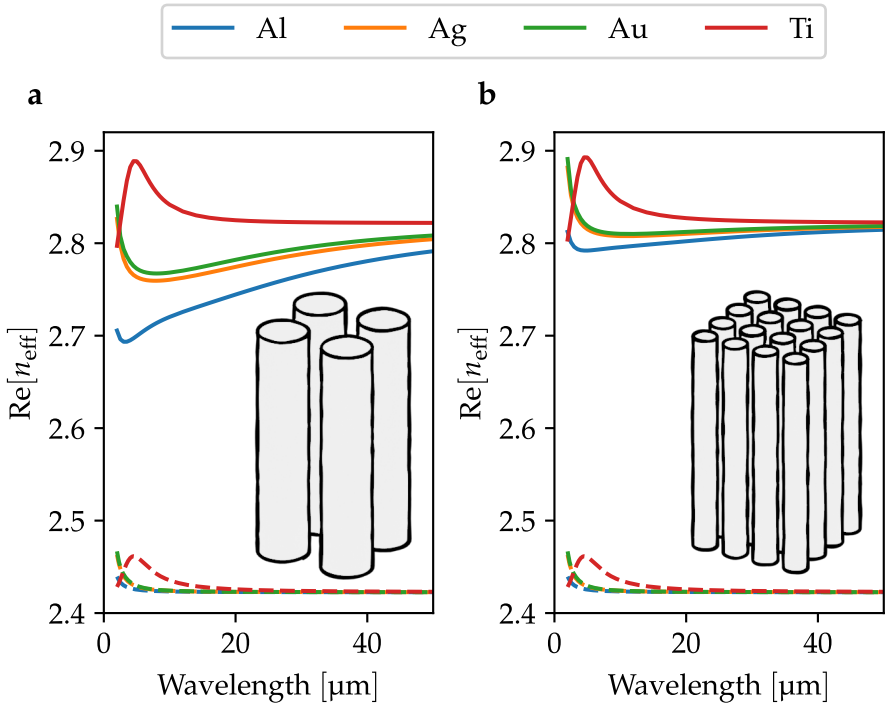

Figure 5.11: Comparison of the real parts of the effective index, Re$[n_{\text{eff}}]$, from the full calculations (solid lines) and the Maxwell Garnett mixing formula (dashed lines) for square lattices of cylinders of different diameters but equal filling fractions of $f \approx 71\%$. In both cases the calculated effective index is higher than the Maxwell Garnett effective index because the particle-particle interactions included in the full calculation raise the effective index. (a) For the lattice of larger cylinders (diameter $d = 38\,\text{nm}$, lattice parameter $L = 40\,\text{nm}$) there is a significant drop in the calculated effective index at smaller wavelengths. This is because at these wavelengths the particles are large compared to the skin depths of the metals and the quasi-electrostatic dipole approximation breaks down. (b) For the lattice of smaller cylinders with an equal filling fraction ($d = 19\,\text{nm}$, $L = 20\,\text{nm}$) the quasi-electrostatic approximation holds better and the effective index is qualitatively more similar to the Maxwell Garnett mixing formula.

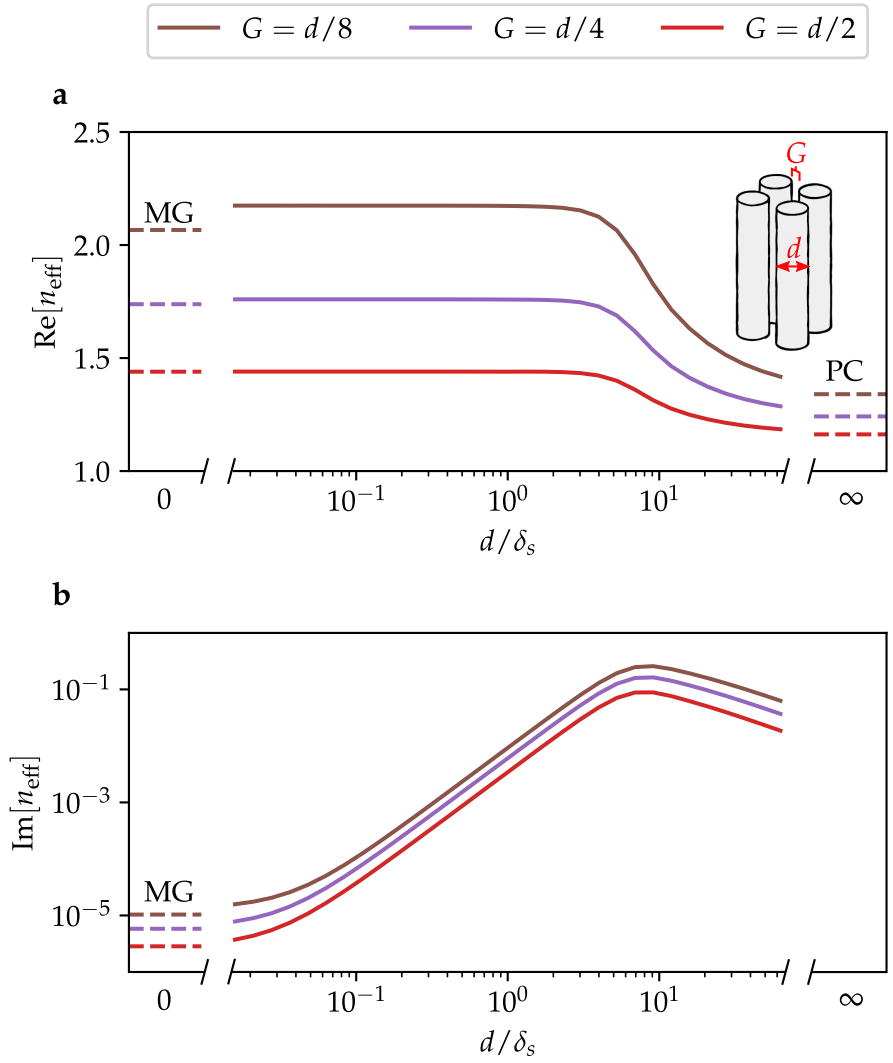

Figure 5.12: The ratio of the particle diameter, d, to the skin depth of the metal, δ_s, determines whether the particles behave as quasi-electrostatic dipoles or perfect conductors. Here we show the real and imaginary parts of effective index, n_{eff}, of square lattices of aluminium cylinders of varying diameters, keeping the filling fraction of each line constant ($f(G = d/8) \approx 62\%$, $f(G = d/4) \approx 50\%$, and $f(G = d/2) \approx 35\%$ for the brown, purple, and red lines, respectively). At the fixed wavelength of $\lambda = 200\,\text{nm}$ the skin depth of the aluminium is $\delta_s \approx 8\,\text{nm}$. We compare the arrays of small particles, $d/\delta_s \ll 1$, to the Maxwell Garnett (MG) mixing formula. The arrays of large particles, $d/\delta_s \gg 1$, are compared to the effective index calculation for an array where the metal is replaced by a perfect conductor (PC). (a) The real part of the effective index is remarkably constant for particles smaller than the skin depth. The particles much smaller than the skin depth are well described by the MG formula for smaller filling fractions where the particle-particle interactions are less significant. (b) The losses of the arrays peak when the particle diameters are around ten times greater than the skin depth, but fall exponentially with smaller and larger diameters. The MG mixing formula provides a minimum bound of the losses for particles much smaller than the skin depth.

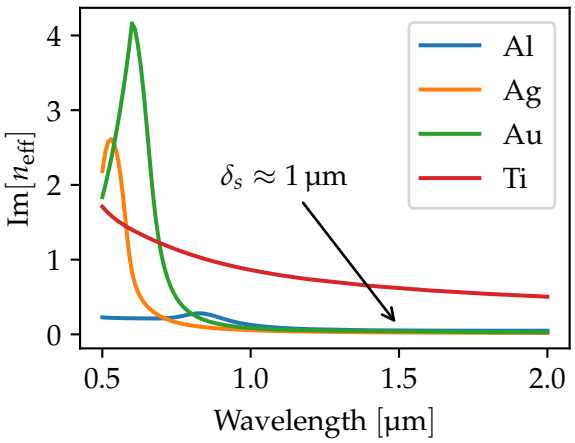

Figure 5.13: Losses in the telecom and visible wavelengths. Losses are given by the imaginary part of the effective index, $\mathrm{Im}[n_{\mathrm{eff}}]$, for aluminium, silver, gold, and titanium cylinders on a triangular lattice. The particles have diameter $d = 38\,\mathrm{nm}$ and surface-to-surface gap $G = 2\,\mathrm{nm}$. At $\lambda = 1.5\,\mu\mathrm{m}$, the effective penetration length is on the order of a micron.

$d \gg \delta_s$, the electric field penetrates a decreasing fractional volume of the metal particles and the losses begin to fall again. In the limit of $d/\delta_s \to \infty$, the effective index is lossless because the fraction of the electric field that penetrates the metals vanishes and the particles behave as perfect conductors.[7]

As a quick aside, we are now in a position to consider the losses in the telecom wavelengths, as shown in Figure 5.13. As discussed in Section 5.4.2, the losses of titanium are high as it is a poor metal at these wavelengths. However, for silver, gold, and aluminium, the imaginary part of the effective index remains relatively low into the telecoms wavelengths. At $\lambda_0 = 1.5\,\mu\mathrm{m}$ the effective penetration length of these arrays, $\delta_{\mathrm{eff}} = \lambda_0/4\pi\mathrm{Im}[n_{\mathrm{eff}}]$, is on the order of a micron. Although this is shorter than at infrared wavelength where the skin depth can be on the order of centimeters, it is still sufficiently transparent for sub-micrometer devices. As we approach the visible wavelengths, the quasi-static dipole approximation is broken by the plasmonic resonances of the metallic particles and the losses are very high.

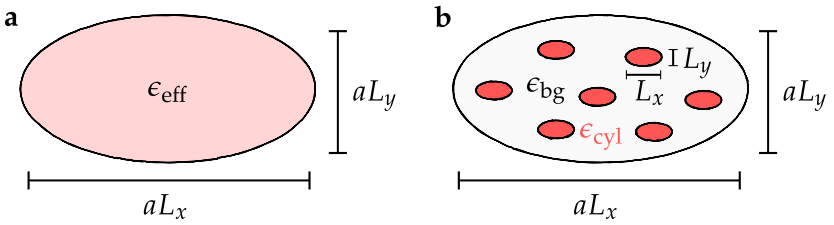

Figure 5.14: Derivation of the Maxwell Garnett mixing formula for elliptic inclusions of width L_x and height L_y. (a) Consider an elliptic region of space of width aL_x and height aL_y. We seek an effective index, ϵ_{eff}, such that the electrostatic polarisability of this region is equal to the average electrostatic polarisability of (b) a collection of N_{inc} inclusions of permittivity ϵ_{cyl} in a background permittivity ϵ_{bg}.

5.4.4 *Effect of aspect ratio*

In this section we study the effective index of arrays of elliptic cylinders. The MG mixing formula for elliptic inclusions may be obtained from [135, 140, 141]

$$\alpha_{\text{eff}} = f\alpha_{\text{inc}}, \tag{5.17}$$

where α_{eff} is the electrostatic polarisability of a larger homogeneous elliptic cylinder with permittivity ϵ_{eff} and dimensions aL_x by aL_y as shown in Figure 5.14a, and $f\alpha_{\text{inc}}$ is the average electrostatic polarisability of N_{inc} elliptic cylindrical inclusions with permittivity ϵ_{cyl} and dimensions $L_x \times L_y$. The inclusions occupy a fraction $f = N_{\text{inc}}/a^2$ of the considered region as shown in Figure 5.14b.[8]

In Appendix E, we derive the electrostatic polarisability of an elliptic cylinder for an electric field applied parallel to the x-axis as

$$\alpha_{\text{qs}}^{\text{ellipse}} = \frac{(\epsilon - \epsilon_0)(1+\Lambda)}{\epsilon_r + \Lambda} V, \tag{5.18}$$

where $\epsilon_r = \epsilon/\epsilon_{\text{bg}}$ is the permittivity of the cylinders relative to the background, V is the volume of the cylinder, and $\Lambda = L_x/L_y$ is the aspect ratio of the cylinder.

Substituting Equation (5.18) into both sides of Equation (5.17),

$$\frac{(\epsilon_{\text{eff}} - \epsilon_0)(1+\Lambda)}{\epsilon_{\text{eff}} + \Lambda} = f\frac{(\epsilon - \epsilon_0)(1+\Lambda)}{\epsilon_r + \Lambda}. \tag{5.19}$$

7 Note that the Perfect Conductor (PC) limit was modelled using the same numerical methods as the regular metallic arrays but with the boundary condition $\hat{n} \cdot H_z = 0$ at the surfaces of the particles. The PC limit shown in Figure 5.12 therefore accounts for the full interactions between the particles, whereas the MG limit does not.

8 We have chosen our larger homogeneous region to have the same shape as the smaller elliptic cylinders. Choosing a different homogeneous shape can lead to a different equations, but the result is equivalent to first order in the filling fraction, f [135].

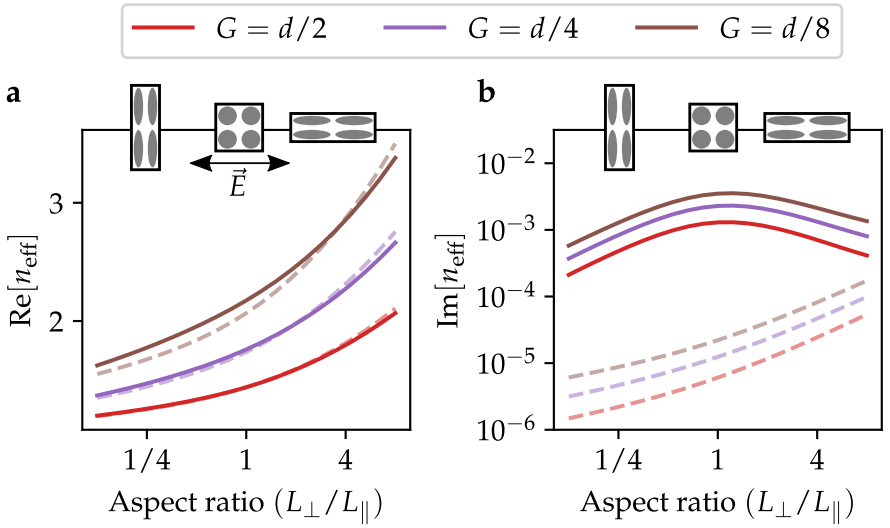

Figure 5.15: Comparison of the real and imaginary parts of the calculated effective index (solid lines) and the Maxwell Garnett mixing formula (dashed lines) for square lattices of gold nanocylinders with varying aspect ratios, $L_\perp/L_\parallel$ where $L_\perp$ and $L_\parallel$ are the lengths of the cylinders perpendicular and parallel to the incident electric field, $\vec{E}$, respectively. The undistorted diameter of the cylinders was $d = 30\,\text{nm}$ and the incident wavelength was $\lambda = 200\,\mu\text{m}$. During the deformation, the volume and surface-to-surface separation of each cylinder was kept constant.

and letting $\epsilon_r = \epsilon/\epsilon_0$ for an ellipse in vacuum or air, we find the MG mixing formula for elliptic inclusions,

$$\epsilon_{\text{eff}}/\epsilon_0 = \frac{\epsilon_r + \Lambda + \Lambda f(\epsilon_r - 1)}{\epsilon_r + \Lambda - f(\epsilon_r - 1)}. \tag{5.20}$$

This could also be obtained by considering the depolarisation factor of a 3D ellipsoid when one axis is much larger than the other two [140].

Figure 5.15 shows the effective index of arrays of elliptical nanocylinders. By controlling the aspect ratio of the nanocylinders, we are able to tune the anisotropic response of the effective dielectric. Our numerical results (solid lines) are compared to the MG mixing formula for elliptical cylinders (dashes). The numerical results demonstrate that we can produce effective dielectrics whose effective index varies by more than 50% with rotation of the lattice. In Figure 5.15a, there was generally good agreement between the numerical results and the MG mixing formula for moderate aspect ratios.

At the more extreme aspect ratios, $L_\parallel/L_\perp \ll 1$ and $L_\parallel/L_\perp \gg 1$, the MG mixing formula over- and underestimated the real part of the effective index, respectively. This is because the interactions between horizontally adjacent particles are enhanced for small aspect ratios, whereas for large aspect ratios it is the interactions between vertically adjacent particles that are enhanced. Since the incident field is applied

horizontally, each particle acts as a horizontally aligned dipole. The effective polarisability of the array was therefore increased by the strengthened horizontal interparticle interactions at small aspect ratios, and decreased by the strengthened vertical interparticle interactions at high aspect ratios.

It is important to note that these interparticle interactions act to reduce the tunability of the system compared to the MG mixing formula. It was for this reason that we chose to vary the aspect ratios of the rectangular arrays while keeping the volume and surface-to-surface gap of each cylinder constant, as shown in the insets of Figure 5.15. If we had not kept the gaps between the cylinders constant, then at high aspect ratios there would have been very small gaps and very strong interactions between the particles, and the tunability would be more limited.

Figure 5.15b shows that the true losses of the distorted array are higher than those predicted by the MG mixing formula, for the same reasons as discussed in Section 5.4.3, but the losses of the array are still much lower than for bulk metal. Interestingly, the losses are lower for the distorted arrays. This is because the retardation inside the distorted particles is reduced because the particles are thinner and the electric field is more uniform inside.

5.5 APPLICATION: A GRADIENT-INDEX LENS FOR ENHANCED SENSING

In this section we propose a Gradient-Index (GRIN) lens (a lens where light is guided by a continuously varied local refractive index [142]) built from our effective dielectric. This exploits the simultaneous transparency, tunability, and high metallic filling fraction of the effective dielectrics. The proposed GRIN lens produces intense 'doubly-enhanced' hotspots by simultaneously guiding light on the microscale and squeezing the electric field on the nanoscale.

5.5.1 *Designing the lens*

In order to produce a gradient index, we placed the nanocylinders on a regular array and varied the diameters as a function of cylinder position. Figure 5.16 shows the range of possible refractive indices for gold nanocylinders on a triangular lattice of lattice parameter 50 nm for an incident wavelength of 2 µm. The diameters of the cylinders were only increased until a minimum surface-to-surface gap of 2 nm, resulting in a maximum effective index of approximately 3.8. For the real part of the effective index in Figure 5.16a there is good agreement between the numerics (solid line) and the MG mixing formula (dashes). On the other hand, Figure 5.16b shows that there is a noticeable increase in the imaginary part of the effective index compared to the

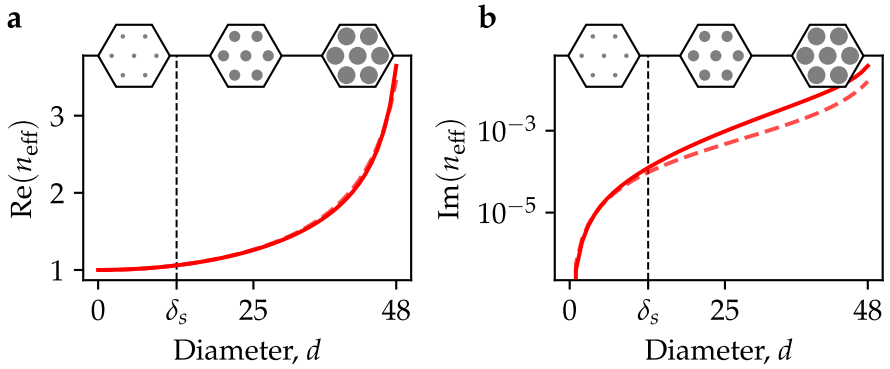

Figure 5.16: Comparison of the real and imaginary parts of the calculated effective index (solid lines) and the Maxwell Garnett mixing formula (dashed lines) for triangular lattices of gold nanocylinders. The effective index is tuned by controlling the cylinder diameter, d. The incident wavelength was $\lambda = 2\,\text{nm}$, the lattice parameter was 50 nm, and the diameters were varied from $0\,\text{nm} \leq d \leq 48\,\text{nm}$. (a) There is good agreement between the calculated effective index and the Maxwell Garnett mixing formula for the real part of the effective index. (b) The losses of the calculated effective index are noticeably higher than that predicted by the Maxwell Garnett mixing formula for cylinders larger than the skin depth of the gold at this wavelength, δ_s.

MG mixing formula for diameters larger than the skin depth. Despite this, the losses remain relatively low with a maximum $\text{Im}(n_{\text{eff}})$ of approximately 10^{-2}.

In order to maximise the squeezing of the electric field, the focal point of the GRIN lens must coincide with the region of closest packing. We therefore chose to create a so-called 'concentrator' lens, $n_{\text{conc}}(r) = R/r$, which focuses an incoming plane wave to $r = 0$ [142]. This was achieved by tuning the diameters of gold nanocylinders on a triangular array as shown schematically in Figure 5.17a. The ideal (dashed line) and achieved (solid line) effective index profiles are shown in Figure 5.17b.

The cylinder diameters were varied slowly enough that the local effective could be estimated from Figure 5.16a. In mapping from effective index to cylinder diameter, it was necessary to truncate the effective index at around $n_{\text{eff}} \approx 3.5$, as shown in Figure 5.17b. This reduced the quality of the focus, but was sufficient for our purposes.

5.5.2 *Performance of the lens*

The magnetic near-fields in Figure 5.18a show that the performance of the concentrator lens closely matches the targeted behaviour. Although the lens was tuned at a wavelength of 2 nm, the dispersion of the effective dielectric is low for all $\lambda \gtrsim 2\,\mu\text{m}$ and we see that the lens performs

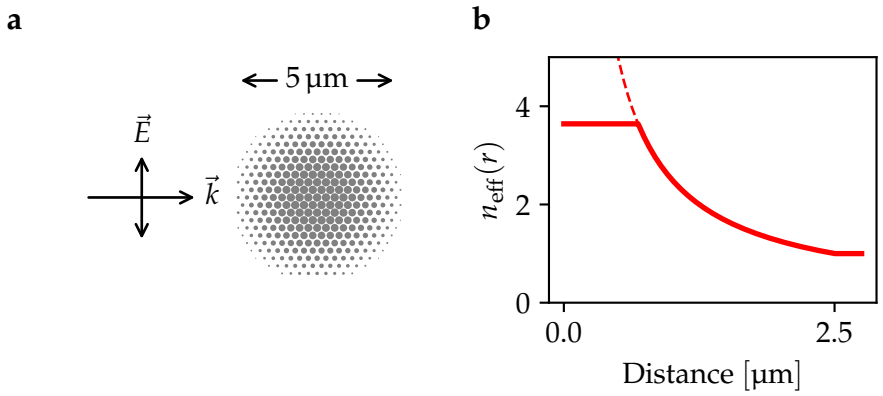

Figure 5.17: Designing a gradient-index lens. (a) Schematic of the 'concentrator' gradient-index lens composed of a triangular lattice of gold nanocylinders with lattice parameter $L = 50\,\text{nm}$ arranged in a circle of diameter $D = 5\,\mu\text{m}$. The transverse-electric polarised electric field, $\vec{E}$, is incident from the side with wave vector $\vec{k}$. (b) The ideal (dashed lines) and achieved (solid lines) effective index profile, $\vec{n}_{\text{eff}}(\vec{r})$, of the concetrator lens.

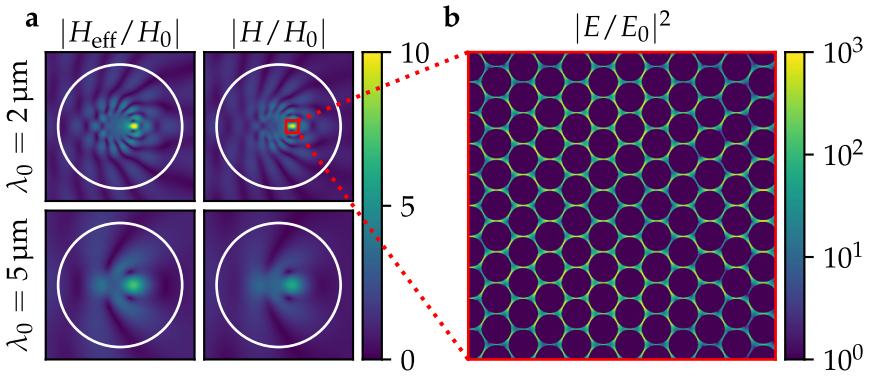

Figure 5.18: Near-fields of the 'concentrator' lens. (a) The amplitudes of observed magnetic near-fields relative to the incident field, calculated using the effective geometry ($|H_{\text{eff}}/H_0|$, first column) and the full geometry ($|H/H_0|$, second column) both confirm that plane waves of free space wavelengths $\lambda_0 = 2\,\mu\text{m}$ and $5\,\mu\text{m}$ are both focused towards the origin of the lens. (b) The combined focusing and squeezing of the electric field, E, produces 'doubly-enhanced' hotspots within the focal point of the lens. These finite element calculations were performed by Dr Xiaofei Xiao [113] using the full and effective geometries that I designed.

well at larger wavelengths, such as $\lambda = 5\,\mu m$. Although the effective index of the lens is relatively constant with wavelength, increasing the wavelength does result in a reduced focus as the diffraction limit is reached.

Figure 5.18b shows the electric near field near the focal point of the concentrator lens. The squeezing of a 2 µm wavelength into 2 nm gaps, combined with the focusing effects of the lens, produced strong hotspots of intensity $|E/E_0|^2 > 10^3$. We believe that these hotspots could be used to enhance non-linear processes, such as infrared spectroscopy, over a much broader range of wavelengths and with lower losses than could be achieved with resonance-based enhancements.

5.6 REMARKS ON CHAPTER 5

In this chapter we studied closely packed metallic particles in a very different context to the topological void-channel networks of Chapter 4. Here, we showed that despite being composed of highly dispersive and lossy metals, the closely packed metallic particle arrays behaved as effective dielectrics that were low-loss and virtually dispersion-free because the metallic particles were small compared to the wavelength and skin depth of the metals.

We introduced a method to calculate the effective index of the arrays inspired by the Slice Absorption Method [132]. This involved solving for the complex wavevector as a function of frequency, $n_{\text{eff}} = k_z(\omega)/k_0$, in order to account for the dispersive nature of the metals. The eigenvalue equation for $k_z(\omega)$ is a quadratic matrix equation, but we exploited the mirror symmetry of our lattices to linearise the quadratic eigenvalue equation without increasing the degrees of freedom. The matrices are $M \times M$ dense matrices, where M is the number of points in a cross-section of the unit cell perpendicular to z. The method is therefore more suited to geometries with relatively short lattice periods in the transverse directions.

We found good agreement between finite-difference time-domain simulations of the full geometries and of homogenised geometries where the metallic particle arrays are replaced with our effective index. We also compared our effective indices to the Maxwell-Garnett mixing formulae [135, 136], and we derived the Maxwell-Garnett mixing formula for elliptical cylinders. There was, as expected, good agreement at low filling fractions. At higher filling fractions, the $\text{Re}[n_{\text{eff}}]$ of the Maxwell Garnett mixing formulae were still surprisingly accurate and offers a fast, simple estimate of the real part of the effective index. However, the Maxwell Garnett formulae do not offer a good estimate of $\text{Im}[n_{\text{eff}}]$ and the full numerics remain important when quantifying the losses via the imaginary part of the effective index.

Finally, we proposed a novel gradient-index lens that exploited the simultaneous transparency and high metallic filling fraction of

the effective dielectrics to create intense 'doubly-enhanced' hotspots where light was focused on the microscale and the electric field was 'squeezed' between the metallic particles on the nanoscale. In the future, we could recreate more designs that are normally built from traditional dielectrics, such as single layer or gradient-index anti-reflection coatings for terahertz radiation [62], flat or gradient-index lenses [142, 143], or dielectric tips for terahertz probes [144].

6 CONCLUSION

While topological phases were first discovered in electronic materials, there is great interest in reproducing such topological phases in photonics. In this thesis, we focused on photonic analogues of two classes of electronic topological phases whose symmetries are more particular to electronic systems: the quantum spin-Hall effect (protected by fermionic time-reversal symmetry) and square-root topological semimetals (protected by chiral symmetry).

In Chapter 1, we introduced topological phases of matter in electronic systems, such as the quantum Hall effect, the quantum spin-Hall effect, the Su-Schrieffer-Heeger model, and a topological semimetal built from cross-linked Su-Schrieffer-Heeger models. Although we introduced the topological indices of these phases such as Berry phases and Chern numbers, the discussion was focused on what it means for two materials to belong to different topological phases rather than how to identify the topological phase of a particular Hamiltonian.

In Chapter 2, we introduced the numerical methods that we used to identify topological photonic phases. In particular, we reviewed the plane-wave expansion method to discretise Maxwell's equations in Fourier space, and calculated the Berry phases, Berry curvature, and Chern numbers of various photonic crystals with worked examples. We released the software for these calculations as `Peacock.jl`, an open-source package for the `Julia` programming language which has been peer reviewed in the Journal of Open Source Software [81].

In Chapter 3, we introduced a new topological index for $C_2\mathcal{T}$ symmetric crystals that emulate the quantum-spin Hall effect using the angular momentum of light to mimic the spin of electrons, such as the photonic crystal proposed by Wu & Hu [1]. We identified the new topological index by reformulating the energy eigenproblem as a Berry curvature eigenproblem. We found that the bands of Berry curvature, which we called the Berry bands, separated into pseudo-spinful and pseudo-spinless subspaces that were well defined across the Brillouin zone for $C_2\mathcal{T}$-symmetric crystals with an odd number of valence bands. The Chern number of the pseudo-spinless subspace is always zero, $C_\varnothing = 0$, but the pseudo-spinful subspaces carried non-zero Chern numbers, $C_\pm$, for the expanded-ring unit cell of Wu & Hu. We identified a $\mathbb{Z}_2$ topological index $\nu = \mathrm{mod}_2(C_\pm)$, which can also be expressed in terms of the C_2 eigenvalues of the bands. By considering the origin-independence of our topological index, we explained how our topological index is distinct from, but compatible with, the interpretation of the crystal of Wu & Hu as a special kind of

trivial phase known as an obstructed atomic limit. Our $C_2\mathcal{T}$-protected $\mathbb{Z}_2$ topological index allows for the prediction of symmetry-protected helical edge states at slowly graded interface regions between the trivial and non-trivial phases, and we therefore concluded that the crystal is indeed a photonic analogue of the quantum spin-Hall effect in the bulk but with weakly broken pseudo-fermionic time-reversal symmetry at the interfaces. This work has been published in Physical Review Research [92].

In Chapter 4, we studied the band topology of light that propagates through the networks of voids and narrow connecting channels that are formed between between closely spaced perfectly conducting particles. Vanel *et al* [104] showed that there is an asymptotically exact mapping between the void-channel networks and mass-spring networks. Using this mapping, we noted that the void-channel networks have vanishing long range interactions as the channels are made increasingly narrow, and that certain void-channel networks therefore have a chiral symmetric limit (up to a shift of constant frequency). We were able to create a photonic analogue of the 1D Su-Schrieffer-Heeger model with a chain of equally sized voids connected by channels of alternating widths, and a photonic analogue of a square-root topological semimetal with the voids positioned on a honeycomb-kagome lattice and narrow channels connecting the nearest-neighbour voids. In the process, we found that we were able to preserve the chiral symmetry at the edges of the system by "capping" the edges of the void-channel networks with large voids. For edge states to occur at frequencies on the order of a terahertz, we estimated that the metallic particles should be millimeter scale and the voids should be micrometer scale. This material is currently in preparation for a journal article.

In Chapter 5, we continued to study arrays of closely spaced metallic particles, but we considered smaller particles that were just tens of nanometers in diameter. In this regime, the particles cannot be treated as perfectly conducting scatterers because the electric field penetrates a significant distance into the particles. We formulated a quadratic eigenvalue problem for the effective index of the arrays, and exploited the mirror symmetry of the arrays to efficiently linearise the eigenproblem. For long wavelengths (near-infrared and longer), we found that the metallic nanoparticle arrays formed effective dielectrics that were low-loss and virtually dispersion-free. There was good agreement between scattering simulations of the full geometries and of homogenised geometries where the metallic particles were replaced with the calculated effective index. The effective dielectrics can be used in place of regular dielectrics, but we also identified an application that is unique to the effective dielectrics: we designed a gradient-index lens that created intense 'doubly-enhanced' hotspots by simultaneously focusing light on the microscale and 'squeezing' the electric field on the nanoscale. This exploited the simultaneous trans-

parency, high metallic filling fraction, and tunability of the effective dielectrics. This work has been published in Nature Communications [113].

In future work, we could study the topology of the Berry bands for a wider variety of systems. For example, we could investigate the Berry bands of other symmetry-protected phases such as mirror-Chern insulators [145], or of the direct electronic analogue of the crystal of Wu & Hu [146], or in systems with gain or loss [24]. For the void-channel networks, it would be useful to quantify the degree to which the chiral symmetry is violated compared to other photonic crystals that also have an approximate chiral symmetry, such as lattices of dielectrics resonators [147], and to quantify the the robustness of the chiral symmetry to disorder. For the effective dielectrics, there are many designs we could persue that are normally built from traditional dielectrics, such as anti-reflection coatings for terahertz radiation [62], flat or gradient-index lenses [142, 143], or dielectric tips for terahertz probes [144].

Finally, we are continuing to develop Peacock.jl [81] to include more utilities such as measuring the symmetry eigenvalues of crystals, adding other discretisation methods such as the finite-difference frequency-domain method [80] (a real space method which could model high contrast dielectrics or metals more efficiently than the plane-wave expansion method), and adding solvers for other types of problem such as scattering problems [148].

APPENDICES

A

SUMMARY OF THE WILSON LOOP WINDINGS

Figure A.1 summarises the possible Wilson loop windings for the photonic crystals introduced by Wu & Hu [1] and Blanco de Paz *et al* [73]. We see that the winding of the Berry bands classifies the crystals of the first two columns as the same trivial topological phase, and the fragile/obstructed atomic limits of the last three columns as the same non-trivial topological phase.

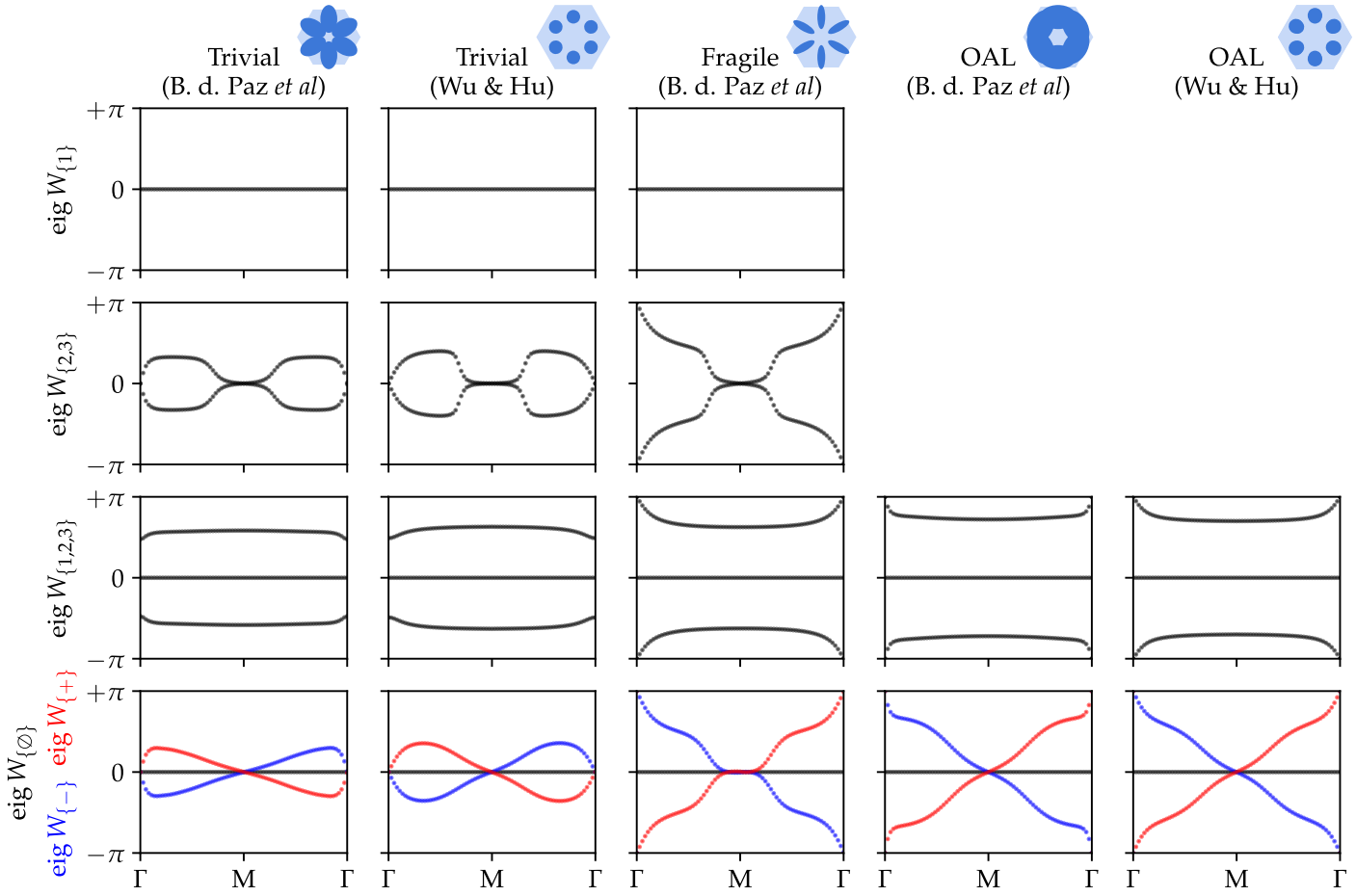

Figure A.1: Wilson loops windings of the first energy band ($W_{\{1\}}$, first row), of the second/third energy bands, ($W_{\{2,3\}}$, second row), of all three valence bands ($W_{\{1,2,3\}}$, third row), and of the Berry bands individually ($W_{\{\varnothing\}}$, $W_{\{-\}}$, $W_{\{+\}}$, fourth row) for the trivial crystal introduced by Blanco de Paz *et al* [73] ($R = a_0/3$, $d_1 = 0.51a_0$, $d_2 = 0.31a_0$, first column), the trivial crystal introduced by Wu and Hu ($R = a_0/3.125$, $d_1 = d_2 = 2R/3$, second column) [1], the fragilely topological crystal introduced by Blanco de Paz *et al* [73] ($R = a_0/3$, $d_1 = 0.4a_0$, $d_2 = 0.13a_0$, third column), the obstructed atomic limit (OAL) crystal introduced by Blanco de Paz *et al* ($R = a_0/3$, $d_1 = 0.4a_0$, $d_2 = 0.61a_0$, fourth column), and the OAL crystal introduced by Wu and Hu *et al* ($R = a_0/2.9$, $d_1 = d_2 = 2R/3$, fifth column). For the final two crystals $W_{\{1\}}$ and $W_{\{2,3\}}$ are not shown since they are not well defined because of the degeneracy between between the first and second energy bands.

B

ROTATIONAL SYMMETRIES OF THE BERRY BANDS

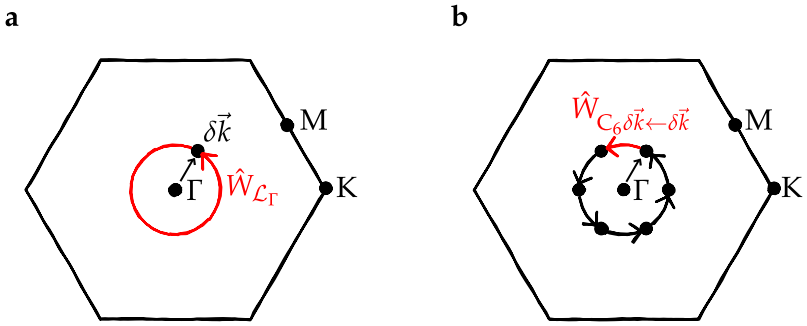

Figure B.1: (a) We define $\hat{W}_{\mathcal{L}_\Gamma}$ as a C_6-symmetric Wilson loop of radius $\delta\vec{k}$ around Γ. (b) $\hat{W}_{\mathcal{L}_\Gamma}$ may be considered as a series of six Wilson lines, $\hat{W}_{(C_6)^{n+1}\delta\vec{k}\leftarrow(C_6)^n\delta\vec{k}}$.

Consider the multiband Wilson loop of the valence bands around a vanishingly small loop $\mathcal{L}_\Gamma$ of radius δk enclosing Γ, as shown in Figure B.1a. Following the approach of [89], the Wilson loop may be written as a series of *Wilson lines*,

$$\hat{W}_{\mathcal{L}_\Gamma} = \hat{W}_{\delta\vec{k}\leftarrow C_6^5\delta\vec{k}}\dots\hat{W}_{C_6^2\delta\vec{k}\leftarrow C_6\delta\vec{k}}\hat{W}_{C_6\delta\vec{k}\leftarrow\delta\vec{k}}\,, \tag{B.1}$$

where each Wilson line is related by the rotation symmetry as shown in Figure B.1b. Note that the eigenvalues of the Wilson lines $\hat{W}_{C_6^{n+1}\delta\vec{k}\leftarrow C_6^n\delta\vec{k}}$ are gauge-dependent as the Wilson line is not taken around a closed loop. Using $\hat{W}_{C_n\mathcal{L}} = C_n\hat{W}_{\mathcal{L}}C_n^{-1}$, Equation (B.1) may instead be written as

$$\begin{aligned}\hat{W} &= C_6^5\hat{W}_{C_6\delta\vec{k}\leftarrow\delta\vec{k}}C_6^{-5}\cdot C_6^4\hat{W}_{C_6\delta\vec{k}\leftarrow\delta\vec{k}}C_6^{-4}\cdot C_6^3\hat{W}_{C_6\delta\vec{k}\leftarrow\delta\vec{k}}C_6^{-3} \\ &\qquad\cdot C_6^2\hat{W}_{C_6\delta\vec{k}\leftarrow\delta\vec{k}}C_6^{-2}\cdot C_6^1\hat{W}_{C_6\delta\vec{k}\leftarrow\delta\vec{k}}C_6^{-1}\cdot\hat{W}_{C_6\delta\vec{k}\leftarrow\delta\vec{k}} \qquad \text{(B.2)} \\ &= (\hat{W}_6)^6, \qquad \text{(B.3)}\end{aligned}$$

where

$$\hat{W}_6 = C_6^{-1}\hat{W}_{C_6\delta\vec{k}\leftarrow\delta\vec{k}} \tag{B.4}$$

is a gauge-invariant *dressed Wilson line* [89].

In the limit that $\mathcal{L}$ is a vanishingly small loop enclosing Γ, the Wilson lines reduce to projection operators onto the valence bands at Γ,

$$\lim_{\delta\vec{k}\to\vec{0}}\hat{W}_{C_6\delta\vec{k}\leftarrow\delta\vec{k}} = \hat{P}_{\text{val}}(\Gamma), \tag{B.5}$$

and the dressed Wilson line therefore reduces to the inverse rotation operator,

$$\lim_{\delta\vec{k}\to\vec{0}}(\boldsymbol{W_6})_{mn} = \left\langle u_m(\Gamma)\middle|C_6^{-1}\middle|u_n(\Gamma)\right\rangle. \tag{B.6}$$

Noting that the full Wilson loop and the dressed Wilson lines commute,

$$[\hat{W}_{\mathcal{L}}, \hat{W}_6] = [\hat{W}_6^6, \hat{W}_6] = 0, \tag{B.7}$$

and recalling the multiband Berry curvature $\hat{\mathcal{F}}(\vec{k}) = \lim_{A_{\mathcal{L}}\to 0}\hat{W}_{\mathcal{L}}/A_{\mathcal{L}}$ from Equation (3.15), we see that the multiband Berry curvature and C_6 rotation operator are simultaneously diagonalised at Γ,

$$[\hat{\mathcal{F}}(\Gamma), C_6] = 0. \tag{B.8}$$

Similarly, it can be shown that the Berry bands at M and K may be simultaneously diagonalised with the C_2 and C_3 rotation operators,

$$[\hat{\mathcal{F}}(M), C_2] = 0, \tag{B.9}$$
$$[\hat{\mathcal{F}}(K), C_3] = 0. \tag{B.10}$$

The symmetries of the Berry bands at Γ and M shall prove essential to defining our $\mathbb{Z}_2$ topological index in $C_2\mathcal{T}$-symmetric photonic crystals.

C

C_2 EIGENVALUES OF THE (SHIFTED) CELLS OF WU & HU

Figure C.1: Positions of M, M′, and M″ within the Brillouin zone, and schematics of the (shifted) shrunken-ring and expanded-ring unit cells introduced by Wu and Hu [1].

Figure C.1 shows the position of the M, M′, and M″ high symmetry points within the Brillouin zone, and the four unit cells we considered in Figure 3.8 of the main text.

In Table C.1, we apply the method of Benalcazar *et al* [97] to classify the $C_n\mathcal{T}$-protected phases according to the rotation symmetry eigenvalues at the high symmetry points of the Brillouin zone. Crystals with $C_2\mathcal{T}$ symmetry on a triangular lattice may be classified by the vector

$$\vec{X} = \left(\left[M_1^{(2)} \right], \left[M_1'^{(2)} \right], \left[M_1''^{(2)} \right] \right), \tag{C.1}$$

where $\left[\Pi_p^{(n)} \right] = \#\Pi_p^{(n)} - \#\Gamma_p^{(n)}$ and $\#\Pi_p^{(n)}$ is the number of bands below the gap of topological interest with eigenvalues $e^{2\pi i(p-1)/n}$ at the high symmetry point Π. Note that the C_2 eigenvalues of the bands at M, M′, and M″ depend on our choice of origin [33]. The shifted and unshifted cells are therefore classified as different topological phases according to this method.

Geometry	C_2 **eigenvalues at:**				$\vec{X}$
	Γ	M	M′	M″	
Shrunken	$+,-,-$	$-,+,-$	$-,+,-$	$-,+,-$	$(0,0,0)$
Shifted shrunken	$+,-,-$	$-,+,-$	$+,-,+$	$+,-,+$	$(0,1,1)$
Expanded	$+,+,+$	$-,+,-$	$-,+,-$	$-,+,-$	$(-2,-2,-2)$
Shifted expanded	$+,+,+$	$-,+,-$	$+,-,+$	$+,-,+$	$(-2,-1,-1)$

Table C.1: C_2 eigenvalues and the resulting classification of the unit cells following the method of Benalcazar *et al* [97].

D

CONVERGENCE OF THE VOID-CHANNEL NETWORKS WITH GAP SIZE

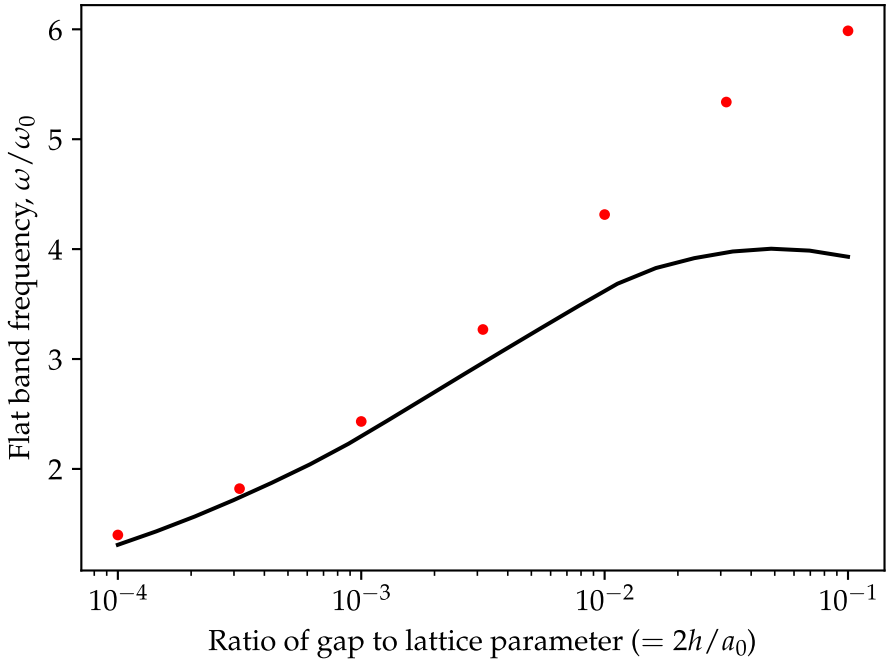

Figure D.1: Normalised frequency of the flat band for the honeycomb-kagome network of masses and springs (black line) and the voids and channels (red points). The agreement between the two models increases as the gap size is decreased.

Figure D.1 shows the frequency of the flat band as a function of gap size in the honeycomb-kagome network of masses and springs (black line) and void-channel (red points) that were originally introduced in Figure 4.8. The agreement between the two models increases as the gap size decreases, as expected from the asymptotic analysis of Vanel *et al* [2, 104].

E

ELECTROSTATIC POLARISABILITY OF ELLIPTIC CYLINDERS

In Section 5.4.4 we derive the Maxwell Garnett mixing formula for the effective index of an array of elliptic cylinders. This requires the electrostatic polarisability of elliptic cylinders, which we obtained by solving Laplace's equation with Maxwell's interface conditions in elliptic cylindrical coordinates as follows. This was originally published in the supplementary material of [113].

E.1 ELLIPTIC CYLINDRICAL COORDINATES

Elliptic cylindrical coordinates are defined as [149]

$$x = a \cosh u \cos v \tag{E.1}$$

$$y = a \sinh u \sin v \tag{E.2}$$

where $u = [0, \infty)$ and $v = [0, 2\pi)$. Note that v is an angular coordinate that runs parallel to the surface of an ellipse, whereas u is a radial coordinate that runs normal to an ellipse, as shown in Figure E.1.

The equation of an elliptic cylinder with aspect ratio $\Lambda = L_x/L_y$ in cartesian coordinates is

$$\frac{x^2}{\Lambda} + \frac{y^2}{1/\Lambda} = \rho^2, \tag{E.3}$$

or in elliptic cylindrical coordinates,

$$u = u_\rho = \tanh^{-1}(1/\Lambda), \tag{E.4}$$

$$a = \rho\sqrt{\Lambda - 1/\Lambda}. \tag{E.5}$$

E.2 SOLVING LAPLACE'S EQUATION

E.2.1 *Laplace's equation in elliptic cylindrical coordinates*

Assuming $\delta_z \phi = 0$, the form of Laplace's equation is unchanged when we transform to elliptic cylindrical coordinates,

$$\left(\frac{\partial^2}{\partial u^2} + \frac{\partial^2}{\partial v^2}\right)\phi(u, v) = 0. \tag{E.6}$$

By separation of variables we can write

$$\phi(u, v) = U(u)V(v), \tag{E.7}$$

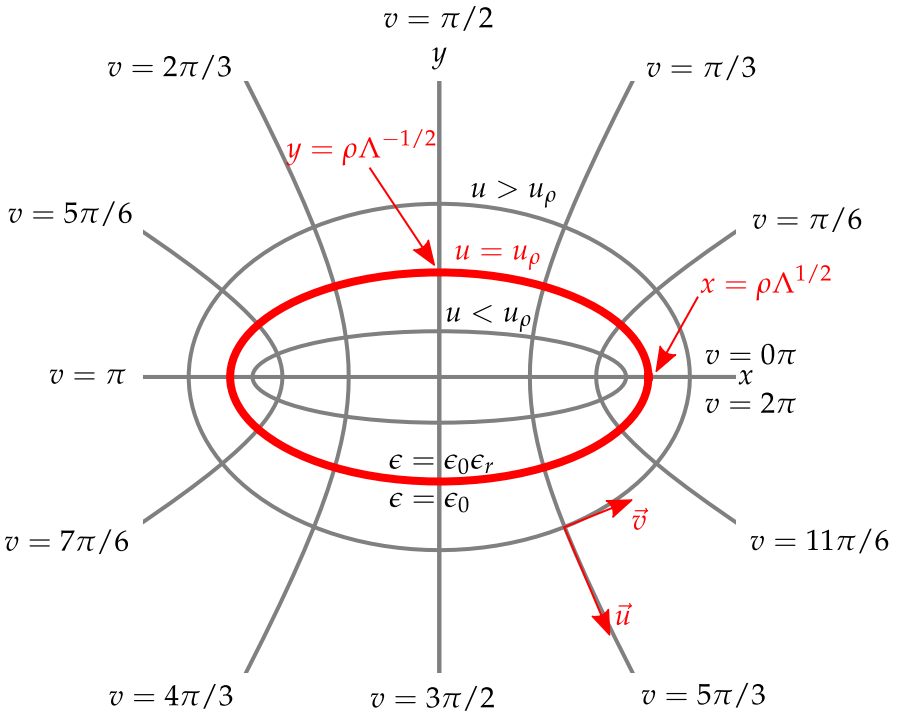

Figure E.1: Lines of constant u and v within the elliptic cylindrical coordinate system. Lines of constant u form ellptic cylinders with the aspect of each cylinder controlled by the magnitude of u.

with

$$\frac{\mathrm{d}^2 U}{\mathrm{d}u^2} = n^2 U, \tag{E.8}$$

$$\frac{\mathrm{d}^2 V}{\mathrm{d}v^2} = -n^2 V, \tag{E.9}$$

where n is the constant of separation. This has solutions $\phi_n = U_n V_n$, where

$$V_n = a_n \cos(nv) + b_n \sin(nv), \tag{E.10}$$

$$U_n = c_n \cosh(nu) + d_n \sinh(nu). \tag{E.11}$$

Enforcing angular periodicity, $V_n(v) = V_n(v + 2\pi)$, we see that n must be integer. Additionally, the elliptic cylinder and the applied field are both symmetric about the x-axis, and therefore $b_n = 0$ such that V_n is even about $v = 0$.

E.2.2 *Potential inside the particle*

In the electrostatic limit, we assume that the field is uniform within the particle,

$$\phi_{\text{in}} = -AE_0 x.$$

In order to calculate the electrostatic polarisability of the particle, we must find A.

E.2.3 *Potential outside the particle*

For an applied field $\vec{E} = E_0 \vec{x}$, the electric potential far from the scatterer must tend to $\phi_{\text{out}}(u \to \infty) = -E_0 x$. This is satisfied by

$$\phi_{\text{out}} = -E_0 x + \sum_{n=1}^{\infty} U_n V_n, \tag{E.12}$$

provided that we chose $d_n = c_n$ such that

$$U_n = c_n \cosh(nu) - c_n \sinh(nu), \tag{E.13}$$

$$= c_n e^{-nu}, \tag{E.14}$$

and $U_n V_n \to \infty$ for $u \to \infty$ for all n.

The potential outside of the particle is therefore of the form

$$\phi_{\text{out}} = -E_0 x + \sum_{n=1}^{\infty} B_n \cos(nv) e^{-nu}, \tag{E.15}$$

where $B_n = a_n c_n$.

E.2.4 *Maxwell's interface conditions*

We may find A by applying Maxwell's interface conditions for the electric field. The tangential component of the E-field is continuous at the surface,

$$\left(\frac{\partial \phi_{\text{in}}}{\partial v}\right)_{u=u_\rho} = \left(\frac{\partial \phi_{\text{out}}}{\partial v}\right)_{u=u_\rho}, \tag{E.16}$$

such that

$$\left(\frac{\partial \phi_{\text{in}}}{\partial v}\right)_{u=u_\rho} = (a \cosh u_\rho \sin v) A E_0, \tag{E.17}$$

$$\left(\frac{\partial \phi_{\text{out}}}{\partial v}\right)_{u=u_\rho} = (a \cosh u_\rho \sin v) E_0 - \sum_{n=1}^{\infty} B_n n \sin(nv) e^{-nu_\rho}, \tag{E.18}$$

where we have used $\partial_v x = -a \cosh u \sin v$. Therefore, by equating coefficients of $\sin(nv)$, we see that $B_{n\neq 1} = 0$ and

$$e^{-u_\rho} B_1 = (1 - A) a \cosh u_\rho \cdot E_0. \tag{E.19}$$

Similarly, the normal component of the D-field is continuous at the surface,

$$\epsilon_r \left(\frac{\partial \phi_{\text{in}}}{\partial u}\right)_{u=u_\rho} = \left(\frac{\partial \phi_{\text{out}}}{\partial u}\right)_{u=u_\rho}, \tag{E.20}$$

such that

$$e^{-u_\rho} B_1 = (\epsilon_r A - 1) a \sinh u_\rho \cdot E_0, \tag{E.21}$$

where we have used $\partial_u x = a \sinh u \cos v$.

By equating Equations (E.19) and (E.21), and recalling that $\tanh u_\rho = 1/\Lambda$, we find

$$A = \frac{1 + \Lambda}{\epsilon_r + \Lambda}. \tag{E.22}$$

E.3 ELECTROSTATIC POLARISABILITY

Now that the internal electric potential is known, we may find the quasi-static electric polarisability,

$$\vec{P} = (\epsilon - \epsilon_0)\vec{E}_{in} = (\epsilon - \epsilon_0) A \vec{E}_0 = \alpha_{\text{qs}} \vec{E}_0, \tag{E.23}$$

such that

$$\alpha_{\text{qs}} = \frac{(\epsilon - \epsilon_0)(1 + \Lambda)}{\epsilon_r + \Lambda} V. \tag{E.24}$$

BIBLIOGRAPHY

[1] L.-H. Wu and X. Hu. "Scheme for achieving a topological photonic crystal by using dielectric material." In: *Physical Review Letters* 114.22 (2015), p. 223901 (cit. on pp. v, 26, 59, 66–71, 73, 76, 78, 79, 83–85, 87–90, 145, 151, 152, 155).

[2] A. L. Vanel, O. Schnitzer, and R. V. Craster. "Asymptotic network models of subwavelength metamaterials formed by closely packed photonic and phononic crystals." In: *EPL (Europhysics Letters)* 119.6 (2017), p. 64002 (cit. on pp. v, 93–95, 102, 115, 157).

[3] K. v. Klitzing, G. Dorda, and M. Pepper. "New method for high-accuracy determination of the fine-structure constant based on quantized Hall resistance." In: *Physical Review Letters* 45.6 (1980), p. 494 (cit. on pp. 2, 10).

[4] D. J. Thouless, M. Kohmoto, M. P. Nightingale, and M. den Nijs. "Quantized Hall conductance in a two-dimensional periodic potential." In: *Physical Review Letters* 49.6 (1982), p. 405 (cit. on pp. 2, 11).

[5] F. D. M. Haldane. "Model for a quantum Hall effect without Landau levels: Condensed-matter realization of the "parity anomaly"." In: *Physical Review Letters* 61.18 (1988), p. 2015 (cit. on pp. 2, 11).

[6] "The Nobel Prize in Physics 2016." In: *The 2016 Nobel Prize in Physics - Press Release* (Oct. 2016). URL: https://www.nobelprize.org/prizes/physics/2016/press-release/ (cit. on p. 2).

[7] D. C. Tsui, H. L. Stormer, and A. C. Gossard. "Two-dimensional magnetotransport in the extreme quantum limit." In: *Physical Review Letters* 48.22 (1982), p. 1559 (cit. on pp. 2, 10).

[8] K. von Klitzing. "Essay: Quantum Hall effect and the new international system of units." In: *Physical Review Letters* 122.20 (2019), p. 200001 (cit. on p. 2).

[9] J. G. Checkelsky, J. Ye, Y. Onose, Y. Iwasa, and Y. Tokura. "Dirac-fermion-mediated ferromagnetism in a topological insulator." In: *Nature Physics* 8.10 (2012), pp. 729–733 (cit. on p. 3).

[10] C.-K. Chiu, J. C. Teo, A. P. Schnyder, and S. Ryu. "Classification of topological quantum matter with symmetries." In: *Reviews of Modern Physics* 88.3 (2016), p. 035005 (cit. on pp. 3, 6, 7).

[11] A. Burkov and D. Hawthorn. "Spin and charge transport on the surface of a topological insulator." In: *Physical Review Letters* 105.6 (2010), p. 066802 (cit. on p. 3).

[12] M. Vali, D. Dideban, and N. Moezi. "A scheme for a topological insulator field effect transistor." In: *Physica E: Low-dimensional Systems and Nanostructures* 69 (2015), pp. 360–363 (cit. on p. 3).

[13] M. He, H. Sun, and Q. L. He. "Topological insulator: Spintronics and quantum computations." In: *Frontiers of Physics* 14.4 (2019), p. 43401 (cit. on p. 3).

[14] A. Y. Kitaev. "Fault-tolerant quantum computation by anyons." In: *Annals of Physics* 303.1 (2003), pp. 2–30 (cit. on p. 3).

[15] C. Nayak, S. H. Simon, A. Stern, M. Freedman, and S. D. Sarma. "Non-Abelian anyons and topological quantum computation." In: *Reviews of Modern Physics* 80.3 (2008), p. 1083 (cit. on p. 3).

[16] M. Z. Hasan and C. L. Kane. "Colloquium: Topological insulators." In: *Reviews of Modern Physics* 82.4 (2010), p. 3045 (cit. on pp. 3, 4).

[17] X. Zhang, M. Xiao, Y. Cheng, M.-H. Lu, and J. Christensen. "Topological sound." In: *Communications Physics* 1.1 (2018), pp. 1–13 (cit. on p. 3).

[18] T. Ozawa et al. "Topological photonics." In: *Reviews of Modern Physics* 91.1 (2019), p. 015006 (cit. on pp. 3, 26, 56, 57).

[19] K. von Klitzing et al. "40 years of the quantum Hall effect." In: *Nature Reviews Physics* (2020), pp. 1–5 (cit. on p. 3).

[20] M. Kim, Z. Jacob, and J. Rho. "Recent advances in 2D, 3D and higher-order topological photonics." In: *Light: Science & Applications* 9.1 (2020), pp. 1–30 (cit. on pp. 3, 26).

[21] M. S. Rider, S. J. Palmer, S. R. Pocock, X. Xiao, P. Arroyo Huidobro, and V. Giannini. "A perspective on topological nanophotonics: current status and future challenges." In: *Journal of Applied Physics* 125.12 (2019), p. 120901 (cit. on pp. 3, 26).

[22] M. A. Bandres, S. Wittek, G. Harari, M. Parto, J. Ren, M. Segev, D. N. Christodoulides, and M. Khajavikhan. "Topological insulator laser: Experiments." In: *Science* 359.6381 (2018) (cit. on p. 3).

[23] Y. Ota, R. Katsumi, K. Watanabe, S. Iwamoto, and Y. Arakawa. "Topological photonic crystal nanocavity laser." In: *Communications Physics* 1.1 (2018), pp. 1–8 (cit. on p. 3).

[24] H. Schomerus. "Topologically protected midgap states in complex photonic lattices." In: *Optical Letters* 38.11 (2013), pp. 1912–1914 (cit. on pp. 3, 44, 147).

[25] P. St-Jean, V. Goblot, E. Galopin, A. Lemaître, T. Ozawa, L. Le Gratiet, I. Sagnes, J. Bloch, and A. Amo. "Lasing in topological edge states of a one-dimensional lattice." In: *Nature Photonics* 11.10 (2017), pp. 651–656 (cit. on p. 3).

[26] H. Zhao, P. Miao, M. H. Teimourpour, S. Malzard, R. El-Ganainy, H. Schomerus, and L. Feng. "Topological hybrid silicon microlasers." In: *Nature Communications* 9.1 (2018), pp. 1–6 (cit. on p. 3).

[27] M. Parto et al. "Edge-mode lasing in 1D topological active arrays." In: *Physical Review Letters* 120.11 (2018), p. 113901 (cit. on p. 3).

[28] B. Bahari, A. Ndao, F. Vallini, A. El Amili, Y. Fainman, and B. Kanté. "Nonreciprocal lasing in topological cavities of arbitrary geometries." In: *Science* 358.6363 (2017), pp. 636–640 (cit. on p. 3).

[29] A. B. Khanikaev, S. H. Mousavi, W.-K. Tse, M. Kargarian, A. H. MacDonald, and G. Shvets. "Photonic topological insulators." In: *Nature Materials* 12.3 (2013), pp. 233–239 (cit. on pp. 3, 26, 56–59, 66, 67).

[30] X.-L. Qi and S.-C. Zhang. "Topological insulators and superconductors." In: *Reviews of Modern Physics* 83.4 (2011), p. 1057 (cit. on pp. 3, 4).

[31] X. Chen, Z.-C. Gu, and X.-G. Wen. "Local unitary transformation, long-range quantum entanglement, wave function renormalization, and topological order." In: *Physical Review B* 82.15 (2010), p. 155138 (cit. on pp. 4, 6).

[32] S. M. Girvin and K. Yang. *Modern condensed matter physics*. Cambridge University Press, 2019 (cit. on p. 6).

[33] J. K. Asbóth, L. Oroszlány, and A. Pályi. "A short course on topological insulators." In: *Lecture notes in physics* 919 (2016), pp. 997–1000 (cit. on pp. 6, 7, 13, 15, 20–22, 41, 45, 47–51, 65, 81, 83, 93, 155).

[34] A. P. Schnyder, S. Ryu, A. Furusaki, and A. W. Ludwig. "Classification of topological insulators and superconductors in three spatial dimensions." In: *Physical Review B* 78.19 (2008), p. 195125 (cit. on pp. 6, 10).

[35] A. Kitaev. "Periodic table for topological insulators and superconductors." In: *AIP conference proceedings*. Vol. 1134. 1. American Institute of Physics. 2009, pp. 22–30 (cit. on pp. 6, 10).

[36] S. Ryu, A. P. Schnyder, A. Furusaki, and A. W. Ludwig. "Topological insulators and superconductors: tenfold way and dimensional hierarchy." In: *New Journal of Physics* 12.6 (2010), p. 065010 (cit. on pp. 6–10, 91).

[37] B. Sutherland. "Localization of electronic wave functions due to local topology." In: *Physical Review B* 34.8 (1986), p. 5208 (cit. on p. 7).

[38] M. R. Zirnbauer. "Riemannian symmetric superspaces and their origin in random-matrix theory." In: *Journal of Mathematical Physics* 37.10 (1996), pp. 4986–5018 (cit. on pp. 8, 91).

[39] A. Altland and M. R. Zirnbauer. "Nonstandard symmetry classes in mesoscopic normal-superconducting hybrid structures." In: *Physical Review B* 55.2 (1997), p. 1142 (cit. on pp. 8, 91).

[40] B. I. Halperin. "Quantized Hall conductance, current-carrying edge states, and the existence of extended states in a two-dimensional disordered potential." In: *Physical Review B* 25.4 (1982), p. 2185 (cit. on pp. 10, 11).

[41] C. L. Kane. "Topological Band Theory and the $\mathbb{Z}_2$ Invariant." In: *Contemporary Concepts of Condensed Matter Science*. Vol. 6. Elsevier, 2013, pp. 3–34 (cit. on pp. 10, 11, 13–15, 17).

[42] B. Bradlyn, L. Elcoro, J. Cano, M. Vergniory, Z. Wang, C. Felser, M. Aroyo, and B. A. Bernevig. "Topological quantum chemistry." In: *Nature* 547.7663 (2017), pp. 298–305 (cit. on pp. 13, 68, 72, 83).

[43] D. Gresch, G. Autes, O. V. Yazyev, M. Troyer, D. Vanderbilt, B. A. Bernevig, and A. A. Soluyanov. "Z2Pack: Numerical implementation of hybrid Wannier centers for identifying topological materials." In: *Physical Review B* 95.7 (2017), p. 075146 (cit. on pp. 13, 17, 48, 51, 52, 62, 64, 65, 67, 81).

[44] D. Vanderbilt. *Berry Phases in Electronic Structure Theory: Electric Polarization, Orbital Magnetization and Topological Insulators*. Cambridge University Press, 2018 (cit. on pp. 13, 14, 22, 37, 40–43, 45, 48, 50–53, 60, 62, 65).

[45] Y. Hatsugai. "Chern number and edge states in the integer quantum Hall effect." In: *Physical Review Letters* 71.22 (1993), p. 3697 (cit. on pp. 13, 50).

[46] C. L. Kane and E. J. Mele. "Z_2 topological order and the quantum spin Hall effect." In: *Physical Review Letters* 95.14 (2005), p. 146802 (cit. on p. 15).

[47] C. L. Kane and E. J. Mele. "Quantum spin Hall effect in graphene." In: *Physical Review Letters* 95.22 (2005), p. 226801 (cit. on p. 15).

[48] W. P. Su, J. R. Schrieffer, and A. J. Heeger. "Soliton excitations in polyacetylene." In: *Physical Review B* 22.4 (1980), p. 2099 (cit. on pp. 17, 19).

[49] G. van Miert and C. Ortix. "On the topological immunity of corner states in two-dimensional crystalline insulators." In: *npj Quantum Materials* 5.1 (Sept. 2020), p. 63 (cit. on p. 20).

[50] R. H. Landau. *Quantum mechanics II: a second course in quantum theory*. John Wiley & Sons, 2008 (cit. on p. 20).

[51] S. R. Pocock, P. A. Huidobro, and V. Giannini. "Bulk-edge correspondence and long-range hopping in the topological plasmonic chain." In: *Nanophotonics* 8.8 (2019), pp. 1337–1347 (cit. on pp. 21, 26, 47, 93).

[52] B. Pérez-González, M. Bello, Á. Gómez-León, and G. Platero. "Interplay between long-range hopping and disorder in topological systems." In: *Physical Review B* 99.3 (2019), p. 035146 (cit. on p. 21).

[53] B.-H. Chen and D.-W. Chiou. "An elementary rigorous proof of bulk-boundary correspondence in the generalized Su-Schrieffer-Heeger model." In: *Physics Letters A* 384.7 (2020), p. 126168 (cit. on pp. 21, 116).

[54] S. Pocock. "Topological physics in one-dimensional chains of metallic nanoparticles." PhD thesis. Imperial College London, 2020 (cit. on pp. 22, 26, 47, 93).

[55] M. Proctor, P. A. Huidobro, B. Bradlyn, M. B. de Paz, M. G. Vergniory, D. Bercioux, and A. García-Etxarri. "Robustness of topological corner modes in photonic crystals." In: *Physical Review Research* 2.4 (2020), p. 042038 (cit. on p. 22).

[56] A. P. Schnyder. "Lecture Notes on Accidental and Symmetry-enforced Band Crossings in Topological Semimetals." In: *Topological Matter School, San Sebastian, Spain* (2018) (cit. on pp. 23, 105).

[57] J. Dong, V. Juričić, and B. Roy. "Topoelectric circuits: Theory and construction." In: *Physical Review Research* 3.2 (2021), p. 023056 (cit. on p. 23).

[58] J. Arkinstall, M. Teimourpour, L. Feng, R. El-Ganainy, and H. Schomerus. "Topological tight-binding models from nontrivial square roots." In: *Physical Review B* 95.16 (2017), p. 165109 (cit. on pp. 24, 93, 103–105).

[59] Z. Zhang, M. H. Teimourpour, J. Arkinstall, M. Pan, P. Miao, H. Schomerus, R. El-Ganainy, and L. Feng. "Experimental realization of multiple topological edge states in a 1d photonic lattice." In: *Laser & Photonics Reviews* 13.2 (2019), p. 1800202 (cit. on p. 24).

[60] T. Mizoguchi, T. Yoshida, and Y. Hatsugai. "Square-root topological semimetals." In: *Physical Review B* 103.4 (2021), p. 045136 (cit. on pp. 24, 103–105, 107, 109, 111, 112).

[61] P. Delplace, D. Ullmo, and G. Montambaux. "Zak phase and the existence of edge states in graphene." In: *Physical Review B* 84.19 (2011), p. 195452 (cit. on pp. 24, 105).

[62] J. D. Joannopoulos, S. G. Johnson, J. N. Winn, and R. D. Meade. *Photonic Crystals: Molding the flow of light*. 2nd ed. Princeton University Press, Princeton, NJ, 2008 (cit. on pp. 25, 37, 39, 143, 147).

[63] S. John. "Strong localization of photons in certain disordered dielectric superlattices." In: *Physical Review Letters* 58.23 (1987), p. 2486 (cit. on p. 25).

[64] H.-X. Wang, G.-Y. Guo, and J.-H. Jiang. "Band topology in classical waves: Wilson-loop approach to topological numbers and fragile topology." In: *New Journal of Physics* 21.9 (2019), p. 093029 (cit. on pp. 25, 44).

[65] F. Haldane and S. Raghu. "Possible realization of directional optical waveguides in photonic crystals with broken time-reversal symmetry." In: *Physical Review Letters* 100.1 (2008), p. 013904 (cit. on pp. 26, 53, 54).

[66] S. Raghu and F. D. M. Haldane. "Analogs of quantum-Hall-effect edge states in photonic crystals." In: *Physical Review A* 78.3 (2008), p. 033834 (cit. on pp. 26, 53, 54).

[67] Z. Wang, Y. Chong, J. D. Joannopoulos, and M. Soljačić. "Observation of unidirectional backscattering-immune topological electromagnetic states." In: *Nature* 461.7265 (2009), pp. 772–775 (cit. on pp. 26, 53).

[68] Y. Poo, R.-x. Wu, Z. Lin, Y. Yang, and C. Chan. "Experimental realization of self-guiding unidirectional electromagnetic edge states." In: *Physical Review Letters* 106.9 (2011), p. 093903 (cit. on p. 26).

[69] D. A. Jacobs, A. E. Miroshnichenko, Y. S. Kivshar, and A. B. Khanikaev. "Photonic topological Chern insulators based on Tellegen metacrystals." In: *New Journal of Physics* 17.12 (2015), p. 125015 (cit. on p. 26).

[70] K. Y. Bliokh, D. Smirnova, and F. Nori. "Quantum spin Hall effect of light." In: *Science* 348.6242 (2015), pp. 1448–1451 (cit. on p. 26).

[71] L. D. Landau and E. M. Lifshitz. *Theoretical Physics, Vol. 8, Electrodynamics of Continuous Media*. Nauka Moscow, 1982 (cit. on p. 26).

[72] X. Zhu, H.-X. Wang, C. Xu, Y. Lai, J.-H. Jiang, and S. John. "Topological transitions in continuously deformed photonic crystals." In: *Physical Review B* 97.8 (2018), p. 085148 (cit. on pp. 26, 67, 90).

[73] M. Blanco de Paz, M. G. Vergniory, D. Bercioux, A. García-Etxarri, and B. Bradlyn. "Engineering fragile topology in photonic crystals: Topological quantum chemistry of light." In: *Physical Review Research* 1.3 (2019), p. 032005 (cit. on pp. 26, 54, 59, 67–69, 71–74, 79, 83, 85, 87, 88, 90, 151, 152).

[74] D. Smirnova, S. Kruk, D. Leykam, E. Melik-Gaykazyan, D.-Y. Choi, and Y. Kivshar. "Third-harmonic generation in photonic topological metasurfaces." In: *Physical Review Letters* 123.10 (2019), p. 103901 (cit. on pp. 26, 67, 90).

[75] B. Orazbayev and R. Fleury. "Quantitative robustness analysis of topological edge modes in C6 and valley-Hall metamaterial waveguides." In: *Nanophotonics* 8.8 (2019), pp. 1433–1441 (cit. on pp. 26, 67, 69, 89, 90).

[76] Z. Li, H.-C. Chan, and Y. Xiang. "Fragile topology based helical edge states in two-dimensional moon-shaped photonic crystals." In: *Physical Review B* 102.24 (2020), p. 245149 (cit. on pp. 26, 67).

[77] A. B. Khanikaev and G. Shvets. "Two-dimensional topological photonics." In: *Nature Photonics* 11.12 (2017), pp. 763–773 (cit. on pp. 26, 56, 59).

[78] L. Novotny and B. Hecht. *Principles of nano-optics*. Cambridge University Press, 2012 (cit. on pp. 27–29, 133).

[79] T. G. Mackay and A. Lakhtakia. *Electromagnetic anisotropy and bianisotropy: a field guide*. World Scientific, 2019 (cit. on pp. 27, 28, 30).

[80] R. Rumpf. "Design and optimization of nano-optical elements by coupling fabrication to optical behavior." PhD thesis. University of Central Florida, 2006 (cit. on pp. 28, 32, 35–38, 65, 126, 147).

[81] S. J. Palmer and V. Giannini. "Peacock.jl: Photonic crystals in Julia." In: *Journal of Open Source Software* 5.54 (2020), p. 2678 (cit. on pp. 32, 65, 145, 147).

[82] J. Zi, X. Yu, Y. Li, X. Hu, C. Xu, X. Wang, X. Liu, and R. Fu. "Coloration strategies in peacock feathers." In: *Proceedings of the National Academy of Sciences* 100.22 (2003), pp. 12576–12578 (cit. on p. 32).

[83] L. Shen and S. He. "Analysis for the convergence problem of the plane-wave expansion method for photonic crystals." In: *JOSA A* 19.5 (2002), pp. 1021–1024 (cit. on pp. 32, 124).

[84] N. W. Ashcroft and N. D. Mermin. *Solid State Physics*. Saunders College Publishing, 1976 (cit. on p. 32).

[85] H. Petter Langtangen and G. K. Pedersen. *Scaling of differential equations*. Springer Nature, 2016 (cit. on p. 38).

[86] R. Zhao, G.-D. Xie, M. L. Chen, Z. Lan, Z. Huang, and E. Wei. "First-principle calculation of Chern number in gyrotropic photonic crystals." In: *Optics Express* 28.4 (2020), pp. 4638–4649 (cit. on p. 41).

[87] M. Xiao, Z. Zhang, and C. T. Chan. "Surface impedance and bulk band geometric phases in one-dimensional systems." In: *Physical Review X* 4.2 (2014), p. 021017 (cit. on pp. 44, 47).

[88] Z. Wang, Y. Chong, J. D. Joannopoulos, and M. Soljačić. "Reflection-free one-way edge modes in a gyromagnetic photonic crystal." In: *Physical Review Letters* 100.1 (2008), p. 013905 (cit. on pp. 53–55, 63, 64).

[89] B. Bradlyn, Z. Wang, J. Cano, and B. A. Bernevig. "Disconnected elementary band representations, fragile topology, and Wilson loops as topological indices: An example on the triangular lattice." In: *Physical Review B* 99.4 (2019), p. 045140 (cit. on pp. 54, 75, 77, 153).

[90] L. Lu, J. D. Joannopoulos, and M. Soljačić. "Topological photonics." In: *Nature Photonics* 8.11 (2014), pp. 821–829 (cit. on p. 56).

[91] A. A. Soluyanov and D. Vanderbilt. "Wannier representation of $\mathbb{Z}_2$ topological insulators." In: *Physical Review B* 83.3 (2011), p. 035108 (cit. on pp. 65, 75).

[92] S. J. Palmer and V. Giannini. "Berry bands and pseudo-spin of topological photonic phases." In: *Physical Review Research* 3.2 (2021), p. L022013 (cit. on pp. 67, 87, 146).

[93] M. Blanco de Paz, C. Devescovi, G. Giedke, J. J. Saenz, M. G. Vergniory, B. Bradlyn, D. Bercioux, and A. García-Etxarri. "Tutorial: computing topological invariants in 2D photonic crystals." In: *Advanced Quantum Technologies* 3.2 (2020), p. 1900117 (cit. on pp. 68, 69).

[94] M. Proctor, X. Xiao, R. V. Craster, S. A. Maier, V. Giannini, and P. Arroyo Huidobro. "Near-and Far-Field Excitation of Topological Plasmonic Metasurfaces." In: *Photonics*. Vol. 7. 4. Multidisciplinary Digital Publishing Institute. 2020, p. 81 (cit. on pp. 68, 75).

[95] B. A. Bernevig, T. L. Hughes, and S.-C. Zhang. "Quantum spin Hall effect and topological phase transition in HgTe quantum wells." In: *Science* 314.5806 (2006), pp. 1757–1761 (cit. on p. 69).

[96] S. G. Johnson and J. D. Joannopoulos. "Block-iterative frequency-domain methods for Maxwell's equations in a planewave basis." In: *Optics Express* 8.3 (2001), pp. 173–190 (cit. on p. 71).

[97] W. A. Benalcazar, T. Li, and T. L. Hughes. "Quantization of fractional corner charge in C_n-symmetric higher-order topological crystalline insulators." In: *Physical Review B* 99.24 (2019), p. 245151 (cit. on pp. 72, 83–85, 155).

[98] H. C. Po, H. Watanabe, and A. Vishwanath. "Fragile Topology and Wannier Obstructions." In: *Physical Review Letters* 121.12 (2018), p. 126402 (cit. on p. 72).

[99] A. Bouhon, A. M. Black-Schaffer, and R.-J. Slager. "Wilson loop approach to fragile topology of split elementary band representations and topological crystalline insulators with time-reversal symmetry." In: *Physical Review B* 100.19 (2019), p. 195135 (cit. on p. 77).

[100] W. A. Benalcazar, B. A. Bernevig, and T. L. Hughes. "Electric multipole moments, topological multipole moment pumping, and chiral hinge states in crystalline insulators." In: *Physical Review B* 96.24 (2017), p. 245115 (cit. on pp. 77, 79).

[101] Y. Hwang, J. Ahn, and B.-J. Yang. "Fragile topology protected by inversion symmetry: Diagnosis, bulk-boundary correspondence, and Wilson loop." In: *Physical Review B* 100.20 (2019), p. 205126 (cit. on pp. 77, 79).

[102] J. Ahn, S. Park, D. Kim, Y. Kim, and B.-J. Yang. "Stiefel–Whitney classes and topological phases in band theory." In: *Chinese Physics B* 28.11 (2019), p. 117101 (cit. on pp. 77, 79).

[103] M. Proctor, R. V. Craster, S. A. Maier, V. Giannini, and P. A. Huidobro. "Exciting pseudospin-dependent edge states in plasmonic metasurfaces." In: *ACS Photonics* 6.11 (2019), pp. 2985–2995 (cit. on p. 89).

[104] A. Vanel. "Asymptotic analysis of discrete and continuous periodic media." In: (2018) (cit. on pp. 93, 94, 102, 115, 146, 157).

[105] W. Maimaiti, B. Dietz, and A. Andreanov. "Microwave photonic crystals as an experimental realization of a combined honeycomb-kagome lattice." In: *Physical Review B* 102.21 (2020), p. 214301 (cit. on pp. 93, 109).

[106] H. Wakao, T. Yoshida, T. Mizoguchi, and Y. Hatsugai. "Topological Modes Protected by Chiral and Two-Fold Rotational Symmetry in a Spring-Mass Model with a Lieb Lattice Structure." In: *Journal of the Physical Society of Japan* 89.8 (2020), p. 083702 (cit. on p. 93).

[107] X. Ni, M. Weiner, A. Alu, and A. B. Khanikaev. "Observation of higher-order topological acoustic states protected by generalized chiral symmetry." In: *Nature Materials* 18.2 (2019), pp. 113–120 (cit. on p. 96).

[108] F. Hecht. "New development in FreeFem++." In: *Journal of Numerical Mathematics* 20.3-4 (2012), pp. 251–265 (cit. on p. 102).

[109] V. Laude. *Phononic crystals: artificial crystals for sonic, acoustic, and elastic waves*. eng. De Gruyter studies in mathematical physics Vol. 26. Berlin: De Gruyter, 2015 (cit. on p. 102).

[110] C. Barreteau, F. Ducastelle, and T. Mallah. "A bird's eye view on the flat and conic band world of the honeycomb and Kagome lattices: towards an understanding of 2D metal-organic frameworks electronic structure." In: *Journal of Physics: Condensed Matter* 29.46 (2017), p. 465302 (cit. on p. 105).

[111] M. Yan, X. Huang, L. Luo, J. Lu, W. Deng, and Z. Liu. "Acoustic square-root topological states." In: *Physical Review B* 102.18 (2020), p. 180102 (cit. on p. 109).

[112] E. D. Palik. *Handbook of optical constants of solids*. Vol. 3. Academic Press, 1998 (cit. on p. 118).

[113] S. J. Palmer, X. Xiao, N. Pazos-Perez, L. Guerrini, M. A. Correa-Duarte, S. A. Maier, R. V. Craster, R. A. Alvarez-Puebla, and V. Giannini. "Extraordinarily transparent compact metallic metamaterials." In: *Nature Communications* 10.1 (2019), pp. 1–7 (cit. on pp. 117, 122, 123, 129, 141, 147, 159).

[114] J. D. Jackson. *Classical electrodynamics*. John Wiley & Sons, 2007 (cit. on p. 118).

[115] J. Pendry, A. Holden, W. Stewart, and I. Youngs. "Extremely low frequency plasmons in metallic mesostructures." In: *Physical Review Letters* 76.25 (1996), p. 4773 (cit. on p. 118).

[116] J. Pendry, A. Holden, D. Robbins, and W. Stewart. "Magnetism from conductors and enhanced nonlinear phenomena." In: *IEEE transactions on microwave theory and techniques* 47.11 (1999), pp. 2075–2084 (cit. on p. 118).

[117] D. Smith, J. Pendry, and M. Wiltshire. "Metamaterials and negative refractive index." In: *Science* 305.5685 (2004), pp. 788–792 (cit. on p. 118).

[118] W. Cai and V. Shalaev. *Optical metamaterials, vol. 10*. 2010 (cit. on p. 118).

[119] W. Kock. "Metallic delay lenses." In: *Bell Labs Technical Journal* 27.1 (1948), pp. 58–82 (cit. on p. 118).

[120] D. Frankl. *Electromagnetic theory*. Prentice Hall, 1986 (cit. on p. 120).

[121] M. Ross, M. Blaber, and G. Schatz. "Using nanoscale and mesoscale anisotropy to engineer the optical response of three-dimensional plasmonic metamaterials." In: *Nature Communications* 5 (2014), p. 4090 (cit. on p. 120).

[122] M. Ross, C. Mirkin, and G. Schatz. "Optical properties of one-, two-, and three-dimensional arrays of plasmonic nanostructures." In: *The Journal of Physical Chemistry C* 120.2 (2016), pp. 816–830 (cit. on p. 120).

[123] V. Mondes, E. Antonsson, J. Plenge, C. Raschpichler, I. Halfpap, A. Menski, C. Graf, M. Kling, and E. Rühl. "Plasmonic electric near-field enhancement in self-organized gold nanoparticles in macroscopic arrays." In: *Applied Physics B* 122.6 (2016), p. 155 (cit. on p. 120).

[124] S. Maier. *Plasmonics: fundamentals and applications*. Springer Science & Business Media, 2007 (cit. on p. 120).

[125] K. Chung, R. Kim, T. Chang, and J. Shin. "Optical effective media with independent control of permittivity and permeability based on conductive particles." In: *Applied Physics Letters* 109.2 (2016), p. 021114 (cit. on pp. 120, 129).

[126] S. Lee. "Colloidal superlattices for unnaturally high-index metamaterials at broadband optical frequencies." In: *Optics Express* 23.22 (2015), pp. 28170–28181 (cit. on p. 120).

[127] D. Doyle, N. Charipar, C. Argyropoulos, S. Trammell, R. Nita, J. Naciri, A. Pique, J. Herzog, and J. Fontana. "Tunable subnanometer gap plasmonic metasurfaces." In: *ACS Photonics* 5.3 (2017), pp. 1012–1018 (cit. on p. 120).

[128] R. Kim, K. Chung, J. Kim, Y. Nam, S. Park, and J. Shin. "Metal Nanoparticle Array as a Tunable Refractive Index Material over Broad Visible and Infrared Wavelengths." In: *ACS Photonics* 5.4 (2018), pp. 1188–1195 (cit. on p. 120).

[129] M. Tebbe, S. Lentz, L. Guerrini, A. Feryc, R. Alvarez-Puebla, and N. Pazos-Perez. "Fabrication and optical enhancing properties of discrete supercrystals." In: *Nanoscale* 8 (2016), pp. 12702–12709 (cit. on p. 123).

[130] A. D. Rakić, A. B. Djurišić, J. M. Elazar, and M. L. Majewski. "Optical properties of metallic films for vertical-cavity optoelectronic devices." In: *Applied Optics* 37.22 (1998), pp. 5271–5283 (cit. on pp. 124, 133).

[131] F. Tisseur and K. Meerbergen. "The quadratic eigenvalue problem." In: *SIAM review* 43.2 (2001), pp. 235–286 (cit. on p. 125).

[132] R. C. Rumpf, A. Tal, and S. M. Kuebler. "Rigorous electromagnetic analysis of volumetrically complex media using the slice absorption method." In: *JOSA A* 24.10 (2007), pp. 3123–3134 (cit. on pp. 128, 142).

[133] I. A. Veres, T. Berer, and O. Matsuda. "Complex band structures of two dimensional phononic crystals: Analysis by the finite element method." In: *Journal of Applied Physics* 114.8 (2013) (cit. on pp. 128, 129).

[134] C. Bohren and D. Huffman. *Absorption and scattering of light by small particles*. John Wiley & Sons, 2008 (cit. on p. 131).

[135] V. A. Markel. "Introduction to the Maxwell Garnett approximation: tutorial." In: *JOSA A* 33.7 (2016), pp. 1244–1256 (cit. on pp. 131, 137, 142).

[136] V. A. Markel. "Maxwell Garnett approximation (advanced topics): tutorial." In: *JOSA A* 33.11 (2016), pp. 2237–2255 (cit. on pp. 131, 142).

[137] H. Wallén, H. Kettunen, and A. Sihvola. "Mixing formulas and plasmonic composites." In: *Metamaterials and plasmonics: fundamentals, modelling, applications*. Springer, 2009, pp. 91–102 (cit. on p. 131).

[138] L. Rayleigh. "On the influence of obstacles arranged in rectangular order upon the properties of a medium." In: *The London, Edinburgh, and Dublin Philosophical Magazine and Journal of Science* 34.211 (1892), pp. 481–502 (cit. on p. 131).

[139] C. A. Balanis. *Advanced Engineering Electromagnetics*. John Wiley & Sons, 1999 (cit. on p. 133).

[140] A. H. Sihvola. *Electromagnetic mixing formulas and applications*. 47. IET, 1999 (cit. on pp. 137, 138).

[141] S. Giordano. "Effective medium theory for dispersions of dielectric ellipsoids." In: *Journal of Electrostatics* 58.1-2 (2003), pp. 59–76 (cit. on p. 137).

[142] A. Climente, D. Torrent, and J. Sánchez-Dehesa. "Gradient index lenses for flexural waves based on thickness variations." In: *Applied Physics Letters* 105.6 (2014), p. 064101 (cit. on pp. 139, 140, 143, 147).

[143] J. Neu, B. Krolla, O. Paul, B. Reinhard, R. Beigang, and M. Rahm. "Metamaterial-based gradient index lens with strong focusing in the THz frequency range." In: *Optics Express* 18.26 (2010), pp. 27748–27757 (cit. on pp. 143, 147).

[144] T. Kurihara, K. Yamaguchi, H. Watanabe, M. Nakajima, and T. Suemoto. "Dielectric probe for scattering-type terahertz scanning near-field optical microscopy." In: *Applied Physics Letters* 103.15 (2013), p. 151105 (cit. on pp. 143, 147).

[145] J. C. Teo, L. Fu, and C. Kane. "Surface states and topological invariants in three-dimensional topological insulators: Application to Bi $Bi_{1-x}Sb_x$." In: *Physical Review B* 78.4 (2008), p. 045426 (cit. on p. 147).

[146] L.-H. Wu and X. Hu. "Topological properties of electrons in honeycomb lattice with detuned hopping energy." In: *Scientific Reports* 6.1 (2016), pp. 1–9 (cit. on p. 147).

[147] C. Poli, M. Bellec, U. Kuhl, F. Mortessagne, and H. Schomerus. "Selective enhancement of topologically induced interface states in a dielectric resonator chain." In: *Nature Communications* 6.1 (2015), pp. 1–5 (cit. on p. 147).

[148] R. C. Rumpf. "Simple implementation of arbitrarily shaped total-field/scattered-field regions in finite-difference frequency-domain." In: *Progress In Electromagnetics Research* 36 (2012), pp. 221–248 (cit. on p. 147).

[149] E. W. Weisstein. *Elliptic cylindrical coordinates*. Wolfram Research, Inc., 2003 (cit. on p. 159).

SPRINGER NATURE LICENSE
TERMS AND CONDITIONS

Apr 27, 2021

This Agreement between Mr. Samuel Palmer ("You") and Springer Nature ("Springer Nature") consists of your license details and the terms and conditions provided by Springer Nature and Copyright Clearance Center.

License Number	5057020541687
License date	Apr 27, 2021
Licensed Content Publisher	Springer Nature
Licensed Content Publication	Nature Materials
Licensed Content Title	Photonic topological insulators
Licensed Content Author	Alexander B. Khanikaev et al
Licensed Content Date	Dec 16, 2012
Type of Use	Thesis/Dissertation
Requestor type	academic/university or research institute
Format	print and electronic
Portion	figures/tables/illustrations
Number of figures/tables/illustrations	1

High-res required	no
Will you be translating?	no
Circulation/distribution	1 - 29
Author of this Springer Nature content	no
Title	Revealing hidden topologies within photonic crystals
Institution name	Imperial College London
Expected presentation date	May 2021
Portions	Figure 1b
Requestor Location	Mr. Samuel Palmer [redacted] Attn: Mr. Samuel PAlmer
Total	0.00 USD

Terms and Conditions

Springer Nature Customer Service Centre GmbH
Terms and Conditions

This agreement sets out the terms and conditions of the licence (the **Licence**) between you and **Springer Nature Customer Service Centre GmbH** (the **Licensor**). By clicking 'accept' and completing the transaction for the material (**Licensed Material**), you also confirm your acceptance of these terms and conditions.

1. Grant of License

1. 1. The Licensor grants you a personal, non-exclusive, non-transferable, world-wide licence to reproduce the Licensed Material for the purpose specified in your order only. Licences are granted for the specific use requested in the order and for no other use, subject to the conditions below.

1. 2. The Licensor warrants that it has, to the best of its knowledge, the rights to license reuse of the Licensed Material. However, you should ensure that the material you are requesting is original to the Licensor and does not carry the copyright of another entity (as credited in the published version).

1. 3. If the credit line on any part of the material you have requested indicates that it was reprinted or adapted with permission from another source, then you should also seek permission from that source to reuse the material.

2. Scope of Licence

2. 1. You may only use the Licensed Content in the manner and to the extent permitted by these Ts&Cs and any applicable laws.

2. 2. A separate licence may be required for any additional use of the Licensed Material, e.g. where a licence has been purchased for print only use, separate permission must be obtained for electronic re-use. Similarly, a licence is only valid in the language selected and does not apply for editions in other languages unless additional translation rights have been granted separately in the licence. Any content owned by third parties are expressly excluded from the licence.

2. 3. Similarly, rights for additional components such as custom editions and derivatives require additional permission and may be subject to an additional fee. Please apply to Journalpermissions@springernature.com/bookpermissions@springernature.com for these rights.

2. 4. Where permission has been granted **free of charge** for material in print, permission may also be granted for any electronic version of that work, provided that the material is incidental to your work as a whole and that the electronic version is essentially equivalent to, or substitutes for, the print version.

2. 5. An alternative scope of licence may apply to signatories of the STM Permissions Guidelines, as amended from time to time.

3. Duration of Licence

3. 1. A licence for is valid from the date of purchase ('Licence Date') at the end of the relevant period in the below table:

Scope of Licence	Duration of Licence
Post on a website	12 months

Presentations	12 months
Books and journals	Lifetime of the edition in the language purchased

4. Acknowledgement

4. 1. The Licensor's permission must be acknowledged next to the Licenced Material in print. In electronic form, this acknowledgement must be visible at the same time as the figures/tables/illustrations or abstract, and must be hyperlinked to the journal/book's homepage. Our required acknowledgement format is in the Appendix below.

5. Restrictions on use

5. 1. Use of the Licensed Material may be permitted for incidental promotional use and minor editing privileges e.g. minor adaptations of single figures, changes of format, colour and/or style where the adaptation is credited as set out in Appendix 1 below. Any other changes including but not limited to, cropping, adapting, omitting material that affect the meaning, intention or moral rights of the author are strictly prohibited.

5. 2. You must not use any Licensed Material as part of any design or trademark.

5. 3. Licensed Material may be used in Open Access Publications (OAP) before publication by Springer Nature, but any Licensed Material must be removed from OAP sites prior to final publication.

6. Ownership of Rights

6. 1. Licensed Material remains the property of either Licensor or the relevant third party and any rights not explicitly granted herein are expressly reserved.

7. Warranty

IN NO EVENT SHALL LICENSOR BE LIABLE TO YOU OR ANY OTHER PARTY OR ANY OTHER PERSON OR FOR ANY SPECIAL, CONSEQUENTIAL, INCIDENTAL OR INDIRECT DAMAGES, HOWEVER CAUSED, ARISING OUT OF OR IN CONNECTION WITH THE DOWNLOADING, VIEWING OR USE OF THE MATERIALS REGARDLESS OF THE FORM OF ACTION, WHETHER FOR BREACH OF CONTRACT, BREACH OF WARRANTY, TORT, NEGLIGENCE, INFRINGEMENT OR OTHERWISE (INCLUDING, WITHOUT LIMITATION, DAMAGES BASED ON LOSS OF PROFITS, DATA, FILES, USE, BUSINESS OPPORTUNITY OR CLAIMS OF THIRD PARTIES), AND
WHETHER OR NOT THE PARTY HAS BEEN ADVISED OF THE POSSIBILITY OF SUCH DAMAGES. THIS LIMITATION SHALL APPLY NOTWITHSTANDING ANY

FAILURE OF ESSENTIAL PURPOSE OF ANY LIMITED REMEDY PROVIDED HEREIN.

8. Limitations

8. 1. ***BOOKS ONLY:*** Where **'reuse in a dissertation/thesis'** has been selected the following terms apply: Print rights of the final author's accepted manuscript (for clarity, NOT the published version) for up to 100 copies, electronic rights for use only on a personal website or institutional repository as defined by the Sherpa guideline (www.sherpa.ac.uk/romeo/).

8. 2. For content reuse requests that qualify for permission under the STM Permissions Guidelines, which may be updated from time to time, the STM Permissions Guidelines supersede the terms and conditions contained in this licence.

9. Termination and Cancellation

9. 1. Licences will expire after the period shown in Clause 3 (above).

9. 2. Licensee reserves the right to terminate the Licence in the event that payment is not received in full or if there has been a breach of this agreement by you.

Appendix 1 — Acknowledgements:

For Journal Content:
Reprinted by permission from [**the Licensor**]: [**Journal Publisher** (e.g. Nature/Springer/Palgrave)] [**JOURNAL NAME**] [**REFERENCE CITATION** (Article name, Author(s) Name), [**COPYRIGHT**] (year of publication)

For **Advance Online Publication papers:**
Reprinted by permission from [**the Licensor**]: [**Journal Publisher** (e.g. Nature/Springer/Palgrave)] [**JOURNAL NAME**] [**REFERENCE CITATION** (Article name, Author(s) Name), [**COPYRIGHT**] (year of publication), advance online publication, day month year (doi: 10.1038/sj.[JOURNAL ACRONYM].)

For Adaptations/Translations:
Adapted/Translated by permission from [**the Licensor**]: [**Journal Publisher** (e.g. Nature/Springer/Palgrave)] [**JOURNAL NAME**] [**REFERENCE CITATION** (Article name, Author(s) Name), [**COPYRIGHT**] (year of publication)

Note: For any republication from the British Journal of Cancer, the following credit line style applies:

Reprinted/adapted/translated by permission from [**the Licensor**]: on behalf of Cancer Research UK: : [**Journal Publisher** (e.g. Nature/Springer/Palgrave)] [**JOURNAL**

NAME] [**REFERENCE CITATION** (Article name, Author(s) Name), [**COPYRIGHT]** (year of publication)

For **Advance Online Publication** papers:
Reprinted by permission from The [**the Licensor**]: on behalf of Cancer Research UK: [**Journal Publisher** (e.g. Nature/Springer/Palgrave)] [**JOURNAL NAME**] [**REFERENCE CITATION** (Article name, Author(s) Name), [**COPYRIGHT**] (year of publication), advance online publication, day month year (doi: 10.1038/sj. [JOURNAL ACRONYM])

For Book content:
Reprinted/adapted by permission from [**the Licensor**]: [**Book Publisher** (e.g. Palgrave Macmillan, Springer etc) [**Book Title**] by [**Book author**(s)] [**COPYRIGHT**] (year of publication)

Other Conditions:

Version 1.3

Questions? customercare@copyright.com or +1-855-239-3415 (toll free in the US) or +1-978-646-2777.

American Physical Society
Reuse and Permissions License

27-Apr-2021

This license agreement between the American Physical Society ("APS") and Samuel John Palmer ("You") consists of your license details and the terms and conditions provided by the American Physical Society and SciPris.

Licensed Content Information

License Number:	**RNP/21/APR/039349**
License date:	27-Apr-2021
DOI:	10.1103/PhysRevLett.100.013905
Title:	Reflection-Free One-Way Edge Modes in a Gyromagnetic Photonic Crystal
Author:	Zheng Wang et al.
Publication:	Physical Review Letters
Publisher:	American Physical Society
Cost:	USD $ 0.00

Request Details

Does your reuse require significant modifications: No

Specify intended distribution locations:	Worldwide
Reuse Category:	Reuse in a thesis/dissertation
Requestor Type:	Student
Items for Reuse:	Figures/Tables
Number of Figure/Tables:	1
Figure/Tables Details:	Figure 3b
Format for Reuse:	Electronic and Print
Total number of print copies:	Up to 1000

Information about New Publication:

University/Publisher:	Imperial College London
Title of dissertation/thesis:	Revealing hidden topologies within photonic crystals
Author(s):	Samuel John Palmer
Expected completion date:	May. 2021

License Requestor Information

Name:	Samuel John Palmer
Affiliation:	Individual
Email Id:	sjp112@ic.ac.uk
Country:	United Kingdom

American Physical Society
Reuse and Permissions License

TERMS AND CONDITIONS

The American Physical Society (APS) is pleased to grant the Requestor of this license a non-exclusive, non-transferable permission, limited to Electronic and Print format, provided all criteria outlined below are followed.

1. You must also obtain permission from at least one of the lead authors for each separate work, if you haven't done so already. The author's name and affiliation can be found on the first page of the published Article.
2. For electronic format permissions, Requestor agrees to provide a hyperlink from the reprinted APS material using the source material's DOI on the web page where the work appears. The hyperlink should use the standard DOI resolution URL, http://dx.doi.org/{DOI}. The hyperlink may be embedded in the copyright credit line.
3. For print format permissions, Requestor agrees to print the required copyright credit line on the first page where the material appears: "Reprinted (abstract/excerpt/figure) with permission from [(FULL REFERENCE CITATION) as follows: Author's Names, APS Journal Title, Volume Number, Page Number and Year of Publication.] Copyright (YEAR) by the American Physical Society."
4. Permission granted in this license is for a one-time use and does not include permission for any future editions, updates, databases, formats or other matters. Permission must be sought for any additional use.
5. Use of the material does not and must not imply any endorsement by APS.
6. APS does not imply, purport or intend to grant permission to reuse materials to which it does not hold copyright. It is the requestor's sole responsibility to ensure the licensed material is original to APS and does not contain the copyright of another entity, and that the copyright notice of the figure, photograph, cover or table does not indicate it was reprinted by APS with permission from another source.
7. The permission granted herein is personal to the Requestor for the use specified and is not transferable or assignable without express written permission of APS. This license may not be amended except in writing by APS.
8. You may not alter, edit or modify the material in any manner.
9. You may translate the materials only when translation rights have been granted.
10. APS is not responsible for any errors or omissions due to translation.
11. You may not use the material for promotional, sales, advertising or marketing purposes.
12. The foregoing license shall not take effect unless and until APS or its agent, Aptara, receives payment in full in accordance with Aptara Billing and Payment Terms and Conditions, which are incorporated herein by reference.
13. Should the terms of this license be violated at any time, APS or Aptara may revoke the license with no refund to you and seek relief to the fullest extent of the laws of the USA. Official written notice will be made using the contact information provided with the permission request. Failure to receive such notice will not nullify revocation of the permission.
14. APS reserves all rights not specifically granted herein.
15. This document, including the Aptara Billing and Payment Terms and Conditions, shall be the entire agreement between the parties relating to the subject matter hereof.